UCLA
UCLA Electronic Theses and Dissertations

Title

Controlling the Morphology and Conductivity of Organic Electronic Devices through Sequential Processing: Use of Solvent Additives as Polymer Swelling Agents and Evaporated F4TCNQ as a Polymer Dopant

Permalink

https://escholarship.org/uc/item/3mk9k55x

Author

Fontana, Matthew Thomas

Publication Date

2018

Peer reviewed|Thesis/dissertation

eScholarship.org Powered by the California Digital Library
University of California

UNIVERSITY OF CALIFORNIA

Los Angeles

Controlling the Morphology and Conductivity of Organic Electronic Devices through Sequential Processing: Use of Solvent Additives as Polymer Swelling Agents and Evaporated F_4TCNQ as a Polymer Dopant

A dissertation submitted in partial satisfaction

of the requirements for the degree

Doctor of Philosophy in Chemistry

by

Matthew Thomas Fontana

2018

© Copyright by

Matthew Thomas Fontana

2018

ABSTRACT OF THE DISSERTATION

Controlling the Morphology and Conductivity of Organic Electronic Devices through Sequential Processing: Use of Solvent Additives as Polymer Swelling Agents and Evaporated F_4TCNQ as a Polymer Dopant

by

Matthew Thomas Fontana
Doctor of Philosophy in Chemistry
University of California, Los Angeles, 2018
Professor Benjamin Joel Schwartz, Chair

This thesis focuses on adding small-molecule acceptor materials to semiconducting polymer films. Semiconducting polymers are widely studied because they share the low-cost processing of plastics, but also have many electronic applications. Semiconducting polymers, however, require nanoscale mixing with an electron acceptor to be useful for these device applications. Based on the energy-level offset of the two materials, two classes of devices are present: mixing the polymer with an electron acceptor for the excited state yields a solar cell while mixing the polymer with a ground-state electron acceptor chemically dopes the polymer and significantly increases the polymer conductivity. My work focuses on investigating the fundamental mechanism of adding acceptor molecules to polymers and how this affects the device properties and structure.

Chapter 1 introduces the field of organic electronics, providing background for organic materials and their device physics in solar cell and doping applications. Chapter 2 is a published book chapter that describes sequential processing (SqP), which is an alternative fabrication technique for intercalating small-molecule acceptors into polymer films. This chapter discusses and connects the various work on SqP to-date. Chapter 3 investigates the widespread use of solvent additives for use in organic photovoltaics. In this chapter I detail how fabricating solar cells via SqP allows the mechanism of low-vapor pressure solvent additives such as 1,8-diiodooctane (DIO) to be

understood: low-vapor-pressure solvent additives act as polymer swelling agents that give extra time and enhanced mobility for the electron acceptor to effectively distribute throughout the polymer network. Since almost all high-performing solar cells require the use of additives such as DIO, this published work helps explain a key component in the solar cell fabrication process. Chapter 4 studies the photophysics of a perylenediimide dimer molecule (di-PDI) used as a solar cell acceptor material. This chapter details that a solution of the di-PDI acts a blend of two molecules, each with very different spectroscopy. The different spectroscopy for each molecule results from the presence of two stable di-PDI conformers: one conformer adopts a 'closed' geometry, with significant pi-stacking between the PDI monomers, while the other conformer adopts an 'open' geometry with little interaction between the monomers. With two conformers present, this leads to important considerations for device applications with regards to extra light absorption and the possibility of traps. Chapter 5 investigates the addition of ground-state acceptor dopant molecules to P3HT by both evaporation and solution sequential processing. In this chapter I describe how both methods effectively dope films of P3HT ranging from 25 nm to 2 μm. The 2 μm thick films are the thickest films doped by single-step fabrication for the materials combination studied. Thermoelectric devices were made via both methods and the thermoelectric performance is quite similar, indicating that one can select from two very different processing techniques to fabricate thermoelectrics. In summary, sequential processing is a reproducible technique that allows fundamental investigations into a broad range of organic electronics in addition to device application studies.

The dissertation of Matthew Thomas Fontana is approved.

Stuart Brown

Yves F Rubin

Benjamin Joel Schwartz, Committee Chair

University of California, Los Angeles

2018

To my mom and dad who have always been my full-time cheerleaders in school.

TABLE OF CONTENTS

LIST OF FIGURES

LIST OF TABLES

ACKNOWLEDGMENTS

First and foremost, I would like to thank my mom and dad. You have always been there for me with your loving care and support. You two were my first teachers and taught me early on the importance of being a kind and caring person. You also set a great role model for how to teach. You always answered my never-ending questions and your explanations were always very clear and thoughtful. In particular, I always enjoyed learning about nature and gardening from you. Thank you for supporting me in many ways throughout my entire education. From helping me with my weekly spelling words to quizzing me on vocabulary you always helped and encouraged me to try my best in school. Thank you for always being there to listen to me talk about how school went and encourage me throughout my many years of school. Thank you so much for being my full-time cheerleaders.

I would like to thank my advisor Ben Schwartz for his guidance and help during my time in graduate school. He is very passionate about science and has the ability to organize data so that the scientific story is clear, articulate, focused, and easier to read. Each time I received feedback from him in preparing for a presentation or writing a new draft for a paper, I improved as a science writer and learned how to better organize data: through the use of colons my writing and titles also improved quite a bit. I would also like to thank Sarah Tolbet and Yves Rubin. Both of them shared science with me weekly over the years and had valuable suggestions for my research. I also benefited from their tips in making science conversational and how to implement graphic design in preparing data plots. I would also like to thank Yves Rubin and Stuart Brown for serving on my committee and offering their guidance with my thesis and career goals.

I want to thank the former graduate students who helped me not only become the scientist and teacher I am today, but also helped make for such a great working environment.

I must start with Guang (AKA: Master Guang), who was my office-mate, mentor, and friend. I was very fortunate and lucky to be paired with him as my lab mentor. He was always very kind, patient, and encouraging. Guang served as a great role model for how I should treat others when explaining science. His advice really helped prepare me for what graduate school would require

and his work-ethic is the best I have ever seen. I really enjoyed our late-night work sessions in the lab or office, and it was nice having him around when experiments ran late.

I was very lucky to work with Jordan who helped teach me solar cell science and share my huge passion for Star Wars. While discussing science I could, and often would, relate it to Star Wars and Jordan would always get the reference. Jordan was always very easy to work with. Furthermore, since our projects were in the same area, I am grateful for his advice and help. Performing nanoscience outreach experience with him was always a lot of fun.

I enjoyed working with Steve and I learned many details regarding device physics from him. His stories about science were always fun to listen to. He is one of the most enthusiastic and well-read scientists I have ever met. He also has the natural ability to know what experiments and projects are worth investigating and in the proper order too. I enjoyed talking to him in the lab about California and its natural landscapes as fun places to visit.

In the rest periods of working in the lab, Ben Fink's office was always a welcome place for movie discussions. Since Ben, like Jordan, was a huge Star Wars fan, us three would spend hours discussing Star Wars and watching every type of movie review. I am also thankful to Ben for helping get me associated with the PEERS program at UCLA and I had the pleasure of working with him for a couple years as a workshop facilitator. I learned a lot from our teaching discussions and always appreciated his questions that allowed me to look at teaching in new ways.

I am very thankful to overlap with Jenny during my time in graduate school. Being a senior student, she was my go-to person for all questions regarding teaching. She was a great help with all the little questions a first-year TA would have and over time, these questions developed into more teaching-practice questions. I always enjoyed discussing teaching with her and through these discussion learned so much about what it means to be a good and thoughtful teacher. She also served as a great role model with how friendly and supportive of others she was. I also enjoyed her "go electron go!" discussions in group meeting.

I am very thankful to have worked with Zongwu. I first met Zongwu when he was a student in my general chemistry lab class. After the first day of class he asked to join the research lab and I had the honor and privilege of mentoring Zongwu for three years. Mentoring him starting from

my first years in graduate school helped make me a better researcher through my discussions and experiment planning with him. I always enjoyed his positive attitude and outstanding work ethic. Not only was Zongwu efficient in the lab, but he was fast and could make solar cells like the rest of us. His excitement for lab research was always much appreciated. It was an honor seeing him spend his first days cleaning glass and silicon substrates to helping me by making entire solar cells from start to finish.

I also want to thank the graduate students who I worked with for the majority of my time in the lab.

I am very glad and honored to have worked with Tyler for the majority of my graduate school years. Tyler is an inspiration as someone who can both efficiently do science and be a family man. Tyler is an outstanding person with great character and serves as a role model to many people in terms of how he acts, treats others, and the science he does. I enjoyed working more closely with him when we started working together on the same project for the new area of polymer doping he pioneered.

I am very glad Taylor joined our lab in her second year of graduate school. She brought to the lab a new perspective of organization and a genuine enthusiasm for science. I especially appreciate her helping build lab community by encouraging more group events. This helped improve the lab community greatly and was a very nice improvement to the lab. She was a major help in fixing many of the broken or run-down equipment in the lab. I enjoyed talking to her about teaching styles and practices, and I am thankful for her bringing to my attention new areas of teaching.

I am very thankful to have joined the research group and graduate school at the same time as Devon and Erik. From working late on physical chemistry problem sets to going through all of the hoops of graduate school, I enjoyed working on this journey together with you two.

I always appreciated Devon's kind attitude and group events she organized. In particular, I enjoyed her hot pot dinners and annual Over the Garden Wall parties. Teaching with Devon were some of the best teaching experiences as I enjoyed writing fun questions with her and learned how to be a better teacher from her. Furthermore, I highly respect Devon's dedication to her family while working on her research and teaching.

I enjoyed talking to Erik about many science and non-science topics during my time in graduate school. I always enjoyed going into his office to talk about some parallels between video games, music, or science. Erik is an outstanding scientist and knowledgeable in many areas. I enjoyed working with him together in the lab and learning the details of laser spectroscopy. I also enjoyed playing video games with Erik after finishing classes and enjoyed LAN parties with him and the rest of the research group.

I had a fun time working with Dane over the past couple years and he is a great new addition to the lab. His eager attitude to do new experiments and science was a great breath of fresh air and it was a great experience working with Dane. I enjoyed talking to Dane in the lab about many topics, especially all of the cool and fun places to visit in California.

I am very thankful and appreciative to everyone who worked in the lab with me for being supporters of my video game music interests. Whether I was listening to a moving piece of music from the credits of a Mario game or music from an epic boss battle, you were all good with me listening to the music as I worked. I enjoyed talking to you all about music and the wide assortment of musical instruments. It was a fun rest for me and I enjoyed sharing my passion for video game music with all of you.

I am very grateful for having shared my office with great people and friends. I shared my office with Guang for over three years and enjoyed his company. Zach was great to have in the office and I enjoyed our teaching discussions. Sanghyun was always fun to talk to and watch TV shows with on Friday afternoons. You all made the non-lab hours enjoyable and the office a place to look forward to be in.

I am thankful to all those who assisted with experiments and analysis for collaboration projects.

I would like to thank all those who helped me in my collaborative projects. Your assistance, scientific input, and teaching me about your area of expertise all helped contribute toward generating exciting multi-dimensional research stories. Hyeyeon was a great help with collection of X-ray data and worked with me in collecting ellipsometry data for the solvent additive project on many samples. Patrick collected neutron reflectometry data also collected X-ray data on many samples. KJ collected and analyzed X-ray data. Laura helped collect XPS data for me. Selvam and Ye-Jin

synthesized polymers for me. Erik spent countless hours running femtosecond measurements for me and helped with temperature-dependent photoluminescence measurements. Chen-Chen and Peiqi performed TD-DFT calculations on the PDI system. Yolanda and Nick synthesized dye molecules for me. Matthew was always a great help whenever I had a question regarding the fluorimeter.

I am very thankful to all those who served as my mentor teachers. Dr. Pang, Dr. Russell, Brent, Dr. Hardinger, Jia, and Elaine collectively share many years of thoughtful teaching experience and I am very thankful to have learned from all of them for multiple years.

I taught the most times with Dr. Pang and am very thankful to have TAed with him during my first quarter of graduate school. By having a quick conversation with Dr. Pang in his office, I was able to learn so many valuable and practical teaching methods and practices. Having his office very close to my lab office, I would frequently drop by his office for an enjoyable chat about the class I was TAing with him or about teaching in general. Dr. Pang is a great role model for demonstrating the importance of being an organized teacher. His classes were always a joy to TA for since he made everything very easy for me to implement. This also applies to his teaching where his helpful explanations and resources allowed his students to master difficult material because they were so well prepared. Meeting Dr. Pang in my first quarter of graduate school allowed me to work with him later on in various roles as a teacher. I very much enjoyed making laboratory instructional videos with him and learned from him countless helpful pointers in how to present material in a video format. I also TAed with Dr. Pang every summer and always enjoyed our liquid nitrogen ice cream parties.

I started working with Dr. Russell when I was a Teaching Assistant Consultant and helped teach the new TAs with her and Dr. Pang. This was when I first started to learn about course development and Dr. Russell is a very helpful mentor in this area. I also took two graduate courses from her: these classes are the Preparing Future Faculty (PFF) course and Scientific Writing course. These two courses are among the most beneficial classes I took in graduate school. The PFF class is a gem of the Chemistry and Biochemistry Department and helped me start thinking early-on about what kind of teaching environment I would like to teach in. Furthermore, based on my teaching goals, Dr. Russell helped me get involved in teaching activities that would give me new teaching experiences. This includes science-teacher mentorship programs that put me in a group

of enthusiastic undergraduate and graduate students who all wanted to become teachers. Being part of this group was very enjoyable and provided me a fantastic community to participate in. The scientific writing course significantly improved my writing and allowed me to better enjoy the English language. Dr. Russell is a very kind and true mentor. She cares about everyone she works with and is very supportive. I am very thankful for all of her advice and encouragement as I worked on my teaching and research goals.

I had the fun time and privilege of working with Brent for over three years in the Program for Excellence and Education in the Research Sciences (PEERS) program. In PEERS, I leaned how to teach in a collaborative-learning workshop environment. Being not as structured as a lecture or discussion, Brent's skillful art in teaching allowed me to learn many tricks of the trade. He has many years of experience and has a talent in allowing students to arrive at answers themselves while having a fun time learning from each other. His facilitator meetings were always fun to attend and he treated everyone with respect. I always enjoyed talking to Brent about various types of teaching and he was great in encouraging me to try both new and old methods that work well. I also enjoyed talking to Brent about California wildflowers and all of the great places to see great sights in the state.

I worked with Dr. Hardinger for two quarters while I TAed introductory organic chemistry. Being the first time I taught an organic chemistry lecture class, he was very helpful and supportive when I would have questions. His course materials are an incredible resource and serve as a great example for teaching organic chemistry. He has a great amount of teaching experience and I am thankful to have learned from him.

I enjoyed working with Jia for all of the California NanoSystems Institute (CNSI) outreach events. Jia is an incredible educator and science communicator. I had the privilege of developing a two-week, summer, high school, nanoscience class with Jia. In this teaching development, I was able to see Jia's creativity and focus with regards to teaching. Jia is also very helpful and will always offer his assistance to any person or group who wants to learn about science. By working with Jia, I learned the best ways to communicate technical science with enthusiasm so everyone can enjoy a shared excitement for science.

I worked with Elaine for all of the CNSI outreach events, including the two-week summer camp. Elaine coordinated and organized all of the outreach events and was always a positive influence on the outreach activity. She helped bring a welcoming and supportive environment to all of the outreach events. Elaine was always very helpful whenever I would need to ask her help for a teaching activity with CNSI or with an activity not related to CNSI. She also was great in getting people into contact with resources that would best teach nanoscience to children and the general public.

I have been very fortunate to work with such a great group of people and thank you for providing me with the fondest memories of UCLA.

Chapter 2 is a version of Reference 8, reproduced with permission from World Scientific Publishing Company. First appeared in, World Scientific Handbook of Organic Optoelectronic Devices - Volume 2: Organic Photovoltaics (OPVs), Ed. Franky So, Vol. Ed. Barry C. Thompson (World Scientific Publishing Company) pp. 309-348 (2018). This chapter is a book chapter written on the work done in the group pertaining to sequential processing. Taylor J. Aubry, D. Tyler Scholes, and Steven A. Hawks assisted with the writing. The project director was Benjamin Joel Schwartz.

Chapter 3 and Appendix A are reproduced with permission from the ACS family of journals. Hyeyeon Kang assisted in collecting the ellipsometry and swelling measurements, and collected the grazing incident wide angle X-ray scattering measurements. Patrick Y. Yee collected the neutron reflectometry data. Zongwu Fan assisted in fabricating solar cells. Steven A. Hawks helped with collection of external quantum efficiency measurements and assisted with helpful discussions. Laura T. Schelhas collected X-ray photoelectron spectroscopy measurements. Selvam Subramaniyan and Ye-Jin Hwang synthesized the polymer PSEHTT. This chapter was supported by the National Science Foundation (NSF) under Grant Numbers CBET-1510353 and CHE-1608957. The XPS instrument used in this work was obtained with support from NSF under grant number 0840531. The X-ray diffraction studies presented in this manuscript were carried out at the Stanford Synchrotron Radiation Lightsource. Use of the Stanford Synchrotron Radiation Lightsource, SLAC National Accelerator Laboratory, is supported by the U.S. Department of Energy, Office of Science, Office of Basic Energy Sciences, under Contract DE-AC02-76SF00515. Neutron reflectometry studies made use of the ORNL Spallation Neutron Source, which is supported by the Scientific User

Facilities Division, Office of Basic Energy Sciences, U.S. Department of Energy. Contributions from Steven A. Hawks were performed under the auspices of the U.S. Department of Energy by LLNL under Contract DE-AC52-07NA27344. I thank Jordan C. Aguirre and Guangye Zhang for helpful discussions. The project directors were Samson A. Jenekhe, Sarah H. Tolbert, and Benjamin Joel Schwartz.

Chapter 4 and Appendix B are versions of unpublished work and will be submitted for publication shortly after filing this dissertation. Erik P. Farr performed the ultrafast measurements, assisted in steady-state spectroscopy measurements, and co-wrote the manuscript. Chen-Chen Zho and Peiqi Wu performed the TD-DFT calculations. Yolanda Li and Nicholas Knutson synthesized the monomer and dimer PDI molecules. The project directors were Yves F. Rubin and Benjamin J. Schwartz.

Chapter 5 and Appendix C are versions of unpublished work and will be submitted for publication shortly after filing this dissertation. D. Tyler Scholes offered many ideas for the project design and implementation. He co-wrote the manuscript, collected the solution-doping measurements, built the thermoelectric setup, and coded the thermoelectric computer interface. Dane A. Stanfield assisted in building the thermoelectric setup, assisted in collecting the thermoelectric results, and collected IR data. The project director was Benjamin J. Schwartz.

VITA

2014	C.Phil. Chemistry, University of California, Los Angeles
2013	M.S. Chemistry, University of California, Los Angeles
2012	B.S. Chemistry, Sonoma State University
2012	B.A. Physics, Sonoma State University
2017	UCLA Academic Senate Distinguished Teaching Assistant Award
2017	UCLA Distinguished Teaching Assistant Dissertation Year Fellowship
2015	UCLA Collegium of University Teaching Fellow
2014	UCLA Chemistry and Biochemistry Hanson-Dow Excellence in Teaching Award

PUBLICATIONS AND PRESENTATIONS

M. T. Fontana, H. Kang, P. Y. Yee, Z. Fan, S. A. Hawks, L. T. Schelhas, S. Subramaniyan, Y. J. Hwang, S. A. Jenekhe, S. H. Tolbert, and B. J. Schwartz, “Low-Vapor-Pressure Solvent Additives Function as Polymer Swelling Agents in Bulk Heterojunction Organic Photovoltaics," *J. Phys. Chem. C*, textbf/122, 16574-16588 (2018).

M. T. Fontana, T. J. Aubry, D. Tyler Scholes, S. A. Hawks and B. J. Schwartz, "Sequential Processing: A Rational Route for BHJ Formation via Polymer Swelling," *World Scientific Handbook of Organic Optoelectronic Devices*, Volume 2: Organic Photovoltaics, Chapter 8 (2018).
DOI: 10.1142/9789813239517_0008

T. J. Aubry, A. S. Ferreira, P. Y. Yee, J. C. Aguirre, S. A. Hawks, **M. T. Fontana**, B. J. Schwartz and S. H. Tolbert, "Processing Methods for Obtaining a Face-On Crystalline Domain Orientation in Conjugated Polymer-Based Photovoltaics," *J. Phys. Chem. C*, **122**, (2018).
DOI: 10.1021/acs.jpcc.8b02859

S. Huang, G. Zhang, N. S. Knutson, **M. T. Fontana**, R. C. Huber, A. S. Ferreira, S. H. Tolbert, B. J. Schwartz and Y. Rubin, "Beyond PCBM: Methoxylated 1,4-bisbenzyl[60] Fullerene Adducts for Efficient Organic Solar Cells," *J. Mater. Chem. A*, **4**, 416-424 (2016).
DOI: 10.1039/C5TA07688A

C. M. J. Campbell, **M. T. Fontana**, B. C. Taggart, M.-C. Su, C.-L. Lin, H.-C. Chang and H.-J. Chen, "Acid Denaturation and Refolding of Cytochrome c on Silica Surface," *Jnl. Chinese Chemical Soc.*, **59**, 140-152 (2013).
DOI: 10.1002/jccs.201200417

D. Khuseynov, **M. T. Fontana** and A. Sanov, "Photoelectron Spectroscopy and Photochemistry of Tetracyanoethylene Radical Anion in the Gas Phase," *Chem. Phys. Lett.*, **550**, 15-18 (2012).
DOI: 10.1016/j.cplett.2012.08.035

M. T. Fontana, "Solvent Additives for Improved Polymer/Fullerene Photovoltaics." Sonoma State University Chemistry Department Seminar, Invited Talk, 2016.

M. T. Fontana, "Tuning the Degree of Intermixing in Sequentially Processed Polymer/Fullerene Photovoltaics: The Role of Swelling by Solvent Additives." ACS National Meeting Talk, 2016.

CHAPTER 1

Introduction: Organic Electronics

1.1 Economics of Solar Energy

The sun is an incredible source of free energy. At the edge of the Earth's atmosphere, the sun supplies an average of 1,370 W of solar power for every square meter. However, on the surface of the Earth, this number drops to 343 W/m^2 since the atmosphere will scatter approximately 30% of this light intensity and absorb another 19%.[9] Converting this solar flux to a power by integrating this flux over the Earth's total surface area, the average total power supplied by the sun to the Earth is calculated as 89,300 TW. Thus, 89,300 TJ of energy is supplied to the Earth every second. However, the Earth is 29% land, which means that 25,897 TW is supplied to available land. Since the sun illuminates a little over 50% of the Earth at any given time, on average 15% of the Earth is illuminated by the sun. Thus, of the 89,300 TJ supplied by the sun, roughly 13,000 TW can be collected. Since this assumes solar panels covering all of the Earth's available land, this value is a maximum. In 2015, the world energy consumption was 4.5 x 10^{20} J.[10] Thus, if all of the energy supplied by the sun were to be collected, it would take approximately ten hours of sunlight to provide the Earth's annual energy needs. Since in practice the entire Earth would not be covered all in solar cells and a fraction of the land illuminated will not all receive sunlight at near-perpendicular angles, this estimate is more realistically on the order of a day. Nonetheless, the sun provides an incredible amount of free energy every day.

Since the Earth reliably provides such a large amount of energy at no cost and no additional environmental impact, it is both an economic and environmental consideration to implement solar energy. However, although the energy itself is free, building the infrastructure to collect this energy is not. At present, the most widely used solar cell technology is crystalline silicon with a commercial

efficiency of approximately 18% to 20% and a laboratory-scale efficiency of 27%.[11,12] Although these numbers may appear to not be high efficiencies, the theoretical limit for a single-junction solar cell is limited to 30%. This is because a solar cell cannot use all of the energy from every photon: if the photon energy does not match the band gap, high energy photons excite electrons above the band-edge that lose energy to heat as they relax to the band edge, while low energy photons are not absorbed.[13] To increase the theoretical limit, multi-junction solar cells may attain theoretical efficiencies of 42% and 49% for two and three junctions, respectively.[14] However, such strategies increase the cost so the marginal gain is not economic. Such multi-junction solar cells find commercial use in space where the need for extra power exceeds takes priority to the cost of the solar cell itself.[15]

The ultimate goal for energy production is cheap and efficient energy collection. One alternative to conventional silicon solar cells are polymer-based solar cells. These solar cells are made using organic materials such as semiconducting polymers and small molecules, as opposed to silicon.[16,17] Being made of plastic, these solar cells are cheap. Furthermore, plastic solar cells strongly absorb light and are typically about 100 nm thick, whereas a silicon solar cell is typically a few microns thick. Thus, plastic solar cells are even lower cost on a per-mass basis and have a shorter energy return on investment.[18,19] However, although being cheap, organic solar cells have lower device efficiencies with the record laboratory-scale plastic solar cell reporting an efficiency of only 14%.[20] This lower efficiency will be explained below in the context of the device operation. Although the record laboratory-scale plastic solar cell reports an efficiency of 14%, large-area devices at best yield efficiencies of a few percent.[21,22] This is because large-area devices relies upon an entirely different fabrication process and, most importantly, different drying kinetics that ultimately require re-optimization of the laboratory-scale procedure.[23]

1.2 Solar Cell Operation and Considerations

Although inorganic and organic solar cells both generate charge carriers to produce a current, the process by which these two technologies do so is different. This is because inorganic and organic materials differ in order, crystallinity, and dielectric constant. Since inorganic materials are

crystalline and conduct charges well, they have a high dielectric constant. Organic materials, on the other hand, are a collection of molecules or polymers that associate with each other through secondary interactions and lack any long-range order. Thus, organic materials are not good conductors and have a low dielectric constant. The difference in order has a profound impact on the corresponding electron-generation mechanism for each type of material and is discussed in the following sections.

1.2.1 Inorganic Solar Cell Power Generation

When an inorganic material absorbs a photon, an excited-state electron is generated and leaves behind an absence of negative charge, which is called a hole. The highly crystalline inorganic crystal lattice supports delocalization of the electron and hole such that they are treated as independent charge carriers from the point they are generated. Furthermore, the high degree of crystallinity and order provides highly conductive pathways for the electron and hole to travel to the electrodes, increasing the current. Thus, every photon generates an electron that contributes to the photocurrent.

1.2.2 Organic Solar Cell Power Generation

When a semiconducting polymer such as poly(3-hexylthiophene-2,5-diyl) (P3HT) absorbs a photon, an excited-state electron and hole are generated, just as the case for inorganic materials. However, since the polymer is much more disordered than an inorganic crystal lattice, the electron and hole are greatly localized on the polymer chain. Considering that polymers have much lower dielectric constants in addition to the structural disorder, the electron and hole experience a greater attraction to one another since they cannot delocalize to a great extent. Since the electron and hole are Coulombically-bound to each other, the Coulomb-bound electron-hole pair is commonly referred to as an exciton. This is shown in Figure 1.1(a). Additionally, the exciton has a lifetime before the electron recombines with the hole. However, this process is detrimental to power generation since a photon was absorbed and a usable electron was not produced.

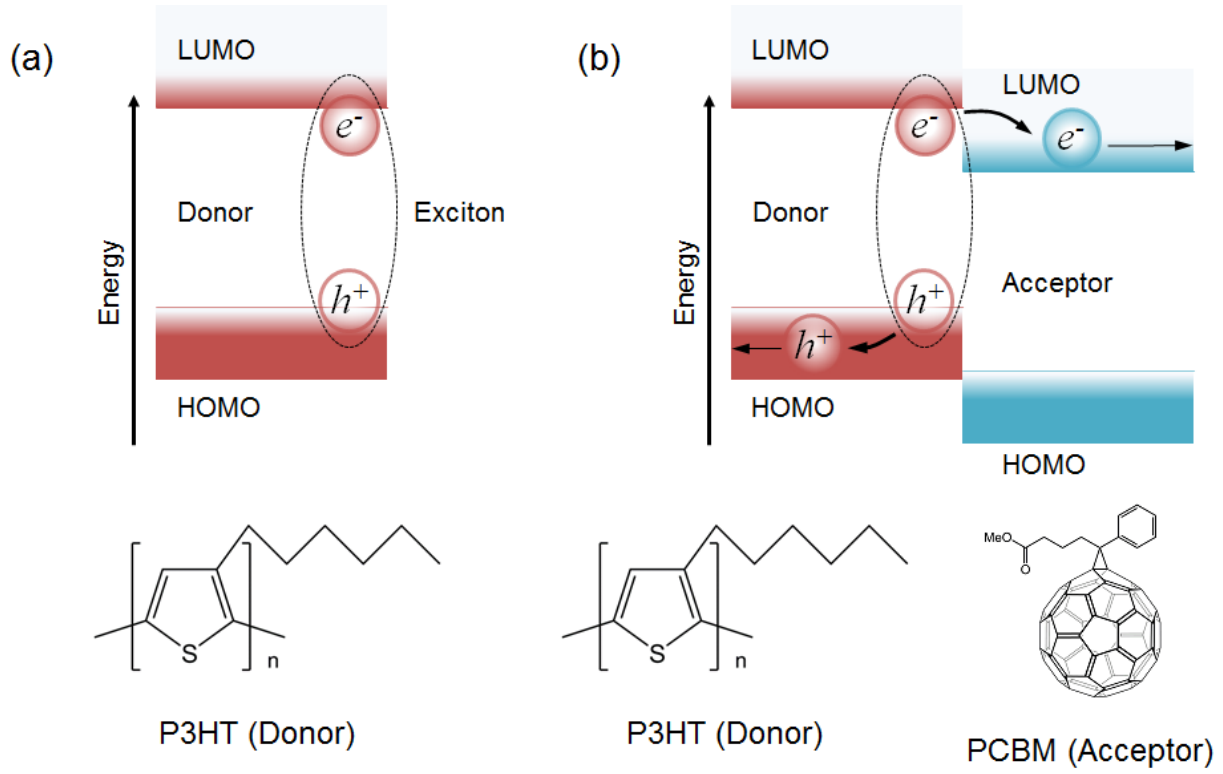

Figure 1.1: (a) Exciton generation upon polymer light absorption. (b) When a polymer electron donor material such as P3HT is paired with an electron acceptor such as PCBM, the electron will undergo charge-transfer from P3HT to PCBM, which is energetically downhill since the P3HT LUMO is higher in energy than the PCBM LUMO. This places an electron on the PCBM and a hole on P3HT.

To avoid exciton recombination, the polymer donor is mixed with a small molecule electron acceptor, typically a fullerene derivative such as phenyl-C_{61}-butyric acid methyl ester (PCBM). As shown in Figure 1.1(b), when the electron acceptor is selected so that its LUMO is lower in energy than the electron donor LUMO, the excited-state electron on the polymer donor will undergo charge-transfer to the electron acceptor. This process is critically important since the electron and hole are now on two separate materials. Furthermore, this separation splits the exciton and produces two polarons: one polaron is negatively charged and the other is positively charged. Being on two separate materials, the driving force for the electron and hole to recombine is less and since polarons are charged species, the two charges are swept out to the respective electrodes to produce a photocurrent. Since the solar cell under dark conditions is still a diode, the photocurrent adds to the dark current to increase the magnitude of the total current. As discussed below, the photocurrent

flows in the opposite direction of the dark current. When illuminated, the diode operates under reverse bias conditions: since the photocurrent exceeds the magnitude of the dark current, the reported current is negative.

1.2.3 Solar Cell Morphology: The Bulk Heterojunction

Organic solar cells require mixing of the donor and acceptor materials to split the exciton into separate charges. This three-dimensional mixing of the two materials is referred to as a bulk heterojunciton (BHJ). The BHJ is critically important because it ensures the presence of donor-acceptor interfaces where the excitons are split. If there is not enough mixing, the excitons will recombine before they reach a donor-acceptor interface. Because excitons have a lifetime and move along the polymer chain in this given time period, they therefore have a length that they that can diffuse. This exciton diffusion length is a key parameter and is typically 5 - 20 nm for polymer materials.[24] Therefore, sufficient mixing of the polymer and fullerene on the length scale of the exciton diffusion length ensures all photogenerated excitons are split. Additionally, it is important that continuous pathway of pure material exists as the electron and hole each have their own mobilities, which are material dependent. As such, electrons have much higher mobility on the fullerene while holes have a much higher mobility on the polymer. If a charge carrier is traveling along a pathway that is interrupted by a low mobility material, this will significantly reduce the current and lower the device efficiency.[25] Therefore, just as undermixing is unfavorable for device performance, overmixing is unfavorable as well. As shown in Figure 1.2, it is important that an optimal degree of mixing ensures both exiton splitting and continuous pathways to the electrodes.

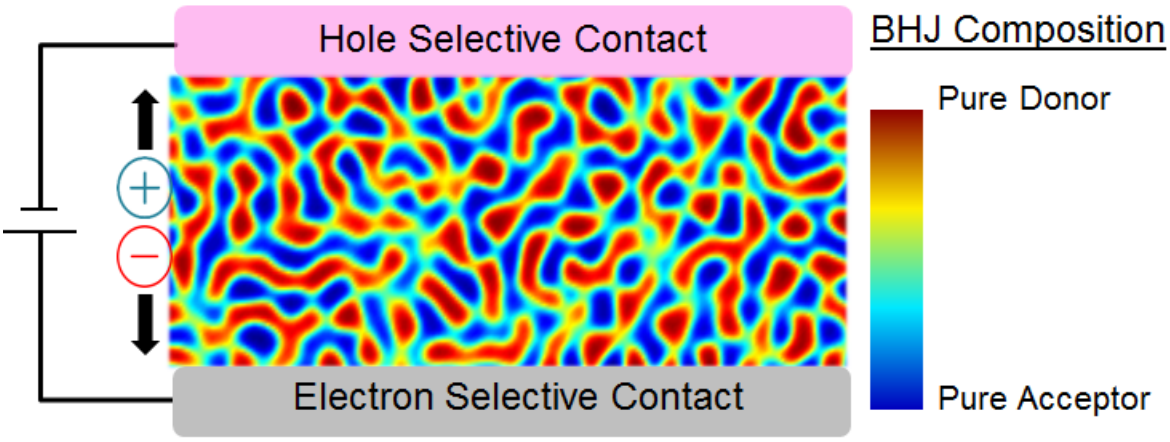

Figure 1.2: An idealized BHJ morphology where there is good mixing and optimal phase segregation. Pure donor domains are shown in red while pure acceptor domains are shown in blue.

1.2.4 Processing the Solar Cell Active Layer

Attaining an ideal morphology is a difficult challenge and depends on the processing conditions. The most widely used and simplest processing technique is blend-casting (BC). In BC, the polymer and fullerene are co-dissolved together in solution. Then the solution is spin-cast onto a substrate and the active layer forms as the host solvent evaporates. However, this leaves little room for tuning the active layer morphology. The most commonly used approach is to add a small amount of low-vapor-pressure co-solvents (commonly called solvent additives) to the blend solution. For the majority of systems that over-phase segregate, the additive swells the polymer film to facilitate improved mixing of the two materials.[3,26–36] Low-vapor-pressure solvent additives such as DIO and ODT acting as swelling agents is the subject of Chapter 3 for this treatise and demonstrates that the swelling properties are responsible for BHJ morphology improvement.

An alternative processing technique is sequential processing (SqP). SqP takes BHJ formation and decouples it into two, separate steps.[37] In the first step, a polymer film is spin-cast from a pure polymer solution. In the second step, a pure fullerene solution is spin-cast onto the polymer film to intercalate fullerene within the polymer film. The selection of the fullerene solvent is key as the solvent must first and foremost dissolve the fullerene. However, the solvent-polymer interaction is also very important: too low of a polymer-solvent interaction provides insufficient swelling and thus prevents fullerene intercalation while too high of an interaction dissolves the polymer film.[38,39]

Thus, the polymer-solvent interaction must be tuned to some optimal point in the middle where the solvent optimally swells the polymer film, but does not dissolve it.[38]

Often a single solvent cannot achieve the aforementioned criteria of both fullerene solubility and polymer swelling. For high-performing amorphous polymers, it is often the case that a good fullerene solvent also will dissolve the polymer film. A method to attain an ideal solvent is through solvent blends.[2,39] Here, a host solvent with high fullerene solubility is selected. However, since this solvent will dissolve many polymer films, a polymer non-solvent is added to the host solvent. This reduces the fullerene solubility, but since the host solvent solvent was selected for its high solubility, the solvent blend will still dissolve the fullerene. Therefore, the solvent blend will dissolve the fullerene and optimally swell the polymer film.

1.2.5 Solar Cell Device Efficiency

The figure of merit for how well a solar cell operates is the device efficiency or power conversion efficiency (PCE). This efficiency is defined as:

$$PCE = \frac{P_{\text{out}}}{P_{\text{in}}}$$

where the power output is P_{out} and the power input is P_{in}. From electronics, power is defined as:

$$P = IV$$

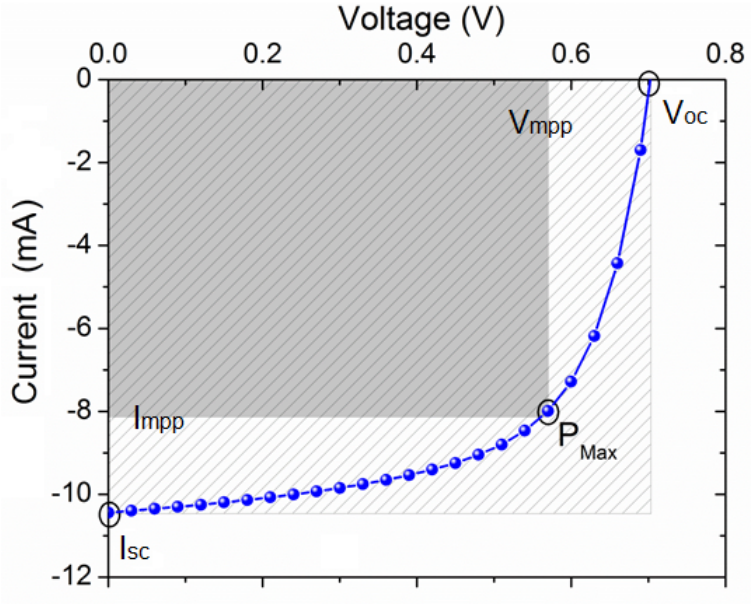

Figure 1.3: Solar cell *IV* curve. The current at zero voltage is the short-circuit current (I_{sc}) and the voltage at zero current is the open-circuit voltage (V_{oc}). The area ratio of the dark gray rectangle to the light gray rectangle is the fill factor (FF). The current and voltage that define the maximum power (P_{max}) are the maximum power point current (I_{mpp}) and voltage(V_{mpp}).

where the current (dark current + photocurrent) is I and the voltage is V. Taking a current vs. voltage sweep facilitates calculating the solar cell device efficiency as shown in Figure 1.3. At every point along the *IV* curve, the solar cell will produce a given power. When no bias voltage is applied, the cell is under short-circuit conditions and the current measured is the short-circuit current (I_{sc}). This current under short-circuit conditions is due to the voltage established by the electrode selection for the solar cell. As the bias voltage increases, charges are injected into the device, which oppose the current flow contributing to the short-circuit current. At the point when these two currents cancel, the voltage recorded is the open-circuit voltage (V_{oc}). Since the maximum current and voltage produced by the device are I_{sc} and V_{oc}, this is the expected maximum power point if everything were ideal. However, upon visual inspection of the *IV* characteristic, I_{mpp} and V_{mpp} do not align with I_{sc} and V_{oc}. This alignment only occurs when the *IV* curve is a perfect rectangle. While this ideal maximum power point is not attainable since a real solar cell is not ideal, as shown below it is useful for describing the maximum power point for real devices. Thus, the ideal maximum power point is defined as:

$$P_{max} = I_{mpp}V_{mpp}$$

With this expression in hand, the PCE based on the maximum power output from the solar cell is defined as:

$$PCE = \frac{P_{\text{max}}}{P_{\text{in}}}$$

$$PCE = \frac{I_{\text{mpp}} V_{\text{mpp}}}{P_{\text{in}}}$$

However, it is desirable to have a power expression in terms of the open-circuit voltage and short-circuit current since these parameters provide specific information about film morphology, light absorption, and recombination.[40–44] Since the power output is the area defined by the operating voltage and current, the ratio of the dark gray rectangle (power output of the experimental solar cell) to the light gray rectangle (power output of an ideal solar cell) gives the scaling factor for how much lower the power of the actual solar cell is when defined by I_{mpp} and V_{mpp}, compared to I_{sc} and V_{oc}. Therefore, P_{max} is defined alternatively as:

$$P_{\text{max}} = FF\, I_{\text{sc}} V_{\text{oc}}$$

where FF is the fill factor. Geometrically, the fill factor is the area of the dark gray rectangle to the light gray rectangle. Although the fill factor is used to introduce the short-circuit current and open-circuit voltage into the efficiency equation, the fill factor itself is a term that is rich in physical meaning. A high fill factor typically means the morphology of the solar cell is closer to the optimum.[40,44] Furthermore, more pure domains will have less recombination, which is also shown in a high fill factor.[43,44] This explains why the the output of the experimental solar cell is less than the power output of an ideal solar cell: even though the materials are capable of higher powers, the blend morphology and recombination dynamics also play a role in determining the device efficiency.

With the term for P_{max} in hand, the device efficiency is defined as:

$$PCE = \frac{I_{\text{sc}} V_{\text{oc}} FF}{P_{\text{in}}}$$

Lastly, it is important to note that the efficiency be independent of the device area. As the area of the solar cell increases, the current will increase due to the increased light absorption. Thus, the current is typically reported as a current density, J and our device efficiency is defined as:

$$PCE = \frac{J_{sc} V_{oc} FF}{P_{in}}$$

Therefore, a high-efficiency solar cell will have a high open-circuit voltage, short-circuit current, and fill factor (more rectangular shape). However, these parameters cannot all be simultaneously optimized. For example, since the open-circuit voltage is related to the difference in the fullerene LUMO and the polymer HOMO, lowering the polymer HOMO is a strategy for increasing the open-circuit voltage.[45] However, this increases the polymer band gap and decreases the overall light absorption of the solar cell. This is because the band gap is now too large for smaller-energy photons to be absorbed. Thus, increasing the open-circuit voltage will decrease the short-circuit current and a balance must be made to optimize the two values. It has been calculated that this balance is achieved at a band gap of 1.1 eV, which is the band gap for silicon.[14] However, organics, which require 0.2 eV to separate the charge, require an optimal band gap of 1.3 eV.[46]

1.3 Perylenediimide (PDI) Dimers as Non-Fullerene Acceptor Materials

Although PCBM is the most widely used electron-acceptor material, improving the properties of the electron acceptor is beneficial. Strategies to improve the device performance include saturating two or more of the double bonds for the fullerene.[47,48] Although this increases the open-circuit voltage, this can lead to deleterious effects on the electronic coupling.[38] By synthesizing 1,4-[60] fullerene bisadducts, we produced fullerene derivatives with higher LUMO levels than PCBM and saw an improvement in device efficiency.[49] Compared to PCBM, this increased the open-circuit voltage and resulted in roughly a 20 % efficiency increase when paired with P3HT. However, a remaining limiting factor in the use of fullerene materials is their poor light absorbing properties. Ideally, a good electron acceptor will have both high electron transport properties and good light absorption.

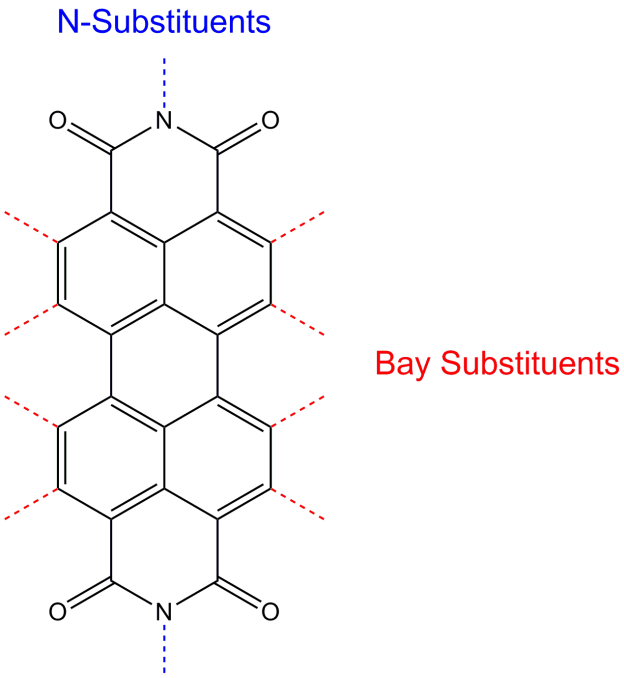

Figure 1.4: Structure of a perylenediimide (PDI) molecule with nitrogen substitution positions shown in blue and bay substitution positions shown in red.

Non-fullerene acceptors such as perylenediimide (PDI) derivatives meet these criteria. As shown by the structure in Figure 1.4, PDIs are widely used since substitutions may be made to the nitrogen position to independently affect solubility while substitutions to the bay positions independently affect the electronic properties.[50,51] Since they are used as paints and pigments they strongly absorb across the solar spectrum.[52] Furthermore, PDIs have high electron mobilities.[53] Because they aggregate well, have good π coupling, and have high emission yields, PDIs are used in organic light emitting diodes.[54,55] Therefore, on paper, PDIs appear as a good candidate for an electron acceptor material for use in organic solar cells. However, due to strong π-stacking intermolecular forces, PDI molecules will overaggregate when cast into a solid-state film.[51] This results in over-phase separation and is deleterious to the device performance: with large regions of aggregated PDI, the donor-acceptor interface is limited, which reduces the total number of excitons split. Thus, the earliest PDI solar cells under-performed compared to PCBM. However, synthetic strategies to disrupt the π-stacking first came through introducing non-planarity into the PDI by making a dimer, formed through a bond from each nitrogen: this resulted in an efficiency increase from 0.13% to 2.78%.[56] Following this, the next major development came through forming a dimer (di-PDI) linked

through the bay position on the PDI, which brought efficiencies of 3%.[57] The non-planarity prevents over-aggregation of PDI dimers with each other and also eliminates the requirement for the electron to exclusively transport in one direction. Through additional modification to the di-PDI, devices with up to 8% efficiency were achieved.[6,58–61] To date, the highest performing PDI-based solar cell has a reported efficiency of 10.58%.[62] Furthermore, these PDI derivatives have gained significant traction as electron-accepting materials since they can be paired with commonly-used polymer materials such poly-3-hexylthiophene (P3HT)[63] and poly(4,8-bis[(2-ethylhexyl)oxy]benzo[1,2-b:4,5-b′]dithiophene-2,6-diyl3-fluoro-2-[(2-ethylhexyl)carbonyl]thieno[3,4-b]thiophenediyl) (PTB7).[58]

Because of their widespread use in organic electronics, the aggregation and optical properties of PDI derivatives are a topic of great interest as the coupling is strongly manifested in the spectroscopy.[64] In the simplest picture, the aggregation will be H or J: in the H aggregate two PDI monomers aggregate "side-by-side" while in the J aggregate they aggregate "head-to-tail."[64,65] H aggregates have blue-shifted absorption spectra and red-shifted photoluminescence that is attenuated. J aggregates, on the other hand, have red-shifted absorption and a very strong photoluminescence.[64,65] However, this picture describes perfectly H-like or J-like character, when for PDI systems it has been shown that aggregation is in fact a combination of both H and J aggregation.[65] Furthermore, the close proximity of each PDI monomer to each other introduces short-range coupling that can match or even exceed the Coulomb coupling that is responsible for H- and J-type aggregation.[65] Therefore, the aggregation and associated spectroscopy for these PDI solar cell materials is a rich topic that requires both detailed spectroscopy and the associated theory in order to attain a more complete understanding.

1.4 Doping Polymer Films

Since semiconducting polymers are poor conductors, there is interest in developing techniques to improve the polymer conductivity. Similar to organic solar cells, which benefit from their low-cost, it is advantageous to have highly-conductive polymer films for niche applications such as thermoelectrics.[66–68] The advantages of flexible thermoelectircs includes applications such as wearable thermoelectrics.[68] This increase in conductivity is achieved by chemically doping the

polymer film: by selecting a dopant molecule with a LUMO that sits below the polymer HOMO, an electron will transfer from the polymer HOMO to the dopant LUMO. As shown in Figure 1.5, this *p*-type doping places an electron on the dopant molecule and a hole on the polymer, which increases the conductivity of the polymer.[69]

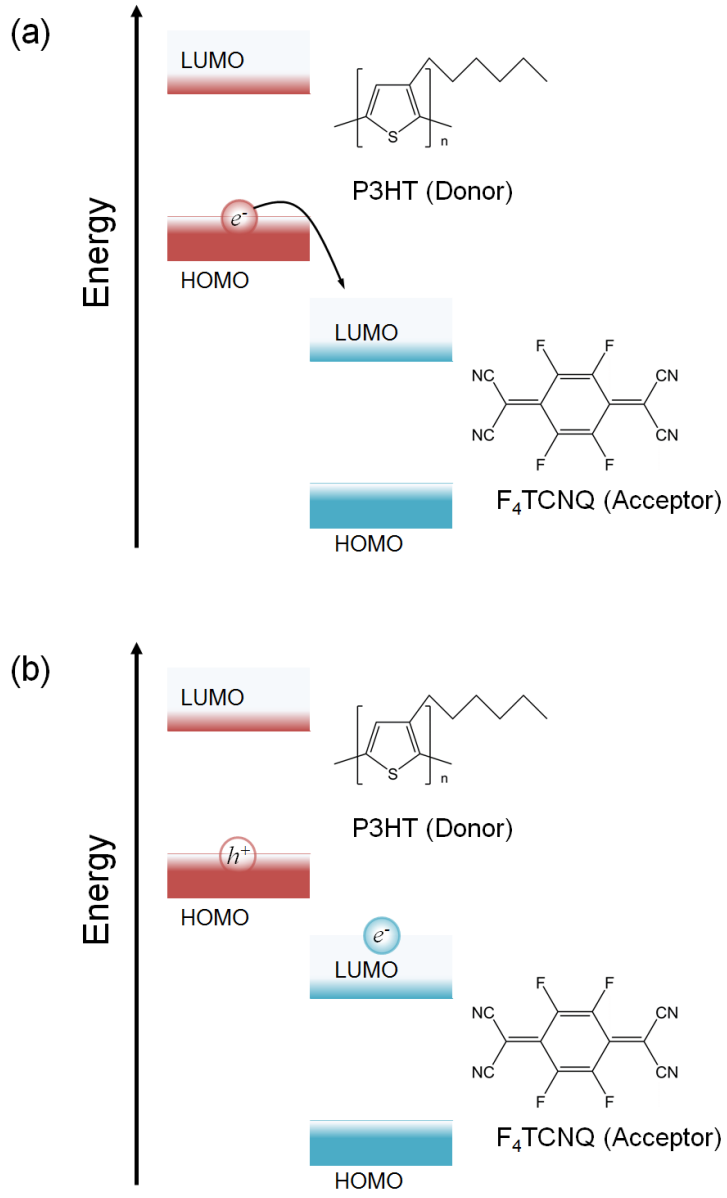

Figure 1.5: (a) Since the F_4TCNQ LUMO lies under the P3HT HOMO an electron will undergo charge-transfer from P3HT to F_4TCNQ. (b) *p*-doping of P3HT leaves a hole on the doped polymer chain, thereby increasing the polymer conductivity.

One of the first widely studied air- and time-stable doped systems is P3HT doped by the

small molecule 2,3,5,6-Tetrafluoro-7,7,8,8-tetracyanoquinodimethane (F_4TCNQ). Similar to blend-casting, where polymer and fullerene are co-dissolved in solution, the first doping studies used blend-doping where polymer and dopant were co-dissolved together in solution before casting a film.[5,69–71] However, this method presents a problem for the high-doping regime. Since polymer dissolution requires using a nonpolar organic solvent to dissolve the polymer film, the buildup of charged species on the polymer causes the polymer to aggregate and crash out of solution as the doping level increases.[72–77] Thus, while blend-doping is straightforward in application, its use is limited to lower doping concentrations.

1.4.1 Sequential Doping

The drawback of blend-cast doping is that charge transfer occurs in solution. Thus, in the high doping regime, the polymer aggregates and crashes out of solution. This makes attaining high-quality doped films very difficult. Thus, it is advantageous to dope the polymer film in a second, sequential step, which is achieved by solution sequential doping or evaporation sequential doping.

1.4.1.1 Solution Sequential Doping

Sequential processing facilitates small molecule intercalation within the polymer film provided the solvent optimally swells the polymer film.[2] In the case of solar cells this small molecule is typically a fullerene. However, in order to dope a polymer film the small molecule can be a molecular dopant. Since the dopant is added to a pre-cast polymer film, solution sequential doping avoids the problems associated with blend-cast doping: films prepared by solution sequential processing are highly doped and maintain excellent film quality.[74,75] Furthermore the doping levels are only limited by the solubility of the dopant in the solvent.[74]

1.4.1.2 Evaporation Sequential Doping

A complementary doping technique is evaporation sequential doping. In this fabrication technique, a polymer film first is spin-cast and in a second step the film is doped by either thermal evaporation or being placed in a chamber saturated with dopant vapor: the doping increases with the increased

evaporated thickness or time exposed to the dopant vapor.[71,78–83] Thus, similar to solution sequential doping, evaporation sequential doping maintains high film quality by intercalating the dopant in a second step. This has been demonstrated by structural measurements that show the polymer morphology remains relatively unchanged after doping.[81,83] It has also been shown that heating the polymer film during the doping process increases the doping level. Since heat increases the polymer *d*-spacing, heating the polymer film increases the available space for dopant to intercalate, thereby increasing the doping concentration.[83]

As the polymer thickness increases, the conductivity decreases via evaporation sequential doping: increasing the polymer thickness and keeping the dopant concentration fixed results in under-doping the polymer film.[79,82] Additionally, increasing the dopant concentration for a given polymer film thickness produces a maximum conductivity followed by a decrease, resulting from over-doping the film.[79] These results suggest that for a given polymer thickness there must be an optimal doping concentration. However, since evaporation doping dopes from the top of the film surface, it is an open question as to whether or not there is a maximum film thickness that can be doped. In contrast, since solution sequential doping swells the polymer film, provided there is enough swelling solvent, we expect it to dope the entire polymer film. These questions will be addressed later in this work.

1.5 Overview of the Thesis

This thesis contains five chapters, each focused on an area of organic electronics. In particular, this thesis investigates the fundamental properties of molecular interactions to gain insight into various processes such as solar cell device improvement and morphology formation, the aggregation and charge-transfer properties of solar cell acceptor materials, and the chemical doping of polymer films. The following sections briefly describe the work contained in these chapters.

1.5.1 Sequential Processing: A Rational Route for BHJ Formation via Polymer Swelling

This chapter is a book chapter highlighting the previous work of the group on sequential processing (SqP). Specifically, this chapter highlights the contribution of SqP to the organic electronics community. In this chapter, SqP is presented as an alternative, yet highly tunable, processing technique for the formation of BHJs. By casting the polymer film in a separate step, one can tune the polymer structure before adding a small molecule such as fullerene derivative in the case of photovoltaics, or a dopant molecule in the case of achieving high-conductivity organic thin film. Furthermore, by decoupling BHJ formation into two separate steps, SqP facilitates the investigation into BHJ formation. Specifically, this approach demonstrates that commonly used low-vapor-pressure solvent additives such as DIO and ODT act as polymer swelling agents for BHJ morphology improvement,

1.5.2 Solvent Additives Function as Polymer Swelling Agents in Bulk Heterojunction Organic Photovoltaics

Bulk heterojunction (BHJ) photovoltaics based on blends of conjugated polymers and fullerenes require an optimized nanoscale morphology. Casting BHJ films using solvent additives, such as 1,8-diiodooctane (DIO), 1,8-octanedithiol (ODT), chloronapthalene (CN) or diphenyl ether (DPE) often helps achieve this proper morphology: adding just a few volume percent of additive to the casting solution can improve polymer/fullerene mixing or phase separation, so that solvent additives have become staples in producing high-efficiency BHJ solar cells. The mechanism by which these additives improve BHJ morphology, however, is poorly understood. Here, we investigate how these additives control polymer/fullerene mixing by taking advantage of sequential processing (SqP), in which the polymer is deposited first and then the fullerene is intercalated into the polymer underlayer in a second processing step using a quasi-orthogonal solvent. In this way, SqP isolates the role of the additives' interactions with the polymer and the fullerene. We find using ellipsometry-based swelling measurements that when adding small amounts of low-vapor-pressure solvent additives such as DIO and ODT to solutions of poly(3-hexylthiophene-2,5-diyl) (P3HT), poly[(4,4′-bis(3-(2-ethyl-hexyl)dithieno[3,2-b:″,3′-

d]silole)-2,6-diyl-alt-(2,5-bis(3-(2-ethyl-hexyl)thiophen-2yl)thiazolo[5,4-d]thiazole)] (PSEHTT), or poly[4,8-bis-(2-ethylhexyloxy)-benzol[1,2-b:4,5-b′]dithiophene-2,6-diyl-alt-4-(2-ethylhexyloxy-1-one)thieno[3,4-b]thiophene-2,6-diyl] (PBDTTT-C), the additives remain in the polymer film, leading to significant swelling. Two-dimensional grazing-incidence wide-angle X-ray scattering measurements show that the swelling is extensive, directly affecting the polymer crystallinity. When we then use SqP and cast phenyl-C_{61}-butyric acid methyl ester (PCBM) onto DIO-swollen polymer films, X-ray photoelectron spectroscopy and neutron reflectometry measurements demonstrate that vertical mixing of the PCBM in additive-swollen polymer films is significantly improved compared to films cast without the additive. Thus, low-vapor-pressure solvent additives function as co-solvent swelling agents or secondary plasticizers, allowing fullerene to mix better into the swollen polymer and enhancing the performance of devices produced by SqP, even when the additive is present only in the polymer layer. DIO and ODT have significantly different fullerene solubilities but swell polymers to a similar extent, demonstrating that swelling, not fullerene solubility, is the key to how such additives improve BHJ morphology. In contrast, higher-vapor-pressure additives such as CN and DPE, which have generally high polymer solubilities, function by a different mechanism, improving polymer crystallinity.

1.5.3 Lessons from Intermolecular Coupling at the Conjugation Limit: ($\beta-\beta$)Bay-Linked Perylenediimide Studied with Ultrafast Spectroscopy, Temperature Dependence, and TDDFT

Bay-linked di-perylenediimide (di-PDI) molecules are finding increasing use in organic electronics due to their steric hindrance that 'twists' the two monomer units relative to one another, decreasing molecular aggregation. In this paper we explore the electronic spectroscopy and ultrafast dynamics of the singly-linked $\beta-\beta$-S-di-PDI (2,9'-di(undecan-5-yl)-2',9-di(undecan-6-yl)-[5,5'-bianthra[2,1,9-def:6,5,10-d'e'f']diisoquinolin]-1,1',3,3',8,8',10,10'(2H,2'H,9H,9'H)-octaone). Excitation-emission spectroscopy reveals two distinct emitting species, which are further characterized by time-dependent density functional theory (TD-DFT), demonstrating that the bay-linked PDI dimers exist in two geometrical conformations. These conformations are an "open" geometry, where the two monomer sub-units are oriented nearly at right angles, giving them more

J-like coupling, and a “closed” geometry, in which the two monomer sub-units are nearly π-stacked, resulting in more H-like coupling. Given the extent of through-space and through-bond coupling, however, neither di-PDI conformer can be well-described simply in terms of independently-coupled monomers; instead, a full quantum chemistry description is required to understand the electronic structure of this molecule. Temperature-dependent experiments and the TD-DFT calculations indicate that the “closed” conformer is ∼70 meV more stable than the “open" conformer, so that both conformers are important to the behavior of the molecule at room temperature and above. We use a combination of steady-state and femtosecond transient absorption and emission spectroscopies to extract global fits of the multiple electronic transitions underlying the spectra of both the “closed” and “open” conformers, which agree well with the TD-DFT calculations. The ultrafast experiments also reveal a viscosity-dependent twisting motion around the bay-linked bond upon photoexcitation, although the two conformers do not interconvert on the time-scale of the excited-state lifetime. The fact that di-PDI molecules are molecular species that adopt two distinct quasi-independent chemical identities has important ramifications for charge trapping and mobility in the organic electronic devices employing these materials.

1.5.4 Homogeneous Doping of Progressively Thicker Semiconducting Polymer Films Achieved by Solution and Evaporation Sequential Processing

For thermoelectric and other device applications, there has been great interest in the molecular doping of conjugated polymer films. In this paper, we compare two methods by which conjugated polymer films can be doped by adding the dopant after the polymer film is already cast: evaporation doping, where a controlled thickness of dopant is added via thermal evaporation to a temperature-controlled polymer film, and solution doping, where the dopant is spin-cast from a solvent chosen to swell but does not dissolve the underlying polymer film. These two methods are forms of sequential doping, which provides the advantage that the structure of the original semiconducting polymer film is largely preserved through the doping process. To compare the different types of sequential doping, we examine the optical and electrical properties of films of poly(3-hexylthiophene-2,5-diyl) (P3HT) doped by both methods with the small-molecule dopant 2,3,5,6-tetrafluoro-7,7,8,8-tetracyanoquinodimethane (F_4TCNQ) as a function of the polymer film thickness. We find that both

methods produce doped films with conductivities well above 1 S/cm and comparable thermoelectric properties, even for films as thick as 400 nm. For the evaporation method, we find that an 'overhead' thickness of $\sim$7 nm is required to induce the structural changes needed for effective doping. After the overhead amount has been deposited, the thickness of the dopant layer that must be evaporated to achieve the optimal electrical conductivity is $\sim$1/3 that of the underlying polymer film. For the solution method, with the appropriate choice of solvent and dopant concentration, we show that films as thick as 2 μm can be doped to achieve conductivities of $\sim$5 S/cm and thermoelectric power factors greater than 1 μW/mK^2. For either method, if excess dopant is applied, it remains in neutral form on top of the film, reducing the conductivity by increasing the film thickness. Finally, we show that for both methods, UV-visible absorption can be used to easily monitor whether the optimal amount of dopant has been reached or exceeded. Overall, we demonstrate that it is straightforward to select a sequential doping method for any desired application: evaporation doping is more amenable to large-area films while solution-doping is lower cost and better suited for polymer films with μm thickness.

CHAPTER 2

Sequential Processing: A Rational Route for BHJ Formation via Polymer Swelling

2.1 Introduction: The Development of Sequential Processing

Constructing solar cells based on organic materials such as conjugated polymers holds great potential for low-cost and lightweight power generating applications. Although organic materials are inexpensive and readily amenable to scale-up, successfully incorporating organic solar cells into the energy sector requires understanding their underlying physics and using this knowledge to increase their efficiency. In contrast to inorganic solar cells, a limitation facing organic solar cells is the inability to produce free charge carriers following light absorption. To overcome this, polymer-based photovoltaics are typically based on a blend of two materials: a conjugated polymer, which acts as the light absorber and electron donor, and an electron acceptor, which is often a fullerene derivative such as phenyl-C_{61}-butyric acid methyl ester (PCBM).[16,84–86]

In polymer-fullerene solar cells, light absorption by the semiconducting polymer produces an excited-state electron and leaves behind a corresponding hole. The electron and hole remain strongly Coulombically-bound in organic materials, and thus are collectively referred to as an exciton. Once the photoexcited electron undergoes charge transfer to the fullerene acceptor (exciton dissociation), the Coulomb attraction between the electron and hole is reduced and the electron and hole effectively become free charge carriers. For this to happen, the polymer and fullerene components must be blended well enough to ensure the close polymer/fullerene contact needed to promote charge separation via electron transfer. But once the charges are separated, both carriers must see a continuous pathway to reach the appropriate electrode in order to collect a photocurrent: the electron must be able to hop between neighboring fullerenes to reach the cathode,

while the hole must move along a network of adjacent polymer chains to reach the anode. This means that some degree of phase separation of the two components is required. A polymer-fullerene mixture that simultaneously satisfies the intimate blending needed for charge separation and the bicontinuous interpenetrating network needed for charge transport is referred to as a bulk heterojunction (BHJ).[16,17,46,87–93]

Clearly, forming an ideal BHJ morphology is critically important for producing high-performance, polymer-fullerene organic photovoltaics. Research from many groups has determined that the typical size of the polymer and fullerene domains in a BHJ architecture must be on the order of the exciton diffusion length of the polymer (typically $\sim$10 nm)[94] to ensure efficient exciton splitting; coarser mixing than this leads to inefficient exciton dissociation and thus poor production of charge carrier, while finer mixing reduces transport to the electrodes[95,96] and increases losses due to recombination.[43] When both the materials and the resulting BHJ morphology are optimized, high-performance, single-junction, polymer-fullerene BHJ devices have power conversion efficiencies approaching 12%.[26]

The most widely used method for fabricating the active layer of organic photovoltaics is blend casting (BC). This processing technique constructs the BHJ morphology by co-dissolving the polymer donor and fullerene derivative acceptor and spin-casting the resulting solution into a solid film; this method relies on the kinetics of solvent evaporation and spontaneous phase-separation of the two materials to form the requisite BHJ.[17] This means that achieving optimized BHJ morphologies through BC is not trivial. Film formation depends on several interdependent factors related to the active layer materials, including: the miscibilities of the two components in the host solvent and with each other, each component's propensity to self- or co-crystallize, each component's surface energy, each component's molecular mobility and diffusivity, and the solvent drying kinetics for a given set of casting conditions.[97] Because of this, BHJ formation is hyper-sensitive to subtle changes in either processing conditions or the polymer or fullerene's molecular structure. Processing parameters that can be used to tune the BHJ morphologies formed by BC include thermal annealing,[98–102] solvent annealing,[103,104] changing the host solvent,,[105] and adding a co-solvent or solvent additive.[3,26,106–110] Unfortunately, despite well over a decade of intense work, no clear design rules have emerged.[17,111] Indeed, many donor-acceptor pairs promise

efficient devices on paper, but for reasons still unknown simply do not form the requisite BHJs needed to work in the laboratory.[111]

The sensitivity of polymer-based photovoltaic performance to the nm-scale BHJ is further underscored by the eventual need to scale up such devices if they are ever to be commercially practical. This is because the formation kinetics of large-area polymer films by blade coating or roll-to-roll fabrication are quite different from those produced on the laboratory scale by spin-coating. This means that BHJ morphologies produced in large-area devices are different from those in smaller devices, so that work done on optimizing BHJ formation in the laboratory does not necessarily translate when scaled up.[22,112–114] As a result, even though blend-cast organic solar cells are making strides towards higher-efficiency devices because of intense Edisonian effort, there are still no commercial devices available from these materials, which is a direct result of BC's inability to rationally control the BHJ nanomorphology during device processing.

To address these difficulties associated with producing polymer solar cells by BC, we developed an alternative processing method that forms the desired BHJ through sequential deposition of polymer and fullerene layers; we refer to this method as sequential processing (SqP).[37,115] The BC and SqP techniques are illustrated in Figure 2.1, with BC in the upper panel and SqP in the lower panel. In SqP, a film of the pure conjugated polymer is spun first, with casting conditions chosen to tune the polymer morphology to what is desirable for a given device. Then, in a second processing step, the fullerene is cast from a solvent that is chosen to swell the underlying polymer layer but not dissolve it.[2] Mass action drives fullerenes from the solution used in the second step into the swollen polymer underlayer, forming a BHJ with a fullerene network that is guaranteed to be connected to the top of the film (since the fullerene enters only from the top rather than starting dispersed throughout the film). Therefore, BHJ morphology is determined by the concentration of the fullerene solution, which tunes the mass action driving force for fullerenes to enter the film, and the thermodynamics of how the fullerene solvent swells the polymer, which alters the free volume in the swollen polymer that allows fullerenes to intercalate. Since mass action and swelling are thermodynamic rather than kinetic effects, this means that SqP provides significantly greater reproducibility and control over the BHJ morphology needed to produced highly efficient polymer solar cells.[2,23]

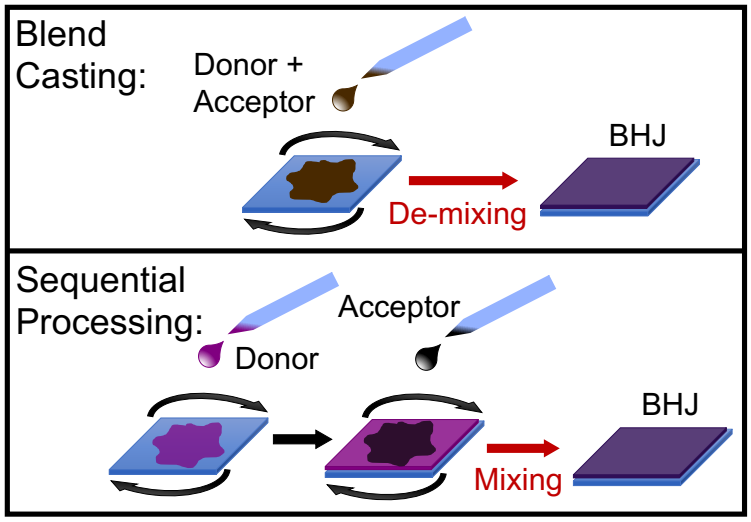

Figure 2.1: Comparison of BHJ active-layer formation via BC and SqP techniques. In BC, the donor and acceptor are spin-coated from a mixed solution in a single step whereas with SqP the donor is spun first followed by the acceptor in separate steps. The traditional BC method relies on the spontaneous de-mixing kinetics of donor and acceptor materials, which are poorly understood and difficult to control. Our two-step SqP method involves the interdiffusion of acceptor material into a pre-formed donor matrix, the extent of which can be controlled via swelling and mass action.

It is worth noting that when we originally developed SqP, we were unaware of the extent to which the solvent in the second step could swell the underlying polymer layer, and indeed our initial goal with SqP was to prepare clean polymer-fullerene bilayers. In fact, the fullerene-casting solvent we initially chose, dichloromethane (DCM), is a relatively poor swelling solvent for our initially-studied conjugated polymer, poly(3-hexylthiophene-2,5-diyl) (P3HT).[37] When we first spun PCBM from a DCM solution onto a pre-cast P3HT film, we found that the top surface was enriched with PCBM crystallites, and that the photovoltaic devices had relatively poor power conversion efficiency. Neutron reflectometry investigations, however, revealed that significant amounts of fullerene mixed into the interior of the polymer film, so that the morphology was more of a quasi-bilayer than either a clean bilayer or a BHJ.[100,101] Subsequent thermal annealing of the SqP-produced P3HT:PCBM quasi-bilayer caused PCBM to further diffuse into the polymer layer, forming a well-mixed BHJ with greatly improved photovoltaic device efficiency.[100,116,117] The change in morphology caused by thermal annealing is caused by two predominant effects: 1) PCBM is a higher surface energy material than P3HT, so thermal annealing tends to drive PCBM towards the bottom of the active layer,[118] better distributing the PCBM throughout the polymer and

improving device performance;[116,119,120] 2) Thermal annealing enhances the crystallinity of the components in the active layer, particularly P3HT, which improves device efficiency by increasing carrier mobilities.[98–102]

Although using thermal annealing to drive fullerenes deposited via SqP into a polymer underlayer might seem like a viable approach to BHJ formation, the improvement in sequentially-processed device performance seen upon thermal annealing is unique to P3HT; most modern high-efficiency low-bandgap polymers degrade or form a homogeneous disordered blend with too little phase separation upon thermal treatment.[86,121–124] For this reason, early studies of SqP focused almost exclusively on P3HT.[86,111,124–126] Despite this early limitation, a wealth of morphological studies investigating BHJ formation via SqP have highlighted the differences in BHJ morphology between devices prepared through BC and those made via SqP.[23,100–102,115,116,119,120,127–144,144–150] More recently, SqP has been successfully applied to the fabrication of organic solar cells based on high-performing, push-pull polymers.[2,132,151–154] Additional studies also have extended SqP to ternary organic blends and the use of alternative fullerene derivatives, such as 1′,1″,4′,4″-Tetrahydro-di[1,4]methanonaphthaleno[1,2:2′,3′,56,60:2″,3″][5,6]fullerene-C_{60} (ICBA).[138,154–157] It is also worth noting that SqP can be used for the infiltration of molecular dopants instead of fullerenes into a polymer underlayer, providing a substantial advance in the quality of doped conjugated polymer films,[74,75] as discussed further below.

One key advantage of SqP is its ability to take advantage of polymer swelling, which makes SqP applicable to any polymer system. Polymer swelling provides a systematic, rational, and tractable avenue towards optimal BHJ construction, including for polymers beyond P3HT that cannot be thermally annealed.[2] In this sense, the degree of polymer swelling is what allows for precise tuning of the BHJ morphology by SqP.[2] If the fullerene-casting solvent poorly swells the underlying polymer, fullerene will not intercalate within the film, leaving large fullerene domains deposited on top of the polymer underlayer.[37,100,101,130,134,146,158] Conversely, a solvent that interacts too favorably with a polymer can dissolve or wash away part or all of the underlying polymer film.[2] Therefore, optimal BHJ formation requires swelling of the polymer without dissolution. As will be discussed further in Section 2.2, this places significant constraints on the choice of fullerene-casting solvent, which must simultaneously possess both high fullerene solubility and yield optimal polymer

swelling. In light of this, we have proposed the use of binary solvent blends that can be tuned to create optimal SqP solvents for casting the fullerene.[2] With solvent blends and other advances, SqP has produced numerous single-junction, polymer-fullerene, photovoltaic devices with high power conversion efficiencies.[2,21,39,44,135,151–154,158–164]

One of the key features of SqP is that swelling is inherently selective to amorphous regions and does not affect crystalline regions of a polymer film.[165,166] Therefore, achieving optimal polymer swelling largely depends upon the degree of polymer crystallinity. Selecting different casting solvents and varying the originally-cast film's drying conditions are well known to control the crystallinity of a spin-cast conjugated polymer film.[2,127] Thus, SqP provides many experimental "knobs" that can be independently tuned for optimizing BHJ formation, as discussed fully in Section 2.2, including controlling the crystallinity of the polymer underlayer and thus the manner in which it swells. This allows for a better opportunity to choose organic semiconductors that have other essential properties that are requisite for high performance (e.g., favorable energy level alignments, absorption spectra, etc.).

In addition to providing a rational pathway for BHJ optimization, SqP provides a route to systematically investigate the mechanisms underlying BHJ formation and to develop design rules that can be extended to any polymer system. For example, the use of solvent additives such as 1,8-diiodooctane (DIO) has become quite commonplace when fabricating blend-cast devices,[3,4,17,26,107,110,167,168] but the mechanism by which these additives improve BHJ formation was poorly understood. Using SqP, we found that solvent additives such as DIO act primarily as non-evaporating swelling agents, as discussed in more detail in Section 2.3. Overall, SqP is clearly a more tractable technique for BHJ formation because it avoids the problems inherently associated with BC. Thus, SqP not only opens new pathways towards BHJ construction, but also facilitates fundamental investigations into the process of BHJ formation.

2.2 Quantification of Polymer-Solvent Swelling Interactions as the Key to Polymer Solar Cell Design

The advantage of SqP is its ability to controllably tune the degree of polymer swelling such that the acceptor is appropriately dispersed into the polymer layer, creating an ideal BHJ morphology. Quantifying the degree of swelling required to achieve the ideal morphology and optimal performance in any given polymer-solvent system is important so that the processing conditions can be chosen based on simple measurements instead of trial-and-error. To this end, our approach has been to use porosimetry-ellipsometry measurements to characterize polymer-solvent interactions, making BHJ device optimization predictable.[2,169–174]

In porosimetry-ellipsometry measurements, a polymer film is placed in a porosimeter and swelled by exposure to solvent vapor, and spectroscopic ellipsometry is used to precisely measure the change in thickness and index of refraction of the vapor-swollen film. The experiment can be done without a porosimeter by simply exposing the polymer film to the saturated solvent vapor of interest during ellipsometry. The ellipsometry-measured change in thickness gives the free volume available in the swollen film for fullerene intercalation. Moreover, the ellipsometry-measured change in index of refraction of the film, combined with the effective medium approximation, provides a means to determine the volume fraction of polymer, ϕ_p, in the swollen film.[174–177] With the volume fraction of polymer in hand, one can calculate the Flory-Huggins χ parameter from:[172–174,178,179]

$$\ln(\frac{p}{p_{\text{sat}}}) = \chi\phi_p^2 + \ln(1-\phi_p) + \phi_p(1-\frac{1}{N}), \tag{2.1}$$

where N is the degree of polymerization and p/p_{sat} is the pressure of the solvent vapor the film is exposed to relative to the solvent's saturated vapor pressure. Lower χ values are associated with stronger solvent-polymer interactions. That is, the lower χ is, the more likely a solvent is to swell (and eventually dissolve) the polymer. In Section 2.2.1 below, we argue that there is a range of optimal χ values that lead to desired BHJ formation and thus improved device performance.

Although there are many factors that influence the value of χ, we focus on two that can be

directly controlled to allow SqP to be used to great effect in controlling BHJ morphology: the choice of solvent and the degree of polymer crystallinity. As mentioned above, a solvent in which the polymer is more soluble will act as a better swelling agent than a solvent in which the same polymer is less soluble. However, the same solvent can give different χ values for the same polymer if the microcrystalline structure of the polymer film is different. This is because the amorphous regions of a polymer film are highly susceptible to swelling by a solvent, whereas crystalline regions can be treated as effectively cross-linked and thus poorly swell.[2,165] In what follows, we explore systems in which solvent choice and polymer crystallinity are controllably varied to illustrate how SqP can follow design rules that can rationally be used to optimize the performance of BHJ solar cells without the need for trial-and-error.

2.2.1 Design Rules: Controlling Swelling via Sequential Processing Solvent Choice

Finding an ideal solvent for the second casting step in SqP is imperative if the method is to be general for any polymer-acceptor system. As mentioned above, the solvent for this step must both wet[2] and optimally swell the polymer underlayer without dissolving it,[127] and also must have high solubility for the acceptor molecule in order to infiltrate meaningful amounts into the polymer film.[39] It is highly unlikely that any single solvent would fulfill all these requirements, particularly for different combinations of polymers and fullerenes. However, we have shown that binary solvent blends can be logically chosen to simultaneously satisfy all of these criteria. The basic idea is to choose a base solvent in which the infiltrant of interest (fullerenes for polymer BHJ solar cells) is highly soluble, and then mix this base solvent with a co-solvent to adjust the degree of swelling for a particular polymer. If the base solvent dissolves the polymer of interest, the co-solvent can be a non-solvent for the polymer, with enough added to stop polymer dissolution and raise χ into the optimal range. Conversely, if the base solvent inadequately swells the polymer, the chosen co-solvent should be a good solvent for the polymer, so that χ can be lowered into the optimal range.[2]

Through a series of measurements, we have found the values of χ that lead to optimal polymer swelling (to an extent sufficient for fullerene intercalation without dissolving) are in the range

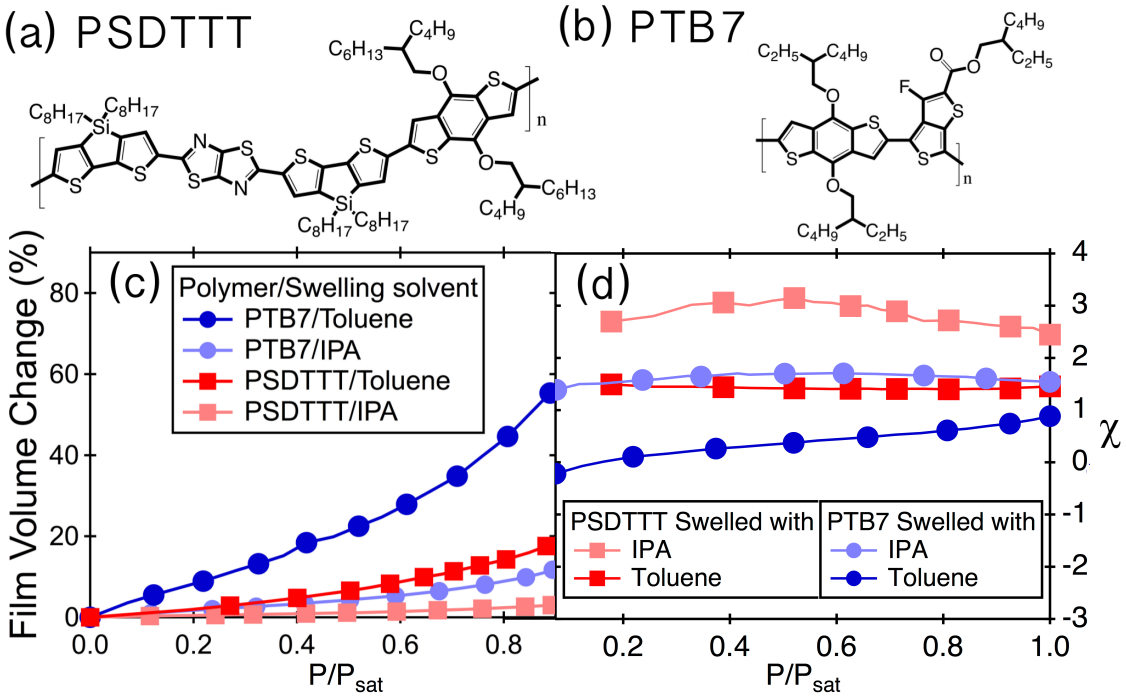

Figure 2.2: Chemical structures of (a) PSDTTT[1,2] and (b) PTB7.[3,4] (c) Swelling of PSDTTT and PTB7 upon exposure to toluene and isopropanol (IPA) vapor measured by porosimetry-ellipsometry. Being more soluble than PSDTTT, PTB7 swells more with both solvents: toluene (dark blue circles) and IPA (light blue circles). Since PSDTTT is poorly soluble it swells less with toluene (dark red squares) and IPA (light red squares). (d) Calculated χ parameters for PSDTTT (light red squares for IPA-swelling and dark red squares for toluene-swelling) and PTB7 (light blue circles for IPA-swelling and dark blue circles for toluene-swelling) films using the ellipsometric swelling data and the effective medium approximation to obtain ϕ_p in Eq. 2.1.[2]

of 1.5 to 2.0.[2] This is readily achievable for any polymer:fullerene system by using a solvent blend for the fullerene-casting step in SqP because the χ value for a solvent blend is roughly the mole-fraction-weighted χ values for the individual components interacting with the polymer. Thus, as long as the fullerene is sufficiently soluble, a series of simple swelling measurements provides a recipe for designing an appropriate solvent blend to produce polymer:fullerene BHJs by SqP without trial-and-error.

Although there are several potentially good choices as base solvents for fabricating polymer:fullerene BHJs by SqP, we decided to focus on 2-chlorophenol (2-CP), which has high a solubility for PCBM (112 mg/mL)[180] and a relatively low solubility for most conjugated polymers. As examples of how to tune a solvent blend with 2-CP to produce the optimal χ for BHJ production, we recently focused on applying SqP to produce solar cells from both PTB7, a slightly crystalline

and highly soluble polymer,[3,181,182] and PSDTTT,[1,2] a completely amorphous polymer with low solubility in most common organic solvents;[1] see Figure 2.2 for the chemical structures of these polymers. We measured the swelling of both polymers ellipsometrically upon exposure to isopropyl alcohol (IPA) vapor, a non-solvent for conjugated polymers, and to toluene vapor, which is generally a good solvent for conjugated polymers. Figure 2.2 shows that, as expected, the swelling by of both PTB7 and PSDTTT with toluene (dark blue circles and dark red squares, respectively) is greater than with IPA (light blue circles, light red squares), and that PTB7 (blue circles) swells about four times more than PSDTTT (red squares) since the latter has poor solubility even in "good" solvents such as toluene. Panel d) shows the calculated χ values for these polymer film-solvent pairs extracted from the ellipsometric data. The data clearly show lower χ values for the polymer-toluene interactions compared to those with IPA, and higher χ values for PSDTTT than for PTB7 in a given solvent. It is worth noting that pure toluene cannot be used as a second-step SqP solvent for either polymer as its χ values are low enough that films of either of these polymers would be dissolved during the fullerene-casting SqP step, and pure IPA cannot be used because the χ is too high to promote sufficient swelling. Alternatively, pure 2-CP slightly dissolves PTB7 (χ too low) and does not dissolve PSDTTT (χ too high). Therefore, we can blend 2-CP with IPA to bring χ into the optimal range for PTB7, or blend 2-CP with toluene to bring χ into the optimal range for PSDTTT.[2]

Figure 2.3 shows the performance of the photovoltaic devices fabricated with solvent blends by SqP. With the optimized co-solvent ratio for PSDTTT:PCBM of 35% 2-CP to 65% toluene (purple triangles), device efficiencies of 3.8% were achieved, which exceeded the 3.6% efficiency of blend-cast devices made with these same materials.[2] As a control experiment, we also see that PSDTTT devices with the fullerene deposited from a 2-CP:IPA blend (green vertical diamonds) perform terribly since IPA can only raise χ relative to 2-CP. For PTB7, the amount of IPA needed to raise the χ high enough so as to not dissolve the polymer underlayer was so large that the fullerene solubility in the solvent blend decreased dramatically. This resulted in insufficient fullerene being driven into the film by mass action and sub-optimal device performance, as seen by the low fill factor (red horizontal diamonds). Since polymer solubility decreases (χ increases) with increasing solvent alcohol chain length, we then tried 1-butanol (1-BuOH) as the fullerene casting co-solvent. With the optimal 50:50 2CP:1-BuOH ratio (black circles), we obtained excellent SqP device performance

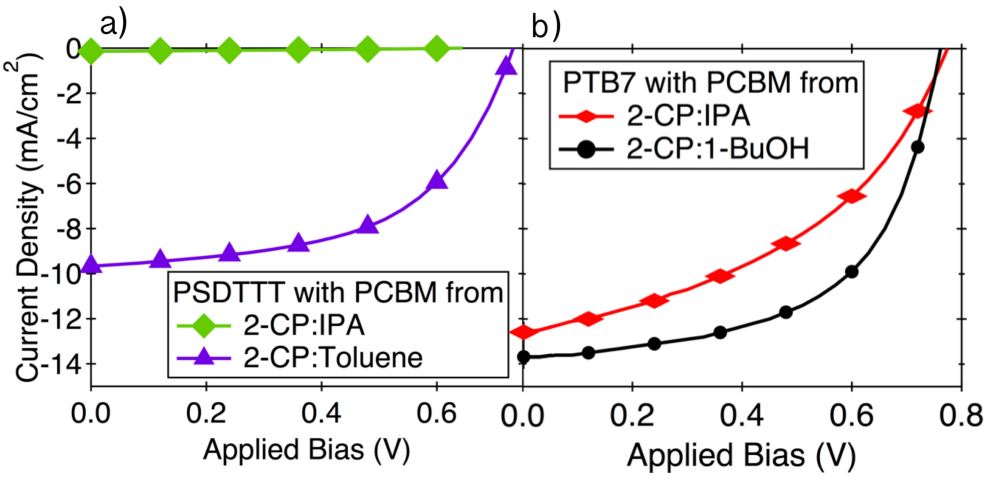

Figure 2.3: Device performance of (a) PSDTTT and (b) PTB7 sequentially-processed devices with optimally-designed solvent blends for the fullerene-casting step. For PSDTTT, the fullerene was cast from 70:30 2-CP:IPA (green vertical diamonds) and 35:65 2-CP:Toluene (purple triangles). For PTB7, the fullerene was cast from 70:30 2-CP:IPA (red horizontal diamonds) and 50:50 2-CP:1-BuOH (black circles). For PTB7, the mixture of 2-CP:IPA has a χ that is still too low and slightly dissolves the film (adding additional IPA leads to too low a PCBM solubility), but blending 2-CP with the higher-χ non-solvent 1-BuOH yields optimal performance.

with a photovoltaic power conversion efficiency of 6.0%, exceeding the 5.9% of the blend-cast equivalent device.[2] It is important to note that SqP fabrication required neither trial-and-error adjustment of the processing conditions nor the use of any solvent additives such as DIO (as discussed further in Section 2.3).

In addition to our work, van Franeker *et al.*[39] examined the influence of swelling interaction, fullerene solubility, and evaporation rate of the fullerene-casting solvent on BHJ device performance. They found that nearly all the aromatic solvents they examined similarly swelled the polymer films. However, only solvents with high fullerene solubility ($\geq$ 200 mg/mL) produced devices with efficiencies that were similar to those of traditional blend-cast devices. This result emphasizes the importance of mass action for driving in fullerene when selecting an SqP swelling solvent: the fullerene solubility must be high enough that the fullerene infiltrates the polymer film once swollen; without a high fullerene solubility the fullerene will not go into the swollen regions.[39,152,160] Furthermore, too low a fullerene solubility in SqP causes the formation of droplet-like features and/or dendritic fullerene crystallites on top of the polymer film, or a quasi-bilayer structure. If there is insufficient fullerene intercalation, this not surprisingly leads to poor electron mobility and

thus lousy photovoltaic performance.[23,38,183,184]

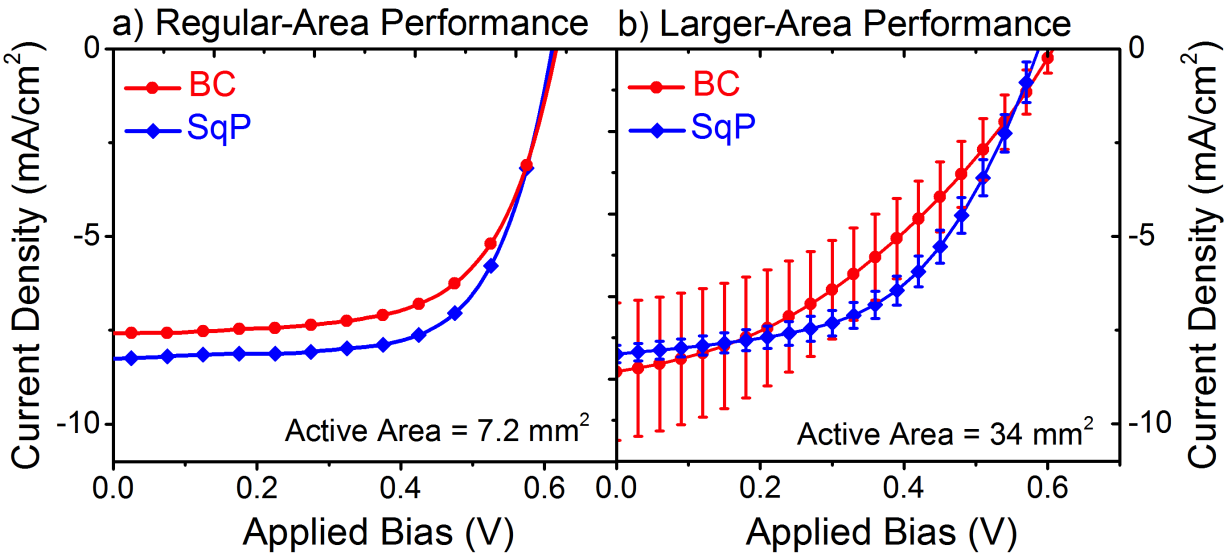

Figure 2.4: Comparison of BC (red circles) and SqP (blue diamonds) P3HT:PCBM photovoltaic performance in (a) regular-area (∼7 mm^2) and (b) larger-area (∼34 mm^2) devices. This data makes clear that SqP is more amenable to scale up since large-area SqP devices are not only better performing, but also are more reproducible.

SqP not only has been demonstrated for an increasingly wide variety of material combinations,[2,114,134,152,153,160] but also provides a route toward potential commercial scale-up. This is because blend-casting relies on spontaneous de-mixing that occurs during film formation, and drying kinetics change with device area. Moreover, commercial production of polymer-based photovoltaics is highly unlikely to be based on spin-coating, the preferred technique at laboratory scales, and the kinetics of solvent evaporation are different with industrial processes such as blade-coating or roll-to-roll processing. Indeed, the limited studies on scalability show that as the active area increases, the performance of blend-cast devices suffer.[112,113] Fortunately, SqP, which is based on the thermodynamics of swelling, avoids these problems with scale-up.[2,23,37,127] Figure 2.4 compares the performance of thickness- and composition-matched P3HT:PCBM devices produced by BC (red circles) and SqP (blue diamonds) at two different size scales. In the small-area devices (∼7 mm^2) shown in Panel a), the BC and SqP devices perform similarly with slightly better performance from the SqP devices at $3.4 \pm 0.2\%$ compared to $2.9 \pm 0.2\%$. For the identically-prepared larger-area devices (∼34 mm^2) in Panel b), not only do the SqP devices exhibit superior device efficiency ($2.5 \pm 0.2\%$ vs. $2.0 \pm 0.4\%$), but their performance is more consistent, as indicated by the lower

standard deviation (error bars) for 20 devices of each type.[23]

2.2.2 Design Rules: Using SqP to Control Polymer Crystallinity

A clear benefit of SqP is the ability to quantify, using χ, the swelling induced by a given solvent or solvent blend and thus understand the resulting interpenetrating BHJ network that is formed. As mentioned above, χ is not only affected by the choice of solvent, but also by the polymer crystallinity.[165,166] Generally, higher polymer crystallinity is better for polymer-based photovoltaics since the regular chain packing provides for improved charge transport. Increasing polymer crystallinity is difficult with blend-cast BHJs, because the presence of fullerenes in the originally-cast film inhibits polymer crystallization (and as mentioned above, most modern push-pull polymers will not tolerate thermal annealing). Fortunately, by separating the polymer and fullerene casting steps, SqP provides a route to independently controlling the polymer crystallinity.

As a demonstration of this type of control, we varied the crystallinity of P3HT films by changing the solvent from which the polymer was cast, and also by thermally annealing the films (as P3HT is one of the few polymers for which thermal annealing is advantageous).[98,99,185,186] When we cast P3HT from a high vapor pressure solvent, such as chloroform, the resulting films are highly amorphous, whereas casting from a slower-drying solvent, such as *ortho*-dichlorobenzene (ODCB), creates P3HT films that are significantly more crystalline, as could be seen by examining both the UV-Visible absorption spectroscopy and X-ray diffraction of the films.[2,37,103,117,187,188] Figure 2.5 shows the results of swelling these P3HT films of varying crystallinity with IPA vapor. We found that the more amorphous films cast from chloroform (red circles) exhibit larger volume changes compared to the more crystalline films cast from ODCB (blue triangles), consistent with the idea that crystalline regions are effectively impenetrable to swelling solvents and thus do not participate in the volume expansion of the film. If we thermally anneal a chloroform-cast P3HT film, we see that its swellability is reduced to be similar to that of an ODCB-cast film (black diamonds). As a result, the calculated χ value for chloroform-cast P3HT is lower than the nearly-matched χ values for the ODCB-cast and chloroform-cast-annealed P3HT films.[2] Thus, SqP allows us to preserve the crystallinity of an ODCB-cast or annealed P3HT film, as long as we choose a solvent with the

second casting step that has an appropriate χ to allow for fullerene intercalation.

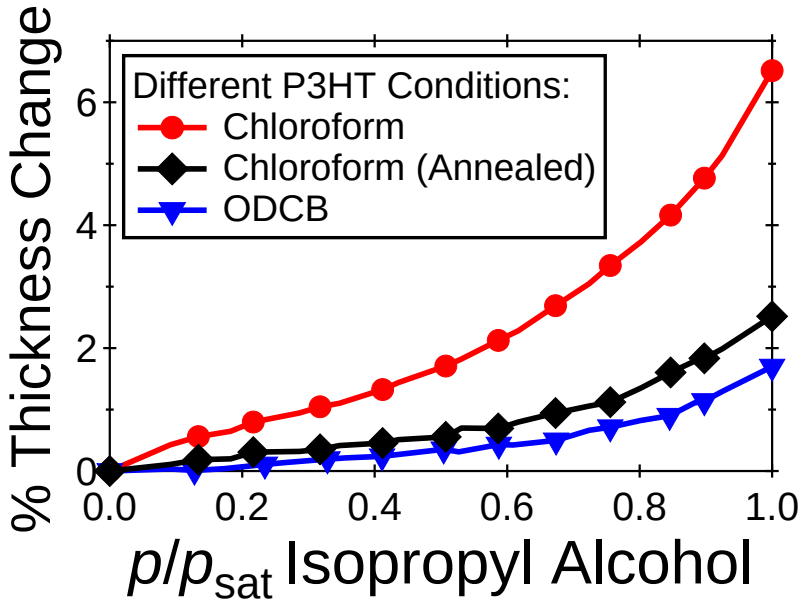

Figure 2.5: Porosimetry-ellipsometry measured swelling of P3HT films cast from different solvents; the chloroform-cast films (red circles) are much less crystalline than the thermally-annealed (black diamonds) or ODCB-cast (blue triangles) films. The more amorphous chloroform-cast film swells more than twice as much with IPA as the more crystalline films.

With the control over both the polymer crystallinity and the degree of fullerene intercalation that SqP affords, it is interesting to compare the differences in the crystallinity of devices made via BC and SqP. We studied the crystallinities of a series of composition-and thickness-matched P3HT:PCBM BHJs using grazing-incidence wide-angle X-ray scattering (GIWAXS).[127] From the GIWAXS images shown in Figure 2.6, it is clear that sequentially-processed BHJs (blue diamonds) have much higher degree of P3HT crystallinity, as evidenced by the much stronger diffraction peaks compared to BC (red circles).[127] Furthermore, electron-energy-loss filtered TEM (EF-TEM) tomography images of composition and thickness matched sequentially-processed and blend-cast P3HT:PCBM films also show that the morphology obtained by the BC approach has larger and less ordered domains compared to that obtained using SqP.[127] As mentioned above, BC nearly always leads to low polymer crystallinity because the presence of fullerene inhibits polymer crystallization.[189,190] SqP, on the other hand, can preserve the higher degrees of crystallinity in pure polymer films since the crystalline regions are not disrupted during BHJ formation, providing a route to independently tuning and optimizing this cystallinity.[127]

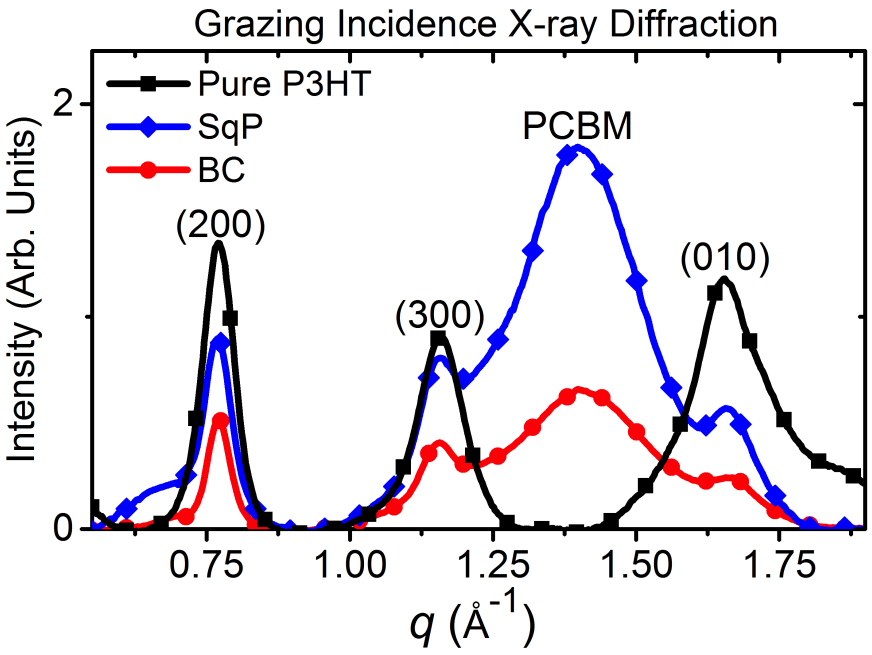

Figure 2.6: GIWAXS from a pure P3HT film (black squares) cast from ODCB and from composition-and-thickness-matched P3HT:PCBM BHJs produced by both SqP (blue diamonds) and BC (red circles). The SqP film retains more of the pure P3HT crystallinty compared to the BC film in which crystallization is hindered by the presence of fullerene.

2.3 Using SqP to Understand How Solvent Additives Improve BHJ Formation

As mentioned in Sections 2.1 and 2.2.2, thermal annealing improves BHJ morphology for semi-crystalline polymers such as P3HT[98,99] and other thiophene-based polymers,[191] but thermal treatment tends to degrade high-performing push-pull conjugated polymers.[86,111,124–126] As a partial solution to this problem, a wealth of literature has demonstrated that adding small amounts of particular co-solvents (so-called solvent additives) to blend-cast donor-acceptor solutions dramatically improves the BHJ morphology and thus device performance.[110,111,167] Indeed, such additives are required for most high-performing, polymer, blend-cast, photovoltaic systems.[3,4,26,30,107–109,168,192,193]

The first solvent additive shown to improve the BHJ morphology was octanedithiol (ODT). Adding small volumes (typically only a few %) of ODT to the polymer-fullerene blend solution led to large improvements in the photoconductive response and carrier mobilities in the resulting

cast films.[106] Perhaps more importantly, the addition of just a few percent ODT when fabricating blend-cast films for the active layer of BHJ solar cells led to a doubling of the power conversion efficiency.[107] After screening numerous liquids, 1,8-diiodooctane (DIO) emerged as the most promising additive for achieving the best BHJ photovoltaic efficiencies.[168] Furthermore, DIO's reputation as the additive-of-choice was solidified after numerous reports of devices based on new high-performing polymers that required DIO to achieve reasonable efficiencies.[3,26,108,109,192,193] Thus, DIO remains as the most frequently-used additive, even though other additives such as ODT and 1-chloronapthalene (CN) are also known to work with different polymer/fullerene materials combinations.[110,167]

2.3.1 Controversy Surrounding the Solvent Additive Mechanism of BHJ Improvement

Because of their reputation for significantly enhancing device efficiencies, solvent additives have received considerable attention, although the mechanism by which they improve the BHJ morphology and thus device performance is still not well understood. Moreover, although numerous additives exist and are well-documented in the literature, there is no clear guiding principle for either additive selection or optimal additive concentration.[17,110] What is known is that in a few select cases, the use of solvent additives leads to morphology improvement by increasing the degree of phase separation of overly-mixed polymer-fullerene BHJs,[107,110,122,168,194–197] but in the majority of systems, additives work by improving mixing of the overly phase-separated morphologies that are naturally formed with most push-pull conjugated polymers.[3,26–36] This is because most high-performing, push-pull polymers naturally over-phase segregate when blended with fullerenes. Overall, however, determining whether or not adding a few percent of an additive such as DIO, ODT or CN will increase or decrease the domain size is still determined empirically, by trial-and-error.

One interesting observation is that DIO, the most widely used solvent additive, demonstrates exceedingly high PCBM solubilities ($>$ 120 mg/mL).[198] Because of this, it has been postulated in the literature that the BHJ morphology control offered by solvent additives is connected with differential solubility:[3,26,27,31,168,197] the idea is that keeping the fullerenes better suspended in solution during film formation somehow promotes improved phase separation. This idea, however,

is not consistent with the fact that DIO can either improve mixing or promote phase separation depending on the system at hand, or that ODT also favorably improves BHJ morphology,[107,195,199] but only has a PCBM solubility of 19 mg/mL.[200] It is also worth noting that the use of solvent additives is neither a scalable nor a desirable avenue towards device optimization: in general, solvent additives are difficult to work with, with only very small amounts required for optimal performance (and an optimal amount that changes upon scale-up).[110,114,201] DIO is particularly difficult to work with since it is sensitive to light and air; with its low vapor pressure, DIO tends to remain in the polymer film, leading to degradation of the device performance once this additive begins to break down.[202–204]

2.3.2 Solvent Additives are Non-Evaporating Swelling Agents

Perhaps the one common feature among the various solvent additives used to improve BHJ morphology is that nearly all of them have high boiling points. Shin *et al*. demonstrated that adding small amounts of ODT or CN to blend solutions of P3HT:PCBM significantly extended the film solidification time, and that increasing the amount of additive produced films with greater thickness.[205] The increased thickness likely arises simply from the fact that these slowly-evaporating solvent additives remain in the film; indeed, the thickness of films cast with solvent additives decreases over long periods of time as the additive evaporates, approaching the additive-free thickness.[190] The fact that solvent additives remain in a polymer BHJ film and increase its thickness has led us to suggest that solvent additives improve device performance by acting as non-evaporating swelling agents, effectively turning BC into SqP.[2]

Our conclusion that solvent additives function by swelling is based on experiments where we spun pure P3HT from solutions containing no solvent additive, 3% DIO, 3% ODT, and 3% CN and then measured the thickness of the resulting films using spectroscopic ellipsometry.[169,171] We found that the P3HT films cast with both DIO and ODT additives were thicker than those cast without additives by hundreds of nanometers (i.e., the small amounts of solvent additive more than doubled the film thickness).[206] The films cast from the solution with the CN additive were only marginally thicker than the additive-free films, but since CN has the lowest boiling point out of the

three solvent additives, we believe that the CN simply evaporated between the time the films were cast and the ellipsometry measurements.

To understand what the presence of so much solvent additive does in a conjugated polymer film, we fabricated sequentially-processed BHJ solar cells by spin-coating PCBM (dissolved in DCM) onto P3HT films cast with and without solvent additives, as described above. As discussed in Section 2.1 above, DCM is a poor swelling solvent for P3HT, so as a result, devices with no solvent additive have poor performance because PCBM is not well-mixed throughout the polymer film. When the P3HT film is pre-swollen by solvent additives, as in the case of ODT and DIO, however, the device performance increased significantly. This suggests that when fullerene is deposited in the second SqP step, the fact that the polymer film was pre-swollen by the additive facilitates more-complete mixing of polymer and fullerene, resulting in an improved BHJ morphology.[206] Thus, non-evaporating solvent additives present another avenue for optimally swelling polymer films via SqP: if the polymer film is pre-swollen, the fullerene-casting solvent no longer needs to have the optimal value of χ to produce BHJs by fullerene infiltration. Moreover, since DCM removes DIO, sequential deposition of PCBM simultaneously removes the majority of DIO, which otherwise is a separate step required after BC of a BHJ film that uses a solvent additive.[202]

The idea that DIO acts as a non-evaporating swelling agent is also consistent with a report by Kong *et al*.[207] In their work, Kong *et al*. created BHJ films from several conjugated polymers, and then spun a DIO buffer solution (a few % DIO dissolved in a marginal polymer solvent) on top of the films. They found that the BHJ morphology was reorganized and significantly improved. Since the DIO in this case was introduced after the BHJ is formed and the fullerene solidified, this provides further evidence that differential solubility of the polymer and fullerene is not the main mechanism for BHJ improvement with solvent additives. But the observed improvement in device performance is consistent with the idea of solvent additives acting as non-evaporating swelling agent: DIO swells the BHJ and remains in the polymer film, giving plenty of time and free volume for the fullerene to reorganize within the BHJ and form more ideal domains.

Overall, we believe that solvent additives work by essentially converting BC into SqP. When there is a small amount of solvent additive present in a blend-cast solution, the resulting BHJ film ends up swollen by the slowly-evaporating additive that remains in the film. This gives the fullerene

time to reorganize within the polymer film even after the main solvent has evaporated; the BHJ morphology is improved in essentially the same manner as in the experiments of Kong *et al*.[207] The reason that blend-cast morphologies are so sensitive to the amount of solvent additive is that different polymers have different χ values with different additives, and as with SqP, it is critical to adjust the amount of polymer swelling to allow for the proper degree of fullerene reorganization. Finally, ODT, CN and other liquids work as solvent additives because they are also good swelling agents for conjugated polymers and have high boiling points, not because they have high fullerene solubility (as ODT does not).

2.4 Doping Conjugated Semiconducting Polymers by the Sequential Processing Approach

The same SqP methodology and design rules described in Section 2.2 to create polymer-fullerene BHJs also can be applied to inserting other small molecules into a pre-cast conjugated polymer film. If the molecule of interest has a LUMO level comparable to the polymer HOMO level, charge transfer occurs, resulting in *p*-type doping of the polymer.[69] Since semiconducting polymers have intrinsically low carrier densities and mobilities, molecular doping can be beneficial as it allows electrical properties such as conductivity to be tuned over several orders of magnitude, thereby enabling these materials to be used for a wider variety of applications.[69,208,209]

Similar to BC in OPVs, molecular doping has traditionally been achieved by co-dissolving the dopant and polymer and using the solution to cast a film.[5,69–71] At low dopant concentrations, BC is a completely adequate preparation method for creating doped conjugated polymer films. As the dopant concentration increases, however, the presence of the charges created on the polymer backbone greatly decreases the solubility of the polymer in organic solvents, causing the polymer to aggregate and eventually crash out of the solution used to co-dissolve the polymer and dopant.[72–77] This is why it has been exceedingly difficult to produce high-quality, scalable highly-doped conjugated polymer films via blend-cast doping.[70,76,210]

Given the success we had using SqP to control BHJ morphologies with conjugated polymer-fullerene blends, we found that we could also use SqP to successfully dope conjugated polymer

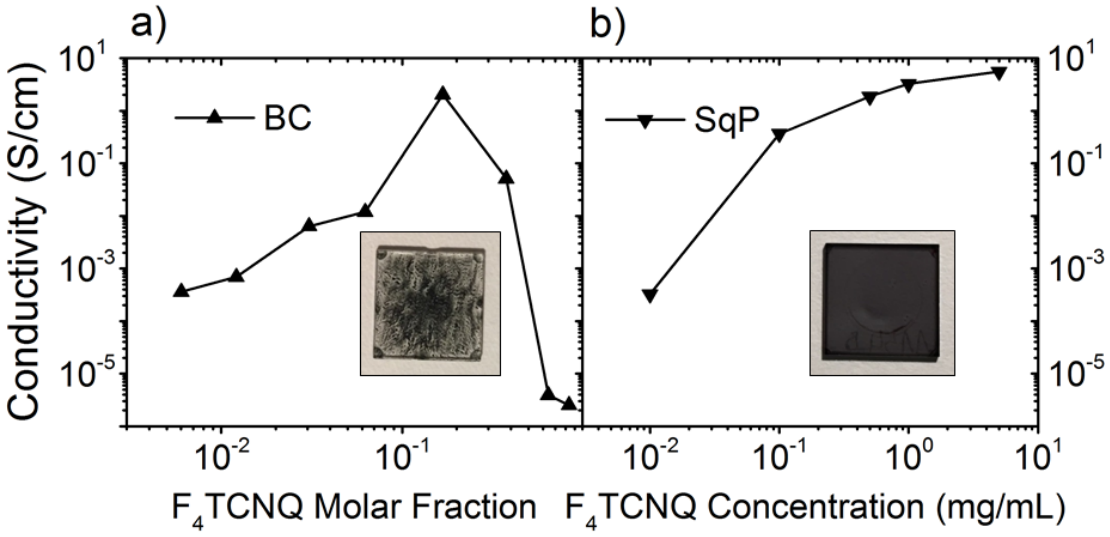

Figure 2.7: Comparison of the conductivity of P3HT films doped by (a) blend casting (data from[5] and (b) sequential processing. The different units on horizontal-axis result from the two distinct doping methods; for BC, doping is reported as a mole fraction of the F_4TCNQ dopant in the blended solution, whereas for SqP, doping is reported as the F_4TCNQ concentration (mg/mL) in the solution from the second casting step. Inset is an image of each doped film.

films with a high degree of morphology control.[74] By simply tuning the concentration of dopant in the selected solvent that appropriately swells the underlying polymer, we were able to achieve high doping levels that were only limited only by the solubility of the dopant in the chosen swelling solvent.[74,75] Several groups have subsequently taken advantage of this idea, using SqP doping of conjugated polymer films for patterning or to improve conductivity.[78,79,211,212] Figure 2.7 shows our use of SqP to dope P3HT by oxidation with 2,3,5,6-Tetrafluoro-7,7,8,8-tetracyanoquinodimethane (F_4TCNQ). We were able to achieve the highest-reported conductivities for this particular materials combination. More importantly, since the quality of the doped film quality was unchanged from the originally-cast polymer film, we were also able to quantify the carrier density and mobility via AC-field Hall Effect measurements,[74] something that even in early 2015 had not been believed to be possible with films fabricated by BC.[213]

2.5 Conclusions and Perspective

Sequential processing makes BHJ design a tractable and more rational process by decoupling BHJ formation into two, independently tunable steps. With SqP, one can choose the solvent in

the first casting step to control the degree of polymer crystallinity. The initial film could also be molecularly doped, patterned, or modified by thermal annealing if desired. Fullerene incorporation into the tailored polymer film is then precisely tuned by selection of the appropriate solvent for the second casting step, along with the fullerene concentration. By making some very simple swelling measurements, it is straightforward to choose an optimal solvent or solvent blend for the SqP fullerene-casting step with the proper χ value to allow for fullerene intercalation without dissolution of the underlying polymer. Because SqP depends on the thermodynamics of swelling and not the kinetics of solvent evaporation, SqP is amenable to large-scale fabrication techniques, avoiding the need to re-optimize small-scale results to the large-scale processing. The SqP technique works for both polymers that are highly soluble in common solvents and those that are not, providing a rational means to create desired BHJ morphologies without need for trial-and-error. The general principles that govern BHJ formation via blend-casting are poorly understood, making SqP the processing technique of choice.

In addition, forming a BHJ in two separate steps facilitates a greater understanding of BHJ formation. In this way, SqP enabled us to argue that solvent additives act as non-evaporating polymer swelling agents, improving BHJ morphology by effectively turning BC into SqP. This also opens the possibility to use solvent additives in the first SqP casting step, pre-swelling the polymer film and allowing for a wider choice of solvents for the second step since it is no longer necessary to optimize χ. Without the ability to independently control swelling and fullerene intercalation, solvent additives would need to be continually re-optimized through trial-and-error.

Finally, since SqP is an efficient method for inserting small molecules into conjugated polymer films, SqP is also a highly effective technique for molecular doping. By swelling, molecular dopants can be effectively inserted into conjugated polymer films, resulting in unprecedented film quality and conductivity. With both BHJ formation and molecular doping, SqP allows us to take advantage of swelling to control conjugated polymers for a wide variety of optoelectronic applications.

CHAPTER 3

Solvent Additives Function as Polymer Swelling Agents in Bulk Heterojunction Organic Photovoltaics

3.1 Introduction

Achieving a high power conversion efficiency (PCE) in organic bulk heterojunction (BHJ) photovoltaics requires forming an ideal nanometer-scale morphology. This morphology must be well-mixed, but also have sufficient phase separation to facilitate contiguous pathways for the different carriers. Most photovoltaics are comprised of a blend of a conjugated polymer and a fullerene derivative such as phenyl-C_{61}-butyric acid methyl ester (PCBM). Although recent advances have pushed the efficiency of single-junction polymer BHJ solar cells over 13%,[214] attaining the ideal morphology for any given set of conjugated polymer and fullerene materials is quite challenging. In fact, most high-performing materials do not achieve ideal phase separation when they are simply mixed and cast into films, resulting in under-performing devices.[3,26,110] To address this issue, a variety of techniques have been developed to control polymer/fullerene phase separation, including thermal[98,99] and solvent annealing[103,104] of already-cast BHJ films, changing the host solvent from which the films are cast,[105] and the inclusion of a few volume percent of solvent additives, such as 1,8-diiodooctane (DIO), 1,8-octanedithiol (ODT) or chloronapthalene (CN), in the solution from which the films are cast.[3,26,29,107,110,122,168,195,215,216]

Unfortunately, none of these methods for improving BHJ morphology can be effectively utilized to improve device efficiency without significant trial-and-error. For example, thermal annealing improves the morphology for semi-crystalline polymers such as poly(3-hexylthiophene-2,5-diyl) (P3HT) and is relatively straightforward in application, but the use of heat tends to degrade the performance of devices based on high-performance push-pull polymers.[86,125] Therefore,

thermal annealing is not widely applicable to polymer photovoltaic systems. The use of solvent additives in the casting solution has become perhaps the most widely used approach for tuning BHJ morphology,[110] but based on the polymer used, their effect is highly system specific. For example, BHJ systems that naturally form large polymer and fullerene domains require additives that can improve mixing and decrease domain size,[3,26,29–31] while BHJ systems that naturally over-mix require additives that can increase phase separation.[107,122,168,195] Thus, it is not always clear when a particular additive will increase or decrease the average domain size, or how much additive is necessary for optimal performance. This need for trial-and-error is a reflection of the fact that the mechanism by which the additives function is not well understood; indeed, a recent review on the use of additives in BHJ formation calls for additional studies to investigate their method of operation.[110]

In addition to the need for Edisonian optimization, the use of solvent additives is problematic on several other fronts: 1) In general, only very small amounts of additives are required for optimal performance. For example, 3% (v/v) additive is frequently reported as the optimal amount needed for many polymer BHJ systems,[110] while in small-molecule BHJ systems, changes in additive concentration of only 0.35% (v/v) from the optimal concentration can cut device efficiency in half.[201] 2) The optimal amount of additive required frequently changes upon scale-up.[114] Since most additives have high boiling points, they alter the drying kinetics during film-formation, so it is perhaps not surprising that large-scale fabrication methods, which have entirely different drying kinetics than spin-coating in the laboratory, require re-optimization. 3) The most widely used solvent additive, DIO, is both light- and air-reactive, making it of questionable use in any type of future commercial process. Moreover, it is well known that DIO tends to remain in BHJ films due to its low vapor pressure, requiring extra processing steps to ensure its removal to prevent device degradation upon exposure to light or air.[202,217,218] 4) Similar to solvent annealing, the time DIO resides within the film can affect the BHJ morphology through 'additive annealing,' thereby requiring further optimization and kinetic control.[219]

In this work, we focus on the role of the solvent additives DIO and ODT in improving the performance of conjugated polymer/fullerene-based BHJ photovoltaics. DIO has an unusually high PCBM solubility of 120 mg/mL,[198] and because of this, many groups have postulated that

the morphology control afforded by DIO is connected with differential solubility of the polymer and fullerene:[3,26,31,168,197] the general idea is that additives help suspend fullerenes in solution for greater periods of time, which in turn affects the fullerene domain size as the film dries. This idea is not consistent, however, with the fact that molecules like ODT and CN are also commonly used as additives to favorably improve the BHJ morphology.[107,168,195,199] ODT has nearly an order of magnitude less fullerene solubility (19 mg/mL for PCBM)[200] than DIO, and as a generally good polymer solvent, CN affords little differential polymer/fullerene solubility.[161] This suggests that the mechanism by which solvent additives operate to improve BHJ morphology likely depends on some property other than differential solubility.

In previous work, we presented an alternate method for controlling BHJ morphology and fabricating high-performing solar cells based on a two-step fabrication process called sequential processing (SqP).[2,99,127] In SqP, a film of pure polymer is deposited first, and then the fullerene is intercalated to form a BHJ in a second step by casting from a quasi-orthogonal solvent that swells but does not dissolve the polymer underlayer. To ensure optimal BHJ formation, we showed that the solvent used in the fullerene-casting step must optimally swell the polymer underlayer.[2] This is because swelling lies on the spectrum between no solvent interaction with the polymer and full polymer dissolution. If the fullerene-casting solvent insufficiently swells the polymer, then there will not be good penetration of the fullerene into the polymer to form the requisite BHJ morphology; if the fullerene-casting solvent over-swells the polymer, it dissolves some of the polymer film away, again leading to poor BHJ formation. It is also important that the fullerene-casting solvent has a high enough fullerene solubility for mass action to drive fullerene into the properly-swollen polymer underlayer.[2,39] We and others have demonstrated that solvent blends can be used to simultaneously optimize both polymer swelling and fullerene solubility, making rational BHJ construction, without the need for significant trial-and-error, tractable via SqP.[2,39] We also have used SqP to infiltrate strong oxidizing agents into films of conjugated polymers to produce highly conductive doped material.[74,75]

In this chapter, we take advantage of the fact that SqP decouples the polymer and fullerene components in BHJ formation to investigate the mechanism by which solvent additives improve BHJ morphology. We find that solvent additives function as swelling agents: additives alter poly-

mer/fullerene mixing by swelling the polymer film, allowing fullerenes to remain mobile as the BHJ is formed. Our evidence is based on experiments in which we add DIO or ODT to conjugated polymer solutions prior to casting pure polymer films. We observe by spectroscopic ellipsometry that low-vapor-pressure additives such as DIO and ODT remain in the polymer film and significantly swell it, in agreement with previous *in situ* experiments on polymer/fullerene blend solutions.[190,205,220] We find by grazing-incidence wide-angle X-ray scattering (GIWAXS) that swelling of P3HT films by solvent additives is so great that the polymer crystallinity is significantly altered; this suggests that additives act as 'secondary plasticizers',[221] since the additive 'plasticizer' primarily enters the amorphous regions of the polymer film. When we then spin-cast PCBM from dichloromethane (DCM) on top of either a pristine or additive-swollen P3HT film in a second SqP step, we find using X-ray photoelectron spectroscopy (XPS) and neutron reflectometry (NR) that the presence of the additive helps to produce complete vertical mixing of P3HT and PCBM into a BHJ, whereas there is significantly less fullerene intercalation when no additive is present in the polymer underlayer. Moreover, the presence of the additive in the polymer underlayer leads to greatly improved sequentially-processed device performance. We also show that these same swelling, morphology, and device performance effects involving solvent additives also hold when considering two higher-performing push-pull polymers, poly[(4,4′-bis(3-(2-ethyl-hexyl)dithieno[3,2-b:″,3′-d]silole)-2,6-diyl-alt-(2,5-bis(3-(2-ethyl-hexyl)thiophen-2yl)thiazolo[5,4-d]thiazole)] (PSE-HTT)[222] and poly[4,8-bis-(2-ethylhexyloxy)-benzol[1,2-b:4,5-b′]dithiophene-2,6-diyl-alt-4-(2-ethylhexyloxy-1-one)thieno[3,4-b]thiophene-2,6-diyl] (PBDTTT-C).[223] Therefore, similar to how solvent blends for fullerene solutions can be tuned to optimally swell a polymer film,[2] the primary mechanism of action for low-vapor-pressure solvent additives to improve BHJ morphology is to function as co-solvents that swell conjugated polymer films. This conclusion should make it possible to rationally choose solvent additives as well as opening additional pathways for BHJ morphology improvement via SqP.

3.2 Experimental

P3HT and PBDTTT-C were purchased commercially and PSEHTT was synthesized[1] in-house. All other materials used in this study were purchased commercially and were used as received. For polymer-based devices, sequentially-processed active layers were prepared by spin-casting a polymer solution onto a PEDOT:PSS-covered substrate. For the P3HT, PSEHTT, and PBDTTT-C solutions, 20 mg, 10 mg, and 10 mg, of polymer, respectively, were dissolved in 1 mL *o*-dichlorobenzene. The P3HT, PSEHTT, and PBDTTT-C solutions were mixed overnight at 55, 100, and 25°C, respectively. DIO or ODT (typically 3% by volume) was added directly to the polymer solution prior to heating (if required). The P3HT and PBDTTT-C solutions were cooled to room temperature prior to spin-coating while PSEHTT was spun hot at 100 °C. To remove solvent additives by methanol washing, methanol was deposited on the freshly-formed polymer films while the films were still on the spin-coater chuck. Fullerene deposition always occurred within one hour of casting the polymer film, and no vacuum step was applied between polymer and fullerene spinning to ensure minimal evaporation of any solvent additives between polymer film preparation and fullerene deposition. The detailed procedures of our film and device fabrication are found in Appendix A.

Film thicknesses at each stage of the SqP fabrication process were measured by both profilometry and spectroscopic ellipsometry. The latter technique measures the film's refractive index in a non-absorbing spectral region and constructs a model to fit the data; since the indices of refraction of the films are known, the parameter representing film thickness was varied until the model fits the experimental data.[2,169,170] For the solvent-swelling experiments, each film was placed in a home-built customized vial, which was designed to contain a solvent (e.g., toluene or DCM). The film was exposed to the vapor of a swelling solvent in the vial and the thickness monitored until it reached steady-state. In this way, the vial allowed us to perform swelling measurements with solvents such as DCM that were not compatible with the porosimeter instrument. Details of the calibration for the swelling vial and ellipsometry fits can be found in Appendix A.

X-ray photoelectron spectroscopy (XPS) experiments were performed in-house on Si/active layer films using a Kratos Axis Ultra DLD with a monochromatic K_α radiation source. 2-D GIWAXS

experiments were performed at the Stanford Synchrotron Radiation Lightsource on beam line 11-3 using a wavelength of 0.9742 Å. This beam line has a 2-D detector that allows us to integrate the full 2-D data (0 – 180°), just the in-plane portion of the data (170 – 180°), and just the out-of-plane portion of the data (100 – 110°). To ensure minimal additive evaporated between film preparation and the measurement, all films were stored in sealed vials after spin-coating and were prepared less than 24 hours from the measurement time. Neutron reflectometry (NR) experiments were performed at Oak Ridge National Laboratory using the Magnetism Reflectometer at the Spallation Neutron Source using a neutron wavelength of 4.41 Å. Scattering length density (SLD) depth profiles were obtained by calculating the reflectivity of a model SLD profile, and iteratively refining the model until the calculated reflectivity profile matched the experimental reflectivity profile. Additional fitting and experimental details can be found in Appendix A.

Detailed procedures for all other techniques and additional information such as device external quantum efficiency curves, photoluminescence measurements, etc. can be found in Appendix A and are similar to those published in our previous SqP work.[2,127,224]

3.3 Results and Discussion

Because most organic solar cells are fabricated via blend-casting, in which the polymer or absorbing molecule, fullerene or acceptor molecule, and additive are all mixed together in solution prior to casting the device's active layer, understanding the role of the additive in device morphology and performance is challenging. Many groups have proposed that differential solubility of the fullerene and polymer in the solvent additive is the mechanism by which BHJ morphology and device performance are improved.[3,26,31,168,197] One clue indicating the solvent additive mechanism for device improvement is not differential solubility comes in work performed by Kong *et al*., in which BHJ films were cast and then a dilute DIO solution was spun onto the BHJ film in a second processing step.[207] This 'post-additive soaking' favorably reorganized the donor and acceptor domains, resulting in significantly improved device efficiencies.[207] Since DIO was added to the film after BHJ formation, this two-step approach indicates the mechanism by which the additive operates is independent of fullerene solubility. Moreover, this work suggests that a fruitful avenue

for further investigation into the role of DIO and other solvent additives in BHJ formation would be to form active layers using an alternative fabrication technique.

3.3.1 Exploring the Role of Solvent Additives by Sequential-Processing

Motivated by the work of Kong *et al.*,[207] we decided to investigate the mechanism by which solvent additives control BHJ morphology using sequential-processing.[2,37,127] We selected P3HT as the first polymer system to study because of P3HT's semi-crystalline nature: this provides a structural handle on the chain spacing and domain orientation via two-dimensional grazing incidence X-ray scattering (GIWAXS), which is something that is more challenging to characterize with generally more amorphous push-pull polymers. Furthermore, P3HT also provides the advantage of having generally weaker interactions with organic solvents (*i.e.*, poorer solubility) than the push-pull polymers we explore below. Because of this weaker interaction, when depositing PCBM onto a P3HT film by SqP using DCM as the fullerene solvent, DCM's marginal swelling of the polymer underlayer promotes formation of a quasi-bilayer with a fullerene-enriched top surface. This is a highly non-ideal BHJ morphology. This quasi-bilayer structure, however, provides an opportunity to demonstrate that the BHJ morphology can be improved by DIO due to improved polymer swelling:[2,39] we will show using three polymer systems of varying crystallinity (P3HT, PSEHTT, and PBDTTT-C) that when the fullerene solvent provides insufficient swelling, the presence of a solvent additive swelling agent in the polymer underlayer converts this non-working system into a working system. Moreover, the extent of the improvement is dependent upon the degree of swelling by the fullerene solvent: if the fullerene solvent promotes near-optimum swelling, the effect of the solvent additive is marginal. Thus, decoupling swelling by solvent additives and swelling by the fullerene solvent allows us to identify swelling as the mechanism for BHJ morphology improvement by solvent additives.

We started by fabricating P3HT/PCBM solar cells using SqP, but with the addition of DIO to the P3HT solution. Since the first step in SqP involves spin-casting a pure polymer film, this decouples the action of DIO from the presence of PCBM, which is added in a second processing step cast from DCM. Figure 3.1 shows the J–V characteristics of sequentially-processed BHJ devices with

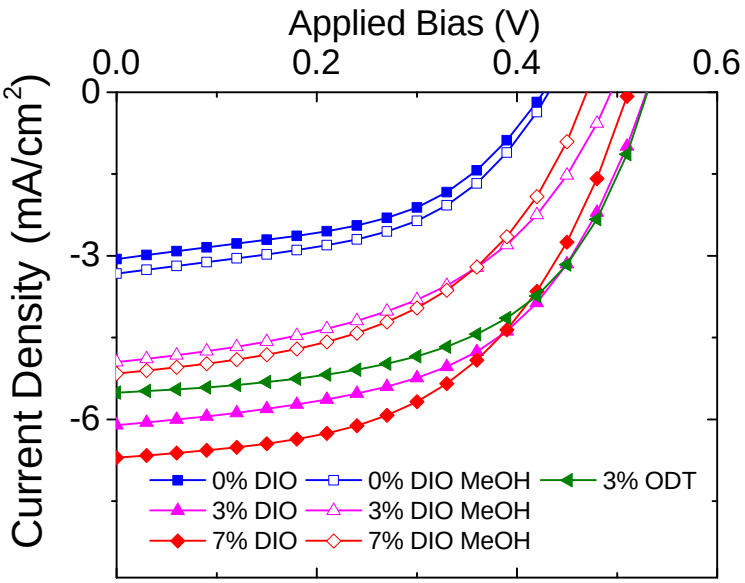

Figure 3.1: *J–V* measurements for sequentially-processed ITO/PEDOT:PSS/P3HT(DIO)/PCBM/Ca/Al solar cells under AM-1.5 illumination, illustrating the effect of different concentrations of DIO or ODT and subsequent methanol washing on device performance. The filled symbols show that devices fabricated with 0% (v/v) DIO (blue squares), 3% (v/v) DIO (pink up-triangles), 7% (v/v) DIO (red diamonds), and 3% (v/v) ODT (green left-triangles) in the polymer solution have improved performance with increasing DIO concentration. By contrast, devices in which the polymer films from the first SqP step was methanol-washed prior to deposition of the PCBM (open symbols) show reduced performance compared to unwashed films: 0% (v/v) DIO (hollow blue squares), 3% (v/v) DIO (hollow pink up-triangles), and 7% (v/v) DIO (hollow red diamonds). Comparison of 3% DIO and 3% ODT $J-V$ curves shows that both DIO and ODT enhance SqP device performance to a similar extent, and the methanol data suggest that the application of a methanol wash prior to casting the fullerene leaves a similar amount of residual additive in the polymer film, regardless of the initial additive concentration.

0, 3, and 7% (v/v) DIO added to the P3HT solution used in the first SqP step. All devices were measured under AM-1.5 solar illumination, and the plotted data are the average of approximately 9 separate devices. Detailed *J–V* parameters for each set of devices are presented in Table A.1 of Appendix A. The corresponding EQE spectra for 0, 3, and 7% (v/v) DIO are presented in Figure A.1 and additional device conditions (blend-cast devices and annealing) are presented in the Table A.1 of Appendix A. Additional device physics such as dark *J-V* curve analysis and dark charge extraction by linearly increasing voltage (CELIV) measurements are also described in Appendix A.

Figure 3.1 shows that without DIO, the currents of the sequentially-processed devices are quite low, but that the currents increase significantly with increasing percent DIO added to the polymer solution in the first SqP step. This strongly suggests the DIO–P3HT interaction is responsible for

device improvement. Since DIO has a very low vapor pressure,[225] DIO remains in the films prior to the second SqP step where the fullerene is deposited. In fact, the tendency of DIO to remain in BHJ films is known to lower device efficiencies due to its deleterious chemistry in the presence of light or air. To counter the detrimental effects of DIO remaining in BHJ films, several groups have used methanol washing, where pure methanol is spun onto the film to remove the remaining DIO without dissolving the polymer and/or fullerene.[202,203,217] Thus, to investigate whether or not the improvement in device performance was due to DIO remaining in our pure P3HT films, we performed methanol-washing experiments in which we performed the washing step directly after P3HT film formation and prior to PCBM spin-coating. When DIO is removed from the polymer film by methanol washing, we find that the device currents decrease, although not to the same extent as when no DIO was initially present. Furthermore, both methanol-washed devices have almost identical currents. This suggests that similar residual concentrations of DIO remain in the film after methanol washing, regardless of the initial volume percentage of DIO used in casting the polymer film.

The data in Fig. 3.1 also show that although the use of DIO produces the best *J*–*V* characteristic, the use of ODT as a solvent additive leads to comparably good sequentially-processed device performance. Indeed, blend-cast P3HT:PCBM photovoltaics fabricated with DIO and ODT also have similar device characteristics (see Appendix A). This suggests DIO and ODT have a similar interaction with P3HT and work via a similar mechanism of operation. Moreover, we also see similar improvements in sequentially-processed device performance with the addition of DIO to films of different push-pull polymers, discussed further below. This leads to the principle lines of inquiry of this chapter: for sequentially-processed polymer/fullerene photovoltaics, why do DIO and ODT significantly improve device performance? And how does what we learn from devices produced by SqP translate to the broader spectrum of BHJ solar cells fabricated using solvent additives via other processing techniques? In the following sections, we present a series of structural and device measurements on a variety of materials to answer these questions and present a clear mechanism – swelling – by which solvent additives alter BHJ morphology and thus photovoltaic device performance.

3.3.2 Effect of Solvent Additives on P3HT Swelling and Crystallinity

How do solvent additives affect the quality of BHJ solar cells produced by SqP when the additive is used before any fullerene is intercalated into the device? In this section, we first examine the swelling properties of solvent additives on pure P3HT films, and then explore the changes such additives make in the structure of pure polymer films using X-ray diffraction.

3.3.2.1 The Swelling Properties of Solvent Additives

In previous work, we demonstrated that polymer swelling is responsible for BHJ morphology control in devices produced via SqP.[2] Furthermore, the degree of polymer swelling is critical for optimal device performance. We showed using spectroscopic ellipsometry that the degree of solvent/polymer interaction can be quantified by the Flory-Huggins χ parameter, and that there is an optimal χ to produce the best sequentially-processed devices.[2] We also found that we could use solvent blends to simultaneously tune χ and maintain enough fullerene solubility to provide sufficient mass action for fullerene intercalation into the sequentially-processed BHJ.[2]

With the idea that optimal solvent swelling is the key to fabricating good sequentially-processed BHJ solar cells, we turn next to investigate the role of DIO and ODT in modifying swelling behavior using spectroscopic ellipsometry. For all our ellipsometry experiments, the various conjugated polymers were spun onto single-crystal Si substrates from solutions of 1,2-dichlorobenzene (ODCB) with or without a small percentage of solvent additive. The height of the bars in Fig. 3.2 show the ellipsometrically-determined thicknesses of P3HT films cast from ODCB with and without varying small amounts of solvent additives. Depending on the additive used, there is a substantial difference in thickness of the resulting films. Films cast with additive present are significantly thicker than control films with no additive; for example, the film cast using 7% DIO is nearly four times thicker than the film cast from pure ODCB under otherwise identical conditions. The enhancement in film thickness with solvent additives is also general to push-polymers, as we discuss in more detail below in Fig. 3.7.

The most logical hypothesis for the increased thickness of the P3HT films cast using solvent additives is that the additives remain in the film after the ODCB has evaporated, leaving a polymer

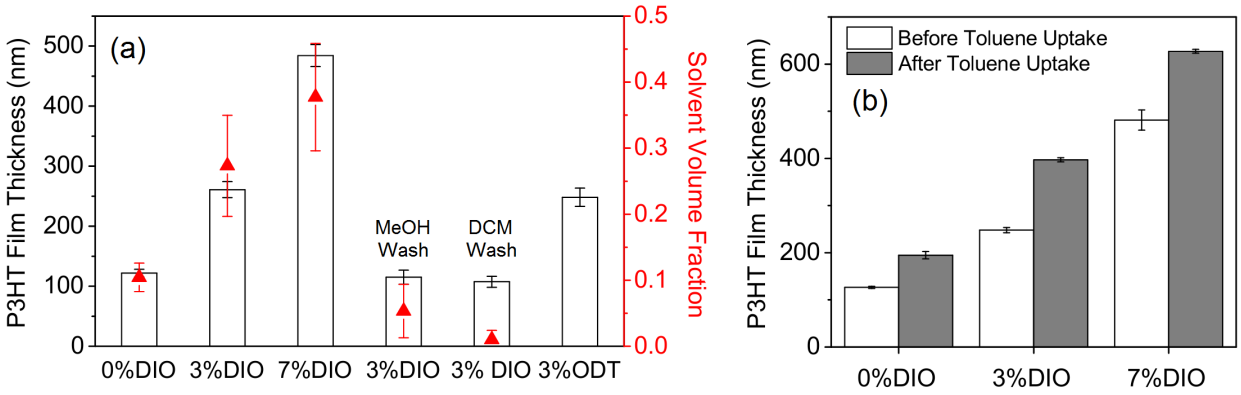

Figure 3.2: (a) Thickness (bar heights) of pure P3HT films obtained by spectroscopic ellipsometry. The thickness was measured directly after spin-casting for pure P3HT films cast from ODCB with no DIO, 3% (v/v) DIO, 7% (v/v) DIO, 3% (v/v) DIO followed by methanol washing, 3% (v/v) DIO followed by dichloromethane washing, and 3% (v/v) ODT. Adding DIO and ODT and increasing the additive concentration produces thicker polymer films. Washing with methanol or DCM reduces the film thickness to close to the point where no additive was used. The red triangles show effective medium approximation fits to the ellipsometry data that yield the solvent volume fraction in the film (which could be either ODCB or DIO, which have similar refractive index profiles). (b) Thickness of P3HT films cast with 0% (v/v) DIO, 3% (v/v) DIO, and 7% (v/v) DIO before toluene vapor uptake (white bar heights) and after toluene vapor uptake (grey bar heights). The additional swelling by toluene vapor for films with DIO demonstrates DIO's ability to increase the swelling range for P3HT. The error bars represent one standard deviation obtained from averaging over at least three different polymer films.

film that is highly swollen. Indeed, the vapor pressures of the most commonly used solvent additives are significantly lower than that of ODCB; at 25 °C the vapor pressures are: 0.04 Pa for DIO;[225] 1.60 Pa for ODT;[226] and 181 Pa for ODCB.[227] The fact that DIO remains in the film longer than higher vapor pressure solvents recently has been confirmed by *in-situ* GIWAXS measurements that demonstrated that DIO remains in polymer films for prolonged periods of time.[220] This is why low-vapor-pressure additives need to be removed prior to device fabrication (because otherwise they remain in the active layer). When we wash our P3HT films with methanol, we see their thickness returns to within 10% of that obtained for films cast from pure ODCB (the slight increase in remaining thickness is consistent with the idea discussed above that methanol does not fully remove DIO from the film,[202] leaving the films slightly swollen). The device data above suggests that ODT acts in a similar manner to DIO, but with a slightly smaller overall effect; this makes sense in light of ODT's higher vapor pressure, which likely leaves less residual additive in the film relative to DIO.

In addition to inferring the presence of low-vapor-pressure solvent additives in our films by the increase in polymer film thickness, we also can use spectroscopic ellipsometry to directly quantify the amount of additive that remains in the polymer film. To do this, we applied the effective medium approximation (EMA), which states that the refractive index of a mixture is the volume-weighted average of the refractive indices of each of the components.[175] Since we know the wavelength-dependent indices of refraction of both P3HT and DIO, we can use the ellipsometrically-measured index of refraction to quantify the DIO volume fraction in each film.[2] The details of our EMA fitting procedure are given in Appendix A. The DIO volume fractions we obtain are 27% and 36% for the P3HT films cast with 3% (v/v) and 7% (v/v) DIO, respectively, and the DIO volume fraction drops to less than 5% after methanol washing; the data are plotted as the red triangles in Fig. 3.2. Since the DIO volume fraction scales directly with the film thickness, it makes sense that the thickness change is attributed to swelling of P3HT by the residual solvent additive: with such a low vapor pressure, significant amounts of DIO remain in the film and are responsible for the thickness increase.

The residual DIO in P3HT films not only is mostly removed by washing with methanol, but it is also removed by washing with dichloromethane, the solvent we employ to cast the fullerene in

our second sequential-processing step. Figure 3.2 shows that for a P3HT film cast from a 3% (v/v) DIO solution in ODCB, washing with DCM reduces the P3HT film thickness to a value similar to that achieved through methanol washing. Moreover, the ellipsometrically-determined residual DIO volume fraction remaining in the film after methanol washing is 5%, while that following DCM washing is only 1%. Thus, DCM more effectively removes DIO from the film than methanol. As a result, when fabricating sequentially-processed BHJs, the second casting process combines additive removal and fullerene incorporation into a single step, thereby removing the need for a subsequent separate washing step. This suggests that not only is SqP a tractable route for controlling BHJ morphology, but that it also allows for the use of low-vapor-pressure solvent additives, with all their advantages, without the need for additional processing steps. Finally, the fact that methanol-washed sequentially-processed devices perform better than the additive-free devices is consistent with the idea that the residual DIO volume fraction of 5% still provides enough swelling to improve fullerene incorporation and device performance.

In addition to the fact that the residual low-vapor-pressure solvent additives left behind after casting swell a polymer film, we also have found that residual additives increase the film's swelling by other solvents. In Fig. 3.2(b), we examine how polymer films with different amounts of additive swell upon exposure to toluene vapor. Toluene strongly interacts with P3HT, and P3HT films cast with no solvent additive are swollen by toluene from a thickness of 127 nm to 194 nm for an effective thickness increase due to toluene-swelling of 67 nm. When P3HT films containing the same thickness of polymer are cast using solvent additives, however, the thickness increase upon swelling with toluene is even larger, with P3HT films cast from 3% (v/v) and 7% (v/v) DIO solutions swell from 250 nm to 397 nm and 482 nm to 627 nm, respectively, yielding a $\sim$150 nm increase in film thickness due to toluene uptake. Thus, the presence of DIO not only swells the polymer film, but also increases the swellability by other solvents. This means that solvent additives modify how polymer films interact with other solvents, providing yet another way to tune the Flory-Huggins χ parameter for optimal BHJ formation by SqP.[2]

3.3.2.2 How Solvent Additives Affect Polymer Crystallinity

As discussed in the previous section, we have established that conjugated polymer films processed using solvent additives are both highly swollen and have increased swellability. It is well known that polymer crystallinity strongly affects swelling because solvent molecules cannot penetrate into highly crystalline regions.[2,75,165,166] To investigate the swelling effects of solvent additives on the structure of pure P3HT films we performed a series of two-dimensional (2-D) grazing incidence wide-angle X-ray scattering (GIWAXS) experiments. Figure 3.3(a) shows integrated diffraction patterns of different P3HT films; the lamellar (100) and π-π stacking (010) peaks lie at q = 0.4 and 1.6 $Å^{-1}$, respectively. P3HT is well known to have an edge-on orientation of the crystallites, showing greater intensity for the (100) diffraction peak in the out-of-plane direction and greater (010) peak intensity in the in-plane directions, as shown in Fig. 3.4. Table 3.1 summarizes the integrated (100) peak area, which is a measure of relative film crystallinity, for each of the P3HT films that we studied.

Film Condition	(100) Peak Area (A.U.)
P3HT	1621
3% DIO	482
7% DIO	295
P3HT MeOH	2213
3% DIO MeOH	1069
7% DIO MeOH	842
3% ODT	942

Table 3.1: Integrated (100) peak areas for P3HT films whose GIWAXS is shown in Fig. 3.3

Figure 3.3 and Table 3.1 show that when P3HT films are cast with DIO or ODT as an additive, the thickness-normalized (100) peak area decreases significantly, indicating that these additives inhibit P3HT crystallinity through polymer swelling, and that higher concentrations of additives lead to lower (100) peak areas. This is consistent with the thickness measurements shown in Fig. 3.2. Figure 3.3 also shows that swelling by solvent additives significantly disrupts the P3HT π-π stacking: the (010) π-π stacking peak is shifted to lower q, corresponding to an increase in d-spacing from 3.8

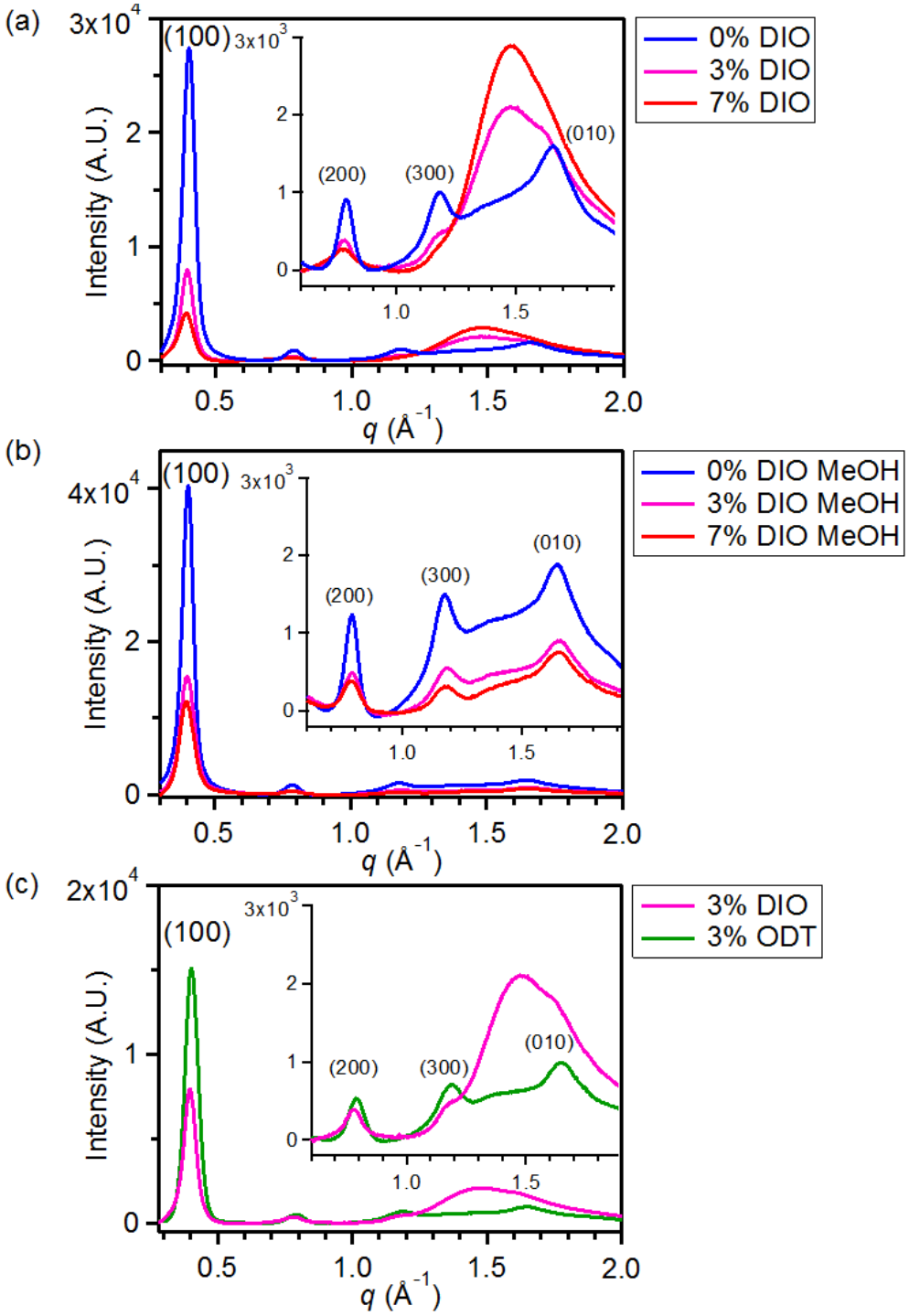

Figure 3.3: 2-D GIWAXS data for P3HT films cast with and without solvent additives and with and without being subsequently washed with methanol. (a) P3HT films cast with 0% (v/v) additive (blue), 3% (v/v) DIO (purple), and 7% (v/v) DIO (red). (b) Methanol-washed films of P3HT cast with 0% (v/v) additive (blue), 3% (v/v) DIO (purple), and 7% (v/v) DIO (red). (c) P3HT films cast with 3% (v/v) DIO (purple) (same as panel (a)) and 3% (v/v) ODT (green). The inset in each panel shows the high-*q* π-stacking region on an expanded vertical scale. As the volume percentage of DIO increases, residual DIO inhibits P3HT crystallization. Upon methanol washing, the P3HT crystallinity and orientation are partially restored; restoration is only partial due to incomplete removal of the additive by methanol.

Å with no solvent additive to 4.3 Å when the film is spun with 7% (v/v) DIO. In addition, the width of the (010) peak increases substantially in the presence of swelling solvent additives, indicative of a disordered π-π stacking network with a wide *d*-spacing distribution.

Figure 3.4 shows the in-plane and out-of-plane portions of the integrated GIWAXS from the various P3HT films. As mentioned above, P3HT is well known to show edge-on polymer chain alignment, with strong (100) lamellar scattering in the out-of-plane direction and strong π-π (010) scattering in the in-plane direction; the blue curves in Fig. 3.4 for P3HT films with no solvent additive reproduce this known trend. When DIO is added to the solutions from which the films are cast, the data in Fig. 3.4(a) again indicate that the total crystallinity decreases, as discussed above. However, the crystalline fraction of the sample that remains actually becomes increasingly edge-on oriented as the DIO concentration increases, as indicated by the nearly complete loss of the in-plane (100) diffraction peak in the more highly DIO-swollen samples. This suggests that non-edge-on domains may be less stabilized by the substrate and thus are more easily swelled by DIO. In contrast to the (100) peak, the disordered π-π (010) peak observed below $q = 1.5$ Å^{-1} is more much isotropic in the DIO-swollen films, reflecting the structure of the swollen fraction of the sample. Figure 3.4(b) also shows that methanol washing recovers most of the standard orientational distribution of the P3HT chains, although the previously-swollen-and-washed films still show more isotropic scattering than films that never contained the solvent additive; this is quantified in Table 3.2. Overall, although a number of factors can modify diffraction peak intensity, the observed decrease in domain orientation is clearly associated with swelling.

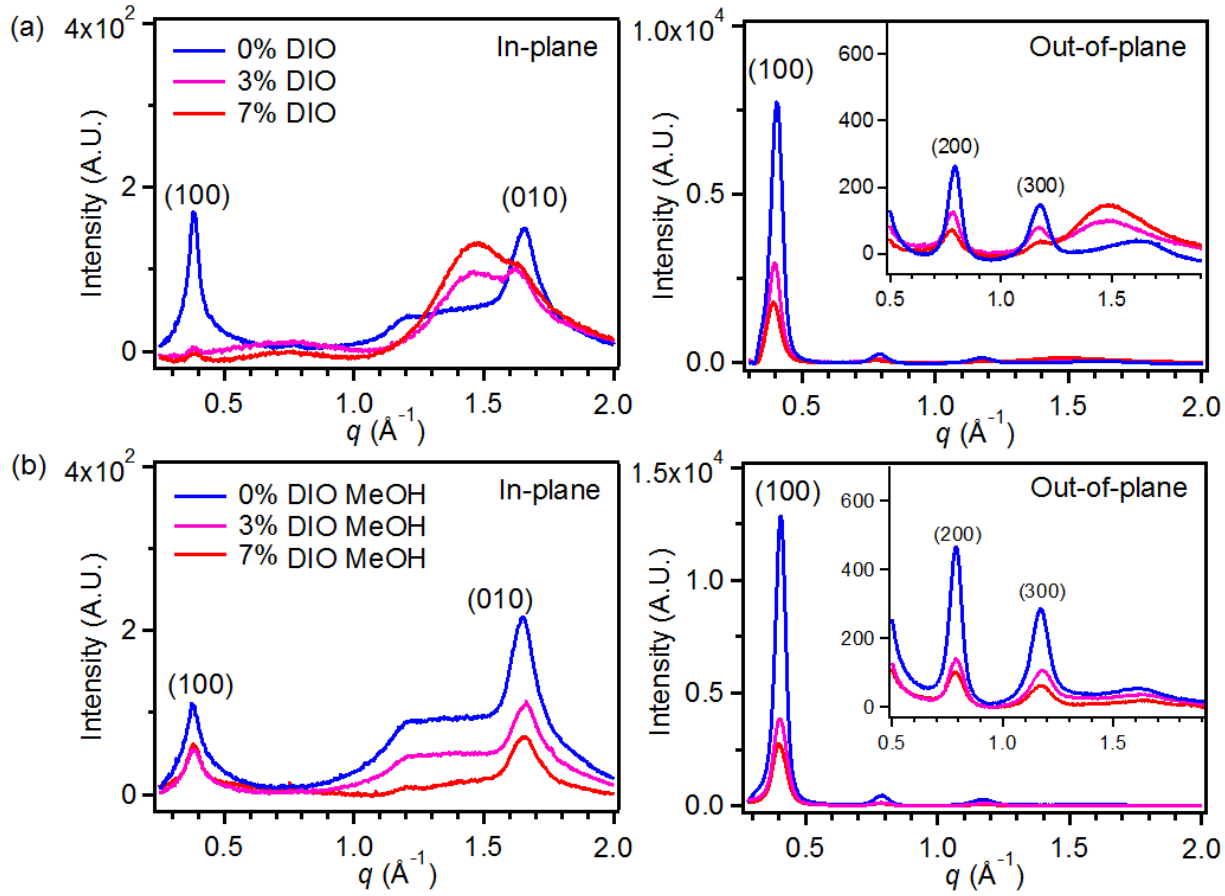

Figure 3.4: In-plane and out-of-plane integrated portion of the full 2D-GIWAXS from P3HT films cast under different conditions. (a) In-plane (left) and out-of-plane (right) integrated scattering from P3HT films with 0% (v/v) additive (blue), 3% (v/v) DIO (purple), and 7% (v/v) DIO (red). (b) In-plane (left) and out-of-plane (right) integrated 2D-GIWAXS on P3HT films washed with methanol. The insets show the high-*q* region on an expanded vertical scale. The data indicate that crystalline domains, those that show strong (100) scattering when DIO is added to the film, maintain the standard P3HT edge-on orientation, but that the DIO-swollen regions, indicated by the shifted (010) peak, are more isotropically oriented. Washing with MeOH recovers a significant fraction of the texturing and edge-on orientation of the (010) peaks (Table 3.2).

Figure 3.3(c) and Table 3.1 also compare the structures of P3HT films cast using 3% v/v DIO and ODT to that of a P3HT film cast with no solvent additive. The data show that the films cast with DIO as the additive have the smallest (100) peak area, and thus the lowest crystallinity. This fits well with the swelling measurements discussed above, reflecting the fact that DIO's vapor pressure is lower than that of ODT, so that more of it remains in the polymer film to inhibit crystallization by swelling. Finally, as also discussed above, Fig. 3.3(b) and Table 3.1 show that washing P3HT with methanol removes most residual solvent additive from the films, as measured by both the integrated

Film Condition	$A_{\text{out-of-plane}}/A_{\text{in-plane}}$	
	(100)	(010)
P3HT (no DIO) MeOH Wash	95.8	2.6
P3HT 3% DIO MeOH Wash	55.8	2.7
P3HT 7% DIO MeOH Wash	43.9	1.1

Table 3.2: Integrated out-of-plane to in-plane peak area ratio from 2-D GIWAXS for the (100) and (010) peaks in the P3HT films after methanol washing.

(100) peak intensity and the return of the (010) peak to its original q position. Table 3.2 shows that although the methanol-washed P3HT films with solvent additives show restored edge-on orientation, the P3HT chains in the washed films are still somewhat less oriented compared to P3HT films cast without any solvent additive. This is also consistent with the fact that methanol washing does not completely remove solvent additives from the films,[202] as we saw via ellipsometry in Fig. 3.2.

3.3.3 Improved Fullerene Mixing and Crystallinity in P3HT/PCBM BHJs with Solvent Additives

Now that we understand the role that solvent additives play in the swelling and reduced crystallinity of pure polymer films, we next consider how solvent additives improve the morphology and performance of bulk heterojunction solar cells produced by SqP, as seen in Figure 3.1. We first use X-ray diffraction to examine how the presence of solvent additives affects the structure of sequentially-processed BHJ active layers, and then use optical spectroscopy, X-ray photoelectron spectroscopy and neutron reflectometry to explore how solvent additives promote mixing of fullerenes throughout the polymer underlayer.

3.3.3.1 How Solvent Additives Affect Sequentially-Processed BHJ Morphology

Figure 3.5 and Table 3.3 show the grazing incidence X-ray diffraction of the sequentially-processed P3HT/PCBM active layers used for the devices shown in Figure 3.1. Unlike what we saw with the pure P3HT layers in Fig. 3.3, where the presence of solvent additives made the polymer less crystalline, we see that with BHJ films, the P3HT (100) and (010) peaks become more intense with

P3HT:PCBM BHJ Film Condition	(100) Peak Area (A.U.)
0% DIO	315
3% DIO	720
7% DIO	829
3% ODT	649

Table 3.3: Integrated (100) peak areas for the sequentially-processed P3HT/PCBM BHJs whose GIWAXS is shown in Figure 3.5

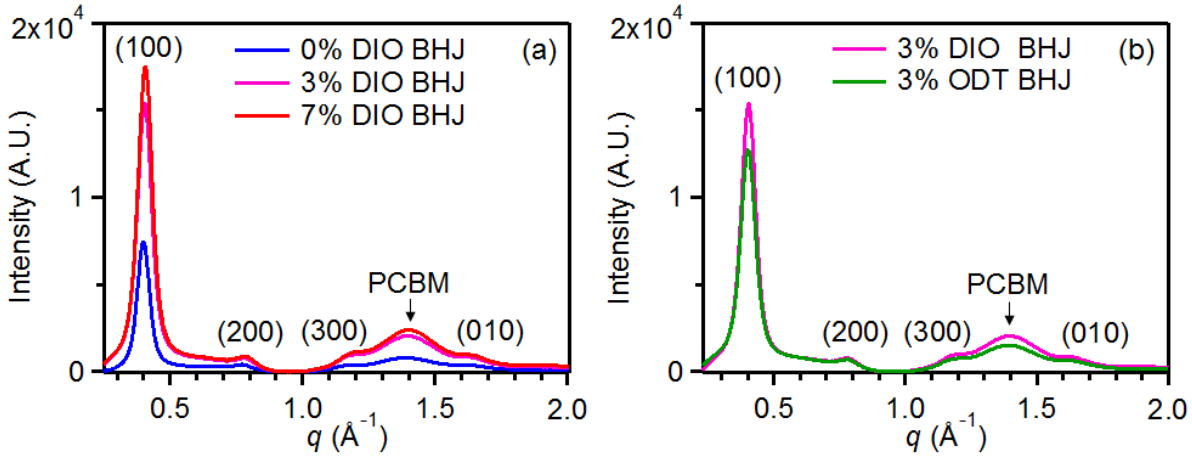

Figure 3.5: 2-D GIWAXS data for SqP-based P3HT:PCBM BHJs cast with (a) no solvent additive (blue) 3% DIO (purple), and 7% DIO (red). (b) 2-D GIWAXS data for SqP-based P3HT:PCBM BHJs cast with 3% DIO (same as panel (a)) and 3% ODT (green). As the % (v/v) DIO increases, the lower vapor pressure DIO increases the film-solidification time, which improves P3HT crystallinity. ODT, with its higher vapor pressure, evaporates faster and produces a less crystalline film.

increasing amounts of solvent additive. Much of this increase follows from washing the solvent additive out of the P3HT underlayer when dichloromethane is used to cast the PCBM overlayer in the second SqP step. In addition, for PCBM cast onto P3HT films that are swollen with solvent additive, the solidification process takes longer due to the low vapor pressure of the solvent additives. In combination, these two effects cause the improved crystallinity for SqP-based BHJs that used solvent additives. This observation is in agreement with previous studies on blend-cast BHJ films cast with solvent additives.[190,205]

Figure 3.5 and Table 3.2 show that the integrated area of the PCBM diffraction peak at $q \approx 1.4$ Å^{-1} also increases with the presence of solvent additives in the polymer underlayer. We believe the increased fullerene scattering results from increased intercalation of fullerene into the film. PCBM

is known to preferentially penetrate into amorphous regions of polymer films during SqP while leaving the crystalline polymer regions intact.[102] Since solvent additives like DIO and ODT lower the overall polymer crystallinity, this offers increased opportunities for PCBM diffusion into the films during SqP, as we document below in the next section. Furthermore, the enhanced mobility of fullerenes within the additive-swollen polymer layer could also lead to enhanced PCBM scattering.

Finally, the data in Fig. 3.5 also show that DIO enhances the scattering from both the P3HT and PCBM in the sequentially-processed BHJs better than ODT. As discussed above, additives like DIO with lower vapor pressures remain in the film longer and thus increase fullerene diffusion into the film and extend the film-solidification time relative to higher vapor-pressure additives like ODT. Clearly, swelling additives with the lowest vapor pressures will yield the most crystalline materials and the highest fullerene fractions in BHJs produced by SqP.

3.3.3.2 How Solvent Additives Improve Mixing in Sequentially-Processed BHJs

Given all the evidence we have presented showing that low-vapor-pressure solvent additives remain in the polymer film and swell it, the final question we need to address is how additives affect the mixing and structure of the fullerene intercalated into the polymer following SqP. The easiest place to start is to examine the amount of fullerene that penetrates into the polymer underlayer in the second SqP step with and without additives present in the polymer film. Unfortunately, the UV-Visible absorption spectrum of a P3HT/PCBM BHJ film does not provide an accurate way to quantify the polymer/fullerene ratio because the P3HT absorption spectrum and cross-section in the film are highly sensitive to the degree of polymer crystallinity; instead, we have shown that the polymer/fullerene ratio can be accurately determined by redissolving the cast BHJ films and quantifying the ratio of polymer to fullerene using UV-Vis spectroscopy of the resultant solution.[127] Using this redissolution method, which is shown in more detail in Fig. A.3 of Appendix A, we find that the PCBM:P3HT mass ratios in sequentially-processed BHJs where the polymer layer was cast with 0, 3, and 7% (v/v) DIO were 0.80, 0.80, and 0.92, respectively. This shows that in addition to mass action[127] and fullerene solvent selection,[2,39] the degree of swelling/swellability of the polymer underlayer plays a critical role in controlling the fullerene loading in SqP.

Given that more fullerene enters the polymer films when solvent additives are present, the next question we address is how those fullerenes are distributed throughout BHJs produced by SqP. First, we probed the composition at the top surface of our sequentially-processed BHJs using X-ray photoelectron spectroscopy (XPS). XPS provides a sensitive measure of composition at the top surface by measuring the sulfur-to-carbon (S/C) ratio; this is because PCBM does not contain sulfur but P3HT does.[117,228,229] We determined this ratio by fitting the measured sulfur 2p and carbon 1s spectral lines (see Appendix A for experimental and analysis details); a higher S/C ratio indicates a lower amount of fullerene at the top surface of the BHJ film and vice-versa. Figure 3.6(a) shows that for a pure P3HT film, the surface composition is about 6.7% sulfur. When PCBM is spun on top of a pure P3HT film from DCM, the top-surface sulfur-to-carbon ratio drops to 0.8%, indicating that most of the top surface of the film is covered with non-sulfur-containing fullerene. This observation is consistent with previous work,[101] and is explained by the fact that DCM is a relatively poor swelling solvent for P3HT, so PCBM cannot uniformly penetrate into the polymer underlayer. This is why sequentially-processed P3HT/PCBM devices without solvent additives have poor device efficiencies unless they are subsequently thermally annealed to drive PCBM, which has a higher surface energy than P3HT, toward the high surface energy substrate.[100,101,130]

In contrast to the fact the SqP leaves fullerene predominantly on top of pure P3HT films, Fig. 3.6(a) also shows that the presence of DIO in the polymer layer increases the top-surface sulfur-to-carbon ratio. With just 3% (v/v) DIO in the P3HT underlayer, the top surface of the film is significantly enriched with P3HT, having a sulfur composition consistent with the bulk 1:0.8 composition ratio measured by re-dissolution UV-Vis.[127] When we proceed to 7% (v/v) DIO additive in the polymer film, we see that the surface composition has an even higher percentage of P3HT at the surface, close to that of a pure P3HT film. This shows that a sufficient amount of solvent additive can swell a polymer film so much that it allows the fullerene to be driven completely through the film: the higher-surface energy PCBM has enough vertical mobility through the swollen film to fully avoid the energetically unfavorable top interface, as has been observed in films of other conjugated polymers in previous work.[230] This increased diffusion of PCBM is consistent with solvent additives acting as plasticizers for the polymer (see Appendix A).

To further characterize the extent of fullerene penetration through the entire BHJ film thickness,

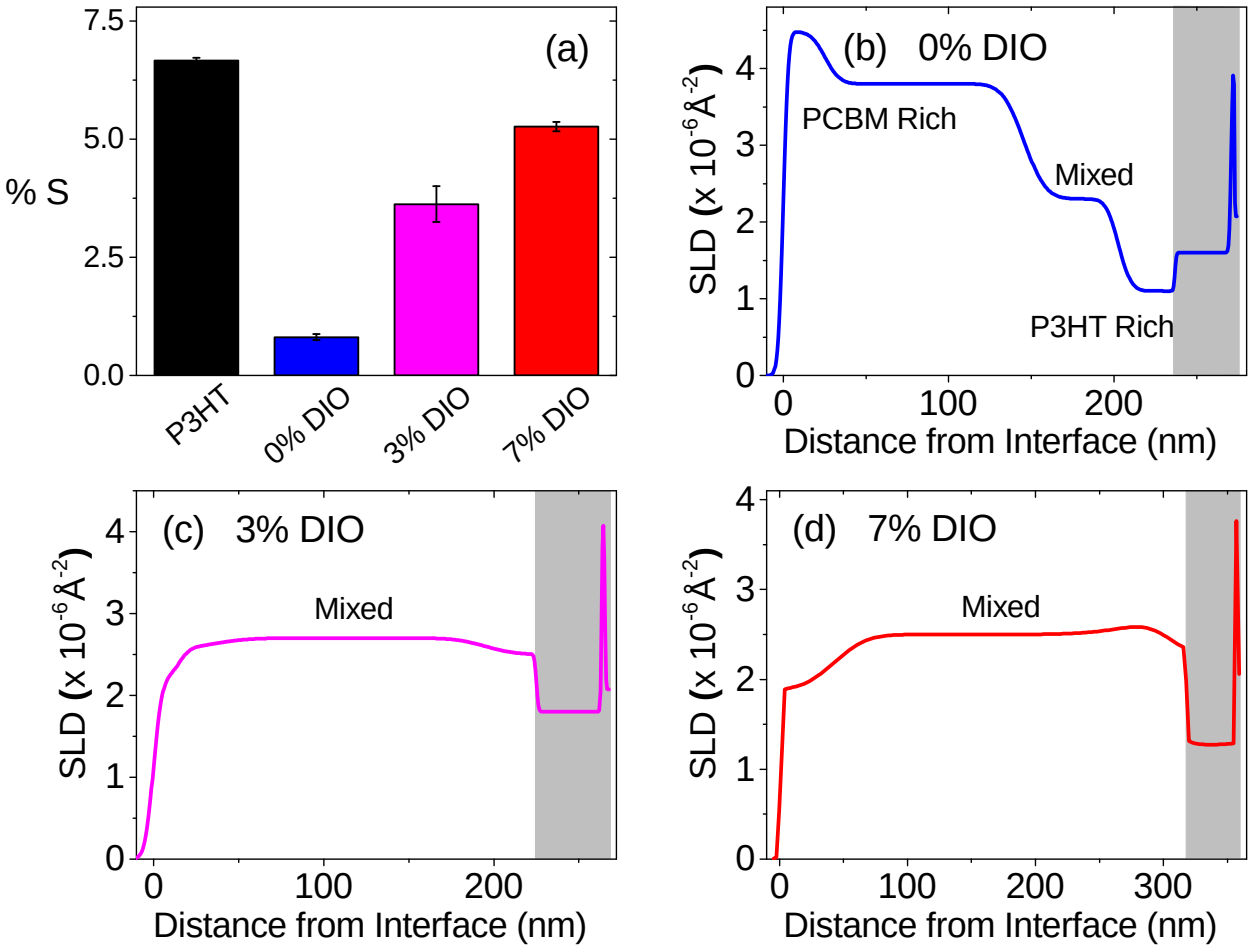

Figure 3.6: (a) Top-surface sulfur-to-carbon (S-to-C) composition ratios of sequentially-processed P3HT:PCBM BHJ films with 0% DIO (blue), 3% DIO (purple), and 7% DIO (red) as measured by XPS; the S-to-C ratio for a pure P3HT film with no PCBM or solvent additive is shown in black for reference. The decreased S-to-C ratio in the 0% additive BHJ indicates that PCBM covers the top surface of the film. The increase in the S-to-C ratio when solvent additives are present demonstrates increased fullerene intercalation upon swelling. The error bars represent one standard deviation with an average taken over at least three different films. (b)-(d) Neutron reflectivity (NR) scattering length density (SLD) depth profiles of SqP-based P3HT:PCBM BHJ films obtained by fitting the NR data in Fig. A.12 for 0% (v/v) DIO (blue, panel (b)), 3% (v/v) DIO (purple, panel (c)), and 7% (v/v) DIO (red, panel (d)). For (b)-(d), our NR model is constructed from multiple layers of variable thicknesses, ensuring the active-layer/air interface is at the origin, with the underlying PEDOT:PSS/Si interface shown in gray. Both the NR and XPS data show that with increasing amounts of solvent additive present in the polymer film prior to SqP, the surface composition of the BHJ film becomes increasingly depleted in fullerene. The most uniform depth profile with a surface composition closest to the bulk composition is found at the optimal DIO additive concentration of 3% (v/v).

we also performed a series of neutron reflectometry (NR) experiments. NR serves as an excellent probe of molecular distribution along the direction perpendicular to the plane of the film.[101] The active layers measured were spin-coated onto PEDOT:PSS-coated Si substrates for the measurement. Additional details regarding the experimental procedure and fitting of the data to produce the scattering length density (SLD) profiles can be found in Appendix A. Interpretation of the SLD profiles is based on the fact that pure P3HT has an SLD of $\sim$0.8 and pure PCBM has an SLD of $\sim$4.5, while BHJ mixtures show a weighted average of the two pure SLD values. This contrast allows us to resolve differences between PCBM-rich, P3HT-rich, and mixed regions of the BHJ films.

The SLD profiles in Figs. 3.6(b)-(d) show the vertical distribution of P3HT and PCBM throughout the BHJ films; the profiles are in excellent agreement with our XPS results. For BHJs made without solvent additives, a higher SLD value representative of nearly pure PCBM is seen at the top surface, while the bottom of the polymer layer near the substrate contains essentially no fullerene. This is because the DCM solvent used in the second SqP step only weakly swells P3HT,[2,102,165,178] and because the high vapor pressure of DCM at 25 °C (58,000 Pa)[231] limits the time available for fullerene diffusion into the film, resulting in a fullerene-rich top surface.[101,129,131,232] Nonetheless, there is enough swelling of P3HT and time prior to DCM evaporation to allow some PCBM to intercalate into the upper part polymer network, establishing a limited mixed region.[100,101] This highly non-uniform vertical density of fullerene explains the low device currents seen in Fig. 3.1.

The story clearly changes, however, when solvent additives are present in the polymer underlayer. With 3% (v/v) DIO, the NR SLD profile shows complete fullerene mixing throughout the entire film thickness, with a surface composition that closely matches that of the bulk. This is perfectly consistent with the idea that solvent additives are swelling agents, providing time and space for mass action from the second SqP solution to drive fullerene into the swollen polymer film. When the additive concentration is increased to 7% (v/v) DIO, the SLD profile shows good mixing of P3HT and PCBM, explaining the similar performance of the devices made from 3% and 7% DIO. The 7% DIO SLD profile, however, also shows a slight deficit of PCBM near the top surface, consistent with the XPS data. This is because 7% (v/v) DIO swells P3HT more than 3% (v/v) DIO, allowing PCBM to move away from the top interface due to its higher surface energy.[117]

This picture of changes in mixing with the presence of additives in the polymer underlayer is supported by the decrease in the number of dark carriers seen in each of the various active layers,[127,224] shown in Figure A.2 and discussed in more detail in Appendix A. Appendix A also shows an analysis of the dark J–V curves for these devices (see Table A.1), in which there is increased dark recombination current and a higher ideality factor when solvent additives are present. This is also consistent with enhanced mixing caused by additives since smaller domains increases charge recombination. Overall, the XPS and NR results paint a clear and consistent picture: solvent additives control both the vertical mixing and overall morphology of polymer/fullerene bulk heterojunction active layers through swelling of polymer films, and this in turn directly controls device performance.

3.3.4 The Generality of Solvent Additives Acting as Swelling Agents: Push-Pull Polymer Systems

Having demonstrated the swelling effect and associated BHJ morphology improvement of solvent additives on the sequentially-processed P3HT system, we turn next to exploring the generality of our conclusions for more modern push-pull polymer systems. We note that push-pull polymers, which are generally much more amorphous than P3HT, require the use of binary solvent blends for efficient SqP and are not easily fabricated using a single fullerene solvent via SqP.[2] Finding a single SqP solvent is difficult because these amorphous polymers and fullerenes have similar solubilities in many organic solvents. The use of solvent blends, however, adds complexity to a fundamental study and could possibly mask the role of solvent additives, so we focus here on single-solvent SqP.

Two systems that are amenable to single-solvent SqP with DCM are the higher-efficiency push-pull polymers PSEHTT[222] and PBDTTT-C.[223] Both of these materials are sufficiently crystalline so as not to dissolve in DCM, allowing us to make a direct comparison to the work on P3HT in the previous sections. For these materials, the relative crystalline order goes as PBDTTT-C < PSEHTT < P3HT. Both PSEHTT and PBDTTT-C are more strongly swollen by DCM than P3HT, so one might expect that solvent additives will have a smaller effect for these systems than for P3HT. In combination, the behaviors we see using this full series of polymers will allow us to understand in

detail the general principles of solvent additives functioning by polymer swelling.

Figure 3.7(a) shows ellipsometry-based swelling measurements on films of both PSEHTT and PBDTTT-C with and without DIO. The film thicknesses without DIO (blue bars) are quite a bit smaller than those of P3HT, reflective of the fact that optimized BHJ devices of the push-pull polymers require thinner films. The data show clearly that as with P3HT (Fig. 2(a)), the push-pull polymers are significantly swollen by DIO, which clearly remains in the polymer films. To verify that DIO-induced swelling is indeed what improves device performance with push-pull polymer systems, we fabricated PSEHTT and PBDTTT-C BHJ devices by SqP using PCBM as the electron acceptor. As shown in Fig. 3.7(b), the performance of sequentially-processed PSEHTT:PCBM devices matches the trends observed for P3HT: sequentially-processed devices without DIO demonstrate a low current but improve markedly when DIO is added to the polymer underlayer. Even though PSEHTT-based devices fabricated by SqP do not work better than those made by blend-casting in this case (largely because DCM does not have the correct Flory-Huggins χ to optimally swell this polymer), we see that with 3% DIO, the current of the sequentially-processed device matches that of the blend-cast device. This indicates that the additional swelling provided by DIO is key to infiltrating fullerene into the device via SqP. We also note that unlike with P3HT, increasing the DIO fraction to 7% leaves the PSEHTT polymer film over-swollen, reducing device efficiency).

Figure 3.7(c) compares the performance of blend-cast and sequentially-processed photovoltaic devices based on the more amorphous PBDTTT-C polymer combined with PCBM, with and without the use of DIO. Because PBDTTT-C swells extremely well with DCM, the efficiency of the sequentially-processed device without DIO is already quite good, and exceeds that of the blend-cast device without DIO. Thus, in the case of PBDTTT-C, DCM acts as an already close-to-optimized SqP solvent: DCM has high fullerene solubility and almost adequate swelling. This means that there is only a marginal improvement to be had by additional swelling with DIO. Indeed, the data show that the sequentially-processed device efficiency does improve upon the addition of 3% DIO, but the improvement is more modest than in the case of P3HT or PSEHTT. Interestingly, when DIO is used for this materials combination, the blend-cast and sequentially-processed devices have identical efficiencies. This indicates that for PBDTTT-C, the combination of 3% DIO and DCM

provides optimal swelling during SqP, leading to a BHJ morphology that is nearly identical to that obtained with blend-casting from ODCB. We note that for all polymer systems studied, 3% DIO is the optimum concentration, consistent with previous polymer-fullerene blend-cast studies that use small fractions of DIO.[195,233,234] Overall, as discussed in the next section, the use of solvent additives can be beneficial with either traditional blend-casting or SqP, but it is important to realize that in the end, additives work by polymer swelling and the optimal amount of polymer swelling varies from one system to the next.

3.3.5 Solvent Additives are Co-Solvent Swelling Agents

We have shown that the mechanism by which low-vapor-pressure solvent additives such as DIO and ODT work to control BHJ morphology is by swelling of conjugated polymer films. This swelling or secondary plasticization[221,235,236] facilitates mixing of the fullerene into the polymer underlayer during the second step of SqP. Thus, solvent additives function as co-solvent swelling agents. DIO and ODT's ability to swell and remain in the polymer film lowers the requirement for swelling power in the fullerene-casting solvent used in SqP. Thus, swelling agents/solvent additives function similarly to solvent blends in controlling BHJ morphology by SqP:[2] the main difference is that solvent additives/swelling agents swell the polymer in the initial casting step, whereas solvent blends are designed to swell the film in the second SqP step.

With the mechanism of action of solvent additives/swelling agents understood, we now have additional routes toward tractable BHJ optimization via SqP. Not only can one swell a polymer film through solvent blends, but one can swell the polymer film during polymer deposition. Indeed, our picture of solvent additives functioning as polymer swelling agents is supported by the post-additive soaking experiments of Kong *et al.* via a secondary solvent washing procedure. In these experiments, over-phase-separated BHJs are treated with a secondary solvent washing step; this solvent is a mixture of a host solvent and DIO. The authors find that upon this post-additive soak, the BHJ is favorably reorganized, resulting in more ideal phase separation for a pre-formed BHJ.[207] Our work demonstrates that solvent additives such as DIO act as polymer swelling agents and explains the post-additive soaking effect: by adding DIO to a pre-formed BHJ, DIO swells the polymer film and

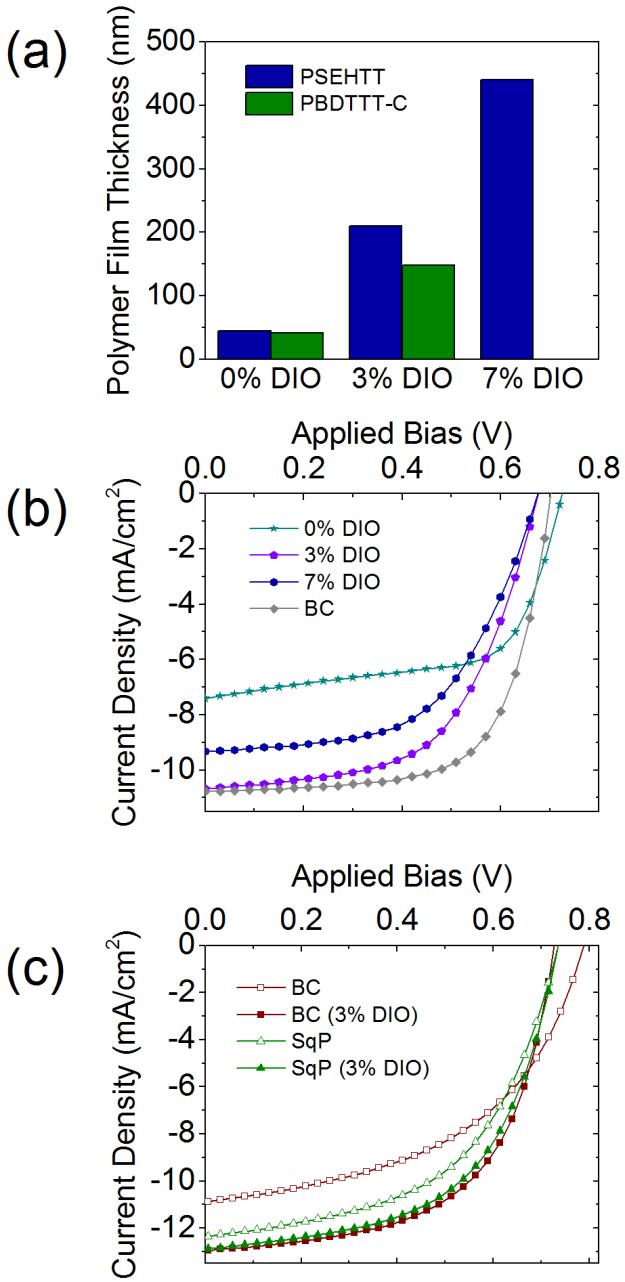

Figure 3.7: (a) Thickness measurements of PSEHTT (blue) and PBDTTT-C (green) polymer films as measured by spectroscopic ellipsometry. The film thickness is measured for films cast from polymer solutions containing 0% DIO, 3% DIO, and 7% DIO. (b) *J-V* curves for PSEHTT:PCBM sequentially-processed devices with 0% DIO (teal stars), 3% DIO (violet pentagons), and 7% DIO (navy hexagons). The blend-cast device *J-V* data is represented by gray diamonds. (c) *J-V* curves for PBDTTT-C:PCBM sequentially-processed (green) and blend-cast (maroon) devices without (hollow symbols) and with 3% DIO (filled symbols). The ITO/PEDOT:PSS/Polymer(DIO)/PCBM/Ca/Al solar cells were tested AM-1.5 illumination and illustrate the effect of different concentrations of DIO for sequentially-processed and blend-cast (BC) devices. For both PSEHTT and PBDTTT-C, the device performance for sequentially-processed devices increases with 3% DIO and matches or closely matches the blend-cast result. The efficiency increase is due to DIO swelling the polymer film prior to PCBM spin-casting.

during the extended film-formation time facilitates polymer/fullerene mixing, driven by the mixing of the fullerene with the DIO in the swollen polymer. The fact that Kong *et al.* report that thicker BHJ films required increased amounts of additive in the post-additive soaking is consistent with our conclusion that DIO acts as a polymer swelling agent, as additional DIO is required to swell more polymer material. Indeed, this idea fits nicely with our results in Figs. 3.2(a) and 3.7(a), where thin films of PSEHTT and PBDTTT-C required only 3% DIO to swell to approximately four times their initial thickness while P3HT films that were more than twice as thick required 7% DIO to be swelled by the same relative amount.

Although this study focuses primarily on sequentially-processed devices as a way to elucidate the mechanism of action of solvent additives, it also helps explain the role of solvent additives in improving the performance of more traditional blend-cast devices. With the polymer and fullerene co-dissolved in a binary solution of host solvent and swelling agent/solvent additive, the additive serves to swell the polymer and delay film solidification due to its low vapor pressure. It also serves to drive mixing between the polymer and fullerene in much the same way as when ternary solvent blends are miscible when binary pairs of the same solvents are not.[237] In this way, swelling alters the degree of polymer and fullerene mixing and thus favorably controls BHJ domain sizes. This mechanism accounts for the majority of trends reported in the literature for high-performing push-pull polymers which tend to over-aggregate,[3,26,29–31,207] and also fits well with studies that have observed an increase in film formation time when DIO is used during blend-casting.[182,220]

3.3.6 Conclusions

In summary, the solvent additives used to improve BHJ morphology in conjugated polymer/fullerene photovoltaics are low-vapor-pressure polymer swelling agents. By fabricating films through sequential-processing and adding swelling agents to the polymer solution, we observed significant structural changes. As verified by spectroscopic ellipsometry, solvent additives such as DIO or ODT swell P3HT, PSEHTT, and PBDTTT-C and remain in the polymer films due to their low vapor pressures. The presence of solvent additives also allows non-optimal fullerene solvents in the second SqP step to more effectively swell polymer films. This means that solvents that are less effective

at swelling (and thus less likely to dissolve a polymer film) can be utilized as fullerene-casting solvents for SqP in conjunction with solvent additives. A direct example of this is the fact that a poor swelling solvent such as DCM still can provide for good fullerene intercalation and crystallization in SqP when solvent additives are present. The dramatic changes in vertical fullerene distribution observed by XPS and neutron reflectometry upon addition of DIO are a testament to the large changes in molecular diffusivity that can be generated using solvent additives.

Although we isolated the swelling role of solvent additives using SqP for three different polymer systems, the fact that such swelling agents have low vapor pressures and remain in the film, providing time and mobility for fullerenes to redistribute, explains their mechanism of operation in traditional blend-casting as well as SqP. Overall, additives like DIO and ODT control BHJ morphology by functioning as secondary plasticizers. Additives such as CN, which have higher vapor pressures, act more as co-solvents and are discussed in more detail in Appendix A.

Overall, this work demonstrates the importance of polymer swelling to ensure both good mixing and good crystallinity of polymer donor and fullerene derivative acceptor materials in BHJ photovoltaics. Furthermore, the use of solvent additives in SqP is an approach that is widely applicable to multiple polymer systems as the low-vapor-pressure swelling agent can be added directly to the pure polymer in solution: by directly swelling a polymer film to a precisely controlled degree using simple swelling measurements, it should be possible to find a tractable route towards optimal BHJ formation.

CHAPTER 4

Bay-Linked Perylenediimides are Two Molecules in One: Insights From Ultrafast Spectroscopy, Temperature Dependence, and TD-DFT Calculations

4.1 Introduction

Perylene and its derivatives are widely studied as model systems of molecular spectroscopy and aggregation, with work spanning many decades.[51,65,238,239] Recently, the organic electronics community has found numerous applications for perylenediimides (PDIs): not only are PDIs used in organic light-emitting diodes due to their generally high emission yields and high electrical conductivies,[54,55] but they also serve as electron transport materials in organic photovoltaics (OPVs), with charge transport properties that can rival those of the more commonly-used fullerenes.[6,51,57–61]

One advantage of PDIs for optoelectronic applications is that their structural and electronic properties can be independently synthetically controlled: substitutions to the electronically isolated N-termini can be used to tune solubility and aggregation without altering the base electronic properties, while substitutions on the α or β carbons (see Figure 4.1) allow for control over the electronic properties of the delocalized π electrons.[50,240] PDIs and their derivatives have served as photostable pigments,[52] been central to studies of photoinduced charge transfer,[241,242] and helped to elucidate details of the physics of molecular aggregation.[52,58,64] For all of these reasons, considerable work has characterized the spectroscopy of PDIs as function of substitution[51,63,243] and degree of aggregation.[55,244]

For all of their advantages, however, monomeric PDI molecules have a strong predilection for π-stacking, which can be detrimental in certainly applications, such as preventing charge separation

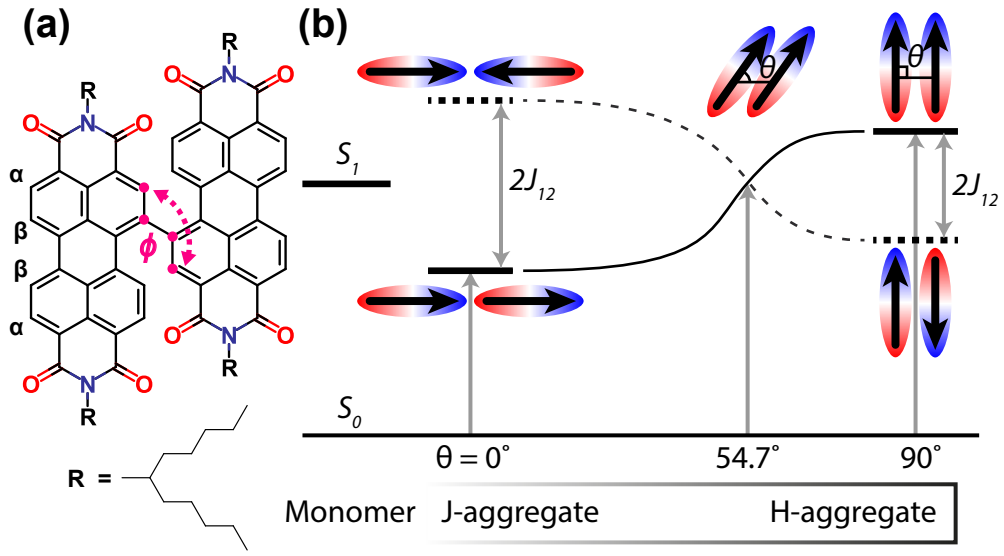

Figure 4.1: (a) General structure of β – β linked di-PDIs. For this (and previous[6]) studies, the -R groups consist of undecan-6-yl dovetails. (b) A qualitative schematic of ideal dipolar coupling (ideal J and H aggregation) between neighboring chromophores, showing the molecular geometries and energies of the excited electronic states whose transitions from the ground state are allowed (solid black) or forbidden (dashed). For the di-PDI whose structure is shown in (a), even though the chromophores are in close proximity due to the covalent bond between them, the sub-units lie far from coplanarity and do not fit the ideal case. Thus, the magnitude of coupling betweeen the PDI sub-units is expected to be smaller than in a truly conjugated single molecule but larger than for typical intermolecular aggregation.

in OPVs.[51] Thus, PDI-based materials for solar cells employ a variety of alternate strategies, the most simple of which is to covalently link two PDIs together into dimers (di-PDIs) or several PDIs into oligomers. By linking PDI units together, steric interactions between the individual monomers can disrupt over-aggregation yet maintain excellent charge transport properties.[58,60,61] When this strategy is employed in conjugated polymer-based photovoltaics, highly competitive power conversion efficiencies of $\sim$10.6% can be obtained.[51,60–62] For this chapter, we choose to study a relatively simple di-PDI whose structure is shown in Figure 4.1(a). This di-PDI has branched alkyl groups at the N positions to confer solubility, and otherwise has only a single degree of freedom between between the PDI monomer units: rotation about the bay-linked bond, ϕ. We note that this particular di-PDI has previously been employed in organic solar cells, yielding an efficiency of 5%.[58]

PDI dimers such as the one whose structure is shown in Figure 4.1(a) are characterized by varying degrees of coupling between the monomer PDI sub-units. There is a vast literature on the spectroscopic signatures of intermolecular coupling between chromophores separated over modest distances, suggesting that 'Coulombic coupling' is the primary interaction.[65,239] The magnitude of this coupling depends strongly on the orientation of the coupled molecules, as explained by the elegant theory developed by Kasha and co-workers,[245,246] which is outlined in Figure 4.1(b). When the the long axes of the two chromophores' transition dipoles are arranged in parallel, H-aggregate behavior (red-shifted emission with low quantum yield) results, whereas a head-to-tail configuration of the transition dipoles leads to J-aggregate behavior (blue-shifted emission with higher quantum yield).[64,247,248] This type of simple H or J aggregate behavior holds only for ideal molecular geometries and for crystal structures/dimers that have only one molecule per unit cell. Outside of ideal conditions, both types of aggregation (and other factors such as charge-transfer interactions) can emerge due to coupling along multiple axes.[64,65,249]

For di-PDIs of the class considered in Figure 4.1(a), there are additional considerations in understanding the coupling between sub-units. The intermolecular distance between chromophores ($\sim$1.3–1.5 Å) is smaller than what is applicable for the Kasha theory, and we also expect strong coupling through the bond linking the two sub-units in addition to through-space; both types of coupling also will be angle dependent. Furthermore, since there may be free rotation around

the β-β linkage, there is the possibility that more than one low-energy conformation could be populated at room temperature. Thus, despite the increasing popularity of di-PDI's for optoelectronic applications, it is clear that there is not a simple picture that explains their electronic structure and spectroscopy.

In this chapter, we employ a suite of spectroscopic techniques, backed up by high-level quantum chemistry calculations, to investigate the fundamental electronic nature of di-PDIs. Through a series of steady-state and ultrafast time-resolved absorption and fluorescence measurements, we show that that the spectroscopy of the di-PDI molecule considered here consists of contributions from two entirely separate chemical conformers. Based on the results of our time-dependent density functional theory (TD-DFT) calculations and the observed viscosity dependence of their excited-state dynamics, we assign these two species to stable "open" (monomer sub-units roughly at right angles) and "closed" (monomer sub-units twisted to π-stack together) conformers at different local minima along the ϕ coordinate. We also show that although the spectral broadening and red-shift of this di-PDI appear H-like, the coupling mechanism is not dominated by the standard aggregation picture. Instead, our experiments and calculations indicate that the through-bond interactions do not allow a simple electronic treatment of this molecule as arising from two independently-coupled monomers. All of our results have important implications for the use of di-PDI's in organic photovoltaics and other optoelectronic devices.

4.2 Methods

All solvents were commercially purchased from Sigma-Aldrich and used as received. The di-PDI of Figure 4.1(a) and the corresponding PDI monomer were synthesized in-house following the procedures in Ref. 57. For the rest of this chapter, except where otherwise specified, we use the term di-PDI to refer to the specific structure of Figure 4.1(a), and the term PDI to refer to the monomer of this molecule.

Thin-film samples were prepared by spin-coating a 1% PDI or di-PDI solution (10 mg dissolved in 1 mL dichloromethane) onto a glass substrate at 4000 rpm for 10 s. The mono- and di-PDI film thicknesses were 80 nm and 55 nm, respectively. The cleaning procedure for the substrates

consisted of sonicating the glass for 10 minutes each in a detergent solution, DI water, acetone, and finally isopropyl alcohol.

Our cryogenic glassy-matrix PDI samples were prepared by dissolving di-PDI in 2-methyl THF to a concentration of $\sim 1 \times 10^{-4}$ M. The di-PDI solution was then transferred to a Starna Cells 0.2-mm path-length cuvette. This cuvette was then placed in a copper holder specifically designed for use with a cryostat. The cryostat was pumped under vacuum and cooled to liquid nitrogen temperature to form a glass. During glass formation, however, cavitation led to bubbles that altered the concentration of the di-PDI by possibly a few tens of percent. Thus, we report only relative yields and qualitative results for our cryogenic spectroscopy experiments.

Quantum chemistry calculations were performed using both the Gaussian16 package[250] and QChem 5.0.[251] Our DFT calculations were based on structures optimized using the PBE0 functional[252] with basis set 6-31++G* and Grimme's empirical D3 dispersion correction.[253] The dihedral angle ϕ of the di-PDI (the angle defined by $\alpha_1 - \beta_1 - \beta_2 - \alpha_2$, labeled in magenta in Figure 4.1(a)) was fixed at a variety of angles from 30 to 140° and the rest of the molecule's geometry optimized at each ϕ to investigate how twisting of di-PDI changes its energetics and photophysics. We defined the zero of the dihedral using atoms from the shorter ends of the di-PDI molecule to minimize the effects of the constrained dihedral on puckering of the PDI subunits.[60,243,254–258] Solvent effects were simulated using a polarizable continuum model (PCM)[259] with a dielectric of 4.81 to represent chloroform. Our TD-DFT calculations were done with the same functionals described above and RPA correction. The Coulombic coupling between the chromophores in the two stable conformations of di-PDI was estimated by interaction of transition charges on each monomeric PDI sub-unit; the transition charges were obtained from Mulliken population analysis[260] of the transition density matrix of the monomer PDI's lowest excitation.

Steady-state absorption and fluorescence measurements were collected using a Lambda 25 UV-Vis spectrometer and FluoroMax-3 (J-Y Horiba) fluorimeter with 2.13×10^{-6} M di-PDI solutions, the concentration chosen to avoid self-absorption. Photoluminescence was collected at 22.5° with respect to the excitation beam and the sample was positioned normal to the excitation axis. For all measurements, the slit widths (1 nm) and integration times (1.5 s) were held constant. Furthermore, all spectra reported in this chapter were corrected for the known wavelength dependence of the

detector and the monochromator response.

We note that most prior experiments exploring the nature of intermolecular coupling have exploited fixed crystalline axes between the chromophores, thereby allowing identification of Davydov splitting through polarization-sensitive spectroscopies.[239] For our di-PDI with its internal dihedral degree of freedom and amorphous solid structure, it is necessary to employ alternative techniques. Thus we took advantage of femtosecond pump-probe spectroscopy in an attempt to independently characterize the distribution of dihedral angles and the nature of the underlying independent electronic transitions. Femtosecond transient absorption was probed in the wavelength range of 450–750 nm to a maximum of roughly 2.5 ns for both the mono-PDI and $\sim 1 \times 10^{-5}$ M di-PDI in solutions and thin films. The power dependence was studied, and for excitation densities <400 μJ cm^{-2}, the signals from the solution samples remained linear and the dynamics intensity-independent. In films, however, the measured spectral dynamics became nonlinear above 200 μJ cm^{-2} and therefore excitation densities were kept below this threshold. No concentration dependence to the solution signals was observed over the range yielding 0.2 to 0.6 OD at λ_{max}. Spectra were chirp-corrected and analyzed assuming a Gaussian instrument response of roughly 80–100 fs. Excitation wavelengths were selected to access either the lowest excited state (540–580 nm) or to promote the molecule directly to a higher-lying excited state (400 nm). Data was acquired using an Ultrafast Systems Helios spectrometer with 4 seconds of averaging per spectrum. More details of this laser system may be found elsewhere.[261]

We further characterized the excited-state dynamics of our chromophores by measuring the time-resolved fluorescence spectra using optical Kerr-gating spectroscopy. Briefly, the Kerr-gating measurement exploits the transient birefringence induced by a strong non-resonant femtosecond pulse in a "Kerr medium" situated between two orthogonal polarizers with a high extinction coefficient (ideally >1:10,000).[262] One short laser pulse is used to excite the fluorescent sample. The fluorescence is directed through the two polarizers and Kerr medium. The second pulse is then applied to the Kerr medium after an appropriate optical delay. The polarization of the sample fluorescence is rotated only when spatio-temporally coincident with the transient birefringence in the Kerr medium: the action of the second pulse thereby allows a small fraction of the fluorescence through the second polarizer while the "Kerr gate" is open. We chose liquid CS_2 as our Kerr

medium, and this choice, along with the collecting optics used in our detection scheme, afforded a time resolution of roughly 2 ps.

4.3 Results and Discussion

The main goal of this chapter is to investigate the effect of having a covalent linkage on the spectroscopy and conformation of di-PDI. It is well known that the choice of the β-β linkage prevents PDI dimer-dimer aggregation, which is desirable for many applications. Di-PDI molecules, however, may occupy a variety of relative positions along the degree of freedom represented by rotation ϕ around the covalent linkage, and it is not immediately obvious which configurations, or how many, will be dominant. We expect the coupling between chromophores, both through-space and through-bond, to depend strongly on ϕ; thus a secondary goal of this work is to understand the origin of the coupling mechanisms in di-PDIs and how they change with ϕ.

4.3.1 Di-PDI Spectroscopy Consists of Two Absorbing and Emitting Species

Figure 4.2 shows the solution and film absorption spectra of our chosen di-PDI molecule. The absorption is quite intense and takes place broadly across the visible, which is a hallmark feature for its selection in organic photovoltaics. The vibronic features and general spectral profile of the di-PDI absorption are far broader than that of the corresponding isolated monomer; see Appendix B. Others have phenomenologically labeled this broadening of the di-PDI spectrum as H-like due to the overall red-shift and lower corresponding emission quantum yield compared to the monomer.[243,263] As discussed in conjunction with Eq. B.1 of Appendix B, however, when we attempted to fit the di-PDI absorption profile based on the idea that its spectrum could be described as that of two weakly coupled monomer PDI monomers, we found that the fits were not robust.

We also performed a series of fluorescence excitation/emission experiments on low-concentration (to avoid self-absorption and any potential aggregation) di-PDI solutions at room temperature, with the raw two-dimensional data shown in Appendix B. Figure 4.3 summarizes the results of deconvoluting this data, demonstrating that there are two clearly separable excitation

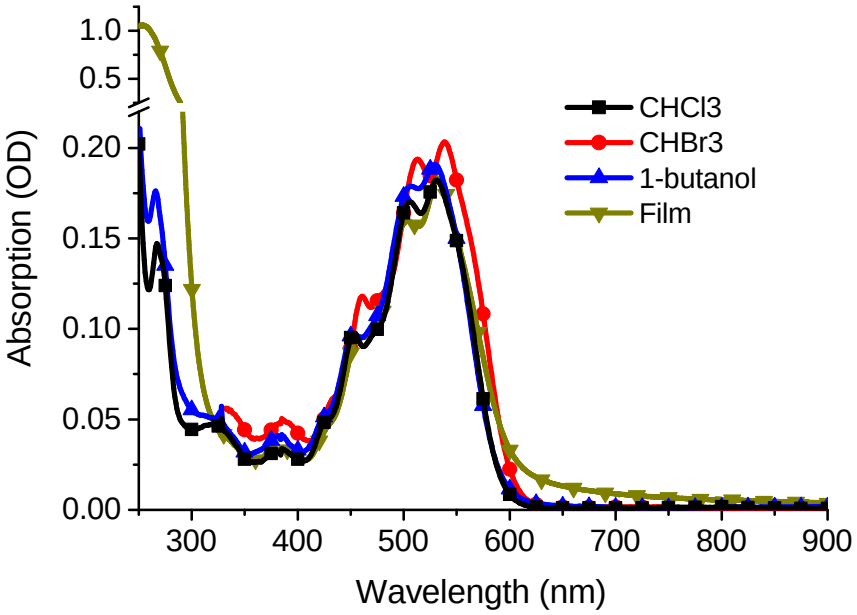

Figure 4.2: Steady-state absorption of purified 2.13×10^{-6} M di-PDI in chloroform, bromoform, 1-butanol, and as a 55-nm-thick spin-cast film (the film absorption has been arbitrarily scaled for ease of comparison). Overall, the spectra are quite similar across solvents except for some fine differences in peak ratios, peak broadness and some slight solvatochromic shifts. The maximum extinction coefficient in chloroform solution is roughly 70,000 $M^{-1}cm^{-1}$ at 535 nm, and when integrated, the oscillator strength is nearly twice that of the monomer.

(solid curves) and emission (dashed curves) bands. We ensured that these spectral components did not change their shape or relative intensities through subsequent rounds of purification; indeed, the di-PDI of interest is present in our samples with high purity (see Appendix B). Thus, these two absorption and emission features are intrinsic to the di-PDI molecule

Figure 4.3(a)-(c) show that in all the solutions we studied, di-PDI has a broad, red-shifted emission band with a correspondingly broad excitation spectrum (blue curves), as well as a second distinct feature that is only slightly red-shifted and has narrower absorption and emission, both with pronounced vibronic structure (orange curves). The presence of two distinct absorption and emission components were unexpected, and are further analyzed below. We note that previous experiments on this same di-PDI showed similar emission features, but offered no explanation or assignment.[263] We reconstructed the absorption profiles by taking the independent emission components in linear combination and fitting the total emission profile with a weighted sum of the two emission components at each excitation wavelength. The weightings thus map out an effective absorption spectrum at the resolution of our excitation-emission spectroscopy excitation step size, which was 10 nm; details of the entire reconstruction procedure are given in Appendix B. The fits show that the relative amounts of each underlying component are not equal: the broad absorption/emission component is clearly dominant, capturing the vast majority (>90%) of the overall room-temperature absorption and emission profiles.

The two di-PDI emission profiles in Figure 4.3 are normalized, but they have very different fluorescence quantum yields. We were able to determine the quantum yield for the broad feature, which can be excited cleanly to the red of 550 nm, by comparison with a fluorescein standard in slightly basic ethanol. Then using the known yield for the broad feature, we were also able to extract the relative emission yield of the narrow feature. The yields for the two di-PDI emission components in each of the solvents we studied in Figure 4.3 are given in Table 4.1. The general trend is that the narrow, blue-shifted feature has a quantum yield that is a factor of 2 to 3 higher than that of the broad, red-shifted feature; neither feature has a quantum yield that approaches that of the PDI monomer, which is essentially unity.[264–266] The quantum yield values we find in chloroform for the broad feature are reasonably similar to those found previously in toluene by Horinouchi *et al*.[263] We also note that when di-PDI is spin-cast into a thin film (Figure 4.3(d)), no narrow emission

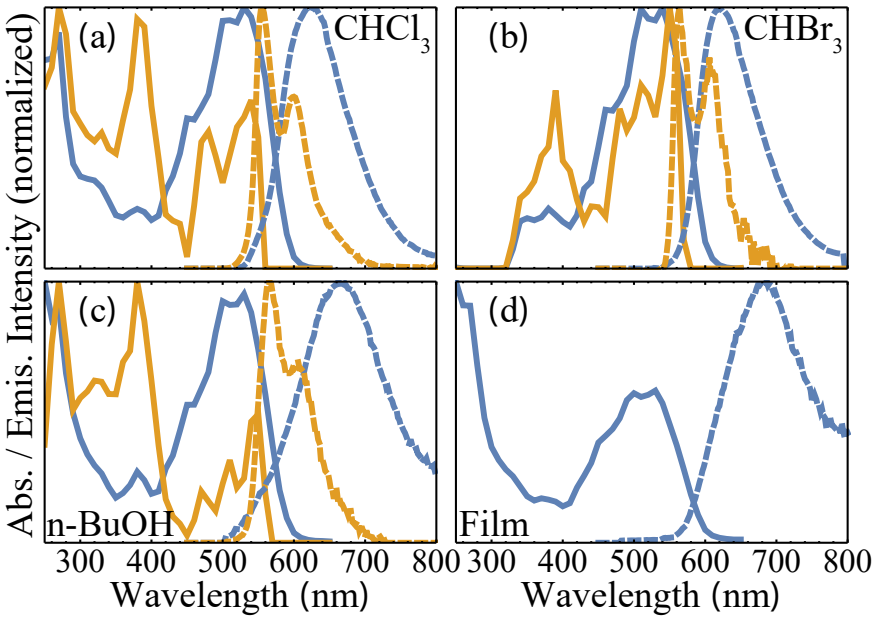

Figure 4.3: Normalized room-temperature emission spectra (dashed curves) and reconstructed absorption spectra (solid curves) of di-PDI in (a) chloroform, (b) bromoform, (c) 1-butanol, and (d) a pure film; the full 2-D excitation/emission spectra from which these data were constructed are given in Appendix B. The red-shifted, broad featureless emission (blue dashed curves) is the major emission contributor while the narrower, blue-shifted component with vibronic character has a much smaller contribution (orange dashed curves). The jagged character seen in the reconstructed absorption spectra results from the fact that the raw excitation-emission spectra were taken with 10-nm steps for excitation.

is observed; the absence of the narrow feature will be discussed below.

Table 4.1: Quantum and Relative Yields for Broad & Narrow Emission Features

Solvent	ε	η (mPa s)	Φ_{broad}	Φ_{narrow}
$CHCl_3$	4.8	0.5	0.15 ± 0.1	0.47 ± 0.3
$CHBr_3$	4.3	1.9	0.23 ± 0.15	0.21 ± 0.14
1-BuOH	17.8	2.6	0.05 ± 0.03	0.49 ± 0.4

Although the origin of the narrow and broad spectral components remains to be understood, it is tempting to borrow the language from the intermolecular aggregation and phenomenologically label the broad red-shifted component as "H-like" and the more narrow blue-shifted feature as "J-like".[64] We will argue below, however, that the intramolecular coupling in this molecule is such that these labels do not really apply. Instead, we will posit that the two components result from two distinct molecular conformations: an "open" conformation with the two monomer sub-units oriented at near right-angles, leading to the broad emission, and a "closed" conformation in which the two monomer sub-units are strongly π-stacked.

4.3.2 Temperature-Dependence and Population Ratios of the Narrow and Broad Emitting Species

With the above experiments pointing to the possibility of two independent spectroscopic species for the di-PDI molecule, we turn now to decoupling their relative absorption cross-sections and population ratios. In particular, in this Section we ask what role temperature plays in the existence of these two species and any interconversion process that might connect them. Thus, we conducted fluorescence experiments as a function of temperature in 2-methyl-tetrahydrofuran (2-Me-THF) and 1,2-dichlorobenzene, the results of which are shown in Figure 4.4. Panel (a) shows normalized emission spectra, which indicate that thermal motions play an important role as far as the breadth of the emission is concerned: at liquid N_2 temperatures (black curve), we see a complete removal of the narrow, blue-shifted emission band. Moreover, the FWHM of the broad di-PDI emission component that remains loses 30 meV of broadening relative to that at room temperature emission (red curve). This strong temperature-dependence to the inhomogeneous broadening may play a

significant role in temperature-dependent carrier mobility of di-PDI films, where the barrier for charge transport by hopping is dependent on the distribution of thermally populated states. The narrowing of the broad emission feature and loss of the blue-shifted emission band are entirely reversible when the sample recovers to room temperature. This observation thus indicates that the broad and narrow features thermally interconvert, and that the narrow feature has a higher-energy ground state than that of the broad component, consistent with the idea that they could be two conformations of the same molecule.

Figure 4.4(b) shows the relative intensities of the broad di-PDI emission in 2-Me-THF at 150 K and 77 K: the emission quantum yield increases by a factor of six at the lower temperature. If we assume that this factor of six increase brings the quantum yield of the broad emission band to near unity, then this puts an upper limit on the room-temperature quantum yield of 1.0/6 = 0.17. This upper limit estimate is in excellent quantitative agreement with the measured room-temperature quantum yield of the broad emission between 0.1–0.2 in Table 4.1. All of these observations provide clear evidence that large-scale thermal motions of the di-PDI molecule, likely involving ϕ, are critical for nonradiative coupling between the ground and excited states.

Next, we turn to calculating the relative population ratios of the two di-PDI emitting species and the relative energy gap between the ground states of the broad and narrow spectral features. At 77 K there is simply too little of the narrow spectral feature to reliably measure. Thus, we turn to higher temperatures in order to obtain a quantitative population ratio of the broad and narrow spectral components. We achieved this by studying di-PDI in 1,2-dichlorobenzene (ODCB) at both 295 K and 373 K, as shown in Figure 4.4(c). Indeed, consistent with the cryogenic experiments discussed above, we see that as the temperature is raised there is an increase in the population leading to the narrow emission feature relative to that of the broad feature. Based on the measured relative emission intensities and assuming Boltzmann statistics, we calculate that the energy gap between the conformations responsible for the broad and narrow emissions is $\sim$71 meV, or just under 3 $k_{\mathrm{B}}T$ at room temperature. This is in good agreement with results of our TD-DFT calculations, discussed below, and is also consistent with the cryogenic experiments, where we would predict that the population of the narrow-emitting feature to be negligibly small at 77 K.

We note that the relative energies/populations of the two di-PDI emitting species may be solvent

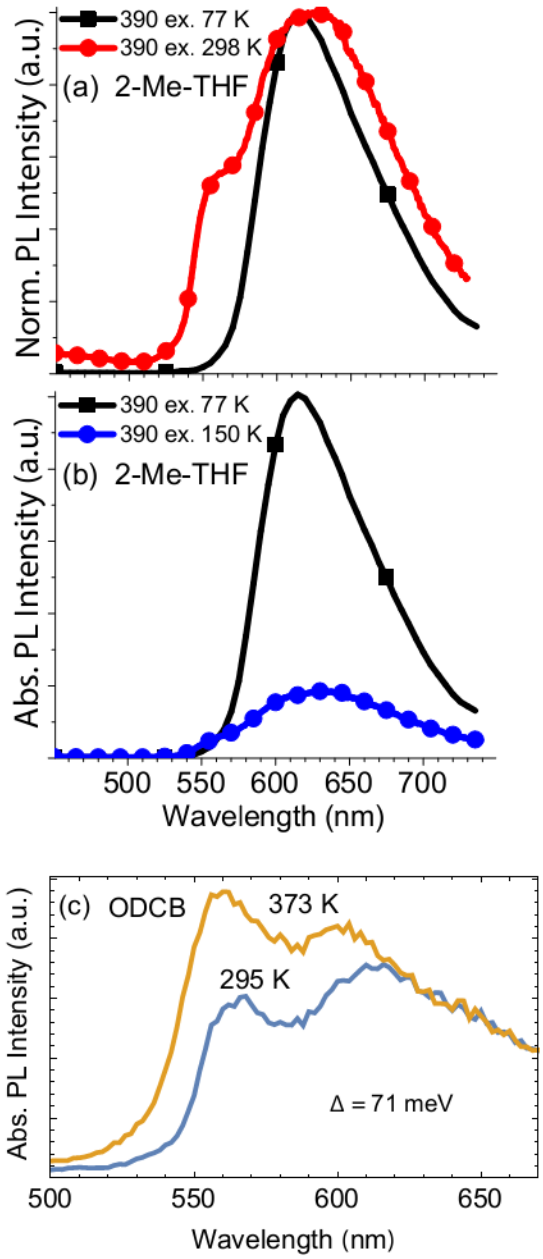

Figure 4.4: (a) Normalized emission of di-PDI in 2-Me-THF collected at 77 K (black squares) and room temperature (red circles). (b) Absolute emission intensity of di-PDI in 2-Me-THF collected at 77 K (black squares) and 150 K (blue circles). At 77 K the emission both narrows and increases by a factor of six in intensity. (c) Absolute fluorescence intensity of di-PDI in 1,2-dichlorobenzene at 295 K (blue) and at 373 K (orange). Based on Boltzmann statistics, the change in relative intensity or the narrow emission between 295 K and 373 K results in an energy gap of ∼71 meV or just under 3 $k_{\mathrm{B}}T$ at room temperature.

dependent. For example, we see less of the narrow feature in chloroform (one of the most widely used solvents for PDIs) than we do in bromoform (Figure 4.3) or ODCB. Unfortunately, due to chloroform's low boiling point, we cannot heat the solution to determine the relative stabilities of the two emitting species as we did with ODCB. As discussed in Appendix B, we estimated the energy difference for the narrow and broad emitting species in chloroform as $\sim 5\ k_{\mathrm{B}}T$ at room temperature based on an argument of conserved oscillator strengths. The fact that the narrow-emitting species is apparently correspondingly less stable in chloroform may help to explain why it has gone unnoticed until now.

Finally, we note that for di-PDI cast into thin films (Figure 4.3(d)), no narrow emission is observed. This is consistent with the idea that excitation of the species that yields the narrow emission feature has a higher-lying LUMO, so that energy transfer can take place to the larger population of neighboring di-PDI molecules that have configurations that produce the broad emission.

4.3.3 TD-DFT Reveals the Broad and Narrow Emitting Di-PDI Features to be "Closed" and "Open" Molecular Conformers

To gain additional insight into the assignment of the narrow and broad emission components, we investigated the ground and electronic excited-state structure of di-PDI via TD-DFT using the methodology described above and in Appendix B. Figure 4.5(a) shows the calculated ground-state potential energy surface of di-PDI along the ϕ coordinate in vacuum (blue squares) and in a PCM dielectric of 4.81, chosen to approximate the solution environment of chloroform (green circles). It is worth noting that our definition of of the ϕ coordinate is inverted with respect to that of previous studies.[60,243,263] The results in Figure 4.5(a) show clearly that there are two distinct energy minima for di-PDI, in accordance with the two observed distinct spectroscopic species observed experimentally. Based on their molecular geometries, shown in Figure 4.5(b), we will refer to these two energetic minima as "closed" (for $\phi = 50^{\circ}$) and "open" (for $\phi = 110^{\circ}$). We also note that previous studies have not observed the global minimum for the closed conformer that we see at 50° (or 130° using the definition of previous studies);[60,243,254–258] we believe that this is the result of the fact that previous studies did not employ dispersion correction, which is necessary for describing

the π-stacking interactions present between the two molecular sub-units when $\phi < 90°$.

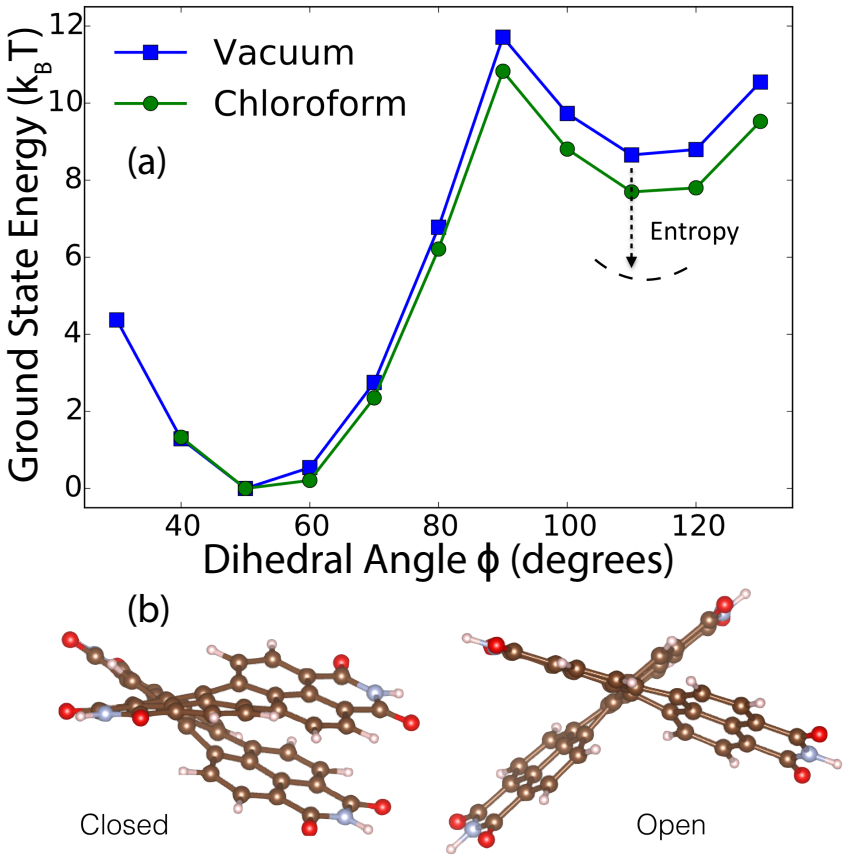

Figure 4.5: (a) Ground-state potential energy surface of di-PDI computed at the PBE0+D3/6-31++G* level of theory in vacuum (blue squares) and in a polarizable continuum with dielectric constant of 4.81 (green circles) along the ϕ coordinate (see Figure 4.1); the zero of energy was chosen to be the global minimum and the energy scale is in k_BT at room temperature. In addition to the global minimum found at 50°, there is a clear local minimum at 110°. The "closed" structure at 50° has strong π-stacking interactions between the two monomer sub-units, as shown at left in panel (b). The more "open" structure with the 110° conformation has the two sub-units lying nearly at right angles, as shown at right in panel (b). When entropy effects (calculated from frequency analysis) are included, the relative stability of the open geometry is increased, as indicated by the dashed black curve in (a).

With the DFT ground-state potential energy surface in hand, we now assign the broad di-PDI emission feature as arising from molecules that have the "closed" geometry. These molecules should predominate in terms of population, have larger coupling between the sub-units due to stronger π-interactions (more 'H-like'), and given the breadth of the potential surface in ϕ, also show significant inhomogeneous broadening. Conversely, we assign the narrow emission feature to di-PDI molecules with the "open" geometry, which have a smaller population, less coupling between sub-

units (more 'J-like' or monomer-like) and less inhomogeneous broadening. Indeed, the calculated energy difference between the di-PDI "open" and "closed" geometries is $\sim$6 $k_{\mathrm{B}}T$ in vacuum and $\sim$5 $k_{\mathrm{B}}T$ in chloroform when entropy effects from frequency analysis are included. These theoretical estimates match well with the population differences we measured via the temperature-dependent fluorescence experiments, described above.

Figure 4.6(a) shows the TD-DFT-calculated energy gaps between the ground state and the first four excited states of di-PDI as a function of ϕ. Panel (b) of this figure shows the ground and first several excited states at the "closed" and "open" geometries; the thickness of the vertical lines represent the oscillator strengths of the transitions between the different states. Clearly, there are many states with transitions contributing to the visible absorption spectrum of the di-PDI molecule, rather than the two states that would be expected from modest coupling between isolated monomer sub-units. The dashed curves in panel (a) show the magnitude and sign of what would be expected from Coulombic coupling between independent PDI monomers (with optimized dimer atomic positions and atom-centered monomeric Mulliken transition charges; see Appendix B for details). As expected, simple Coulombic coupling changes sign at 90° (the expected switch from H-like to J-like aggregation), and although this somewhat mimics the behavior of the higher-energy transitions, the idea of simple coupling clearly does not work for the di-PDI molecule. Instead, some other form(s) of coupling are more dominant, and/or the molecule cannot be considered as two weakly-coupled monomer sub-units due to the conjugated bay-linked bridge that connects them. Indeed, because of the bridge, the two monomer sub-units are actually radicals rather than closed-shell PDI monomers, and it is the mixing of these states with radical character that we believe leads to the complexity observed in the electronic structure of di-PDI; see Figure B.11 and the accompanying discussion in Appendix B. All of this explains why it is not possible to fit the absorption spectrum of di-PDI with simple coupling theories based on the monomer PDI spectrum, as mentioned above.

Despite the fact that the electronic structure of di-PDI cannot be explained by simple Davydov splitting, Figure 4.6 shows that of the lowest four excitations, the upper two transitions carry most of the oscillator strength for the "closed" configuration, while the lower states play a similar role for the "open" geometry. Thus, considered collectively, we see that the "closed" state is still roughly

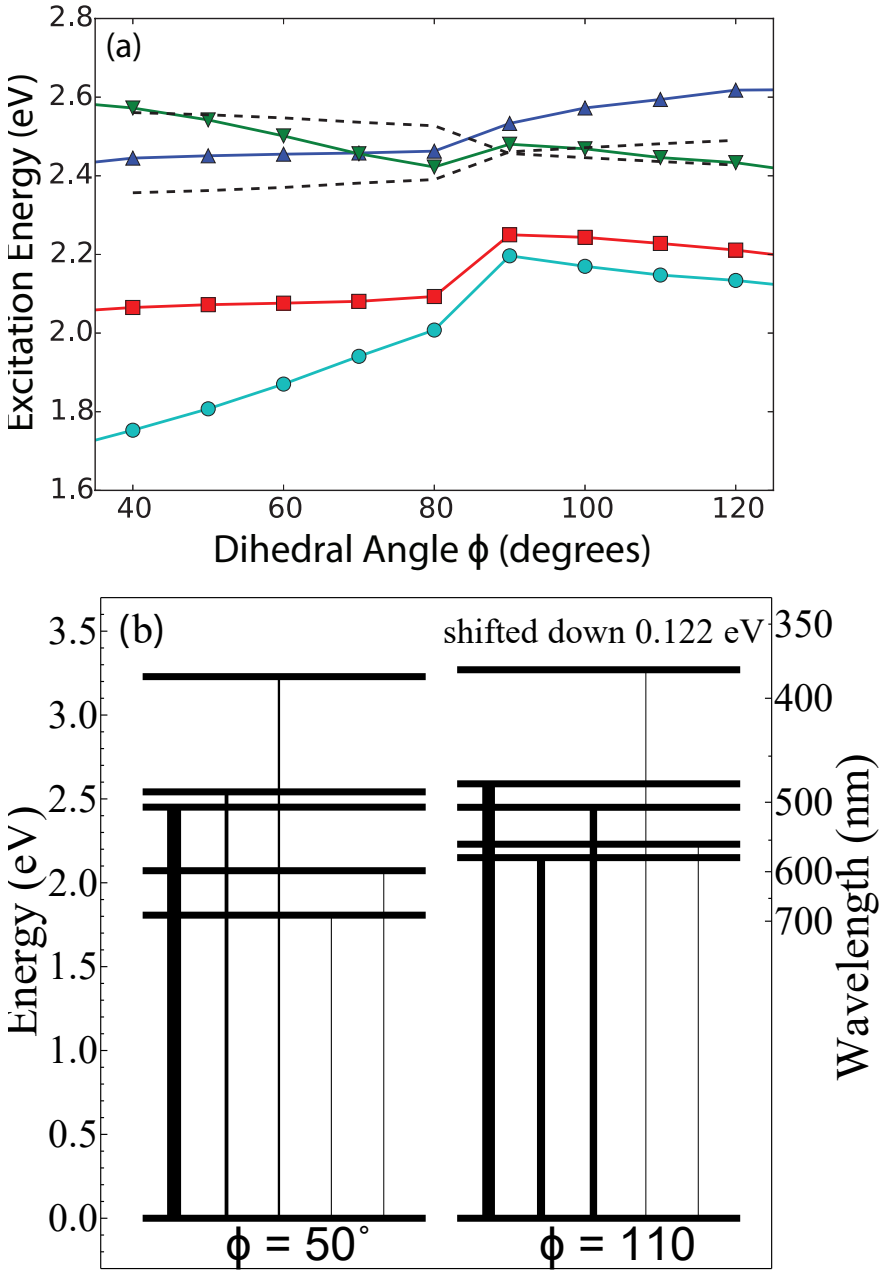

Figure 4.6: (a) Calculated TD-DFT photoexcitation energies for the first (teal circles), second (red squares), third (green inverted triangles), and fourth (blue upright triangles) excited states of di-PDI as a function of ϕ. The black dashed curves are the estimated Coulombic couplings for two independent monomers calculated from transition point charges. (b) TD-DFT-based energy level diagram for the two di-PDI ground-state minima including the first 5 excited states; the widths and color saturation of the vertical lines correspond to the oscillator strengths for transitions to each excited state from the ground state. The full ϕ dependence of the oscillator strengths to each of the lowest excited states is available in Appendix B.

H-like in character, while the "open" geometry can be loosely considered to be J-like. This rough observation is consistent with all of the experiments described above: the "closed" geometry has redder absorption and emission spectra, a weak emission quantum yield, and a greater degree of inhomogeneous broadening, and the "open" geometry has higher oscillator strength to the lowest excited state and thus should exhibit higher fluorescent quantum yields as well as blue-shifted absorption and emission spectra.

4.3.4 Femtosecond Spectroscopy as a Tool to Understand Di-PDI Spectra and Dynamics

With the basic picture of the di-PDI molecule existing in two distinct conformations with different spectral properties strongly supported by both steady-state spectroscopy and TD-DFT calculations, we turn next to femtosecond spectroscopy to understand the conformational dynamics of this molecule. If our picture is correct, then it should be possible to spectrally isolate the "closed" and "open" di-PDI conformers by selective excitation, allowing for independent characterization and the observation of any differences in solvation dynamics or motion along the ϕ coordinate. We also performed an identical set of ultrafast spectroscopy experiments on the PDI monomer, which are detailed in Appendix B for comparison. The data shown in this chapter were taken with the pump and probe polarizations at the magic angle; polarization-dependent transient absorption is shown in Appendix B.

4.3.4.1 Deconvolving the Absorption Spectra of the Two Di-PDI Conformers with Femtosecond Transient Absorption

Figure 4.7 shows the results of transient absorption experiments performed with the best excitation wavelengths for isolating the "closed" di-PDI geometry (580 nm, panel (a)) and the "open" di-PDI geometry (400 nm, panel (b)). For both excitation wavelengths, the negative change in absorption seen to the blue of $\sim$550 nm consists of a combination of ground-state bleach (GSB)/spectral hole-burning and stimulated emission (SE). The positive ΔOD seen to the red of $\sim$650 nm is due excited-state absorption (ESA), and the region between 550 and 650 nm contains overlapping ESA and SE signals. The fact that the shape of the GSB is different for the two excitation wavelengths

provides conformation that the steady-state di-PDI absorption spectrum is indeed an inhomogeneous superposition of two different conformers, each of which can be separately excited. The fact that the GSB spectral profiles do not appreciably change (other than in overall intensity) from 20 ps to 2 ns also strongly suggests that the two di-PDI conformers do not interchange during the excited-state lifetime: excitation at neither wavelength ultimately leads to the bleaching of the entire steady-state absorption spectrum. This observation is also consistent with the fact that we see separate emission spectra for the two species, so that for all intents and purposes, di-PDI really is a superposition of two effectively different molecules.

Given the total steady-state absorption spectrum, the reconstructed narrow absorption spectrum of the “open" conformer from fluorescence excitation spectroscopy, and the GSB spectra from both 580-nm and 400-nm transient absorption spectroscopy, we now have sufficient information from each of these independent pieces of data to extract the underlying electronic transitions for each di-PDI geometry. We used the standard Gaussian vibronic progression model (described in Eq. B.1 and the accompanying discussion in Appendix B). The results of our global fitting procedure are shown in Figure 4.8, where the data in all four panels (blue circles) were simultaneously fit with the same underlying transitions having fixed amplitude ratios within the “closed” and “open” geometries. Three separate transitions were required to fit the spectral profiles at each geometry, leading to 6 total vibronic progressions. Panels (a) (the steady-state absorption) and (d) (the GSB with 400-nm excitation) contain information about both di-PDI conformations, while panels (b) (the GSB with 580-nm excitation) and (c) (the reconstructed absorption spectrum leading to the narrow emission) contain information primarily about the individual “closed” and “open” geometries, respectively. We constrained the fit to use a single vibronic spacing parameter for each of the three electronic transitions belonging to the “open” and “closed” geometries. Clearly, the results of the fit (solid black curves) are excellent.

When examining the individual electronic transitions comprising the global fit in Figure 4.8, we see that the “closed” di-PDI geometry electronic transitions are all phenomenologically H-like in their Huang-Rhys parameters (with less oscillator strength in the 0–0 transition), while the narrow emission “open” di-PDI geometry transitions appear to have more monomer-like vibronic progressions. This result is qualitatively consistent with the TD-DFT calculations discussed above.

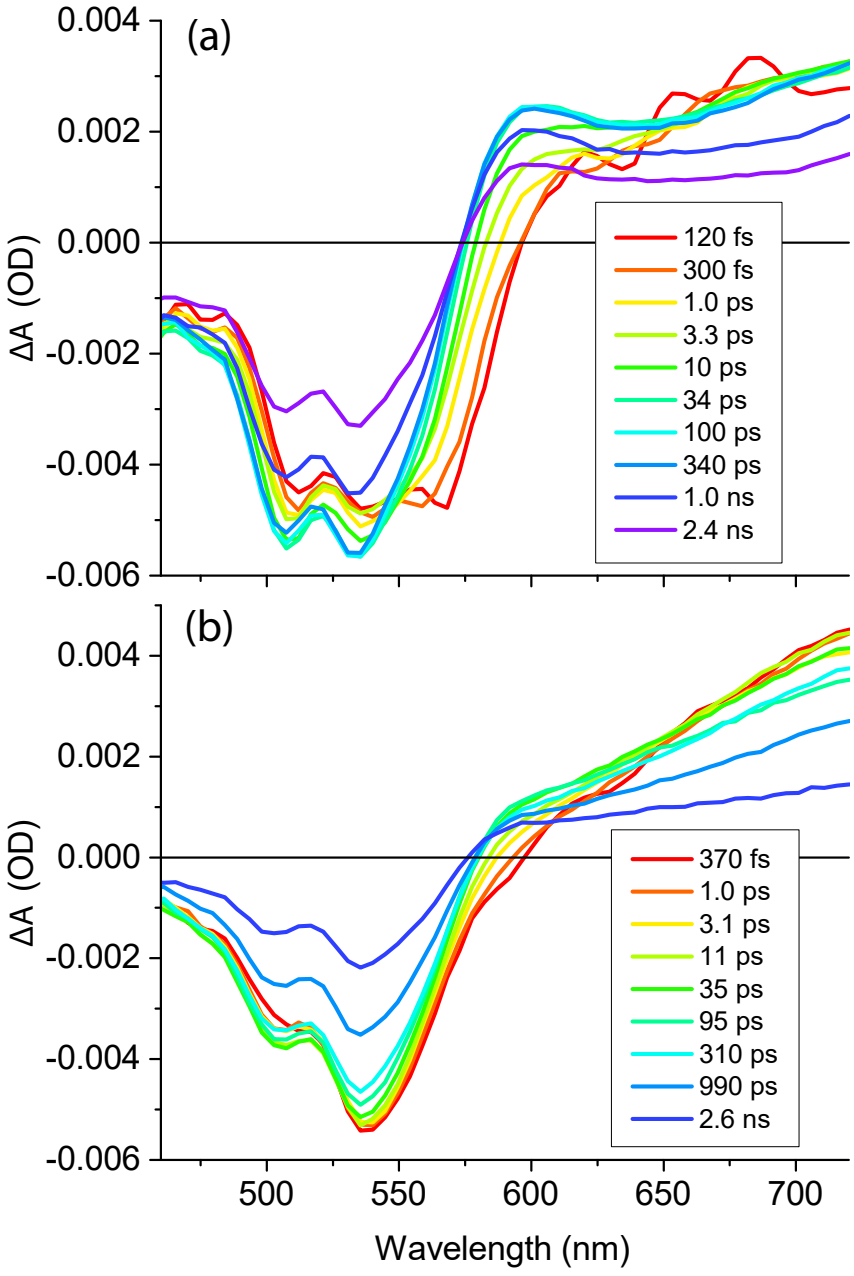

Figure 4.7: Time-resolved broadband transient absorption of di-PDI in chloroform with 580 nm (upper) and 400 nm (lower) excitation. Spectra are shown in logarithmically-spaced time intervals increasing from red to violet. The fact that the transient spectra at the two excitation wavelengths are so different is the direct result of the fact that di-PDI consists of an inhomogeneous superposition of two different conformers.

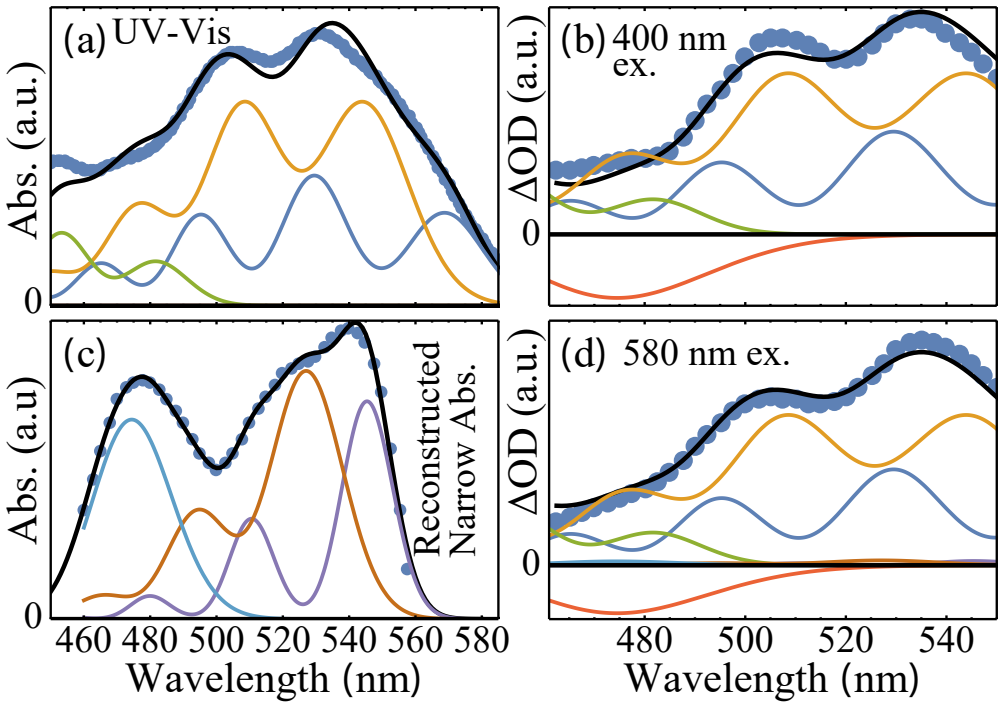

Figure 4.8: Global fit (black curves) to data from independent spectroscopy experiments (blue circles) performed on di-PDI: (a) steady-state absorption spectrum, (b) ultrafast GSB following 580-nm excitation, (c) reconstructed absorption profile leading to the narrow-band "open" emission, and (d) ultrafast GSB following 400-nm excitation. In panels (b) and (d), the bleach data are multiplied by -1 for ease of comparison to the absorption spectra, and the horizontal black line marks the zero of transient absorption. The various colored curves show the Gaussian vibronic progressions used to globally fit the data (see Appendix B for details). A Gaussian ESA component, required to fit the two transient absorption GSB profiles, is shown as the negative red curve in panels (b) and (d).

It is worth noting that the best fit to the di-PDI absorption spectrum from Horinouchi *et al*. is similar, but the additional information in our global fit here constrains the fit better over a wider wavelength range. We also repeated the global fit for di-PDI in other solvents (as detailed in Appendix B); the only major difference between solvents is in the relative oscillator strength of the highest energy transition, shown in light blue in panel (c), which decreases with increasing solvent dielectric constant.

4.3.4.2 Femtosecond Dynamics and Excited-State Lifetimes of the Di-PDI Conformers

Having established that di-PDI is in fact a mixture of "closed" and "open" conformers with cleanly deconvolved spectral profiles, in this section we focus on the early-time dynamics of the molecule following excitation. We began characterizing the observed dynamics by fitting the transient spectroscopy to multi-exponential decays, with no kinetic model implied. The results of this time-domain fitting procedure (see Appendix B for details) for both 580-nm and 400-nm excitation are given in Table 4.2, which makes clear that di-PDI dynamics take place on a variety of time scales. For both conformers, we observe a small-amplitude fast (< 500 fs) component. The amplitude of this component, which is likely due to inertial solvation dynamics, is small enough that it makes little difference in any of the subsequent analysis.

Table 4.2 and Figure 4.7 also show that following excitation, di-PDI undergoes a larger-amplitude $\leq$ 12-ps (in $CHCl_3$) spectral shift that is evident on both edges of the GSB and in the peak position of the ESA. The observed timescale of this shift scales linearly with solvent viscosity, and thus it makes sense to assign this time scale to large-amplitude torsional motion along the ϕ coordinate. This diffusive motion along the internal rotation coordinate is, within error, indistinguishable between the two excitation wavelengths: both "open" and "closed" geometries relax on a similar time scale. This makes sense given that twisting of a monomeric PDI sub-unit needs to push roughly the same amount of solvent out of the way no matter what the initial geometry.

To better understand these early-time dynamics along the ϕ coordinate, we also measured the time-resolved fluorescence from di-PDI employing Kerr-gated detection, shown in Figure 4.9 for 580-nm ("closed") excitation in chloroform. The time-resolved Stokes shift shows the same $\sim$12-ps

shift observed in transient absorption, and the overall fluorescence lifetime matches within error that found by recovery of the GSB. Also of interest is the sharp emission feature near 590 nm that exists for < 10 ps following excitation. We believe that this short-lived narrow feature results from emission from the Franck-Condon region prior to equilibration along the ϕ coordinate. This narrow feature is also manifest in the transient absorption data in Figure 4.7 as a stimulated emission (negative) signal peaking near 575 nm for the first few ps.

The longest timescale reported in Table 4.2 is the excited-state lifetime of di-PDI, which is on the order of 2-4 ns depending on solvent environment. The lifetimes of two conformers are similar, although it appears that the "open" geometry may have a somewhat shorter lifetime than that of the "closed" geometry (see Appendix B for a more detailed analysis). We also see that the total lifetime for both conformers scales inversely with the solvent dielectric constant. Given that the room temperature quantum yield is only 10–20%, this dielectric constant dependence suggests that there may be some slight charge-transfer character to the coordinate that non-adiabatically couples the electronic excited and ground states of both conformers.

Table 4.2: Fitting parameters to the dynamics of the transient absorption spectroscopy on di-PDI (Figure 4.7) at two excitation wavelengths (580 nm and 400 nm) and in several solvent environments (see Appendix B for relative amplitudes of exponential components). The results with 580-nm excitation in chloroform agree within error to the measured Kerr-gated fluorescence spectroscopy in Figure 4.9.

Environment	τ_1(ns)	τ_{shift}(ps)	τ_{fast}(ps)
$CHCl_{3,\ 580ex}$	3.9 ± 0.1	12 ± 2	0.3 ± 0.1
$CHBr_{3,\ 580ex}$	3.3 ± 0.7	40 ± 10	0.35 ± 0.2
$1\text{-}BuOH_{580ex}$	1.3 ± 0.4	60 ± 20	< 0.15
$Film_{580ex}$	1.8 ± 0.6	60 ± 40	0.3 ± 0.1
$CHCl_{3,\ 400ex}$	3.2 ± 0.4	13 ± 8	-
$CHBr_{3,\ 400ex}$	2.8 ± 0.8	45 ± 20	-
$1\text{-}BuOH_{400ex}$	1.5 ± 0.2	80 ± 30	< 0.2

Finally, we also attempted a detailed study of di-PDI orientational dynamics by performing femtosecond pump-probe polarized anisotropy experiments for the "open" and "closed " geometries; the results are shown in Figure B.12 in Appendix B, and the measured anisotropy decay times are presented in Table 4.3. Unfortunately, di-PDI shows very little anisotropy, even at the earliest

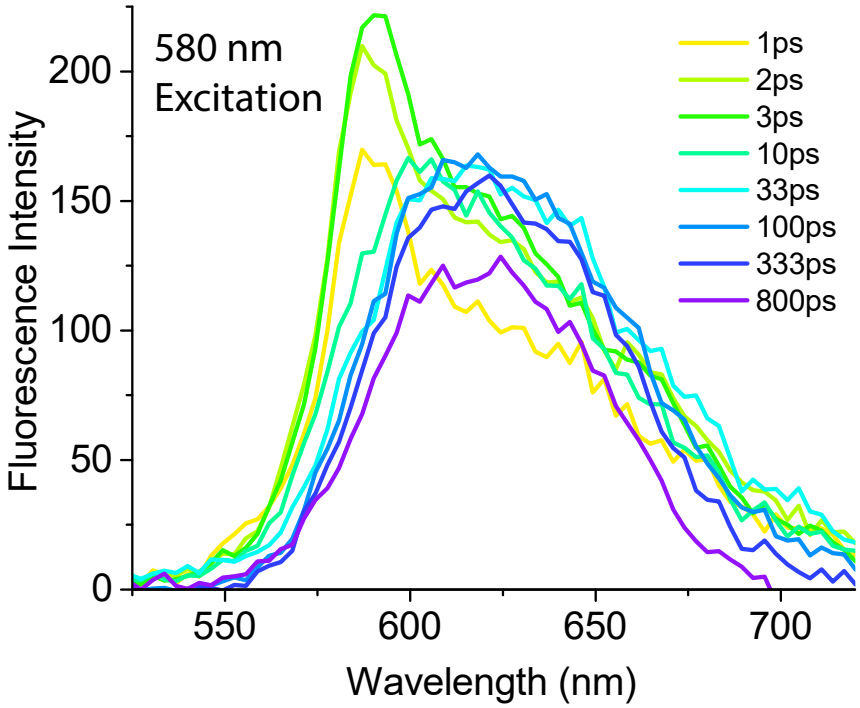

Figure 4.9: Time-resolved fluorescence from di-PDI in chloroform excited at 580 nm. The data were collected via femtosecond Kerr-gating with carbon disulfide with an effective ∼2 ps time resolution.

times (∼100 fs). This is a direct result of the fact that both di-PDI conformers have multiple overlapping electronic states, which our TD-DFT calculations suggest are orthogonally polarized (see Appendix B for details). Thus, despite our best attempts, little information could be extracted from our time-resolved anisotropy data besides the rotational diffusion times shown in Table 4.3.

Table 4.3: Rotational diffusion time of di-PDI in different solution measured via the decay of transient polarization anisotropy. For reference, the PDI monomer in chloroform exhibits a rotational diffusion time of ∼200 ps.

Environment	$\tau_{r,580}$(ns)	$\tau_{r,400}$(ns)
$CHCl_3$	0.5 ± 0.2	0.35 ± 0.3
$CHBr_3$	2.0 ± 0.5	2.1 ± 0.4
1-BuOH	2.2 ± 0.6	2.2 ± 0.7

4.3.5 Photophysical Picture of Di-PDI as Two Molecules in One

Overall, our results from steady-state spectroscopy, TD-DFT calculations, transient absorption and Kerr-gated fluorescence measurements allow us to propose a complete photophysical picture

for di-PDI in solution. Clearly the molecule exists in two conformations along the dihedral ϕ coordinate. The global minimum "closed" geometry is energetically preferred and accounts for over 90% of di-PDI molecules in solution at room temperature. This conformer is somewhat H-like in its electronic character, with a broad and highly Stokes shifted emission and an excited-state lifetime of 3.9 ns. The "open" geometry is somewhat harder to characterize given that it comprises $<$ 10% of the di-PDI population at room temperature, but it has more J-like character with narrower absorption and emission with little Stokes shift, as well as a somewhat shorter excited-state lifetime.

Following excitation, we see that the GSB, ESA and luminescence undergo spectral shifts on a viscosity-dependent time scale, which takes $\sim$12 ps in chloroform. This single time scale appears to describe equilibration on both the ground and excited-state surfaces for both di-PDI conformers, making it is natural to assign this to motion along the important large-amplitude di-PDI degree of freedom: ϕ. Our TD-DFT calculations indicate that the relaxed excited-state geometries are farther from the barrier than the ground-state geometry, especially for the "closed" conformer, as seen in Figure 4.6. Thus, excitation leads to excited-state twisting along ϕ, and spectral hole-burning along ϕ shows a similar recovery time scale on the ground state.

With our combination of different spectroscopies and quantum chemistry calculations, we see that each of the two di-PDI conformations has three (or potentially more) underlying electronic transitions spanning the visible, and that the two conformers are spectrally distinct, behaving as distinct molecules that do not interconvert on the time scale of their excited-state lifetimes. Moreover, while these two conformers show some phenomenological similarities to the typical manifestations of H and J intermolecular aggregates, their intramolecular coupling cannot be neglected, requiring a more detailed molecular orbital picture to understand their electronic structure, such as that shown in Figure B.11 of Appendix B.

4.4 Conclusions

In summary, we have investigated the properties of β-β-S-di-PDI using a host of steady-state and time-resolved spectroscopies, and have found that there are two distinct conformations of di-PDI at room temperature. The dominant of these conformers has strong π-stacking interactions and is more

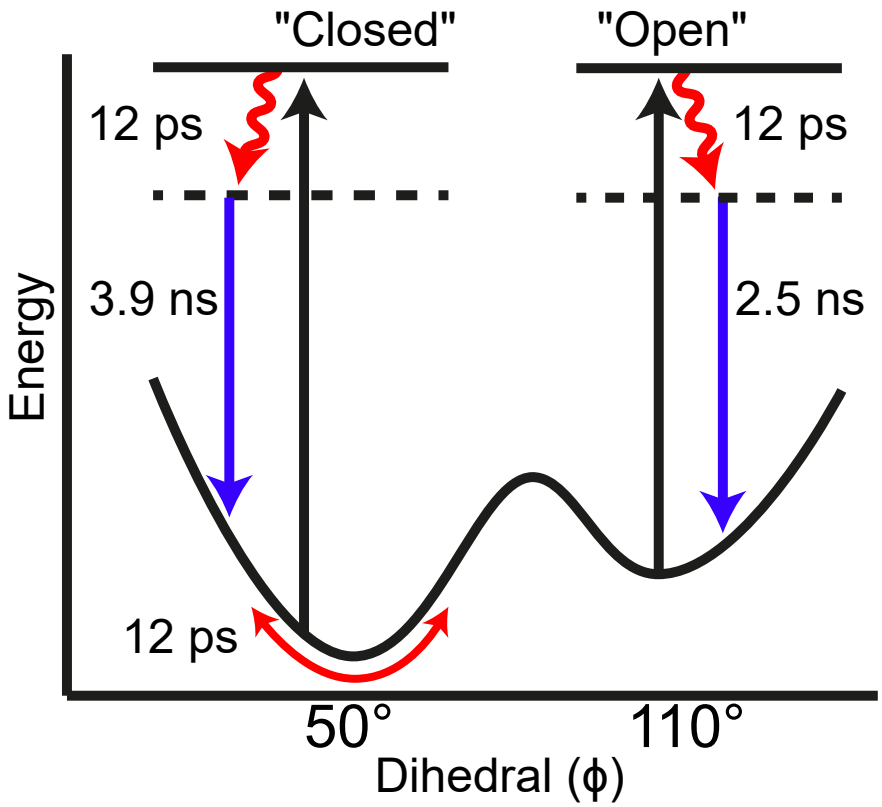

Figure 4.10: Schematic showing dynamics following photoexcitation of di-PDI. Following excitation and a fast (< 300 fs) relaxation to the lowest excited state, both the "open" and "closed" conformers undergo a ∼12-ps (viscosity-dependent) relaxation on their ground and electronic excited states. After the dynamics along ϕ are complete, the two conformers recover to their ground states on a similar ns time scale.

planar, leading to stronger through-space and through-bond intramolecular coupling, manifesting as inhomogeneous broadening with phenomenological H-like spectral properties. The other conformer, previously thought to be dominant from quantum chemistry methods that did not include dispersion, has less intramolecular coupling and appears to have more a more monomer-like spectrum. Despite the H-like and J-like labels, however, there are multiple electronic transitions for each conformer that result from direct coupling through the bridging bond, so that simple aggregation language is not appropriate for describing either form of this molecule.

Our temperature-dependent studies, along with the TD-DFT calculations, allowed us to determine that there is an energy difference of 71 meV, or $\leq 3\ k_{\mathrm{B}}T$ at room temperature, between the two di-PDI ground-state conformers; indeed, we can 'freeze out' the higher-energy "open" conformation by cooling the di-PDI solution to 77 K. The combination of our steady-state and time-resolved spectroscopies allowed us to perform a global fit of the spectra of the two conformers and deconvolve their multiple underlying electronic transitions.

The presence of two conformers has important implications for the use of this class of molecules in optoelectronic devices. The presence of a second conformer in low concentration could act as an exciton or electron trap, possibly diminishing the performance of solar cells or other devices incorporating di-PDIs. On the other hand, if one could engineer the relative distribution of the two conformers, it might be possible to increase light absorption or emission for photovoltaic or OLED applications. Overall, the most important conclusion is that di-PDIs are really two molecules in one, and that di-PDIs need to be treated accordingly if they are to be exploited in working devices.

CHAPTER 5

Evaporation vs. Solution Sequential Doping of Conjugated Polymers: F_4TCNQ Doping of Microns-Thick P3HT Films for Thermoelectrics

5.1 Introduction

Conjugated polymers are of considerable interest due to the fact that they not only are semiconducting,[112,267,268] but they are also low-cost,[111,269] have mechanical flexibility,[270,271] are easily solution processed,[16,111] and their properties can be readily tuned synthetically.[111,272] As a result, these materials are ideally suited for a wide variety of device applications.[17,54,55,273]

As with inorganic semiconductors, it is possible to dope conjugated polymers to increase their equilibrium carrier density and thus modify their electrical properties. Unlike inorganic semiconductors, which are doped by atomic substitution, organic semiconductors are usually doped chemically by adding a strong oxidizing (or reducing) agent. When doped, semiconducting polymers show particular promise as potential active materials for thermoelectrics[67,255,267,274–278] due to their reasonably high doped electrical conductivities and generally poor thermal conductivities.[66–68,255] This explains why there was been a recent surge of research on the variety of ways to produce molecularly-doped conjugated polymers, including studies on the methodologies used to produce doped polymer films as well as on the performance of devices fabricated from such materials.[5,8,69–71,74,75]

It is well established that the electrical conductivity of semiconducting polymers can be effectively tuned over several orders of magnitude by increasing the amount of dopant used.[69,81,208,209] What is less clear, however, is the maximum possible degree of doping that can be achieved. Part of

the reason for this is that there are multiple different methods for producing doped polymer films. The most common method involves casting a film of pre-doped polymer created by co-blending the polymer and dopant in solution, which we refer to as blend-cast doping.[8,68,74,78,81,274,277,279] This method makes it difficult to produce high doping levels, however, because as conjugated polymers become charged in solution, they generally become much less soluble, precluding the ability to cast high-quality films.[72–74,76,77,274] Because of this, there has been a great deal of recent effort aimed at starting with undoped conjugated polymer films and then exposing the pre-cast films to the dopant in a secondary step.

Different groups have implemented this latter approach, which we term sequential doping, in different ways. Some researchers expose the polymer film to the dopant molecules in the vapor phase,[79,79,81–83,280] as outlined schematically in Fig. 5.1(a). Alternatively, some groups, including ours, have pursued a solution-based technique in which the dopant is directly spin-coated from solution onto a pre-cast polymer film,[8,74,75,211,276,281] represented in Fig. 5.1(b). The purpose of this chapter is to compare in detail the evaporation- and solution-based sequential doping methods to determine which method, if either, is better for particular applications, with a focus on thermoelectrics.

Evaporation sequential doping has been the subject of many recent reports, most of which have focused on the doping of poly(3-hexylthiophene-2,5-diyl) (P3HT) by 2,3,5,6-Tetrafluoro-7,7,8,8-tetracyanoquinodimethane (F_4TCNQ).[81,83] These reports attributed the high electrical conductivities observed after doping to the idea that the crystalline order of the pre-cast polymer films is preserved after doping. Similar conclusions have been reached upon evaporation doping of poly(2,5-bis(3-alkylthiophen-2-yl)thieno[3,2-*b*]thiophene) (PBTTT).[80] Although evaporation sequential doping yields high conductivities, most reports focus on films that are only a few tens of nm thick,[79,80,82,83] and it remains unclear how evaporative doping might scale to the thicker films that would be required for most applications.[282]

Another open question with evaporation doping is how to reproducibly control the amount of dopant delivered. This is because most experimental evaporation doping setups add the dopant by sublimation in a home-built chamber with no way to precisely monitor the amount of dopant to which a polymer film has been exposed.[81–83,280] An additional issue is the fact that the sublimation

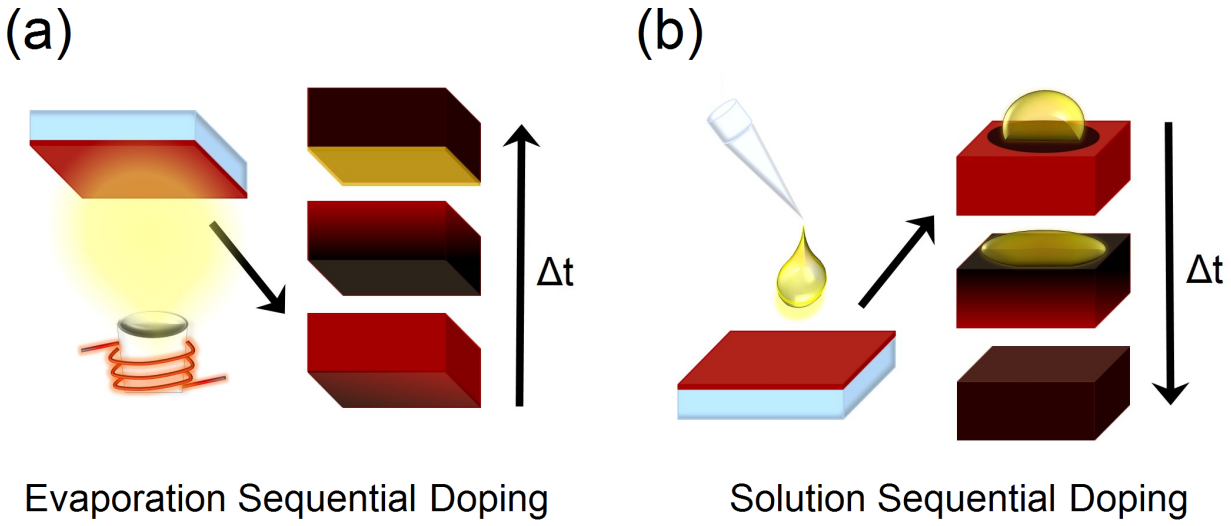

Figure 5.1: Schematic showing sequential-doping of conjugated polymer films using (a) evaporation sequential doping and (b) solution sequential doping; after the initial step, the arrow in each panel indicates the changes that take place as a function of time. Panel (a) shows that for evaporation doping, the crucible is resistively heated, producing dopant vapor (yellow) that can intercalate into a pre-cast polymer film (red). With additional time, a greater amount of dopant intercalates within the polymer film (doped film is indicated with black color). If evaporation continues, the dopant is added in excess, eventually coating the top of the film. Panel (b) shows that for solution doping, a dopant solution (yellow) is spin-cast onto a pre-cast polymer film (red). The solvent for the dopant solution is chosen to swell but not dissolve the polymer, allowing mass action to drive the dopant from the solution into the swollen film. Films can be more strongly doped (increasing black color) by increasing the concentration of the dopant in solution.

process tends to heat polymer films. When heated, polymer films expand, possibly changing the amount of dopant that can intercalate, thus leading to additional difficulties with reproducibility if the temperature of the film cannot be precisely controlled.[82,83] Very few studies have focused on more quantitative methods for delivering a precise amount of dopant, such as using a thermal evaporator with thickness monitoring.[79]

Solution sequential doping also has been the focus of a great deal of recent work.[8,74,75,211,276,277,281] In solution sequential doping, the dopant is dissolved in a solvent that is chosen to optimally swell but not dissolve the polymer of interest. When the dopant solution is spin-coated onto a pre-cast polymer film, mass action drives the dopant from the solution into the swollen polymer underlayer.[2,8,74,75,127,206] As with evaporation doping, solution sequential doping maintains much of the pre-cast polymer film's morphology, leading to excellent film quality and high electrical conductivities.[8,74,75] Moreover, because the method involves spin-coating of a dopant solution with a precisely defined concentration, the reproducibility of the method is high.[8,74,75,211] Solution sequential processing is limited, however, by the need to find solvents that can simultaneously dissolve the dopant and optimally swell but not dissolve the polymer. Since it is generally straightforward to find solvents or solvent blends that can optimally swell a conjugated polymer film,[2] the limiting factor for dopant intercalation with solution sequential doping is usually the solubility of the dopant in the selected solvent.[283]

In this work, we compare the effectiveness of the evaporation and solution sequential doping methods, focusing on the well-studied P3HT/F_4TCNQ materials combination. Of particular interest is the way each method scales for doping conjugated polymer films with different thicknesses. For our evaporation sequential doping experiments, we use a thermal evaporator with a thickness monitor to intercalate the F_4TCNQ dopant into P3HT films that are actively held at a fixed temperature, providing quantitative and reproducible dopant delivery. Our solution sequential doping measurements rely on spinning F_4TCNQ from dicholormethane (DCM), which is a near-optimal solvent for swelling P3HT.[2,8,23,37,74,75,206] Since both techniques are sequential, we are able to make head-to-head comparisons between them by doping identical pre-cast P3HT films with the same dopant in two different ways.

Using these two methods, we find that the electrical conductivities and thermoelectric perfor-

mance of doped films are comparable if each method is properly applied. For evaporation doping, after an "overhead" thickness of ∼7 nm is deposited, the optimal degree of doping is achieved when a thickness ratio of ∼1:3 dopant:polymer is employed. For solution doping, the dopant solution concentration must be adjusted depending on the polymer film thickness. We also find that both solution and evaporation sequential doping can effectively dope very thick semiconducting polymers films, which have thermoelectric properties that match those previously reported for thinner films. Both the evaporation and solution methods can create 400-nm-thick doped P3HT films with electrical conductivities in the ∼5 S/cm range and thermoelectric power factors near 2 μW/mK_2; these same properties can be maintained for films as thick as 2 μm when doped via the solution method. When the doping process is optimized by either method, we see that the amplitude ratio of the P3HT neutral to F_4TCNQ anion/P2 polaron optical absorption peaks is near 1:1, providing a simple guideline to achieve optimal doping when the evaporation thickness cannot be easily controlled. Overall, we conclude that both solution- and evaporation-based doping methods are well-suited to achieve high doping concentrations for applications across a wide range of polymer film thicknesses.

5.2 Experimental Methods

All materials and solvent were purchased commercially and used as received. P3HT was purchased from Rieke Metals, Inc. and F_4TCNQ was purchased from TCI America.

P3HT solutions at concentrations of 0.5%, 2%, and 5% weight/volume were prepared by dissolving 5 mg, 20 mg, and 50 mg P3HT in 1 mL of *o*-dichlorobenzene, respectively. Films were prepared in a nitrogen atmosphere by spin-casting the P3HT solutions onto glass substrates at 1000 rpm for 60 s followed by 3000 rpm for 5 s. With this spin-casting condition, the 0.5%, 2%, and 5% P3HT solutions yielded 25-nm, 110-nm, and 400-nm thick films, respectively. Films that were 2-μm thick were prepared by drop-casting 30 μL of a 2% P3HT solution onto glass substrates, which were then slow-dried by being placed into a small, covered, Petri dish for two days. Thickness measurements were carried out using a Dektak 150 profilometer and UV-visible absorption spectra were collected using a Lambda 25 UV-visibile spectrophotometer.

We performed our evaporation sequential doping via controlled thermal evaporation. F_4TCNQ was thermally evaporated onto pre-cast P3HT films using an Angstrom Engineering Nexdep thermal evaporator, in which the F_4TCNQ powder was placed into an alumina crucible that was resistively heated at pressures $<1 \times 10^{-6}$ Torr to induce sublimation. The pre-cast P3HT films were fixed to a rotating sample stage that was actively cooled using $\sim$15 °C chilled water. The evaporation rate was held constant 0.5 Å/s and the thickness of evaporated dopant was monitored using a quartz crystal microbalance located next to the sample holder. Solution sequential doping proceeded via spin coating solutions of F_4TCNQ dissolved in dichloromethane (DCM) at specified concentrations onto pre-cast P3HT films at 4000 rpm for 10 s.

Four-point electrical conductivity measurements were performed in ambient conditions on samples fabricated as described above using the Van der Pauw geometry[284] with silver paste electrodes placed at the corner of a 1.5 × 1.5 cm square as in our previous work.[74,75] Electrical conductivities were determined by dividing the measured sheet resistance by either the measured doped film thickness or by the thickness of the pre-cast P3HT film (effective conductivity), as discussed further below. For measurements of the thermovoltage/Seebeck coefficient, the samples were prepared as for the electrical conductivity measurements except the electrodes were fabricated by evaporating 15 nm of molybdenum oxide (MoO_3) followed by 60 nm of silver to reduce the contact resistance; these electrodes had a 7-mm spacing. The samples were placed at the interface of two thermoelectric devices to establish a temperature difference between the two electrodes, generating a thermovoltage. We measured the thermovoltage generated at applied temperature differences ranging from 2 to 9 °C, and calculated the Seebeck coefficient as the slope of the best-fit line of the thermovoltage vs. temperature difference. Details of our home-built thermoelectric characterization setup and data analysis are further described in Appendix C.

5.3 Results and Discussion

The main goal of this work is to compare the evaporation and solution sequential doping methods using the same dopant and the same pre-cast conjugated polymer films to determine under which conditions, if any, either method provides a significant advantage. For both types of sequential

doping, we will focus on the previously-unexplored limit of thick films, which are expected to function better in thermoelectric and other applications. As mentioned above, the evaporation doping literature has only explored film thicknesses of a few tens of nm, and it is not clear if thick polymer films can be fully saturated with dopant by this method and where the optimal doping level resides. Solution doping has been explored for thicker films using a multi-layer method,[281] but it is unknown whether the concentration of dopant can be made high enough in an optimal polymer swelling solvent to effectively dope thick films in a single processing step. Here, we show that when properly tuned, both methods are able to dope films that are surprisingly thick, yielding comparable conductivities and thermoelectric performance.

5.3.1 Sequential-Doping of P3HT by Thermal Evaporation

We begin our comparison by studying doping via thermal evaporation. We evaporated between 5 and 200 nm of F_4TCNQ onto pre-cast P3HT films of 25 nm, 110 nm, or 400 nm thickness. The electrical conductivities of these evaporation-doped films are explored in Fig. 5.2 and Table 5.1. The open blue circles/dashed lines in panel (a) show that the conductivity of 25-nm pre-cast P3HT films is low when only small amounts of evaporated F_4TCNQ are employed, reaches a maximum with 15 nm of evaporated F_4TCNQ, and then decreases upon the evaporation of additional dopant. For 110-nm-thick P3HT films, the open red circles/dashed lines in panel (b) show that the optimal conductivity is reached using 40 nm of evaporated dopant. The increased thickness of dopant required to achieve the optimal conductivity makes sense given the greater pre-cast polymer film thickness: additional dopant is clearly required to optimally dope the additional polymer in the thicker film. For 400-nm-thick pre-cast P3HT films, the open green circles/dashed lines in Fig. 5.2(c) show that 150 nm of evaporated F_4TCNQ is needed to achieve the optimal conductivity. As far as we aware, this represents the first time a film this thick has been successfully doped by the evaporation method. Previous work has shown that evaporated bulky dopants that are larger than F_4TCNQ can effectively diffuse through P3HT at room temperature, but only for 50-nm-thick P3HT films.[282] Our results here show that this diffusion holds for films at least eight times as thick.

Previous work has indicated that evaporated F_4TCNQ is better able to penetrate P3HT films if

the temperature of the film is raised during the evaporation. The data in Fig. 5.2 were taken on films that were actively cooled and held at 15 °C. This suggests that evaporation doping readily could be applied to even thicker films if heating were applied to increase the solid-state diffusion of the dopant into the polymer. We did not explore this limit, however, because the thermal evaporation of hundreds of nm of F_4TCNQ that would likely be needed to achieve optimal conductivity would require a substantial amount of material and thus become quite costly.

The conductivity values discussed above were calculated from the electrical sheet resistance using the measured film thickness after doping. For the thicker doping levls, however, we evaporated so much dopant that the thickness of the film increased significantly after doping. For example, Table 5.1 shows that the pre-cast 400-nm-thick P3HT with the optimal 150 nm of evaporated F_4TCNQ becomes 512 nm thick after doping. We know, however, that the dopant does not participate in the electrical conduction of the films, so in some sense, the 'conductive thickness' of the doped film is at most only that of the original pre-cast polymer. Thus, to better compare the electrical properties of doped films with different thicknesses and different amounts of evaporated dopant, we also calculated an 'effective conductivity' for each film, using the measured sheet resistance and the pre-cast film thickness. These effective conductivities are shown as the closed circles/solid lines in Fig. 5.2. To make the two conductivities easier to distinguish, the conductivities are plotted with their evaporated F_4TCNQ thickness offset by -1 nm while the effective conductivities are plotted with a $+1$-nm offset.

The effective conductivities in Fig. 5.2 show a similar trend as the conductivities as a function of evaporated F_4TCNQ thickness, but the effective conductivity values tend not to fall off at larger evaporated thicknesses when the evaporated thickness is comparable to or greater than the pre-cast film thickness. This strongly suggests that that once optimal doping is achieved, the maximal possible number of P3HT units are doped, and that the addition of more dopant accomplishes little other than increasing the film thickness.

Fig. 5.2 and Table 5.1 also show that we obtain higher optimal conductivities and effective conductivities with increasing thicknesses of the pre-cast P3HT films. This may result from the fact that our P3HT films with different thicknesses have different degrees of crystallinity: the thicker films take longer to dry after spin-coating and thus have a higher degree of 'solvent annealing'

Pre-Cast P3HT (nm)	Evaporated F_4TCNQ (nm)	Doped P3HT Film Thickness (nm)	Conductivity (S/cm)	Effective Conductivity (S/cm)
25	5	25 ± 5	0.26 ± 0.02	0.26 ± 0.02
	10	26 ± 5	0.67 ± 0.07	0.70 ± 0.07
	15	27 ± 5	1.04 ± 0.07	1.12 ± 0.08
	20	33 ± 5	0.47 ± 0.03	0.72 ± 0.04
	25	45 ± 5	0.43 ± 0.04	0.77 ± 0.07
	35	53 ± 5	0.34 ± 0.02	0.73 ± 0.05
	50	70 ± 5	0.22 ± 0.03	0.63 ± 0.08
110	25	142 ± 5	0.57 ± 0.03	0.74 ± 0.04
	35	145 ± 5	1.74 ± 0.13	2.29 ± 0.17
	40	149 ± 5	2.75 ± 0.14	3.73 ± 0.19
	50	154 ± 5	1.50 ± 0.14	2.10 ± 0.19
400	25	403 ± 5	0.00041 ± 0.00004	0.00041 ± 0.00004
	35	407 ± 5	0.019 ± 0.003	0.019 ± 0.003
	50	430 ± 5	0.18 ± 0.02	0.20 ± 0.03
	75	441 ± 5	1.52 ± 0.06	1.67 ± 0.07
	100	480 ± 5	2.22 ± 0.14	2.66 ± 0.17
	150	512 ± 5	4.20 ± 0.17	5.38 ± 0.22
	200	564 ± 5	3.52 ± 0.10	4.97 ± 0.14

Table 5.1: Summary of the conductivity and effective conductivity for sequential doping of pre-cast P3HT films with different thicknesses. The conductivity values were calculated using the measured thickness of the doped film while the effective conductivity values used the pre-cast P3HT film thickness.

or 'slow-drying' that increases their crystallinity, as is readily apparent from their UV-visible absorption spectrum, discussed further below.[64,75,285–287] We have shown in previous work that both the conductivity and carrier mobility of F_4TCNQ-doped P3HT films increase with increasing polymer crystallinity.[75]

To gain further insight into the changes taking place in our P3HT films upon evaporation doping, Fig. 5.3 shows the UV-visible absorption spectrum of each of the films whose conductivities were explored in Fig. 5.2. The spectroscopy of F_4TCNQ-doped P3HT films has been explored previously by many groups,[74,75,82,211,213,276] and we show a reference spectrum of a doped film assigning the various features in Appendix C. For purposes of the discussion here, we will focus on the P3HT neutral exciton absorption peak spanning the region from 2.0 to 2.8 eV and the overlapping P3HT P2 polaron and F_4TCNQ anion peaks near 1.6 eV.[74,213] Figure 5.3 shows that for all three pre-cast P3HT film thicknesses, as the amount of evaporated dopant is increased, the amplitude of the P3HT

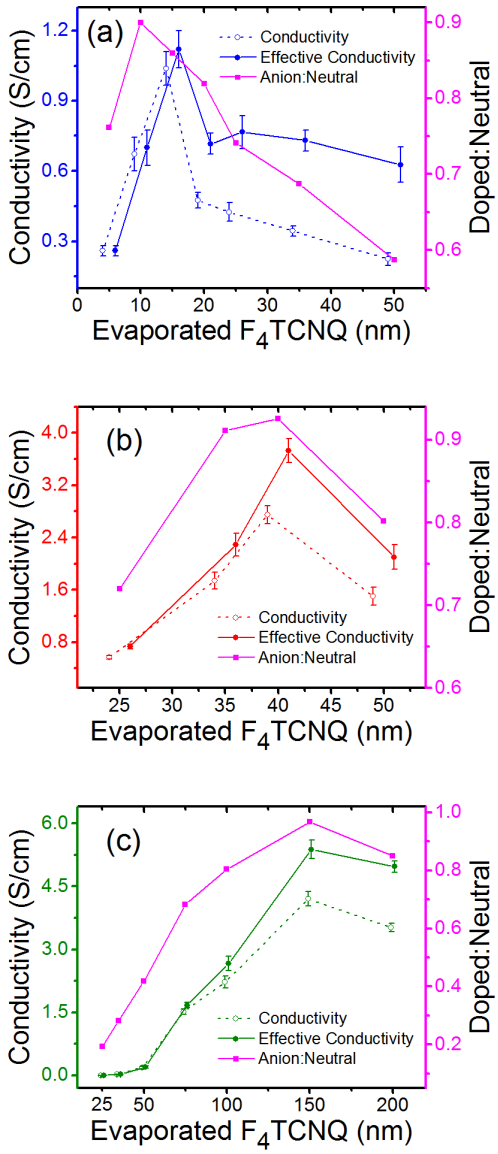

Figure 5.2: Conductivity (open circles and dashed lines, calculated using the measured film thickness after doping and shifted by -1 nm along the x-axis for clarity) and effective conductivity (filled circles and solid lines, calculated using the pre-cast film thickness and shifted by $+1$ nm along the x-axis for clarity) measurements for (a) 25-nm pre-cast P3HT films (blue), (b) 110-nm pre-cast P3HT films (red), and (c) 400-nm pre-cast P3HT films (green) doped with different evaporated thicknesses of F_4TCNQ. The ratio of the optical absorbance at 1.6 eV (corresponding roughly to the amount of doped material) to that at 2.4 eV (corresponding roughly to the amount of neutral material) for each film is plotted as the magenta squares (right axis); cf. Fig. 5.3. As the evaporated F_4TCNQ thickness increases, the conductivity and effective conductivity increase to reach an optimum value, which depends on the pre-cast film thickness. Beyond this optimum thickness, evaporated F_4TCNQ has saturated the film, leading to a conductivity decrease, but relatively little change in effective conductivity. The ratio of the optical absorption at 1.6 to 2.4 eV (magenta squares, right axis), which roughly represents the ratio of doped to neutral material, empirically tracks the conductivity and reaches a peak of 0.9 at the optimal conductivity.

neutral exciton absorption decreases while the amplitude of the overlapping P2 polaron and dopant anion absorption band concomitantly increases. Moreover, the data also show that once we have passed the point of optimal conductivity for each film, a broad absorption centered near ∼3.1 eV appears due to the presence of neutral F_4TCNQ; Appendix C shows the absorption spectrum of a pure film of evaporated F_4TCNQ for comparison. This indicates that once the optimal conductivity is achieved, additional F_4TCNQ does little except cake onto the surface of the film, justifying our use of the effective conductivity when comparing the electrical properties of different doped conjugated polymer films.

Figure 5.3 also shows that for all three pre-cast P3HT film thicknesses, the absorption spectra of the doped films with the optimal amount of evaporated F_4TCNQ for the best conductivity are essentially identical. In particular, we see that the optimally-doped films always have a roughly 0.9:1 ratio of the absorbance at 1.6 to 2.4 eV; these two energies correspond roughly to the amounts of doped and neutral material in the film, respectively. We plot the ratio of the absorbance at these two energies for each of our evaporated doped films as the magenta squares/lines in Fig. 5.2. Below we will also show that optimally-doped films created by solution sequential doping have a similar absorbance ratio at these two energies. This indicates that this ratio corresponds to optimal doping in all situations for this materials combination. This suggests that when the amount of evaporated dopant cannot be readily controlled (such as in a home-made sublimation set-up), one could use the absorbance ratio at these two wavelengths as a useful proxy for determining the optimal amount of F_4TCNQ needed to dope a given P3HT film.

As summarized in Table 5.1, the 25-nm, 110-nm, and 400-nm pre-cast P3HT films require 15, 40, and 150 nm of evaporated F_4TCNQ, respectively, in order to achieve their optimal conductivity. When we examine the ratio of optimal evaporated dopant thickness to pre-cast polymer film thickness, we see that it is 0.36 and 0.38 for the 110-nm and 400-nm pre-cast films, respectively. This strongly suggests that there is an optimal doping ratio that is independent of the polymer film thickness. The 25-nm-thick pre-cast film, however, has a much higher evaporated dopant:polymer thickness ratio (∼0.6) at the optimal conductivity point. We believe that this discrepancy results from the fact that there is a structural transition that occurs when P3HT is doped with F_4TCNQ: at a certain threshold concentration of dopant, the P3HT lamellar spacing becomes larger, which has

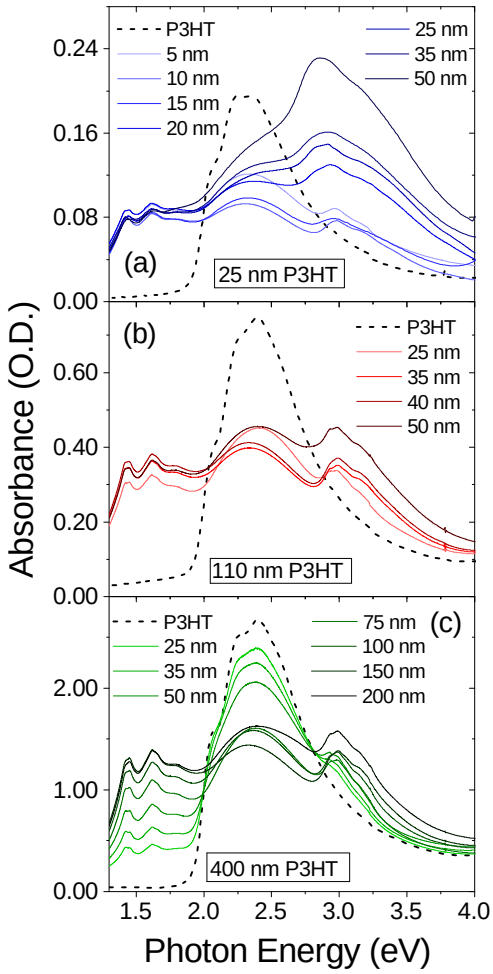

Figure 5.3: UV-visible absorbance spectra for (a) 25-nm pre-cast P3HT films (blue), (b) 110-nm pre-cast P3HT films (red), and (c) 400-nm pre-cast P3HT films (green) doped with varying thicknesses of evaporated F_4TCNQ; more saturated/darker colors correspond to thicker amounts of evaporated dopant. As the pre-cast P3HT film thickness is increased, an increasing thickness of evaporated F_4TCNQ is required to effectively dope the film, as indicated by an increase of the F_4TCNQ/P2 polaron absorbance peak near 1.6 eV and a corresponding decrease the in P3HT neutral absorption peak near 2.4 eV. At the F_4TCNQ thickness for optimal electrical conductivity, the ratio of the absorbance at these two energies (plotted in Fig. 5.2) is $\sim$0.9:1. For all three P3HT film thicknesses, once the optimal conductivity point is passed, a new absorbance feature at 3.1 eV due to presence of neutral F_4TCNQ grows in, indicating that the ability to dope the film is saturated.

been attributed to an expansion/reorientation of the P3HT unit cell to accommodate the presence of the dopant.[276] In Appendix C, we argue that there likely exists a threshold or "overhead" thickness of evaporated dopant that is required to induce this structural transition. If we assume that the required "overhead" thickness of evaporated F_4TCNQ is 7 nm, then we find an identical dopant-to-polymer thickness ratio of $\sim\frac{1}{3}$ for all three P3HT film thicknesses, as shown in Appendix C.

To further explain the conductivity increase, we measured the absorption spectrum of the P1 polaron transition for our 110-nm and 400-nm pre-cast P3HT films; these films are doped for optimal electrical conductivity via evaporation and solution sequential doping. As shown in Figure 5.4, we observe a red-shifted P1 band at 0.48 eV and higher-intensity IR-active vibrations (IRAV) below 0.18 eV for the 400-nm pre-cast P3HT films doped by both solution and evaporation sequential doping.[288] These spectral features are both correlated with higher mobility, which agrees with the higher conductivites for the 400-nm film relative to the 110-nm film.[75,289–291] This indicates that the 400-nm films are generally more ordered because they are slow-dried relative to the thinner films.[75]

Finally, we note that previous studies of evaporation doping of conjugated polymers have reported that when the the amount of evaporated F_4TCNQ is held constant, the conductivity passes through a maximum and then decreases as the polymer film thickness increases.[79,82] Our data indicate that at a constant evaporated dopant thickness, the conductivity decreases with increasing film thickness simply due to the films being under-doped. In other words, these previous experiments[79,82] did not provide sufficient F_4TCNQ to reach the required $\frac{1}{3}$ ratio for optimal conductivity. Indeed, we see that if we continue to supply additional dopant to reach this ratio, even for 400-nm thick polymer films, we can continue to reach the optimal conductivity. And of course, as mentioned above, in our experiments the substrate was actively cooled during dopant evaporation, but it may be possible to further increase F_4TCNQ diffusion into P3HT films on actively heated substrates,[82,83,282] possibly allowing evaporation doping of even thicker films, and/or altering the required "overhead" thickness for doping.

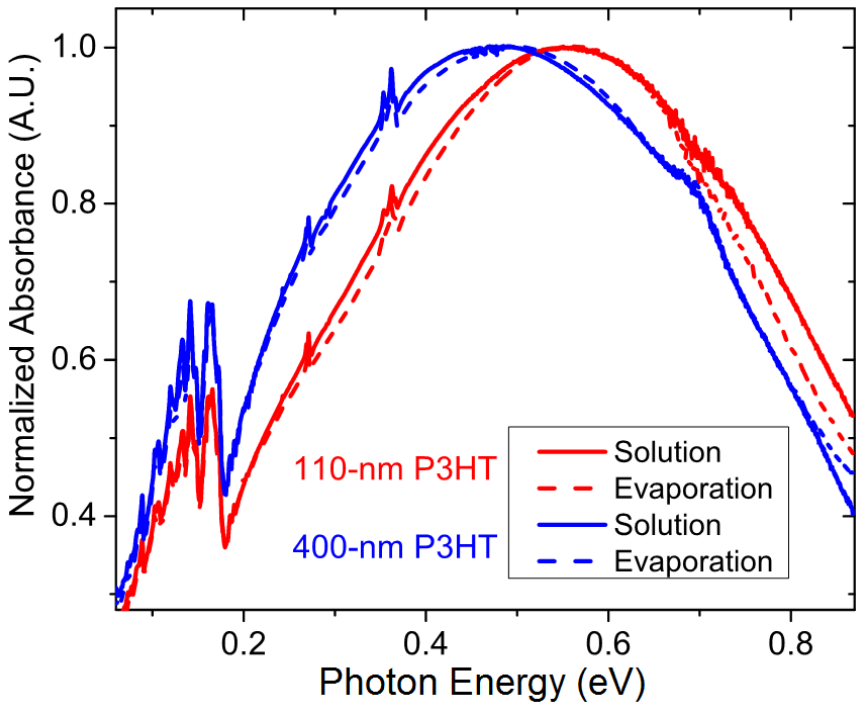

Figure 5.4: Absorption spectra of the P1 polaron transition for the doped 110-nm (red) and 400-nm (blue) pre-cast P3HT films. The films are doped by solution (solid lines) and evaporation (dashed lines) sequential doping; the doping conditions were selected to optimize the electrical conductivity. The P1 band for both the solution and evaporation sequential doped 400-nm pre-cast P3HT films are red-shifted, indicating greater polymer ordering a higher hole mobility.

5.3.2 Sequential-Doping of P3HT by Solution-Processing

We continue our comparison of sequential doping methods in this section by exploring the properties of P3HT films doped via solution sequential doping. For our case, this involves spin-coating solutions of F_4TCNQ dissolved in DCM at different concentrations on top of pre-cast P3HT films of different thicknesses. DCM is known to swell P3HT films without dissolving them, and it also has a reasonable solubility for F_4TCNQ, allowing mass action to drive the dopant into the swollen polymer underlayer. In previous work, we have successfully used this method to dope P3HT films of roughly 100-nm thickness with F_4TCNQ,[8,74,75] and other groups have developed a layer-by-layer version of solution doping to produce thicker doped films for thermoelectrics.[281]

We begin by investigating how the use of different F_4TCNQ solution concentrations (0.01 mg/mL, 0.1 mg/mL, and 1 mg/mL) influence the resultant electrical conductivity of doped P3HT films with different thicknesses. Figure 5.5 shows that when using a 0.01 mg/mL F_4TCNQ solution (orange diamond), we are able to measure the conductivity of a pre-cast 25-nm-thick P3HT film, but thicker films show no conductivity as they are highly under-doped. When we increase the dopant concentration to 0.1 mg/mL (maroon squares), we see respectable conductivities ($\leq$1 S/cm) for pre-cast 25-nm, 110-nm, and 400-nm thick P3HT films. But when we use a 1 mg/mL F_4TCNQ solution, which is close to the F_4TCNQ solubility limit in DCM, we find that we can effectively dope P3HT films with thicknesses ranging from 25 nm to 2 μm: these conductivities are all above 1 S/cm. This demonstrates that solution sequential doping can be used in a single step to optimize the conductivity of even very thick conjugated polymer films. Similar to our evaporation results, the thickest pre-cast P3HT films have the highest electrical conductivities, which we attribute to the greater polymer ordering and hole mobility.

Figure 5.6 presents the UV-visible absorption spectra of the solution-doped films, which show similar trends as for the evaporation-doped films (Fig. 5.3): as the dopant concentration increases, the neutral P3HT peak intensity decreases while that of the F_4TCNQ anion/P2 polaron peak increases. Figure 5.6(a) shows that 25-nm-thick pre-cast P3HT films are already highly doped even when using a low solution F_4TCNQ concentration of 0.01 mg/mL. When the dopant solution concentration is increased to 1 mg/mL, we observe significant absorbance at 3.1 eV from neutral F_4TCNQ, indicating

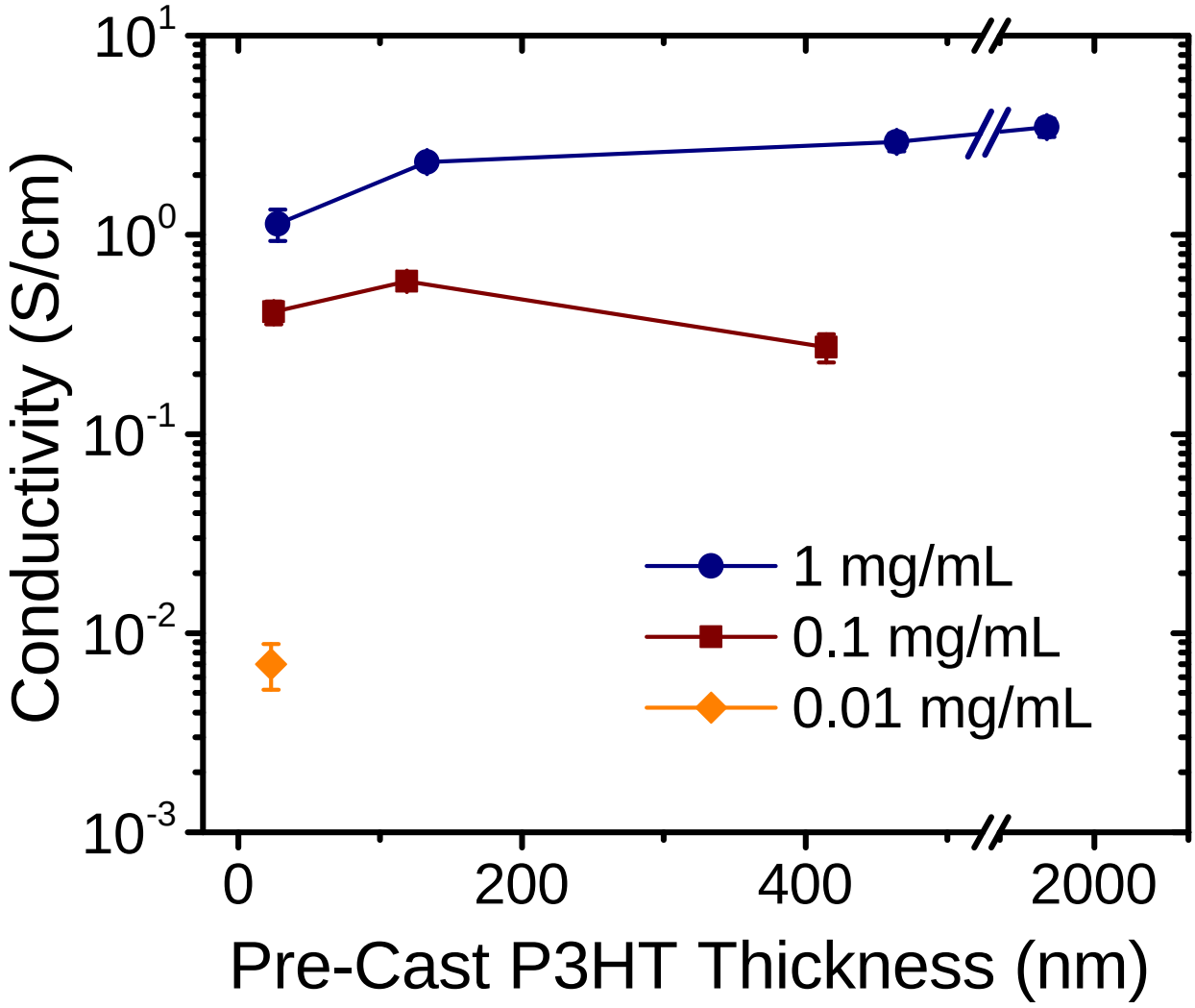

Figure 5.5: Conductivity measurements for solution-doped pre-cast P3HT films ranging in thickness from 25 nm to 2,000 nm. The films are solution-doped with 0.01 mg/mL (orange diamond), 0.1 mg/mL (maroon squares), or 1 mg/mL (navy circles) solutions of F_4TCNQ in DCM. Film conductivity increases with increasing F_4TCNQ concentration until an optimal value is reached. Note the *x*-axis scale break between 525 and 1,900 nm.

we are past the optimal doping point and have over-saturated the films with F_4TCNQ. For 110-nm-thick pre-cast P3HT films, Fig. 5.6(b) shows a similar trend, but at low dopant concentrations the extent of doping is reduced. This fits with our expectation that additional polymer material requires additional dopant to achieve the same doping levels. Figure 5.6(c) indicates for 400-nm-thick pre-cast P3HT films, the extra polymer material demands the higher-concentration 1 mg/mL dopant solution to achieve sufficient doping levels. We were unable to perform UV-visible spectroscopy on 2-μm-thick P3HT films because their optical density is greater than 10.

When we examine the UV-visible spectra in more detail, see that the ratio of the doped material absorption peak at 1.6 eV to the neutral P3HT absorption peak at 2.4 eV is $\sim$1.1:1, very similar to the optimal ratio of $\sim$0.9:1 that we saw with evaporation doping. We note that the absorbance peak ratio for the 25-nm-thick film is lower, but this likely results from overlap of the neutral P3HT peak with the tail of the neutral F_4TCNQ absorption, as this film is over-doped even at the lowest F_4TCNQ solution concentration. Thus, as mentioned above, the UV-visible absorption spectrum can serve as a rough guide to find the optimal doping concentration for electrical conductivity by roughly matching the intensities of the neutral and doped P3HT absorbance peaks.

5.3.3 Thermoelectric Properties of P3HT Films Prepared by Evaporation and Solution Sequential Doping

Having compared two methods for effective sequential doping P3HT films of varying thickness, we now turn to investigating how F_4TCNQ-doped P3HT films fabricated by the different routes function as active layers in thermoelectrics up to 2-μm thick. Figure 5.7 presents the thermoelectric properties of the evaporated (black squares) and solution (red circles) doped P3HT films that yielded the highest electrical conductivities for each pre-cast film thickness. Panel (a) shows that the electrical conductivity increases with increasing pre-cast P3HT film thickness for both doping methods. As mentioned above, this is because the thicker P3HT films are more crystalline, yielding higher-mobility carriers,[75] and serving to demonstrate that both sequential doping methods are able to preserve the pre-cast polymer film structure. The evaporated samples yield slightly higher conductivities at the same film thickness, which is due to evaporation processing better preserving

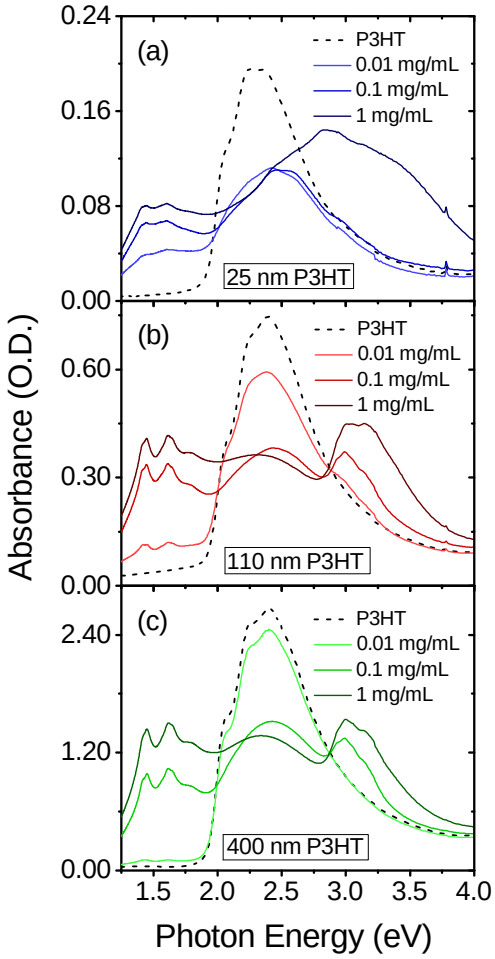

Figure 5.6: UV-visible absorption spectra for (a) 25-nm pre-cast P3HT films (blue), (b) 110-nm pre-cast P3HT films (red), and (c) 400-nm pre-cast P3HT films (green); as with Fig. 5.3, more saturated/darker colors correspond to increased dopant concentrations of 0.01 mg/mL, 0.1 mg/mL, and 1 mg/mL. As the thickness of P3HT increases, an increasing concentration of F_4TCNQ is required to effectively dope the film, as indicated by the decrease of the P3HT neutral peak near 2.4 eV and the increase of the F_4TCNQ anion/polaron P2 peak near 1.6 eV. As with the evaporated doped films, the optimal electrical conductivity occurs when the doped:neutral ratio is $\sim$1.1. For all films in this thickness range, the doping becomes saturated at higher concentrations, as evidenced by the appearance of absorbance due to neutral F_4TCNQ peak near 3.1 eV.

the underlying polymer structure than solution processing. The UV-visible absorbance spectra of these optimal-conductivity films are all quite similar, as shown in Appendix C.

Figure 5.7(b) shows the Seebeck coefficients of the doped polymer films, which are determined by the magnitude of the thermovoltage produced for a given temperature gradient. The data show that the Seebeck coefficient decreases for the thicker, more conductive doped P3HT films. This trend agrees with the well-known anti-correlation between electrical conductivity and Seebeck coefficient, where the Seebeck coefficient is seen empirically to vary as electrical conductivity to the $-\frac{1}{4}$ power,[67,68] as shown in more detail in Appendix C. Indeed, the Seebeck coefficients for the solution-doped films are higher than those for the evaporation-doped films, in agreement with their lower electrical conductivities. The Seebeck coefficients we measure in the tens of μV/K range are consistent with those found in other studies (on thinner films) of doped polythiophenes.[68,78]

Finally, we calculated the thermoelectric power factor, which is the product of the electrical conductivity and the square of the Seebeck coefficient and serves as a strong indicator of thermoelectric efficiency, shown in Fig. 5.7(c).[67,68] For all the P3HT film thicknesses we investigated, the devices show similar power factors of order 1–2 μW/mK^2. The fact that the power factor holds for the 2-μm-thick film shows that solution sequential processing is an effective method for producing organic thermoelectric active layers. In fact, to the best of our knowledge, this is the thickest reported solution-processed P3HT:F_4TCNQ thermoelectric device, exceeding that prepared using a multi-layer doping method.[281] Overall, we see that regardless of doping methodology, the thermoelectric properties of solution- and evaporation-doped polymer films are quite similar. Even though the two methods deliver the dopant in different ways, they both preserve the P3HT structure by doping in a sequential manner[8,74,75,81,83] and thus both offer potential for creating active layers for organic thermoelectrics. Overall, both evaporation and solution doping methods have distinct advantages, and our results show that one can use whichever method best suits the particular device fabrication needs: solution processing benefits from lower cost while evaporation methods are generally amenable for larger device areas.

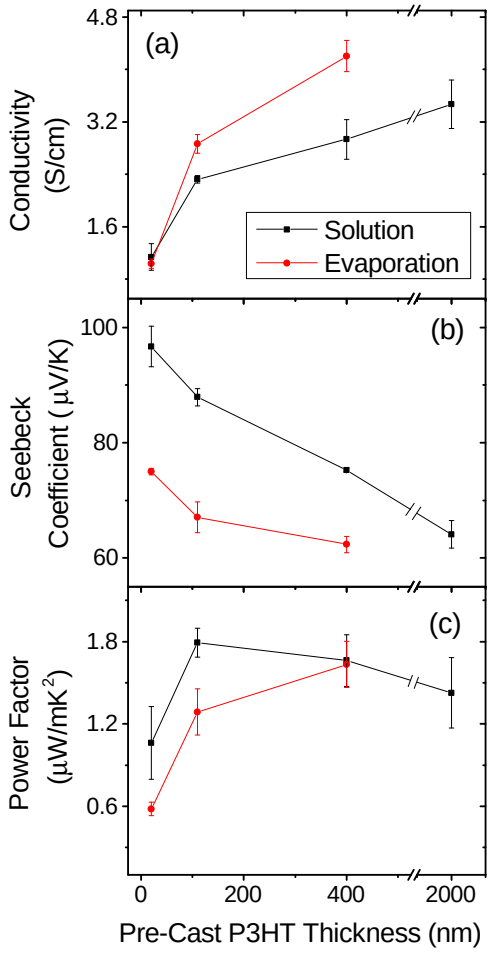

Figure 5.7: Thermoelectric properties of 25-nm, 110-nm, 400-nm, and 2000-nm pre-cast P3HT films doped with F_4TCNQ by solution (black squares) and evaporation (red circles) sequential processing. The processing conditions for each method were chosen to produce the most electrically conductive films. For evaporation sequential doping, the 25-nm, 110-nm, and 400-nm-thick pre-cast P3HT films were doped with 15 nm, 40 nm, and 150 nm of F_4TCNQ. For solution sequential doping, all P3HT films were doped with a 1 mg/mL F_4TCNQ solution. (a) Thicker P3HT films have slightly higher electrical conductivities than thinner films, and evaporation doping produces slightly higher conductivities than solution doping. (b) The Seebeck coefficient of doped P3HT films decreases with increasing film thickness, and solution-processed films yield slightly higher values than evaporation-processed films. (c) The thermoelectric power factors across all P3HT films thicknesses are similar in value, indicating that both processing techniques produce films equally well-suited for use in thermoelectrics. Note the scale break on the *x*-axis between 525 and 1,900 nm.

5.4 Conclusions

In this chapter we demonstrate that sequential processing is a highly effective method for chemically doping conjugated polymer films. Sequential doping starts with a pre-cast polymer film, which is then doped either by thermally evaporating dopant (evaporation sequential doping) or by spin-casting a solution of dopant on top of the polymer film (solution sequential doping). Both methods have the advantage of leaving the structure of the pre-cast polymer film intact, and thus the methods give similar electrical conductivities with similar degrees of doping. More importantly, we have demonstrated that both methods can be used to dope very thick semiconductor polymer films. For evaporation sequential doping, we demonstrated the ability to dope films up to 400 nm thick, and the doping of thicker films should readily be possible (particularly if heating is employed to improve diffusion of the dopant into the film), limited only by cost of evaporating large amounts of dopant. For solution sequential doping, we have shown that films up to 2-μm thick can be doped in a single processing step; to the best of our knowledge these are the thickest F_4TCNQ-doped P3HT films fabricated to date. Evaporation doping, which leaves the structure of the pre-cast polymer film more intact, achieves slightly higher electrical conductivities than solution doping, but requires an "overhead" thickness of $\sim$7 nm, presumably to induce restructuring of the polymer crystal lattice to accommodate the dopant. Solution doping, on the other hand, allows access to the doping of thicker films with less expense than evaporating large amounts of material, but finding the optimal solvent to dissolve the dopant and swell but not dissolve the polymer may not be straightforward with every materials combination.

For both sequential doping methods, we find empirically that UV-visible absorption spectroscopy provides a good indication that the optimal electrical conductivity has been achieved when the ratio of the doped to neutral P3HT absorption approaches 1:1. When less dopant than the optimal is used, the films have poor conductivity because much of the polymer remains undoped. When more dopant than usual is employed, the film conductivity decreases slightly, mostly due to the increase in thickness from the excess dopant that cakes onto the top of the film. The effective conductivity of films with too much dopant, however, remains close to the optimal, indicating that the doped polymer retains its electrical properties even when excess dopant is present. Thicker pre-cast P3HT

films demonstrate higher electrical conductivities due to greater polymer ordering, which increases the hole mobility.

When we fabricate thermoelectric devices out of F_4TCNQ films created by both sequential doping methods, we find that their thermoelectric properties are quite similar. For each polymer film thickness studied, the power factors are quite similar and fall across only a narrow range. This demonstrates that a wide range of processing techniques can be successfully applied to the fabrication of thermoelectric devices, with the choice based on convenience. Finally, although we have pushed the limit of sequential doping to 2-μm-thick films, it is clear that either technique could be possibly extended to still thicker films.

APPENDIX A

Supporting Information for Chapter 3

A.1 Experimental Details

A.1.1 Solar Cell Materials

P3HT and PBDTTT-C were purchased commercially and PSEHTT was synthesized[1] in-house. All other materials used in this study were purchased commercially and were used as received. P3HT was purchased from Rieke Metals, Inc. (Sepiolid P200: $M_n \sim$ 50-60 kDa, RR $\sim$ 94% and PDI $\sim$ 2.20), and PBDTTT-C was purchased from Solamer. PSEHTT was synthesized according to published literature.[222] PCBM was purchased from Nano-C. PEDOT:PSS (AI 4083) was purchased from Ossila.

A.2 Photovoltaic Device and Active Layer Fabrication Procedures

The first step in the P3HT:PCBM solar cell fabrication process was cleaning glass substrates pre-patterned with 150 nm tin-doped indium oxide (ITO; TFD Inc.). First, the ITO substrates were sonicated for approximately ten minutes in each cleaning solution (detergent, deionized water, acetone, and isopropanol). Following this, the ITO substrates were dried in vacuum for at least 30 min before being treated with an air plasma (200 mTorr, 15 min). A thin layer of PEDOT:PSS (35 nm) was deposited by spin-coating the PEDOT:PSS solution in air at 5000 rpm for 20 s. The PEDOT:PSS-covered substrates were then baked at 150 °C for 20 min in air.

Sequentially-processed P3HT:PCBM active layers were prepared by spin-casting a polymer solution onto one of the pre-prepared PEDOT:PSS-covered substrates. ITO on glass substrates were used for device studies, while single-crystal silicon substrates with a native silicon oxide layer were

used for X-ray diffraction, ellipsometry, and neutron reflectometry. Because both of these substrates display polar surfaces, they both allow for the fabrication of quality PEDOT:PSS films, which causes all subsequent layer deposition to be nearly identical on both substrates. The P3HT solution was prepared by dissolving 20 mg P3HT in 1 mL *o*-dichlorobenzene followed by mixing overnight at 55 °C. The PSEHTT solution was prepared by dissolving 10 mg PSEHTT in 1 mL *o*-dichlorobenzene followed by mixing overnight at 100 °C. The PBDTTT-C solution was prepared by dissolving 10 mg PBDTTT-C in 1 mL *o*-dichlorobenzene followed by mixing overnight at room temperature. DIO, ODT or CN (typically 3% by volume) was added directly to the polymer solution prior to heating. Before spinning, the P3HT and PBDTTT-C solutions were cooled to room temperature. PSEHTT films were spun hot at 100 °C. P3HT films were spin-cast in two successive steps (1000 rpm for 60 s; 3000 rpm for 5 s). PSEHTT films were spin-cast in two successive steps (2200 rpm for 60 s; 3000 rpm for 5 s). PBDTTT-C films were spin-cast in two successive steps (2000 rpm for 60 s; 3000 rpm for 5 s). To remove solvent additives by methanol washing, methanol was deposited on the freshly formed polymer film while the polymer film was still on the spin coater chuck; a spin speed of 2500 rpm for 40 s followed by 3300 rpm for 5 s was used for methanol washes.

PCBM was deposited by spin-casting (4000 rpm for 5 s) a 1 % PCBM solution directly onto the polymer film. The PCBM solution was prepared by dissolving 10 mg PCBM in 1 mL DCM and mixed at room temperature for at least 20 minutes. Fullerene deposition occurred within one hour of casting the polymer film, and no vacuum step was applied between polymer and fullerene spinning. This ensured minimal evaporation of any co-solvents/solvent additives between polymer film preparation and fullerene deposition.

P3HT:PCBM blend solutions were prepared by co-dissolving P3HT and PCBM with a weight ratio of 1:0.8 (P3HT:PCBM) in *o*-dichlorobenzene. The concentration with respect to P3HT was 20 mg/mL and the solutions were stirred at 60 °C overnight. After cooling to room temperature, the solutions were spun in two successive steps (1160 rpm for 20 s; 3000 rpm for 5 s) onto a PEDOT:PSS-covered substrate. DIO, ODT, or CN was directly added to the composite solution prior to heating to provide the desired concentration.

PSEHTT:PCBM blend solutions were prepared by co-dissolving PSEHTT and PCBM with a weight ratio of 1:2 (PSEHTT:PCBM) in *o*-dichlorobenzene. The concentration with respect

to PSEHTT was 7.5 mg/mL and the solutions were stirred at 100 °C overnight. The solutions were spun hot at 100 °C in two successive steps (1000 rpm for 60 s; 3000 rpm for 5 s) onto a PEDOT:PSS-covered substrate.

PBDTTT-C:PCBM blend solutions were prepared by co-dissolving PBDTTT-C and PCBM with a weight ratio of 1:1.5 (PBDTTT-C:PCBM) in *o*-dichlorobenzene. The concentration with respect to PBDTTT-C was 10 mg/mL and the solutions were stirred at room temperature overnight. DIO was directly added to the composite solution to provide the desired concentration. The solutions were spun in two successive steps (2000 rpm for 60 s; 3000 rpm for 5 s) onto a PEDOT:PSS-covered substrate.

For thermally annealed P3HT films, the annealing process occurred in an argon atmosphere after BHJ formation. Sequentially-processed films were annealed at 150 °C for 15 min on a hot plate while blend-cast films were annealed at 110 °C for 20 minutes. Directly after annealing, the films were placed on a metal surface to assist in cooling back to room temperature.

For devices, electrodes were evaporated onto the active layers using functional incremental equipment such as a thermal evaporator (Angstrom Engineering). Cathodes consisted of approximately 10 nm of Ca evaporated at a rate of $\sim$0.5 Å/s followed by evaporating $\sim$70 nm Al at a rate of $\sim$1 Å/s. The first 10 nm of Al were evaporated at a rate of $\sim$0.5 Å/s. Evaporation pressures were 10^{-7} Torr or less. The active areas of the resulting solar cells were 7.2 mm^2.

A.3 Optoelectronic Analysis

A.3.1 *J-V* Measurements

J-V measurements were performed in an argon atmosphere using a Keithley 2400 source meter. A xenon arc lamp equipped with an AM-1.5 filter was used as the excitation source, with the intensity calibrated to match 1 sun. The *J-V* data shown are the average of at least 9 separate devices and the error bars shown are $\pm$1 standard deviation. Dark *J-V* parameters were discarded from devices that did not perform as good diodes and therefore did not fit well to the diode equation.

We report that the open-circuit voltage decreases slightly with increasing % DIO added to

	V_{oc} (V)	J_{sc} (mA/cm^2)	FF $(\%)$	PCE $(\%)$	n_{id}	J_0 $(\times 10^{-5}\, mA/cm^2)$	R_{series} $(\Omega \cdot cm^2)$	R_{shunt} $(\times 10^5\, \Omega \cdot cm^2)$
0% Co-Solvent SqP	0.422 ± 0.026	3.10 ± 0.16	48.16 ± 3.88	0.63 ± 0.10	1.50 ± 0.07	1.95 ± 1.25	27.5 ± 1.3	4.5 ± 3.8
0% Co-Solvent MeOH SqP	0.430 ± 0.021	3.32 ± 0.11	49.82 ± 4.58	0.71 ± 0.08				
0% Co-Solvent Annealed SqP	0.644 ± 0.001	6.34 ± 0.08	67.42 ± 1.29	2.76 ± 0.08	1.32 ± 0.04	0.00200 ± 0.00117	2.5 ± 0.4	16.3 ± 20.3
0% Co-Solvent BC	0.626 ± 0.002	7.05 ± 0.21	59.13 ± 0.37	2.61 ± 0.06	1.38 ± 0.01	0.00455 ± 0.00075	4.4 ± 0.2	4.1 ± 0.6
0% Co-Solvent Annealed BC	0.620 ± 0.002	8.16 ± 0.13	60.38 ± 3.23	3.06 ± 0.16	1.39 ± 0.04	0.00857 ± 0.00400	2.4 ± 0.1	2.4 ± 0.4
3% DIO SqP	0.531 ± 0.006	6.11 ± 0.29	53.58 ± 2.69	1.74 ± 0.15	2.01 ± 0.07	5.79 ± 2.04	3.8 ± 0.2	4.5 ± 1.7
3% DIO Annealed SqP	0.618 ± 0.002	6.16 ± 0.16	65.35 ± 1.13	2.48 ± 0.08	1.36 ± 0.03	0.00588 ± 0.00182	2.1 ± 0.7	15.6 ± 5.1
3% DIO BC	0.573 ± 0.001	9.05 ± 0.49	57.97 ± 0.42	3.00 ± 0.18	1.45 ± 0.02	0.0739 ± 0.0092	3.1 ± 1.1	14.2 ± 5.4
3% DIO Annealed BC	0.626 ± 0.002	8.35 ± 0.24	63.13 ± 0.63	3.30 ± 0.10	1.37 ± 0.01	0.00578 ± 0.00056	2.9 ± 0.7	2.6 ± 1.5
3% DIO MeOH SqP	0.495 ± 0.009	4.95 ± 0.15	47.72 ± 1.05	1.17 ± 0.06				
7% DIO SqP	0.511 ± 0.007	7.15 ± 0.27	50.34 ± 1.32	1.84 ± 0.14	1.95 ± 0.01	6.14 ± 0.83	3.8 ± 0.4	6.9 ± 3.9
7% DIO MeOH SqP	0.475 ± 0.017	5.16 ± 0.48	48.78 ± 2.51	1.20 ± 0.13				
7% DIO DCM SqP	0.545 ± 0.003	5.31 ± 0.12	51.53 ± 0.85	1.49 ± 0.03				
3% ODT SqP	0.531 ± 0.011	5.51 ± 0.28	55.06 ± 1.11	1.65 ± 0.19	1.66 ± 0.01	0.859 ± 0.040	3.3 ± 0.6	4.7 ± 1.0
3% ODT Annealed SqP	0.599 ± 0.002	6.50 ± 0.20	65.62 ± 0.35	2.58 ± 0.04	1.46 ± 0.05	0.0410 ± 0.0281	3.0 ± 1.0	2.5 ± 2.2
3% CN SqP	0.441 ± 0.030	6.38 ± 0.50	42.30 ± 1.40	1.22 ± 0.23				
3% CN Annealed SqP	0.623 ± 0.002	6.12 ± 0.07	67.47 ± 0.49	2.59 ± 0.06	1.32 ± 0.04	0.00424 ± 0.00025	3.5 ± 1.6	8.7 ± 0.2

Table A.1: Summary of P3HT Device Parameters.

	V_{oc} (V)	J_{sc} (mA/cm^2)	FF $(\%)$	PCE $(\%)$
0% Co-Solvent SqP	0.725 ± 0.003	7.41 ± 0.10	62.99 ± 1.11	3.38 ± 0.04
3% DIO SqP	0.677 ± 0.004	10.67 ± 0.34	57.06 ± 0.31	4.13 ± 0.14
7% DIO SqP	0.677 ± 0.005	9.33 ± 0.42	55.71 ± 0.74	3.51 ± 0.10
0% Co-Solvent BC	0.700 ± 0.005	10.73 ± 0.27	65.10 ± 3.01	4.89 ± 0.31

Table A.2: Summary of PSEHTT Device Parameters.

the polymer underlayer. This reduction in open-circuit voltage attributed to improved polymer crystallinity.[40,102]

A.3.2 External Quantum Efficiency (EQE) Measurements

EQE measurements were collected following a procedure similar to that described elsewhere.[292] The EQE was measured as the photocurrent produced from a chopped (211 Hz) monochromatic

	V_{oc} (V)	J_{sc} $\left(mA/cm^2\right)$	FF $(\%)$	PCE $(\%)$
0% Co-Solvent SqP	0.734 ± 0.004	12.36 ± 0.70	52.97 ± 1.06	4.81 ± 0.27
3% DIO SqP	0.736 ± 0.002	12.88 ± 0.34	56.34 ± 1.12	5.33 ± 0.05
0% Co-Solvent BC	0.788 ± 0.001	10.88 ± 0.26	49.40 ± 0.57	4.24 ± 0.08
3% DIO BC	0.727 ± 0.002	12.96 ± 0.37	58.60 ± 1.09	5.52 ± 0.14

Table A.3: Summary of PBDTTT-C Device Parameters.

light beam (Newport TLS-300X) impinging on the active area of the device as a function of the wavelength of the light. The photocurrent was measured across a 0.1 kΩ or 1 kΩ resistor using a SR830 lock-in amplifier. When the signal across the 0.1 kΩ resistor was less than 80 nV, the 1 kΩ resistor (10^6 current amplification mode) was used. Short-circuit conditions were well-maintained at all times since the currents were low and the voltage across the resistor and device was small. To remove lower-order reflections, which introduce high-energy light that could be transmitted through the monochromator, multiple long-wave pass filters (90% transmission cut-on at 345 nm, 605 nm, 850 nm, 1030 nm, or 1550 nm) were used. Each data point was taken from the amplitude (R) readout of the lock-in and averaged for $\sim$5 time constants. A Thor Labs FDS1010-CAL Si photodiode was used for wavelength below 1050 nm and a Thor Labs FDG05-CAL Ge photodiode was used for wavelengths above 1050 nm.

Device	J_{sc} (mA/cm^2)
0% Co-Solvent	2.95
3% DIO	6.09
7% DIO	7.17

Table A.4: EQE Integrated Currents Summary

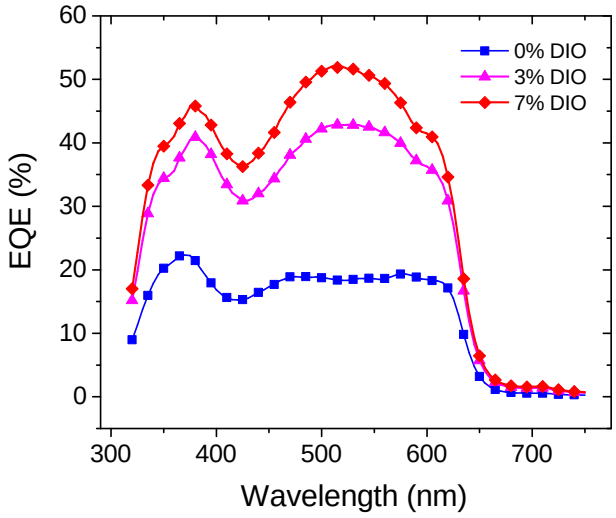

Figure A.1: External quantum efficiency curves for devices cast with 0 % (v/v) DIO (blue squares), 3 % (v/v) DIO (purple up triangles), and 7 % (v/v) DIO (red diamonds). The EQE curves show a uniform increase with % (v/v) DIO.

As a calibration check, we verified that the wavelength-integrated currents collected by EQE agree within 5% of short-circuit currents measured in the AM-1.5 *J*-*V* testing.

A.3.3 2. Recombination Effects on Photodiode Characteristics

To investigate the effect of co-solvents on the charge recombination, we performed a full fit of the dark diode equation to determine the dark ideality factor, n_{ideal}. Ideality factors are a measure of the primary recombination mechanism in a device: ideality factors of 1 characterize pure, bi-molecular (direct band-to-band) recombination while ideality factors of 2 indicate trap-assisted recombination, which generally occurs though a trap state within the band gap.[293] For cases where $1 < n_{ideal} < 2$ and the mechanism is not purely band-to-band or trap-assisted, but rather accepted as having some

degree of enhanced trap-assisted recombination.[41] Ideality factors $\gg$2 are attributed to increased recombination or other effects such as contact resistance.[41,294]

Analysis of the dark *J*-*V* characteristics (Table A.1) shows that devices fabricated with DIO have larger ideality factors, which indicates that additional, trap-assisted, recombination pathways are present. Since DIO swells P3HT and therefore increase mixing throughout the film, the increased mixing reduces domain purity and provides additional recombination pathways through additional domain boundaries.[25] The recombination parameter, J_0, which is a direct measure of the recombination provides another measure for recombination.[295,296] For devices fabricated with DIO, J_0 increases, which is consistent with the higher ideality factors and improved mixing. Devices fabricated with ODT demonstrate a similar ideality factor and J_0 with respect to the control devices. Given that 3% (v/v) DIO and 3% (v/v) ODT devices perform similarly, we speculate that the similar performance arises from a competition between increased exciton splitting from more mixing and the associated increased recombination from the added domain boundaries.[25] Since DIO swells P3HT more than ODT, devices fabricated with DIO are more mixed and have higher currents. However, this also introduces more recombination pathways, such as grain boundaries, which lowers the fill factor, thereby resulting in similar overall device performance.

A.3.4 Dark Charge Extraction by Linearly Increasing Voltage (CELIV) Measurements

The equilibrium dark doping density was measured by dark CELIV. CELIV measures the current produced by applying by applying a linear, reverse-bias, voltage ramp.[297] Because the device is measured in the dark and is thus depleted of photogenerated charges and is run in reverse bias, the device acts as a capacitor. Therefore, the signal mainly results from the capacitive displacement current. However, additional mobile carriers from doping can add to this signal. By integrating the CELIV transient and subtracting the contribution from the displacement current, the doping density can be accurately measured.[127] Furthermore, this doping is associated with evaporated metals encountering PCBM molecules on the top surface.[127,224] Therefore, greater doping densities are recorded for films with more PCBM on the top surface.

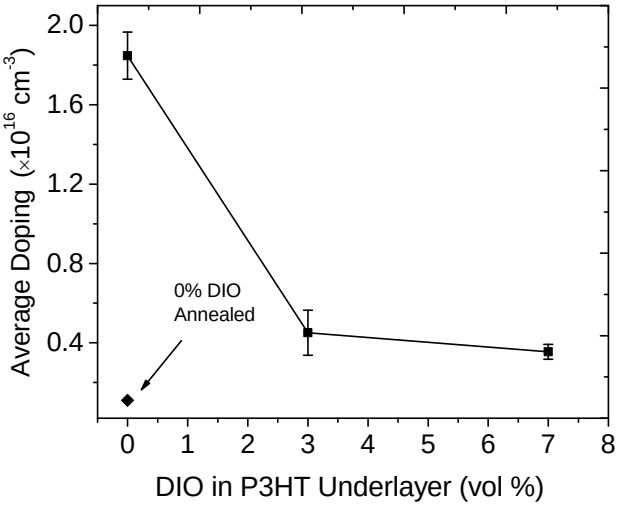

Figure A.2: Doping density recorded by dark CELIV measurements. With increasing % DIO, the doping density decreases, consistent with less fullerene present on the top-surface of the active layer. The value for the annealed doping density comes from Reference 1.

A.3.5 Active-Layer Composition Analysis by the Redissolving Technique

Because SqP provides only indirect control over BHJ composition (the final composition depends on both the concentration of fullerene in solution and the degree to which the chosen solvent swells the polymer), it is important to accurately determine the final composition produced by SqP. The procedure for determining the active layer composition was performed on ITO/PEDOT/Active Layer/ substrates that were processed identically to the procedure above, except without evaporation of the Ca/Al top electrodes.[127] First, the outer edges ($\sim$1-2 mm) of the active layer were removed with a razor blade, leaving only the center portion of the film where the solar cells would have been fabricated. This removal is because the outer edge can be anomalously rich in PCBM in SqP films, which is the result of surface tension and wetting effects during the spin-coating deposition process.[127]

Once the edges were removed, the substrates were then cleaned with nitrogen and the active layer was redissolved by directly pipetting two to three drops of ODCB onto the active layer with a glass pipette. With ODCB still on the substrate, ODCB containing the dissolved active layer was drawn up into the pipette and redeposited onto the active layer several times. Following this, the

active layer solution was placed in a 1 mm thick quartz cuvette. This entire process was repeated two to three additional times, each time using a clean glass pipette to redissolve the active layer. After transferring all of the dissolved active layer solution, the cuvette was vigorously shaken to yield a uniformly mixed and completely dissolved solution.

The active layer composition was then determined using a UV-Visible spectrometer to examine the absorption spectrum of the redissolved film, with the PCBM:P3HT ratio determined by fitting the redissolved film's absorption spectrum to a linear combination of the pure P3HT and pure PCBM absorption spectra:[127]

$$OD_{\mathrm{Soln}}(\lambda) = A_{\mathrm{PCBM}} OD_{\mathrm{PCBM}}(\lambda) + A_{\mathrm{P3HT}} OD_{\mathrm{P3HT}}(\lambda)$$

where A_{PCBM} and A_{P3HT} are fitting coefficients that represent the amount of each material. Therefore, the PCBM:PCBM mass ratio is given by $A_{\mathrm{PCBM}}/A_{\mathrm{P3HT}}$.

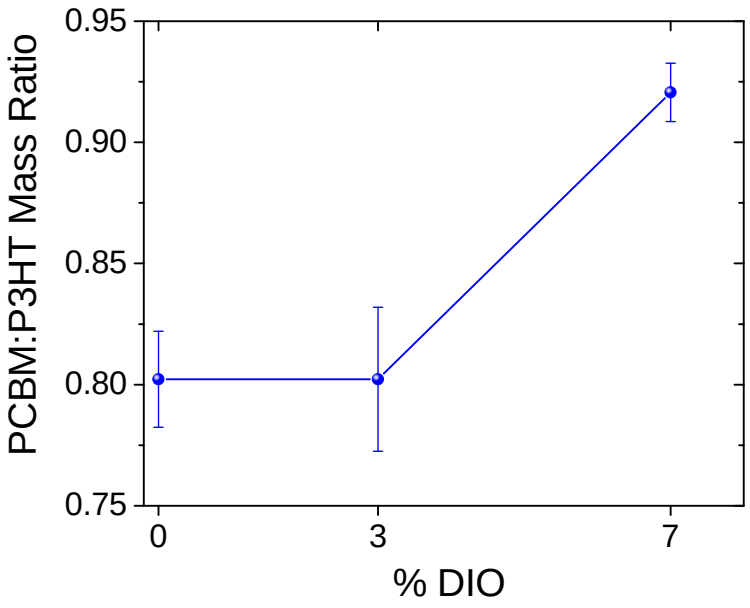

Figure A.3: Redissolved sequentially-processed P3HT(DIO):PCBM active layers. With higher % DIO (v/v), the PCBM:P3HT mass ratio increases. The error bars represent one standard deviation obtained from averaging over three films.

A.4 Optical and Structural Characterization

A.4.1 UV-Visible Spectroscopy Experiments and Analysis

UV-Visible absorption experiments were performed using a Lambda 25 UV-Vis spectrometer to collect absorption spectra.

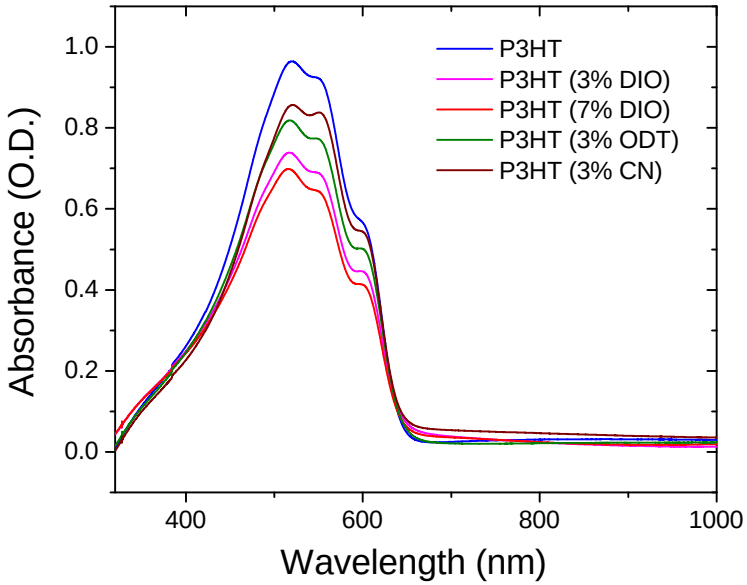

Figure A.4: UV-Vis for P3HT swollen with no co-solvent (blue), 3% DIO (purple), 7% DIO (red), 3% ODT (green), and 3% CN (maroon).

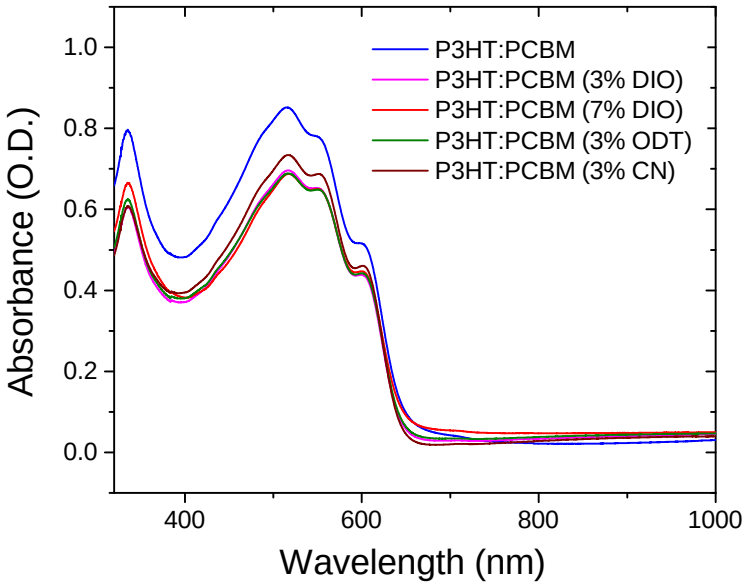

Figure A.5: UV-Vis for P3HT:PCBM active layers with no co-solvent (blue), 3% DIO (purple), 7% DIO (red), 3% ODT (green), and 3% CN (maroon).

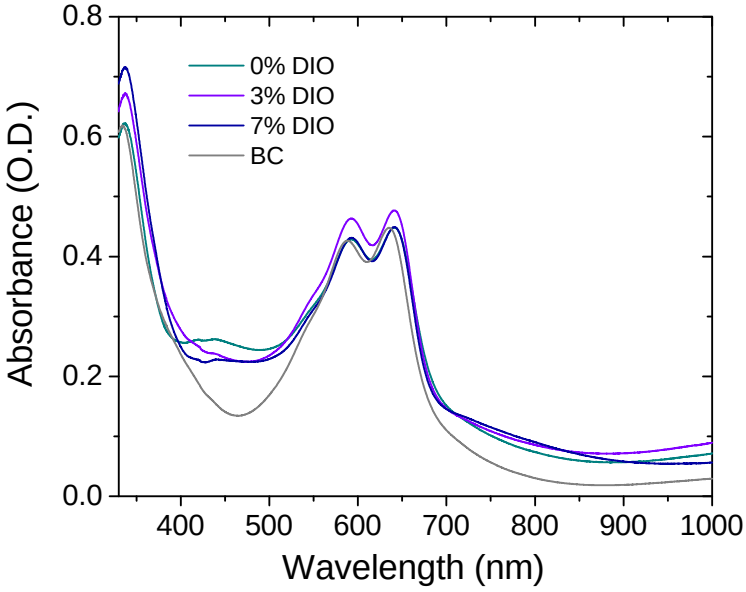

Figure A.6: UV-Vis for sequentially-processed PSEHTT:PCBM active layers with no co-solvent (dark cyan), 3% DIO (violet), 7% DIO (royal blue), and a blend-cast active layer (gray).

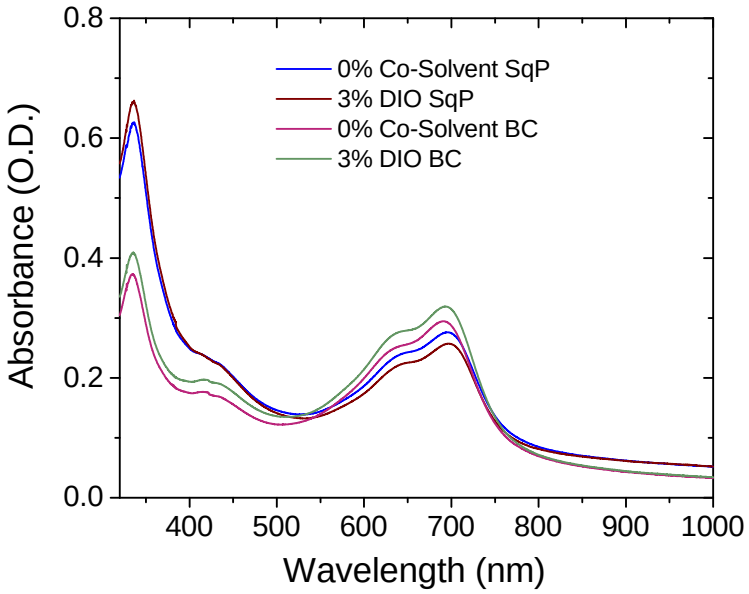

Figure A.7: UV-Vis for sequentially-processed PBDTTT-C:PCBM SqP active layers with no co-solvent (light green) and 3% DIO (dark green). UV-Vis for blend-cast PBDTTT-C:PCBM active layers with no co-solvent (light yellow) and 3% DIO (dark yellow).

A.4.2 Spectroscopic Ellipsometry Experiments and Analysis

For the swelling experiments, spectroscopic ellipsometry was used to measure the film thickness. Each film was placed in a home-built customized vial, which is designed to contain a solvent (e.g., toluene or DCM). The film thickness in the vial is monitored until it reaches steady-state while the P3HT film is exposed to the solvent vapor in the vial and subsequently swollen. The relative solvent vapor pressure in the vial can reach $p/p_0 = 0.90$, where p_0 is the solvent's vapor pressure at room temperature. To determine the relative solvent vapor pressure, we first carried out swelling experiments using toluene with the ellipsometric porosimeter. This provided a toluene swelling calibration curve, showing the change in film thickness as function of p/p_0. Then, we mapped the thickness change of P3HT film collected from the home-made vial onto the swelling calibration curve. To minimize the error, all the ellipsometric experiments were repeated at least three times and were collected immediately after film preparation. To ensure minimal co-solvent/solvent additive evaporated between film preparation and the measurement, all films were stored in sealed vials after spin-coating and were prepared less than one hour from the measurement time. In this way, the vial allowed us to perform swelling measurements with solvents such as DCM that were not compatible

with the porosimeter instrument.

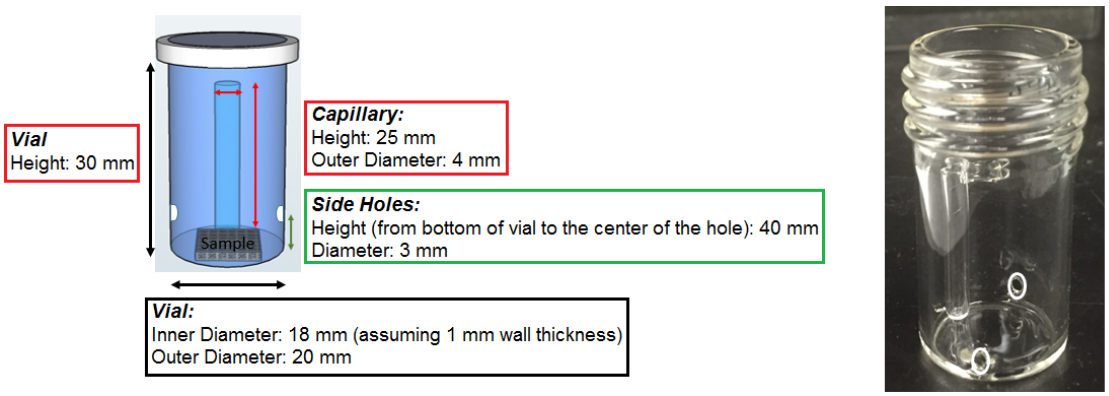

Figure A.8: Schematic and picture for home-built swelling vial.

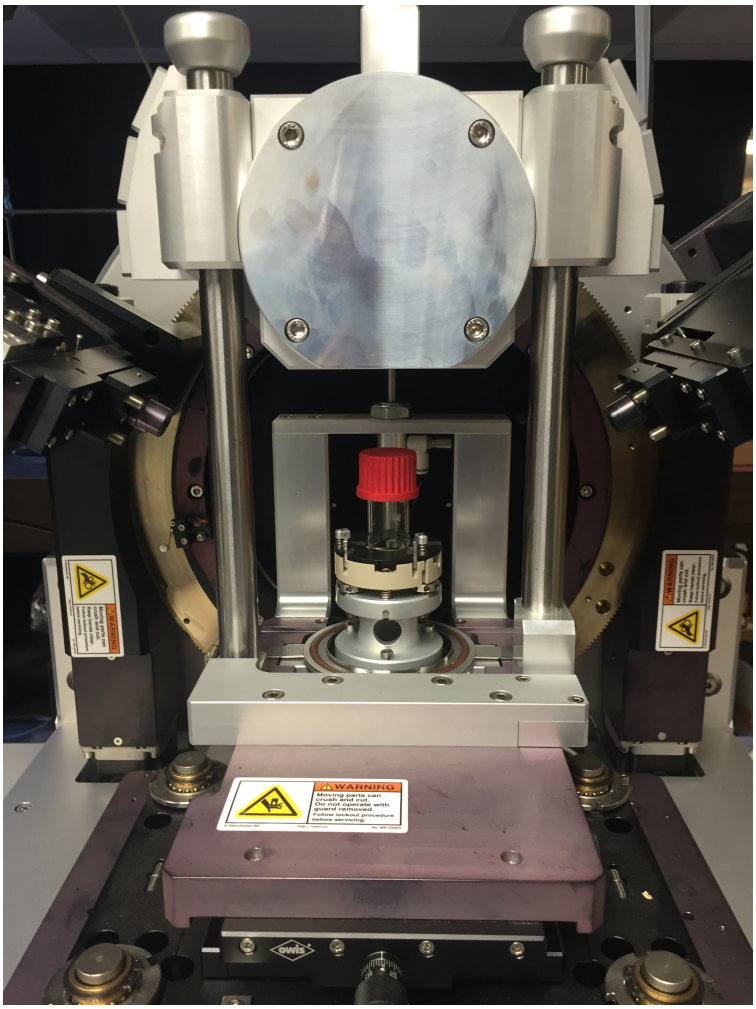

Figure A.9: Swelling vial in spectroscopic ellipsometer sample stage.

Film Condition	Average R^2
0% Co-Solvent	0.99
3% DIO	0.96
7% DIO	0.96
3% DIO MeOH	0.97
3% ODT	0.99

Table A.5: Ellipsometry fits for Figure A.1.

Film Condition	Average R^2	
	Before Toluene Uptake	After Toluene Uptake
0% Co-Solvent	0.99	0.97
3% DIO	0.90	0.97
7% DIO	0.95	0.98

Table A.6: Ellipsometry fits for Figure A.1(b).

A.4.3 Grazing Incidence Wide-Angle X-ray Scattering (GIWAXS) Experiments and Analysis

2-D GIWAXS experiments were performed at the Stanford Synchrotron Radiation Lightsource on beam line 11-3 using a wavelength of 0.9742 Å. A grazing incidence angle of 0.12° was used in combination with a Rayonix model MX225 X-ray CCD. The beam spot was approximately 150 μm and a helium chamber was used to reduce the noise. Each data curve shown corresponds to the radially integrated pattern of the data from the full 2-D diffractogram and is the average of at least three different samples prepared under the same conditions. The 2-D images were collected on a plate with the detector 250 mm away from the center of the measured sample. The software package WxDiff was used to analyze the GIWAXS data. To ensure minimal co-solvent evaporated between film preparation and the measurement, all films were stored in sealed vials after spin-coating and were prepared less than 24 hours prior to the measurement time.

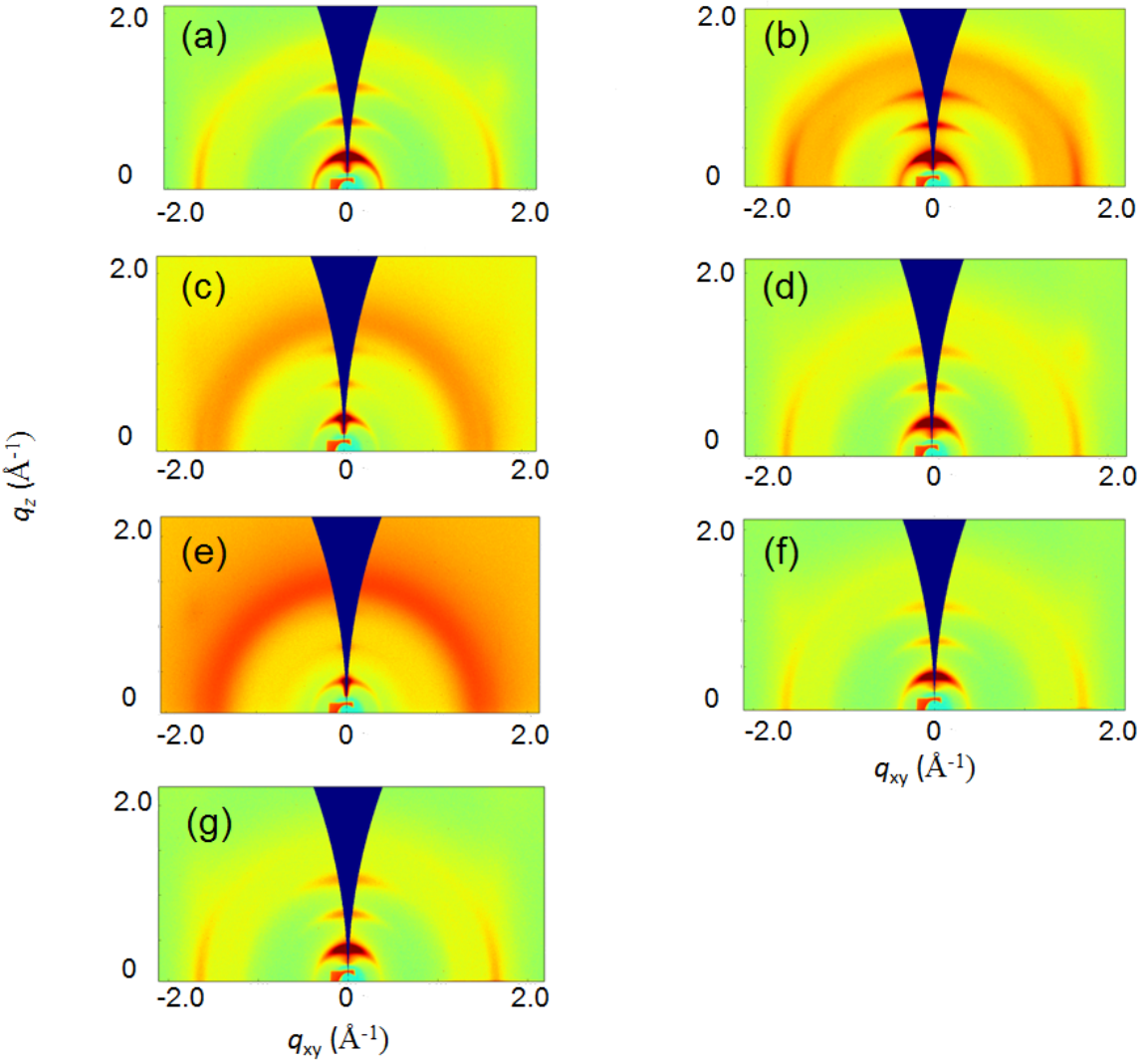

Figure A.10: 2-D GIWAXS diffractograms for P3HT films cast with and without solvent additives and with and without being subsequently washed with methanol. P3HT films cast with (a) 0% (v/v) additive, (c) 3% (v/v) DIO, (e) 7% (v/v) DIO, and (g) 3% (v/v) ODT. Methanol-washed films of P3HT cast with (b) 0% (v/v) additive, (d) 3% (v/v) DIO, and (f) 7% (v/v) DIO. The removed wedges take into account the grazing incidence geometry.

A.4.4 X-ray Photoelectron Spectroscopy (XPS) Experiments and Analysis

X-ray photoelectron spectroscopy (XPS) experiments were performed on Si/active layer films using a Kratos Axis Ultra DLD with a monochromatic K_α radiation source. We did not use PEDOT:PSS/Si substrates since PEDOT:PSS contains sulfur, which can alter the measured S/C ratios. A charge

neutralizer filament controlled charging of the sample. For the beam, a 20-eV-pass energy was used with a 0.05 eV step and scans were calibrated by shifting the C 1s peak to 284.8 eV. CasaXPS software integrated the peaks to find the respective peak areas in addition to determining atomic ratios. The Kratos library and Casa software provided the atomic sensitivity factors used.

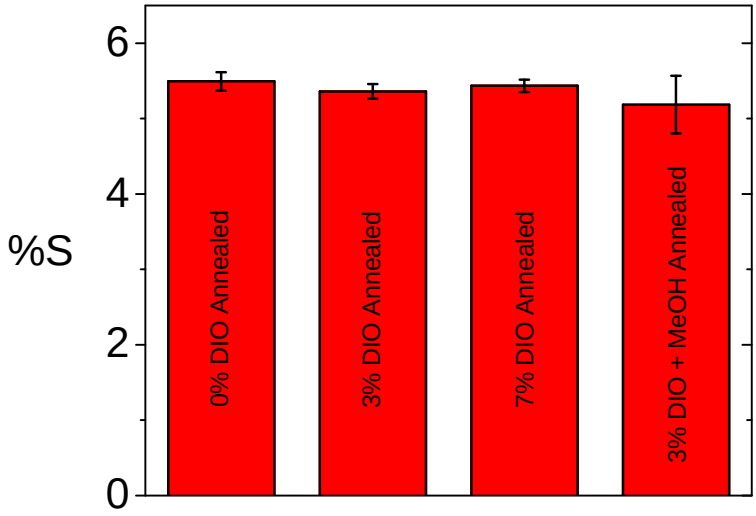

Figure A.11: Top-surface sulfur-to-carbon composition of sequentially-processed P3HT:PCBM BHJ films of 0% DIO annealed, 3% DIO annealed, 7% DIO annealed, and 3% DIO methanol washed with annealing, as measured by XPS. The error bars represent one standard deviation for the average of at least three films.

A.4.5 Neutron Reflectometry Experiments and Analysis

Neutron reflectometry (NR) experiments were performed at Oak Ridge National Laboratory using the Magnetism Reflectometer at the Spallation Neutron Source using a neutron wavelength of 4.41 Å and an effective q-range of 0.008-0.153 $Å^{-1}$ ($q = 4\pi/\lambda sin\theta$, where λ is the neutron wavelength and θ is the scattering angle). Motofit Software was used to determine the vertical distribution of the thin films by fitting the reflectivity.

The active layers measured were spin-coated onto PEDOT:PSS-coated Si substrates for the measurement. To obtain scattering length density (SLD) depth profiles, we calculated the reflectivity of a model SLD profile and iteratively refined the model until the calculated reflectivity profile matched the experimental reflectivity profile. Multiple layers comprise the model depth profiles of the samples, accounting for the 2-nm thermal oxide layer on the Si substrate, the PEDOT:PSS

hole-transport layer, and the active layer of interest. The SLD, thickness, and roughness of each layer are floating parameters in the fits. SLD values of pure P3HT and PCBM were obtained by fitting neutron reflectivity profiles of the pure components and were determined to be 4.4×10^{-6} Å^{-1} for PCBM and 0.6×10^{-6} Å^{-1} for P3HT, which agrees with literature values.[101,298,299]

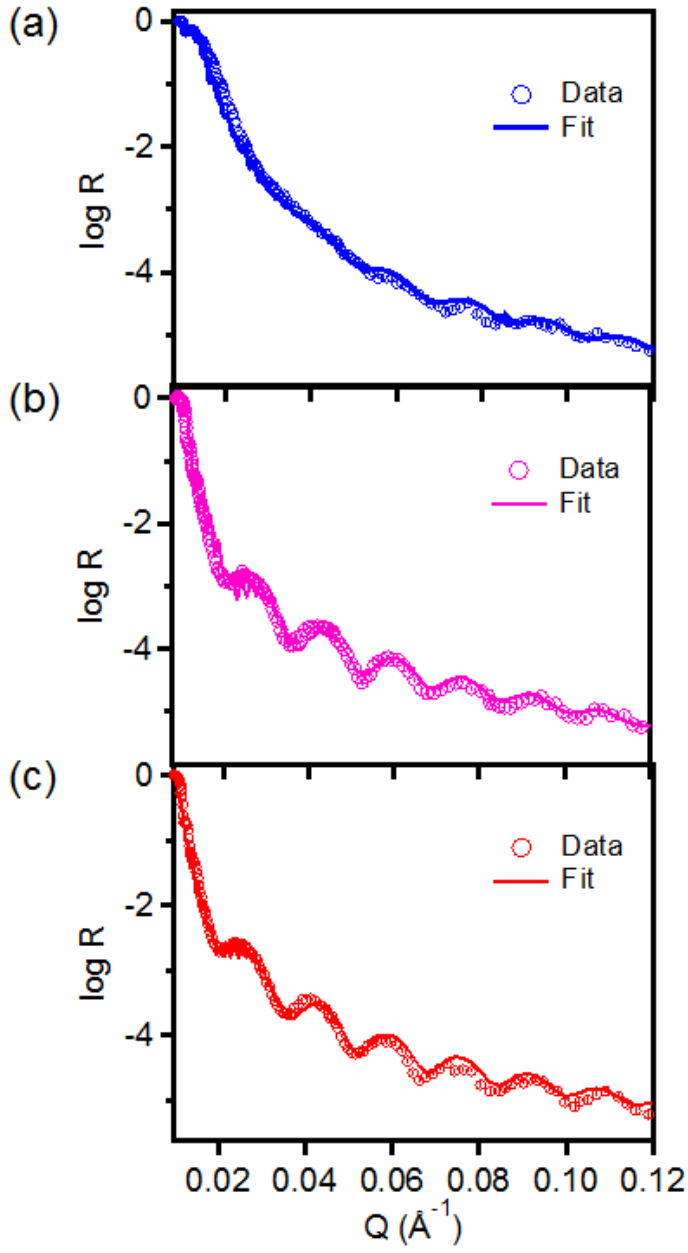

Figure A.12: Neutron reflectivity data for SqP P3HT:PCBM films on Si with (a) 0% DIO (blue), (b) 3% DIO (purple), and (c) 7% DIO (red). The solid lines are fits to the raw reflectivity data.

A.4.6 Photoluminescence (PL) Quenching Experiments

Steady-state PL measurements were collected with a FluoroMax-3 (J-Y Horiba) fluorimeter. All measurements were collected in air at 22.5° with respect to the excitation beam and the sample was positioned normal to the excitation axis. The selected excitation wavelength was 532 nm. For all measurements the slit widths and integrations were held constant. Additionally, the spectra were corrected for the wavelength dependence of the detector and monochromator responses.

The active-layer photoluminescence demonstrates that 3% (v/v) DIO modestly increases the PL quenching of P3HT. We note that the PCBM concentration in the active layer is not significantly increased with 3% (v/v) DIO, as shown in Figure A.3. Thus, neutron reflectometry shows that PCBM in the 3% (v/v) DIO film is better-mixed vertically throughout the device, so that the change in PL quenching results from morphology changes in the film, as discussed above. An appreciable increase in quenching is observed with 7% (v/v) DIO, which arises from more extensive swelling and increased fullerene intercalation. In contrast to the 7% (v/v) DIO result, P3HT films cast with 3% (v/v) CN as the solvent additive demonstrate reduced PL quenching. Since CN produces highly crystalline P3HT films due to its higher vapor pressure, the film swells less readily when PCBM is spin-cast from DCM. This limits the ability of DCM to swell the polymer film and intercalate PCBM.[2,102] As a result, we expect that PCBM is most likely to be concentrated on the top surface, which inhibits PL quenching. We note that the smallest PCBM peak is observed for P3HT 3% (v/v) CN:PCBM in the integrated 2-D GIWAXS for S11(d), which also indicates the difficulty of PCBM intercalation.

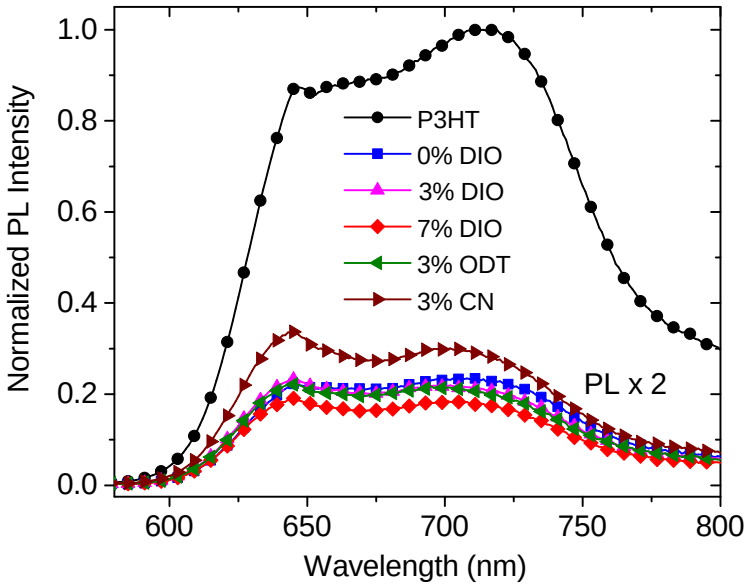

Figure A.13: PL quenching for pure P3HT (black circles) and P3HT:PCBM BHJs cast with 0% (v/v) DIO (blue squares), 3% (v/v) DIO (purple up triangles), 7% (v/v) DIO (red diamonds), 3% (v/v) ODT (green left triangles), and 3% (v/v) CN (maroon right triangles). BHJs cast with additives are multiplied by 2 for clarity. The PL measurements show additives do not significantly increase P3HT PL quenching.

A.5 Solvent Additives as Secondary Plasticizers

Overall, we now know that low-vapor-pressure solvent additives remain in polymer films and delay film solidification by swelling. Indeed, the fact that solvent additives delay polymer film solidification is consistent with recent *in situ* thickness measurements on doctor-bladed, blend-cast, BHJ films cast with solvent additives.[300,301] Thus, we propose that DIO and ODT act as plasticizers.[221,235,236,302,303] The degree of plasticization depends upon the plasticizer-polymer interaction strength: greater plasticizer-polymer interaction enhances plasticization.[221,235,236,302] Structurally, the degree of plasticization is achieved through polar regions on the plasticizer molecule that can interact with the polymer to promote swelling and non-polar regions that ensure good compatibility with the polymer: polar regions must reversibly bind to the polymer and therefore soften it, while non-polar regions reduce the overall plasticizer interaction and prevents the plasticizer from being too strong a solvator that dissolves the crystalline regions.[235,302] Thus, greater non-polar character reduces the overall plasticization effect. When plasticizers penetrate only the amorphous regions of

polymer films and do not dissolve or enter the crystalline regions, they are referred to as 'secondary plasticizers'.[221] Secondary plasticizers are also known for their low vapor pressures, interaction with polymers via swelling, and ability to be subsequently removed by rapidly-evaporating solvents.[221] Since DIO and ODT share the properties of secondary plasticizers, we propose that DIO and ODT act as secondary plasticizers: the polar end groups of DIO and ODT interact with P3HT to swell the amorphous regions (act as a softener) while the non-polar alkyl chain connecting the polar groups limits strong interactions with the crystalline regions. Since the polymer film was cast from a solution containing P3HT dissolved in a ODCB/DIO solution, the presence of DIO inhibits formation of P3HT crystallites, as verified by X-ray measurements. Therefore, DIO and ODT plasticize P3HT following the same action as small molecules plasticizing polyvinyl chloride (PVC).[235] The fact that solvent additives act as secondary plasticizers provides a mechanistic origin for why most solvent additives are selected for their low polymer solubility: the additives need to be good swelling agents, but cannot dissolve the polymer films.

A.6 Chloronaphthalene Experiments

CN, with its higher vapor pressure than DIO and ODT, does not remain in the polymer film after spin-coating. Since CN has a lower vapor pressure than ODCB, however, CN extends film solidification and produces highly crystalline films that inhibit PCBM intercalation. This results in P3HT films not being swollen with CN. Furthermore, the increased crystallinity results in poor swelling by DCM, which results in lower device performance as compared to devices made with DIO or ODT solvent additives.

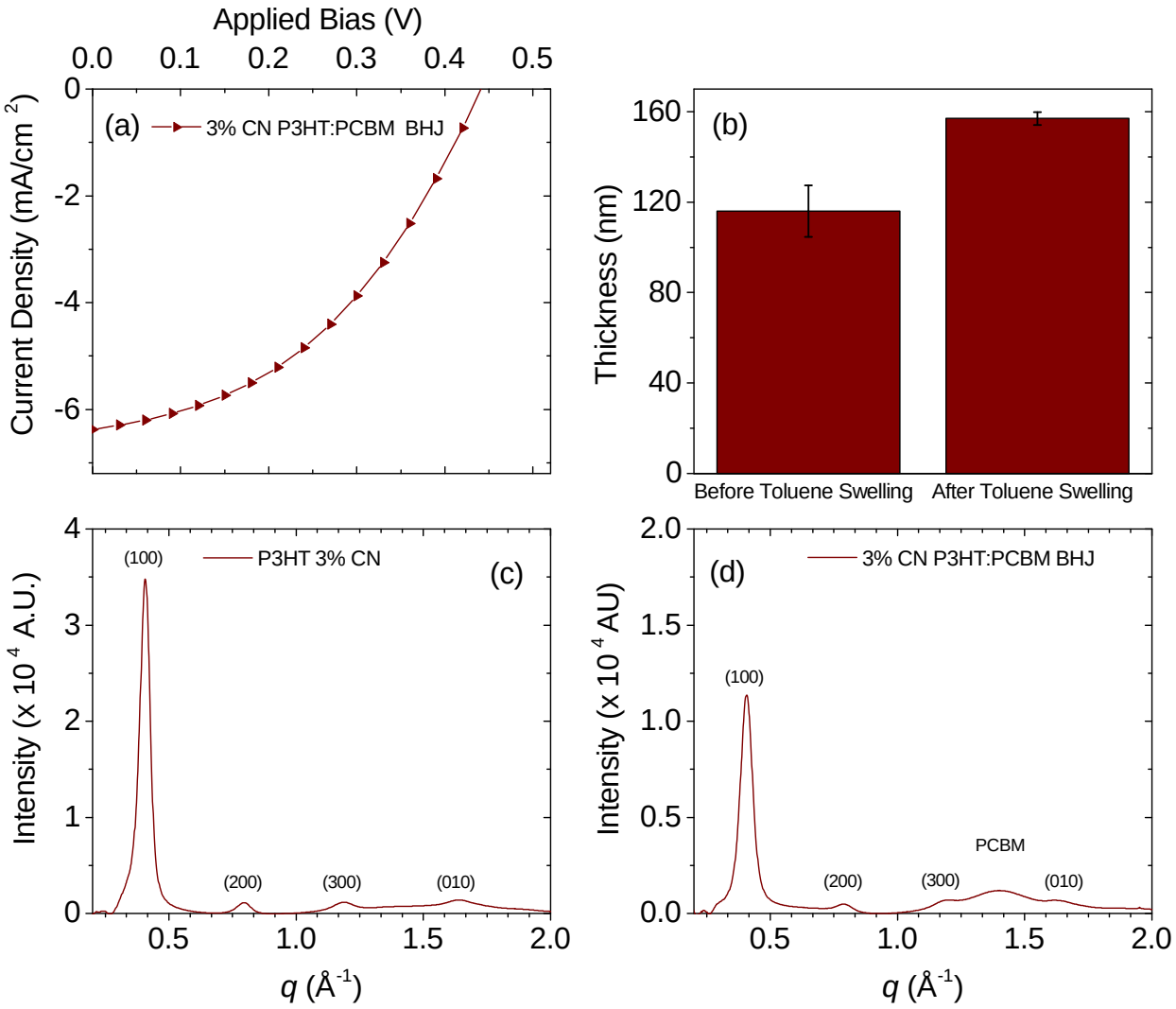

Figure A.14: CN (a) *J-V* data, (b) swelling data before and after toluene swelling, and 2-D GIWAXS data for (c) a 3% P3HT film, and (d) a 3% CN P3HT:PCBM BHJ. The lower device performance is explained by the lower swelling of CN films, which is attributed to the increased crystallinity prior to PCBM deposition.

APPENDIX B

Supporting Information for Chapter 4

B.1 Appendix B Information Preface

This appendix is organized in the same fashion as Chapter 4. We first discuss pertinent details regarding the synthesis and experimental methods, then steady-state spectroscopy and the spectral fits, then we present additional time-dependent density functional theory (TD-DFT) calculations, and lastly we delve into the details of the time-resolved experiments on our chosen PDI and di-PDI molecules in different solvents and cast into films. Most of this appendix presents raw data, particularly from our time-resolved experiments, however key details about calculations, fits, and other subtleties of analysis or interpretation are also included.

We note that the through-space angular dependence of the coupling has been studied previously for several PDI aggregate systems,[304,305] but not in a bay-linked system with through-bond coupling as for the di-PDI studied here. That said, there has been previous work examining our chosen di-PDI, including optical, time-resolved, nuclear magnetic resonance, and electrochemical spectra.[60,240,243,263] There have also been a number of recent publications using (TD-DFT) to calculate the orbitals of our chosen PDI monomer, bay-linked di-PDI molecule and other related PDI oligomers.[263,306,307] These previous studies form a strong foundation for the work presented in Chapter 4 and here.

B.2 Synthesis and Purification Details

Our bay-linked di-PDI molecule (2,9'-di(undecan-5-yl)-2',9-di(undecan-6-yl)-[5,5'-bianthra[2,1,9-def:6,5,10-d'e'f']diisoquinolin]-1,1',3,3',8,8',10,10'(2H,2'H,9H,9'H)-octaone) was synthesized

according to literature procedures (see Methods section). Column chromatography yielded several similar products (not characterized) necessitating several rounds of purification. The final product characterization consisted of ^{1}H and ^{13}C NMR and mass spectrometry (MS). The MS yielded a clean peak at 1394.788 m/Z, compared to the expected HRMS (DART) calculated 1394.80107 m/Z for $C_{92}H_{106}N_4O_8$ [$M^{\bullet+}$]. The NMR spectra of the final purified product are shown in Figures B.1 and B.2.

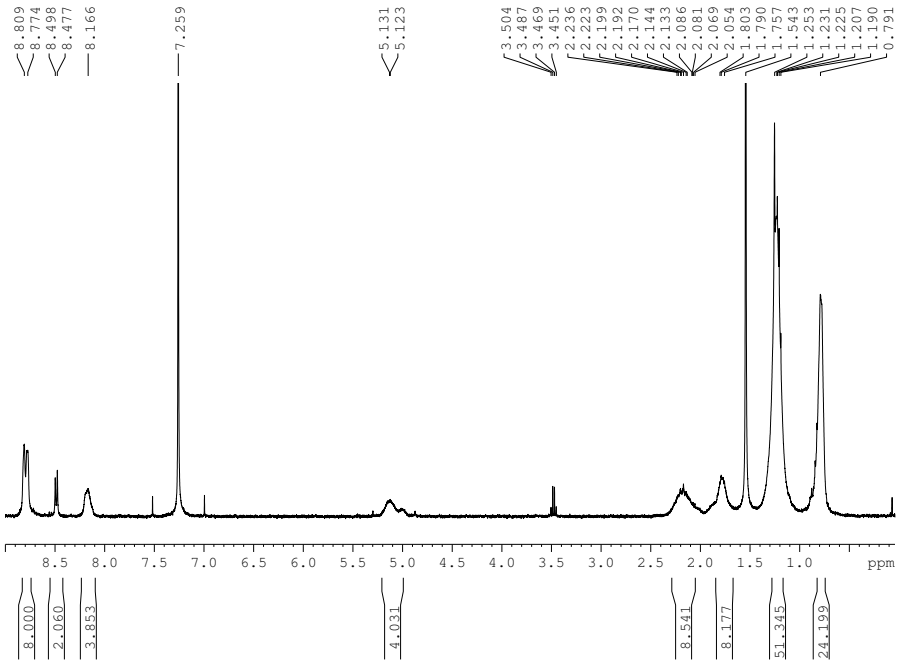

Figure B.1: Proton NMR spectrum of di-PDI after purification.

B.3 Vibronic Model for Fitting the Di-PDI Optical Spectroscopy

In our first attempt to fit the di-PDI absorption spectrum, we employed Gaussian vibronic progressions with the following functional form:

$$\sum_{0}^{n} \frac{e^{-\lambda^2}\lambda^{2n}}{n!} e^{\frac{1}{2}\frac{\omega-\omega_0-n\cdot s}{\sigma}} \tag{B.1}$$

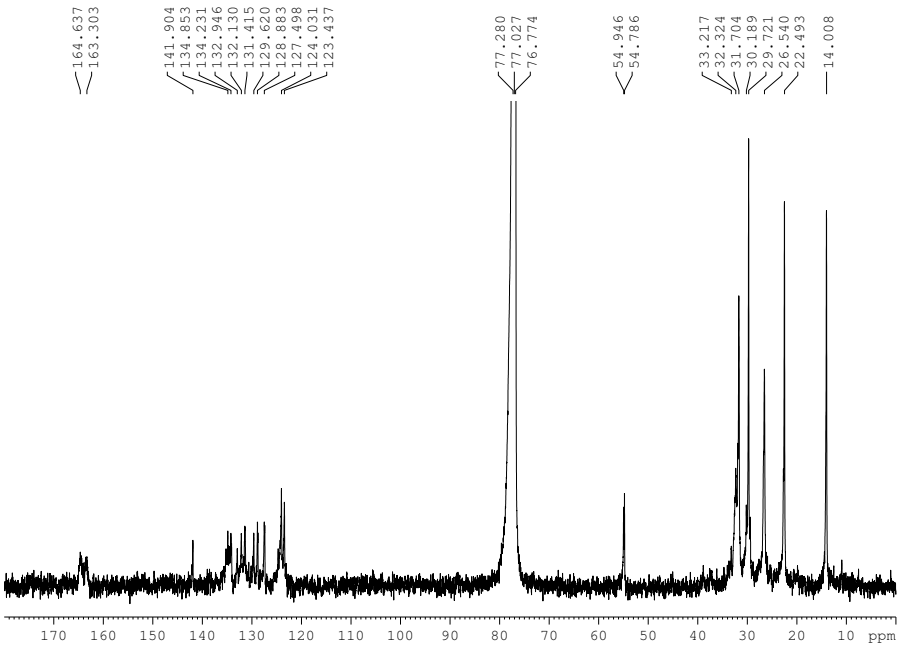

Figure B.2: Carbon-13 NMR spectrum of di-PDI after purification.

where λ is the Huang-Rhys parameter, n is the number of vibronic peaks, ω_0 is the center position of the 0–0 vibronic peak and s is the vibronic splitting. We found that at least two different vibronic progressions of the form of Equation (B.1) were required for a reasonable fit of the absorption profile down to 450 nm. Unfortunately, these fits were not robust, with many local minima, and thus were extremely sensitive to the chosen starting parameters. For this reason, we do not show these fit attempts. In fact, we found that even the previously-measured absorption spectrum at 77 K,[263] which was repeated by us as shown in Chapter 4, could be fit with a wide variety of parameters with a high degree of correlation. This makes it clear that the di-PDI absorption spectrum alone is far too convoluted to fit directly. Indeed, we show below in Figure B.10 that the theoretical absorption spectrum obtained from TD-DFT is complex enough that there is no obvious way to fit or deconvolve it in isolation. As discussed in Chapter 4 and further below, this situation arises from the wide distribution of different electronic states populated along the di-PDI ϕ coordinate.

B.4 Steady-State Spectroscopy Details

The first experimental evidence that convincingly showed multiple absorbing and emitting species was 2-D excitation-emission spectroscopy. We note that in the data presented in Figures B.3 and B.4, there are several very weak residual emission features that we attribute to impurities. One such feature is visible at excitation wavelengths of 490 and 520 nm, which produced an emission shoulder at 540 nm. This feature decreased in intensity upon repeated purification steps, concomitantly with a decrease in an extraneous feature in the nuclear magnetic resonance spectrum.

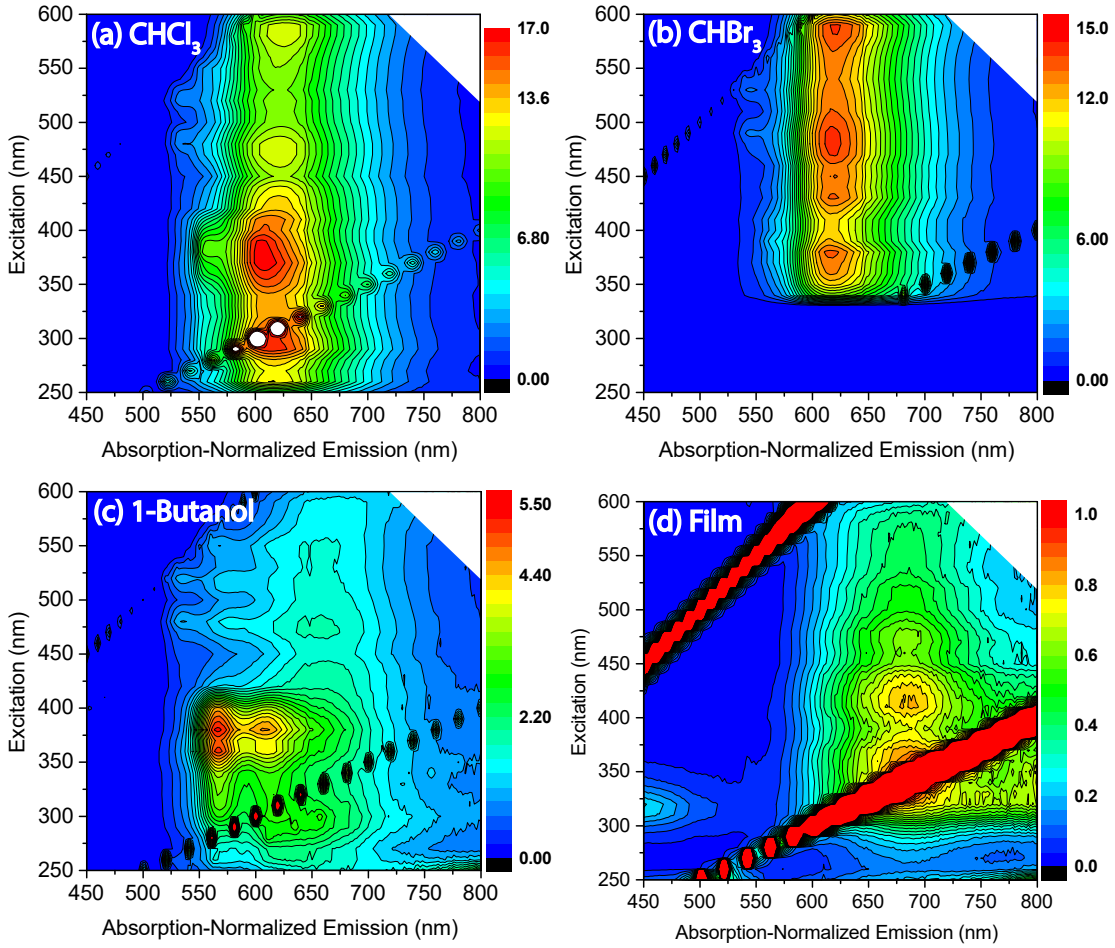

Figure B.3: Excitation-emission spectra collected for 2.13×10^{-6} M di-PDI in chloroform, bromoform, 1-butanol, and as a spin-cast film. All spectra are normalized by their respective absorption spectra at each excitation wavelength. Excitation wavelengths were taken in 10 nm intervals from 250 nm to 600 nm. The two linearly-tracking progressions are the first- and second-order excitation scatter and should be ignored. For the di-PDI in bromoform, the solvent absorbs heavily below 330 nm so we have not shown data in this region. The absolute emission intensities from di-PDI in the different solutions are directly comparable, but the film intensities have been arbitrarily normalized.

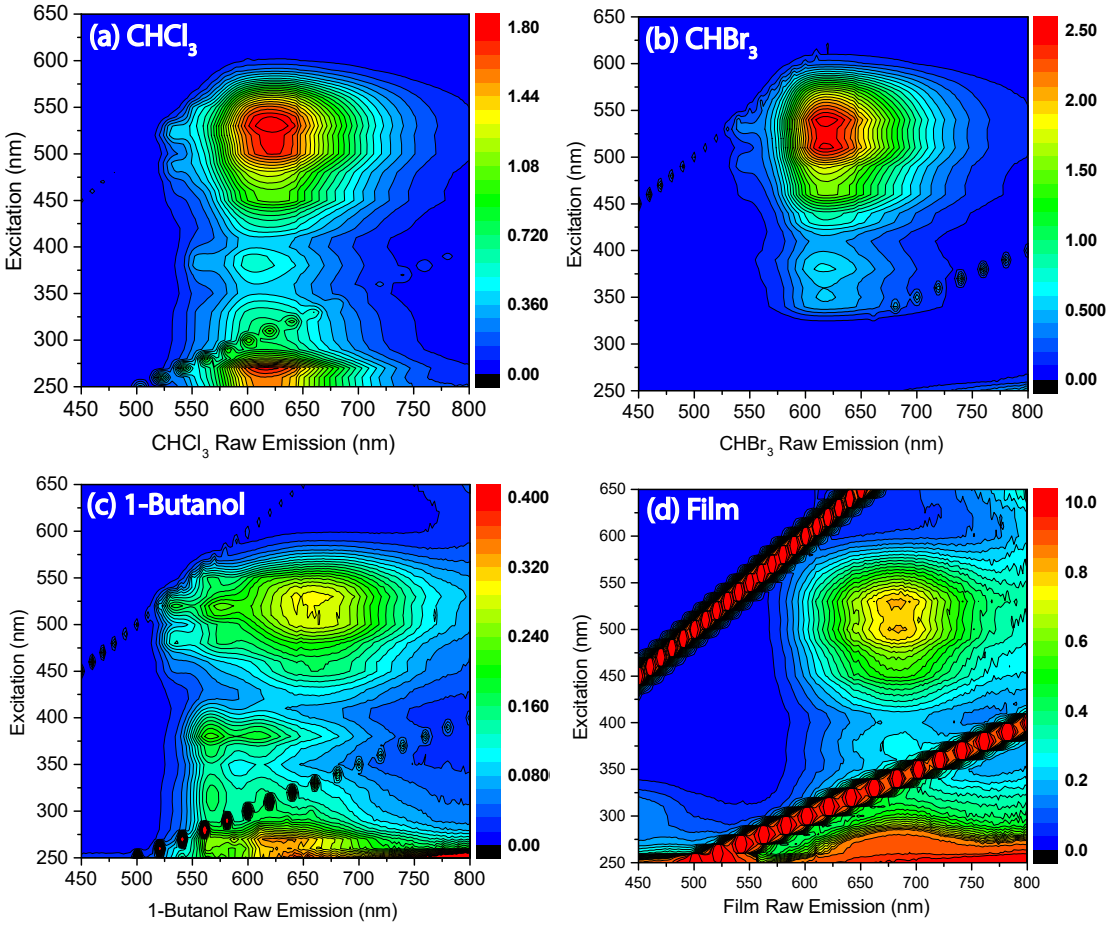

Figure B.4: Raw EES for 2.13×10^{-6} M di-PDI in chloroform, bromoform, 1-butanol, and as a spin-coated film. Data from bromoform below 325 nm excitation artificially weakened due to competing absorption of the solvent or impurities. Note that for the film, the final contour colors between orange and red no longer have linear spacings: between orange and red there is roughly a factor of 10 increase in the per-contour scaling. This is because the di-PDI emission when exciting in the UV is very strong, perhaps because direct excitations to delocalized states become available.

Figures B.3 and B.4 quantitatively compares di-PDI photophysics in the three solvent environments and in spin-cast films. Qualitatively, in bromoform the narrow-band emission from the open conformer is somewhat noisy due to its much lower yield compared to that in chloroform or 1-butanol. For di-PDI in 1-butanol, with its higher dielectric and viscosity, we see several interesting trends: the closed geometry emission is even broader and red-shifted by an additional 50 nm with respect to that in chloroform and bromoform. In contrast, the narrow emission feature from the open conformer remains relatively unchanged, save for a small 5-nm red-shift. This is in line with our expectations that the solvent dielectric will more sensitively affect the strongly-coupled

closed di-PDI geometry than the more monomer-like open geometry. The unchanged narrow feature is consistent with excited-state optimization in our TD-DFT calculations, discussed in Chapter 4 and further below, which suggest that there is only a small Stokes shift for the occupied first excited state in the open conformation. (Unfortunately, the excited-state optimization for the closed geometry did not converge, but the vertical transition while the ground state is occupied suggests this conformation would relax by having ϕ decrease to $<50^{\circ}$). Finally, Figure B.4 also shows that the film scatters significantly more, producing larger first and second order scattering peak progressions in the raw data. The di-PDI emission in the film has the largest effective Stokes shift, red-shifted by an extra 50 nm compared to solutions, presumably due the ease of exciton migration to the lowest available emitting states.

From the excitation-emission spectra, non-negative matrix factorization provided rough profiles for the two underlying spectral components. However, this analysis yielded significant bleeding between spectral components. We found that the simplest procedure yielding the cleanest spectral components was simply adjacent subtraction. First, we isolated the broad emission feature from 580-nm excitation, which is cleanly resolved, and then scaled and subtracted this from spectra collected where the narrow feature was present. The data make clear that in all three solution environments, besides small shifts in position, Huang-Rhys factors, and broadening, the molecule emits with the same two emission components. In the film, other than a high-energy feature associated with UV excitation, we see only the broad emission feature. The narrow emission feature due to the open conformation is lost due to energy transfer because of the proximity of neighboring di-PDI molecules in the film, as discussed in Chapter 4.

B.4.1 Temperature-Dependent Spectroscopy

In Chapter 4, we used the temperature dependence of the di-PDI emission spectrum in 2-Me-THF and ODCB to determine the energy gap between the open and closed di-PDI ground-state conformations. We were not able to perform this estimate in $CHCl_3$ due to its low boiling point, which prevented us from heating the solutions. We also note that the narrow absorption feature, which corresponds to the open conformation, only weakly absorbs, making it difficult to estimate the molar extinction based on the reconstructed absorption profiles weighted by the determined quantum yields. However, the absorption cross-section of the closed conformer absorption, which leads to the broad emission in Figure 4.3 of the main chapter, was found to have a maximum of roughly 70,000 $M^{-1}cm^{-1}$ at 535 nm, similar to reported values elsewhere.[308] With this cross-section, we estimate an integrated oscillator strength for di-PDI that is approximately twice that of the monomer. Thus, we can roughly estimate the molar extinction coefficient of the narrow feature from the open conformer by assuming its oscillator strength should also be roughly twice that of the monomer. Using this assumed oscillator strength in conjunction with the measured fluorescence yield of both emitting features, we calculated an energy gap between the two conformers of about 5 $k_B T$ in chloroform—in excellent agreement with the experimental results in ODCB and the TD-DFT calculations presented in Chapter 4. This large gap explains why the open conformer/narrow spectral feature had gone previously unnoticed in solvents such as chloroform.

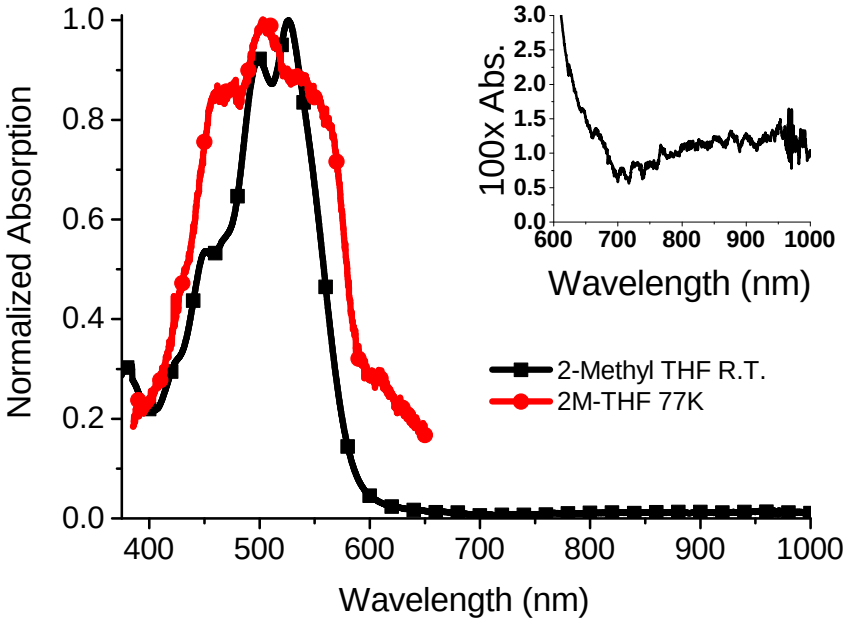

Figure B.5: The absorption spectrum of di-PDI in 2-methyl-tetrahydrofuran at room temperature (black squares) and at 77 K (red circles).

Figure B.5 compares the absorption spectrum of di-PDI in 2-methyl-THF taken at both room temperature (black squares, curve) and at 77 K (red circles, curve). The overall shape of the absorption spectrum we see at cryogenic temperatures is consistent with that reported in the literature, although we note that a higher-resolution spectrum of di-PDI in glassy 2-methyl-tetrahydrofuran is available in the literature.[263] The major difference in the glass at 77 K is the intense broadening of the main absorption feature and the large red tail. We are not entirely sure of the origin of the red absorption tail at cryogenic temperatures. One possibility is that the di-PDI molecules tend to aggregate in the cryogenic matrix. Another possibility is that a wider variety of di-PDI dihedral angles (<60°, >110°) are trapped in the frozen matrix.

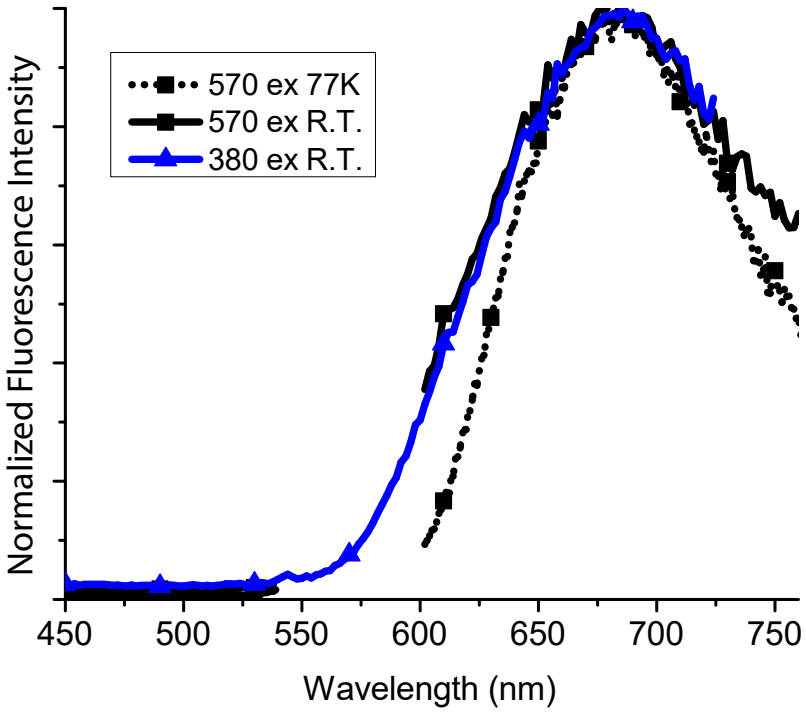

Figure B.6: Temperature dependence of the emission from a spin-cast di-PDI film.

Fluorescence spectra were collected for films of di-PDI as a function of temperature, similar to what is shown in Chapter 4 for the di-PDI in solution. The di-PDI film emission spectrum excited at 570 nm at 77 K is as shown as the black dotted curve in Figure B.6. The major finding is that for films, the fluorescence spectrum narrows. This could arise from a number of effects, including as slower exciton hopping at lower temperatures and/or a narrower range of dihedral angles (ϕ) thermally populated within the film.

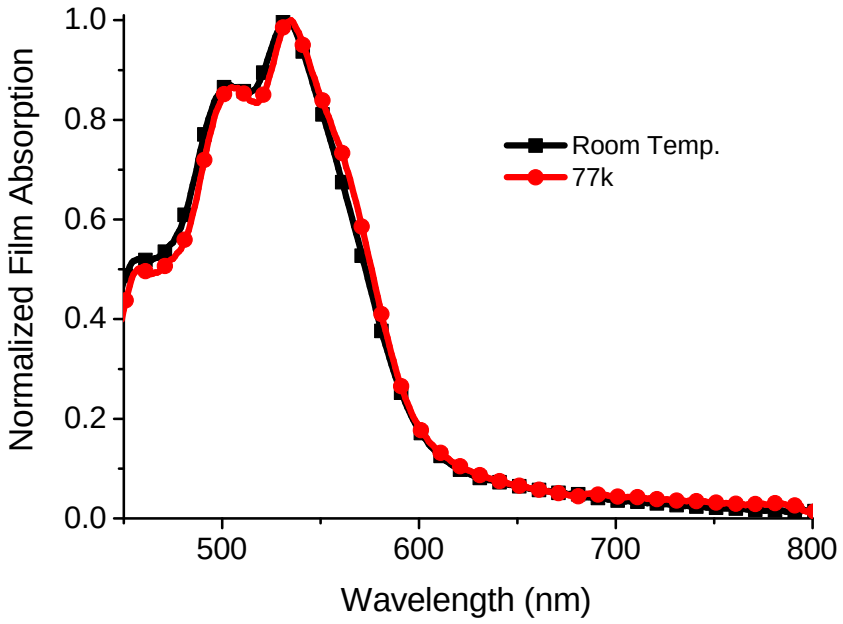

Figure B.7: Normalized absorption spectra of a spin-coated film of di-PDI at room temperature (black squares) and 77 K (red circles) in a vacuum cryostat.

Although the emission spectrum of di-PDI in spin-cast films has a strongly temperature-dependent spectral width, as shown above, Figure B.7 shows that the di-PDI film absorption spectrum remains virtually unchanged with temperature. This bolsters our suggestion that thermal motions along the dihedral ϕ coordinate are responsible for controlling relaxation and transport dynamics within the film.

B.5 Global Fitting Details

In this section, we discuss the details of how we arrived at the global fit of the closed and open conformation spectra discussed in Chapter 4. The functional form which best fit our global data sets, shown in Figure 4.8 of the main chapter, is a vibronic progression of Gaussian widths shown in Equation (B.1). We found that at least three independent components were required to fit the spectra of the isolated closed (broad) and open (narrow) conformations; this means that we used a sum of 6 transitions (each with form Equation (B.1)) to globally fit the data. The parameters providing the best fit are listed in Table B.1.

Table B.1: Global Fitting Parameters for di-PDI Open and Closed Geometry Electronic Transitions

Parameter	"Closed"	"Open"
$s_{1=2=3}$ (eV)	0.162	0.155
I_1 (normalized)	1*	1*
I_2	1.45	1.11
I_3	0.61	0.58
I_{ESA}	-0.55	—
$\omega_{0,\,1}$ (eV)	2.18	2.27
$\omega_{0,\,2}$ (eV)	2.28	2.35
$\omega_{0,\,3}$ (eV)	2.57	2.61
$\omega_{0,\,ESA}$ (eV)	2.61	—
λ_1	1.18	0.68
λ_2	1.00	0.66
λ_3	1.28	—
σ_1 (eV)	0.036	0.026
σ_2 (eV)	0.046	0.040
σ_3 (eV)	0.041	0.055
σ_{ESA} (eV)	0.081	—

The scalar intensities *I* of each of Gaussian vibronic progression, which included the sum of 5 Gaussians, were normalized for both the open and closed geometries relative to the lowest energy component, as noted by the asterisks in Table B.1. The relative intensities of each component of the two conformers change drastically depending on the choice of solvent, excitation frequency

and temperature, as discussed in Chapter 4. To reduce the number of fitting parameters, we held the spacings of the respective components of the open and closed geometry components fixed. We believe that this is a physically reasonable assumption given that electronic transitions are likely to couple to similar vibrations; without this assumption the fits lost much of their robustness.

When globally fitting the data, we did not include a progression for the stimulated emission of the narrow (open geometry) component, which would have also contributed the overall intensity of the maximum bleach feature to red of 535 nm (for the 400-nm pump TA data). With this omission, we found that the results were robust and did not sensitively depend on the chosen starting conditions for the fit. We also found that an ESA component was required to fit the transient absorption signals to blue of 500 nm regardless of excitation frequency, suggesting that this contribution likely originates from the closed di-DPI conformation.

B.6 Theoretical Details: Going Beyond Simple Molecular Aggregation

B.6.1 Failure of the Standard Aggregation Picture

One of the important conclusions of this chapter is that one cannot use standard aggregation theories to explain the spectroscopy of the di-PDI molecule from the spectra of the PDI monomer. The standard picture of molecular aggregates was developed by Kasha and coworkers[245,246] under the point-dipole approximation, leading to expressions for the coupling between interacting monomers, with the two most commonly cited results being the H- and J-aggregate geometries.[65] The vector addition of the transition dipole moments (TDMs) and their effects on the molecular aggregate spectroscopy are shown in Figure 4.1 of the main chapter.

The simplest description of Coulombic interaction for two adjacent molecules with transition dipoles μ_1 and μ_2 at some intermolecular separation R_{12} is given by:

$$V = \frac{\boldsymbol{\mu}_1 \cdot \boldsymbol{\mu}_2}{4\pi\varepsilon_0 n^2 R_{12}^3} - \frac{3(\boldsymbol{\mu}_1 \cdot \boldsymbol{R}_{12})(\boldsymbol{\mu}_2 \cdot \boldsymbol{R}_{12})}{4\pi\varepsilon_0 n^2 R_{12}^5}. \tag{B.2}$$

The solutions to the Schrödinger equation for this potential are then:

$$\Psi^{\pm} = \frac{1}{\sqrt{2}}(|\phi_1^*\phi_2\rangle \pm |\phi_1\phi_2^*\rangle) \; ; \; E^{\pm} = E_0 \pm V, \tag{B.3}$$

with

$$E^{\pm} = E_0 \pm V. \tag{B.4}$$

For the general cases of TDM arrangements leading to H-aggregation, the TDM vectors of the lower-energy configuration obey $\mu_1 = -\mu_2$, leading to:

$$M^{\pm} = \int \Psi^{\pm *}(\mu_1 \pm \mu_2)\Psi_g d\boldsymbol{r}, \tag{B.5}$$

where it becomes clear that the allowed transition carries twice the oscillator strength of an isolated monomer.[309] However, this description fails when the interchromophore distance becomes comparable to the delocalization length scale.[65] One may instead use the extended dipole approximation, or as we did here, calculate the Coulombic interaction using Mulliken transition charges.[260]

We performed this calculation by estimating the interacting transition densities using atomic charges calculated according to Mulliken population analysis for the monomer wave function held at the twisted nuclear coordinate of the di-PDI in each geometry. We computed the transition density of the PDI monomers using the same level of theory used for di-PDI. The Coulombic coupling for a given dimer geometry was then determined by:

$$J = \sum_{i,j}^{N} \frac{q_i q_j}{|\mathbf{r}_{Ai} - \mathbf{r}_{Bj}|}, \tag{B.6}$$

where i, j run over all the atoms on separate monomer subunits in the dimer geometry; q_i, q_j are the computed transition atomic charges on the i^{th} and j^{th} atoms, respectively; $\mathbf{r}_{Ai}$ is the position of i^{th} atom on chromophore A and $\mathbf{r}_{Bj}$ is the position of the j^{th} atom on chromophore B. In other words, J sums up the pair interactions of atomic transition charges of two monomer-like PDI branches in a di-PDI molecule.

With this formalism, we find the Coulomb couplings to be $\sim$100 meV and $\sim$25 meV for the 50° and 110° di-PDI conformations (we also see that if we had used the point dipole approximation,

we would obtain significantly smaller estimated couplings). The larger splitting for the closed conformer at 50° is due to the favorable pi-stacking configuration

Even though Coulomb coupling is insufficient to explain the electronic structure of di-PDI, as discussed in Chapter 4, the expected forms of coupling for this molecule can be qualitatively predicted. We would expect the Coulomb coupling to be minimized when the two monomers are at the magic angle condition (main chapter Figure 4.1(b)) and the through-bond coupling to be minimized at 90° where the overlap of the π MOs is poorest. Our TD-DFT calculations are indeed roughly consistent with these ideas, with the 90° di-PDI geometry clearly having the weakest coupling and the strongest coupling occurring for geometries with ϕ<70° where the through-space π-stacking is maximal.

We note that in condensed phases with relatively high dielectric constants, the stabilizing effect of the environment often supports low-energy charge transfer (CT) states. Such CT states tend to carry very little oscillator strength, and their presence is usually indicated by red-shifted, broadened, and strongly quenched fluorescence. This type of CT intermolecular aggregation has been thought to be present in our di-PDI,[65,263,310–314] but we find no concrete evidence for it: there is no significant change in the lower-energy emission of di-PDI in solutions with dielectric constants ranging from 4.3 (bromoform) to 17.8 (1-butanol). Instead, the generally low quantum yield of the broad emission from the closed conformation is due to the inherently poor oscillator strength of the lowest excited state in this geometry. Although we do see a lifetime and quantum yield decrease in higher dielectric environments, we believe that this is due more to changes in the preference for the closed and open conformers than the presence of a spectroscopically important CT state.

B.6.2 Full Electronic Structure via TD-DFT

Some of the general spectroscopic manifestations basic Coulombic coupling[64,65,249] do carry over to the di-PDI studied here, but a full description of the electronic structure requires detailed quantum chemistry calculations. The di-PDI studied here is challenging from a theoretical standpoint: it is a large molecule that contains many delocalized electrons that are sensitive to exchange. Thus, the TD-DFT results presented in Chapter 4 and detailed here provide only rough guidelines to

understand the conformational and electronic structure of di-PDI. Figure 4.5 of the main chapter shows the calculated ground-state potential energy surface of di-PDI in vacuum and in PCM dielectric of 4.81, calculated with the PBE0 functional and Grimme's D3 dispersion correction at fixed dihedral angles between 30°–140°). Note as also mentioned in Chapter 4 that our definition of dihedral results in a reflected ϕ axis with respect to previous studies.[60,243,254–258] To the best of our knowledge, our calculations are the first to include the dispersion corrections necessary for describing the π-interactions present for closed geometries when ϕ<90°. When dispersion corrections are included, the ground-state molecule prefers to maximize this π-interaction, as shown in Figure 4.5 of the Chapter 4. In contrast, previous studies[61,240,243,263,308,315,316] that do not use this correction suggest that the open conformation would be energetically preferred, contrary to what we observe spectroscopically.

The lower part of Figure B.8 shows isosurface plots of the TD-DFT-calculated charge density of the di-PDI HOMO in the open and closed conformations, with the geometries shown in the upper part of the figure for reference, providing a rough idea of the individual chromophore interactions. The closed geometry has a fair amount of slip-stacked π-π interactions between monomer subunits due to significant distortion of the perylene backbone. In the open geometry, the two monomeric subunits still interact, but primarily through (and around) the β–β connecting bond.

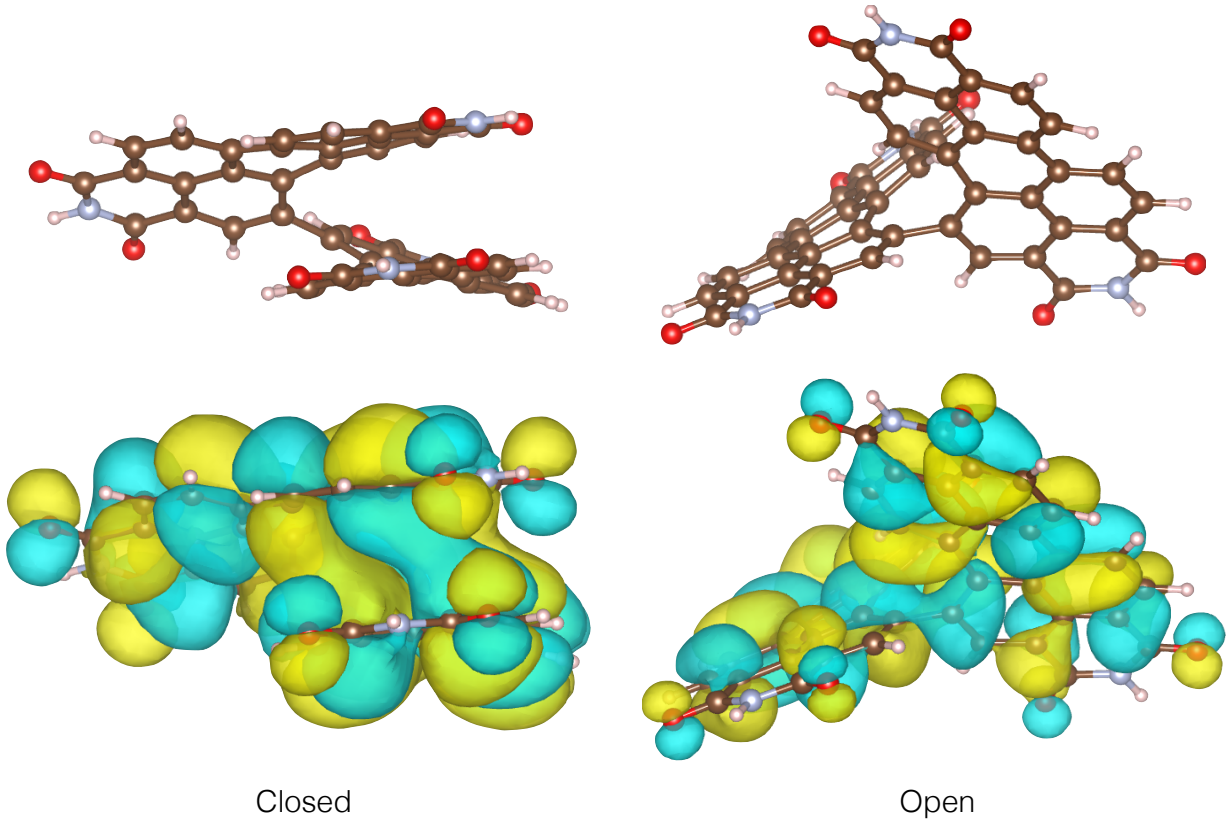

Figure B.8: The nuclear geometries (upper) and isosurfaces of the HOMO wave function (lower) of the di-PDI closed (left) and open (right) conformations.

Figure B.9 shows the oscillator strengths of the four lowest-energy electronic transitions from te ground state as determined from our TD-DFT calculations. The oscillator strengths show several notable features. The fact that both geometries behave electronically roughly as with H aggregation is clear from the lower oscillator strengths of the first two excited states, while the transition to the fourth excited state retains the largest oscillator strength. For the open geometry, however, there is a more balanced character to the oscillator strengths, with the lowest transition becoming quite strongly allowed. Though the energies of transitions to excited states three and four cross as shown in the Chapter 4, the oscillator strengths remain continuous. The predicted Coulombic coupling described above is unable to explain these angle-dependent features of the excited state energies or oscillator strengths.

As shown in Chapter 4, our di-PDI of interest is known to have a twisted geometry of the PDI subunits, and for the closed geometry there appears to be an unphysical amount of twist

and puckering in order to maximize the π-stacking. This is likely artificially bringing down the energy of the ground and excited states for this 50° case. Qualitatively speaking, if these two effects are corrected in the expected direction, the resulting spectrum would be more similar to experiment: with weak transitions around 600 nm and the majority of oscillator strength around 530 nm. However no immediate features from alternative molecular geometries are discernible from either the predicted or experimental absorption spectra alone.

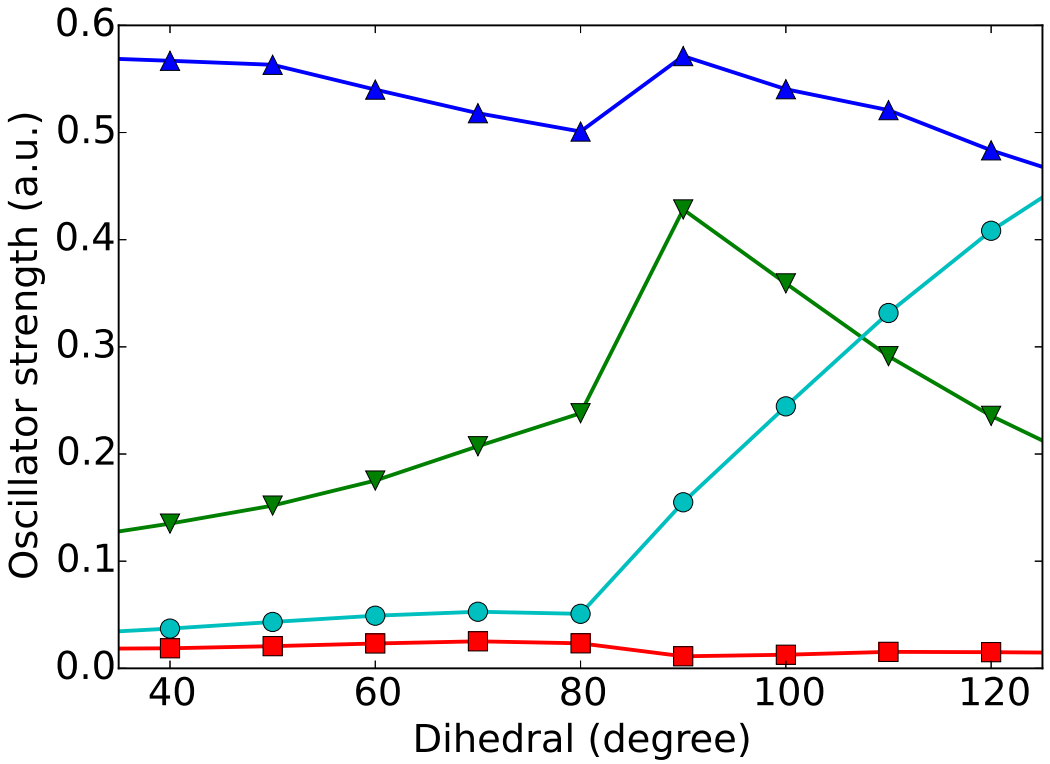

Figure B.9: Oscillator strengths for the vertical transitions from the ground state for the range of dihedral angles ϕ explored in Chapter 4 for the first (teal circles), second (red squares), third (green inverted triangles), and fourth (blue upright triangles) excited states of di-PDI as a function of ϕ.

With the transition energies, oscillator strengths and the ground-state potential energy surface (PES) from our TD-DFT calculations, we are able to estimate the steady-state absorption spectrum, which is shown in Figure B.10. The predicted spectrum leads to two main conclusions: (1) the bulk of the absorption profile is centered near 510 nm, which has only a small energy discrepancy from the experimentally-observed absorption profile peaking near 540 nm, and (2) there are small

absorption contributions at calculated wavelengths to the red of 600 nm, perhaps corresponding to the experimentally-observed weak absorption feature near 580 nm in experiment.

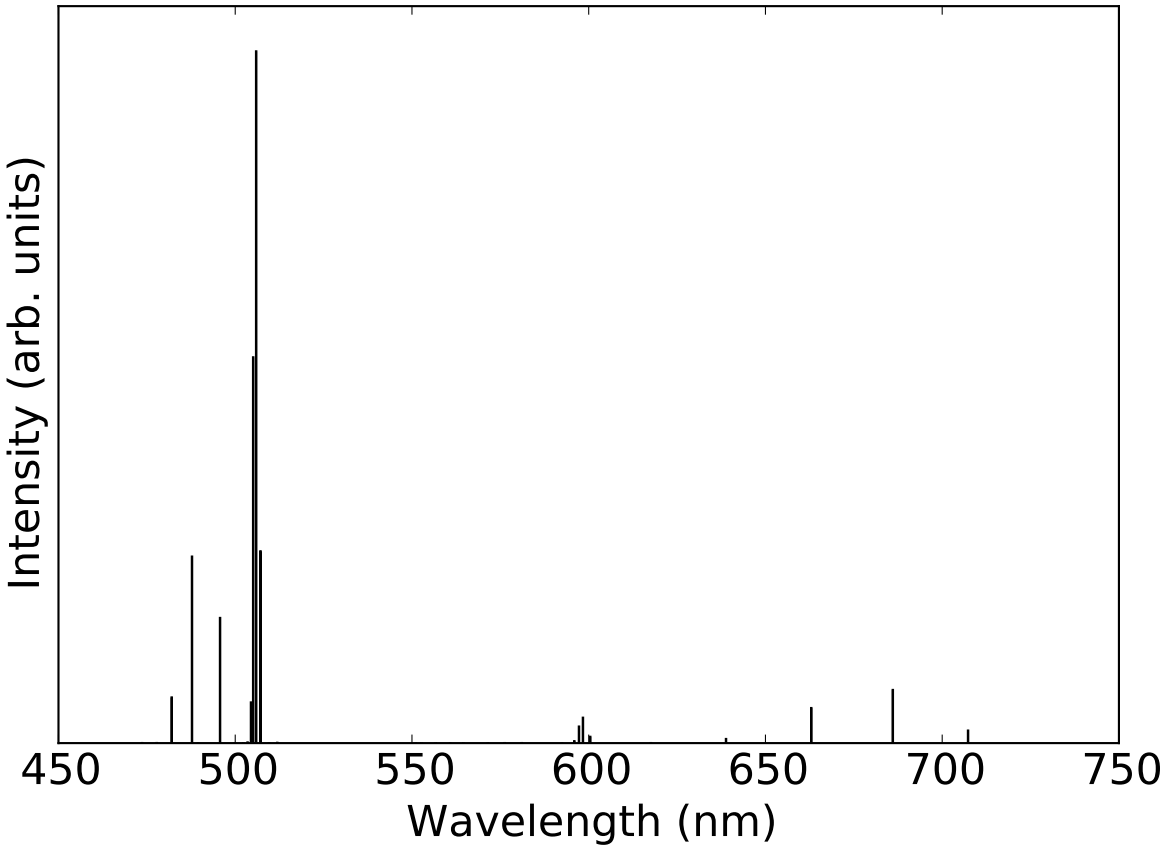

Figure B.10: Absorption spectrum of di-PDI calculated from TD-DFT with a PCM dielectric of 4.81, mimicking chloroform. Each dihedral conformation contributes four electronic transitions within the visible range in fixed steps of $\phi \pm 10^{\circ}$. The intensities are derived from the oscillator strengths weighted by Boltzmann coefficients derived from each dihedral conformation's energy in the ground state.

To better understand how the electronic structure of di-PDI arises, Figure B.11 compares the TD-DFT calculated one-electron orbitals for a lone radical monomer (i.e., half of the di-PDI with the connecting bond broken and one electron assigned to each monomer), di-PDI one-electron MOs, and the full multiconfigurational states of di-PDI. There is reasonable agreement between the radical monomer and the dimer one-electron orbitals, further solidifying the idea that di-PDI's electronic structure cannot be explained as two interacting closed-shell monomers. Thus, by linking the PDI monomers through the bay position, the di-PDI molecule behaves more like two mixed

radicals than like two separate molecules being held in proximity. Further confounding this is the importance of correlation and exchange in mixing of these one-electron orbitals. It is this fact that perhaps best explains why the simple Kasha picture does not hold for this molecule and why the underlying spectroscopy, even for a single dihedral configuration, is so complex.

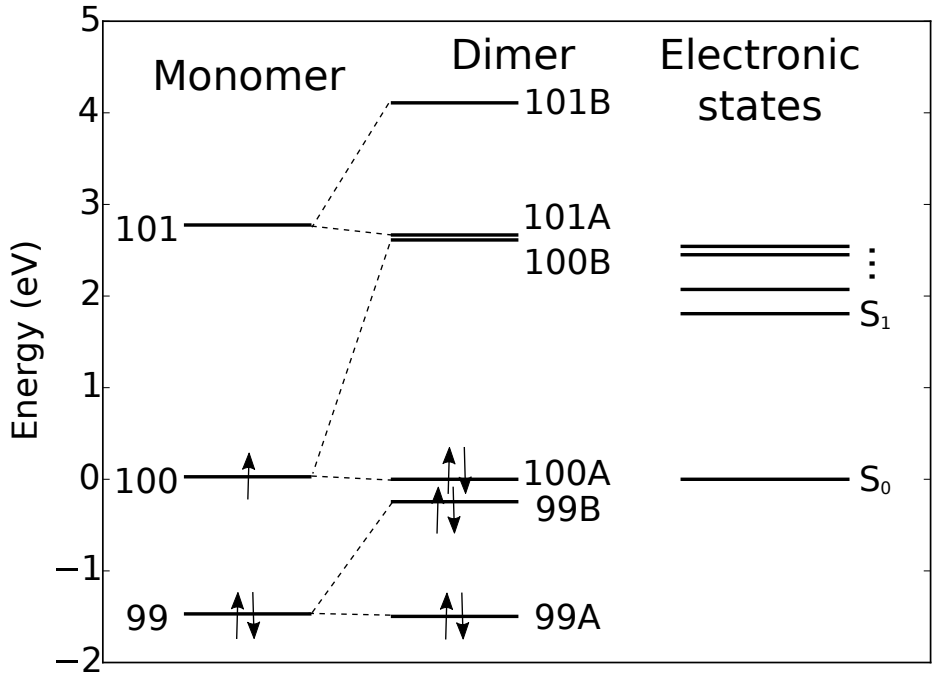

Figure B.11: The TD-DFT determined MO electronic energy levels of a radical monomer PDI (i.e. half of the di-PDI molecule), di-PDI one-electron MOs and di-PDI mixed electronic states are plotted on the same energy axis. The monomer has an unpaired electron since the dimer is covalently bonded and splitting the bond would results in a radical forming on each half. Note the MOs of the monomers combine to give MOs with different symmetries (labeled A and B).

B.7 Time-Resolved Spectroscopy Details

One common method used to study intermolecular coupling and aggregation is to use polarization-dependent spectroscopies on crystals of π-conjugated molecules, where the molecules have macroscopic orientation and ordering.[239,305] However, our di-PDI of interest was explicitly created for its inability to form large ordered domains.[51,56,58,254,317] Thus, although we have performed femtosecond transient absorption (fsTA) spectroscopy, including polarized spectroscopy, the results we obtain are not as detailed as those which have been applied to a variety of other PDI systems.[61,310,311,314,318–342] Here, we detail the fitting procedures used to analyze the data presented in Chapter 4 as well as discuss the polarization-dependent spectroscopy experiments on di-PDI that we performed.

B.7.1 Excited-State Kinetic Fit

For all the fsTA data on di-PDI that we collected, we fit the data in the time domain to a sum of three exponentials, whose lifetimes were given in Table 4.2 of the Chapter 4. The corresponding amplitudes of the fit are given below in Table B.2. We reiterate that this fit was performed primarily to characterize the data, with no particular kinetic model implied.

Table B.2: Amplitudes of the time-domain fitting parameters to transient absorption spectroscopy on di-PDI (Figure 4.7) at two excitation wavelengths (580 nm and 400 nm) and in several solvent environments. Amplitude a_1 corresponds to the longest component of the tri-exponential fit (1.5–3.9 ns across all solvents).

Environment	a_1	a_{shift}	a_{fast}
$CHCl_{3,\ 580\ ex}$	1	0.3	0.22
$CHBr_{3,\ 580\ ex}$	1	0.29	0.1
$1\text{-}BuOH_{580\ ex}$	1	0.17	0.11
$Film_{580\ ex}$	0.85	0.53	1
$CHCl_{3,\ 400\ ex}$	1	.3	-
$CHBr_{3,\ 400\ ex}$	0.68	1	-
$1\text{-}BuOH_{400\ ex}$	1	.19	0.05

B.7.2 Details of Obtaining the Lifetime of the "Open" Geometry

From Figure 4.7 in the Chapter 4, it is clear that the ground-state bleach spectral shape hardly changes with time, even when exciting at 400 nm, which produces the maximal fraction of exciting the narrow-absorption feature open di-PDI conformer. We found from the bleach recovery that the lifetimes of the closed and open di-PDI geometries are similar; here, we provide additional details of how the 2.5-ns lifetime of the open conformer was extracted from the data. First, we attempted to fit the 400-nm excitation fsTA data with a bi-exponential at times longer than 400 ps in an attempt to separate the lifetimes of the two conformers. We fixed one component to 3.9 ns, which is the lifetime of the closed conformer measured directly from exciting di-PDI at 580 nm, but found that the other lifetime at 400-nm excitation could freely vary anywhere between 1.5 ns and 10 ns within error. This indicates that our fsTA data alone is technically unable to distinguish the lifetimes of the two di-PDI conformer. The 2.5-ns lifetime we quote for the open conformer in Chapter 4 was the best-fit time from this procedure. We know, however, that the overall lifetime (when fit to a single exponential) is shorter when a higher fraction of the open conformer is excited (3.2 ns) than when the closed conformer is excited (3.9 ns), consistent with our assignment of a shorter lifetime ($\sim$2.5 ns) for the open di-PDI geometry compared to the closed geometry.

B.7.3 Femtosecond Excited-State Dynamics and Spectral Assignments

As mentioned in Chapter 4, we see a short-lived ($\sim$12 ps) excess bleach feature near 550 nm in the fsTA of di-PDI in chloroform following 580-nm excitation. This feature could be attributed to multiple processes: stimulated emission (which would then be related to the Kerr-gated fluorescence spectrum through a factor of ω^3), inhomogeneous broadening in which 580-nm excitation excites only a preferential sub-population of di-PDI that also absorbs at 550 nm, or the presence of an excited-state absorption that quickly shifts into place and masks what would otherwise be a permanent bleach at that wavelength. However, we saw in Figure 4.7(b) in Chapter 4 that 400-nm excitation does not produce this excess bleach feature. This suggests the excess bleach must originate from a combination of either stimulated emission and/or inhomogeneous broadening with the 12-ps timescale in chloroform.

We believe that the 12-ps fsTA feature we see for di-PDI in chloroform could be similar for both conformations: the time scale is likely due to torsional dynamics on the ϕ coordinate and/or solvation dynamics, and either of these would be similar for both conformers. One hypothesis consistent with both this idea and the similar excited-state lifetimes is that both are directly tied to the timescale of di-PDI sampling the barrier between conformers: we expected the ground and excited states may better nonadiabatically couple near $\phi = 90^\circ$, as has been seen previously in photoisomerization of stilbene.[343] This would explain why we do not see signs of the two conformations interconverting in our experiments: because of high nonadiabatic coupling or a conical intersection near 90°, relaxation may take place before interconversion, imposing an upper limit on the lifetime regardless of which side of the barrier (i.e., which conformer) is initially excited. The slightly shorter lifetime of the open conformer (which has a higher-energy excitation) would be consistent with sampling the barrier faster.

B.7.4 Femtosecond Pump-Probe Anisotropy

Although all the fsTA experiments in Chapter 4 were reported with the pump and probe polarizations set to the magic angle ($54.7^{c}irc$), we also performed similar experiments using parallel and perpendicular pump-probe polarizations. We then used this polarized fsTA to calculate the time-resolved anisotropy according to:

$$r = \frac{I_{\parallel} - I_{\perp}}{I_{\parallel} + 2I_{\perp}}, \tag{B.7}$$

which can take values from -0.2 to +0.4 (assuming a degeneracy of 1 and absorption or bleaching of only a single state).[7] The measured transient anisotropy data for di-PDI excited at 580 nm in chloroform is shown in Figure B.12. We also verified that when adding the parallel plus twice the perpendicular polarized transient spectra, we recovered what we measured directly at the magic angle condition within error.

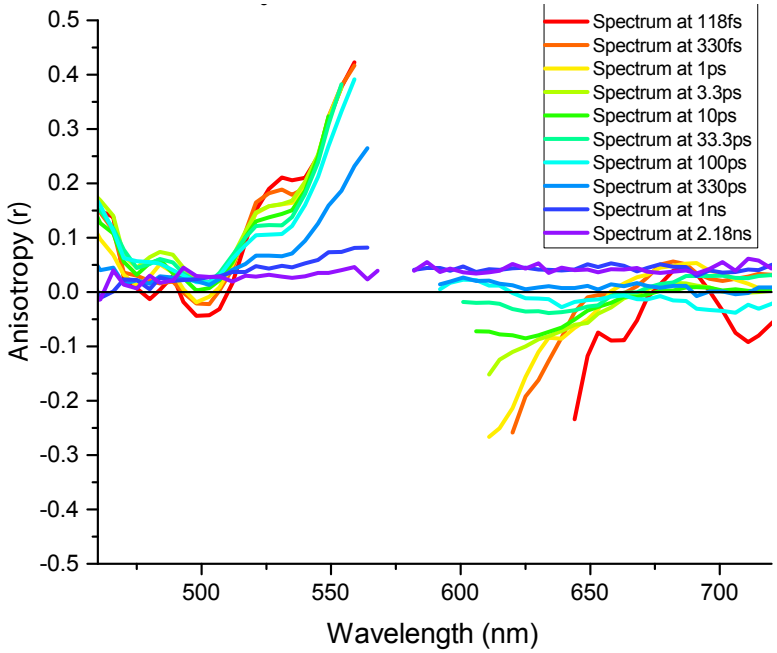

Figure B.12: Ultrafast anisotropy of di-PDI in chloroform following excitation at 580 nm. The gap in the data is where the net TA crosses zero, leading to a divergent anisotropy.

Even though the 580-nm pump wavelength excites only the closed PDI conformer, the data in Figure B.12 shows clearly that the early-time anisotropy is not 0.4, as is the case with the

corresponding PDI monomer, shown below in Figure B.17. To understand the observed di-PDI anisotropy, we used the transition dipole orientations and strengths from our TD-DFT calculations to predict the expected anisotropy as a function of ϕ using a recent formalism;[7] the predicted anisotropy is shown in Figure B.13. We assume that the lowest excited state is is populated, and find that the predicted anisotropy agrees qualitatively well with the experimental values in Figure B.12. In particular, the prediction captures the general trend of the experimental anisotropies with values generally between -0.1 and 0.2, with an anisotropy of nearly 0.4 around 560 nm, which trails lower towards the blue part of the spectrum where more components overlap. We note that our anisotropy prediction, however, is not quantitative as our TD-DFT calculations do not provide detailed information about the absorption amplitudes or vibronic progressions overlapping in the blue part of the spectrum.

We also note that the although most of the initial di-PDI anisotropies in the bleach part of the spectrum are small there is the large anisotropy near 580 nm, which we believe consists of strongly polarized stimulated emission from the pre-relaxed Franck-Condon region. This anisotropy decays mono-exponentially with a lifetime slower than the PDI monomer by a factor of 2.5 (as summarized in Table 4.3). This slower reorientation is reasonable considering the increased bulkiness of di-PDI relative to the monomer, resulting in slower rotational diffusion.

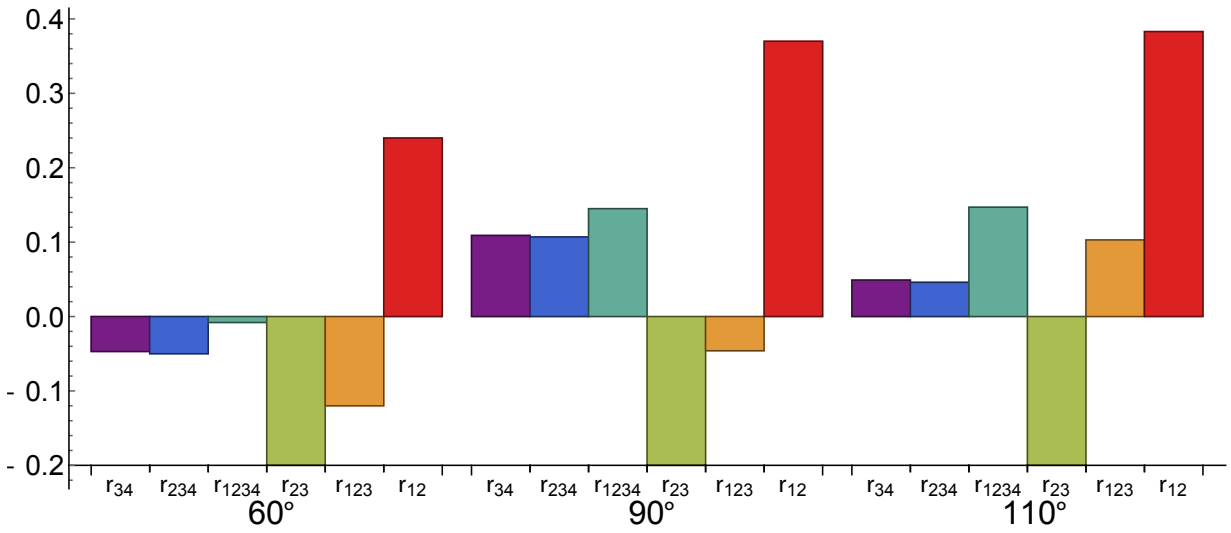

Figure B.13: Predicted di-PDI transient anisotropy using oscillator strengths and transition dipole orientations from our TD-DFT calculations, including overlapping transitions. These values were calculated using the full pump-probe orientational integrals[7] assuming that only the lowest energy state with appreciable oscillator strength was excited. The right-most red bar for each value of ϕ is the predicted anisotropy from the two lowest excited states (r_{12}), the next bar to the left of this includes the two previous states and the third highest state (r_{123}), and so forth.

Kerr-gated fluorescence spectra of di-PDI were also collected as a function of polarization but due to the limited time-resolution and maximum delay adds very little to the anisotropy obtained from transient absorption. The anisotropy for the emission appears to be roughly constant across the emission envelope (570–700 nm) with a small positive value of $\sim$0.2 for the first 5 ps, which then decays to between 0 and 0.1 by 1 ns. This is consistent with the fsTA anisotropy.

B.7.5 Raw fsTA Data of Di-PDI in Various Environments

Additional femtosecond spectroscopic data for both di-PDI and the corresponding PDI monomer (referred to here as m-PDI) are shown in the subsections below, organized by their environment.

B.7.5.1 Chloroform

The fsTA, Kerr-gated fluorescence, and anisotropy for both 400 and 580-nm excitation are shown for both m- and di-PDI in chloroform in Figures B.14 to B.19.

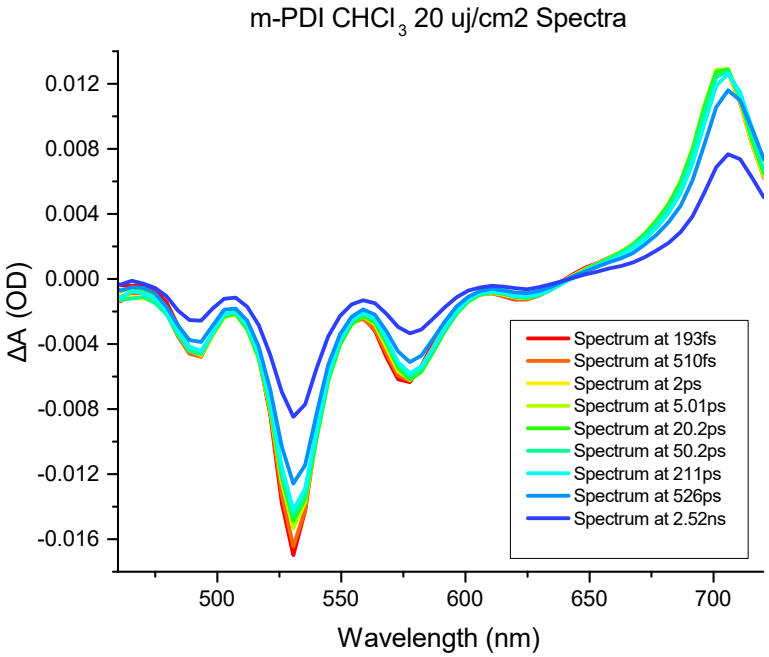

Figure B.14: Raw fsTA of m-PDI in chloroform. We show this data here for the purpose of comparison to the di-PDI data. The monomeric PDI in chloroform exhibits a single lifetime of roughly 3 ns with minimal shifting of the spectral components, as evidenced by the isosbestic point around 630 nm that persists for all measured times.

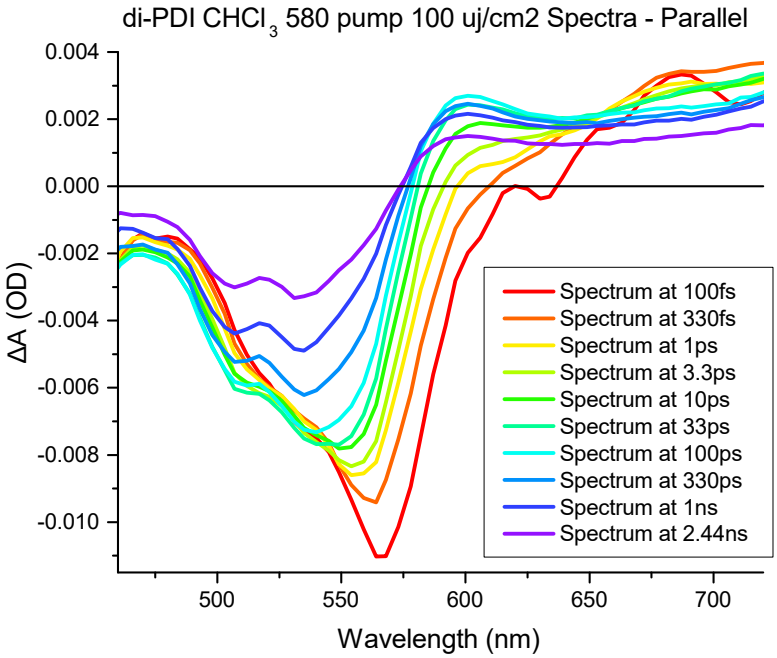

Figure B.15: Selected fsTA spectra of di-PDI in chloroform after excitation at 580 nm with parallel pump-probe polarizations. The excess bleach near the pump wavelength is due either to stimulated emission or spectral hole-burning.

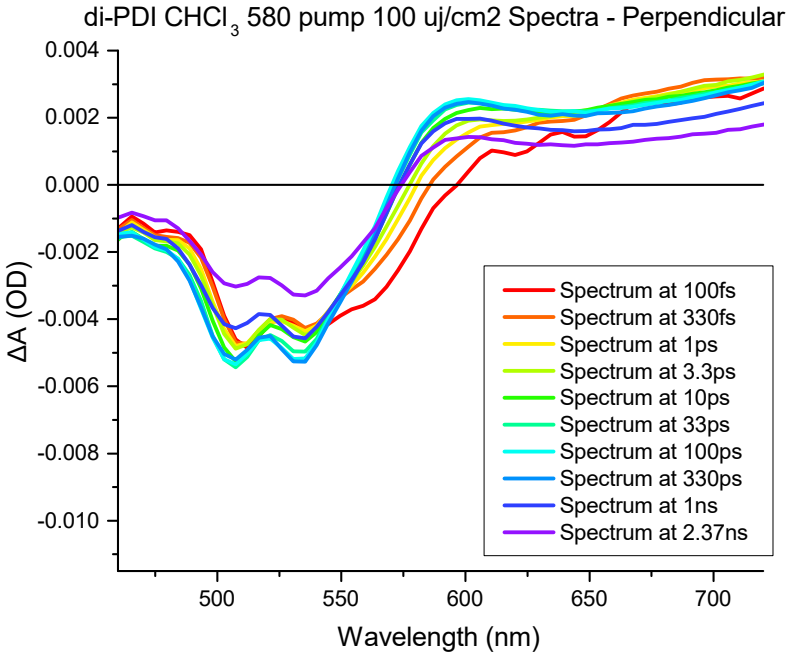

Figure B.16: Selected fsTA spectra of di-PDI in chloroform after 580-nm excitation with perpendicular pump-probe polarizations.

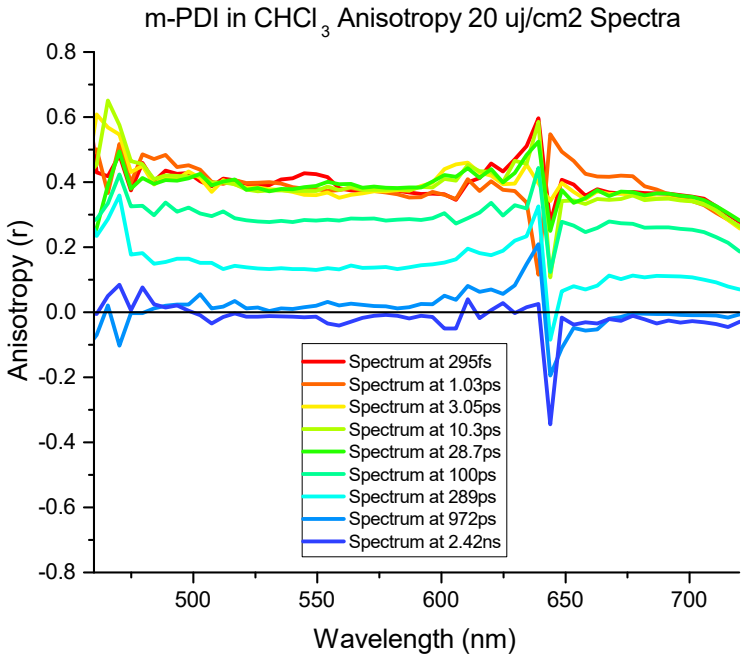

Figure B.17: The anisotropy of m-PDI (shown for comparison to di-PDI) in chloroform solution, which follows a uniform decay at all wavelengths. This results fro the fact that the ground and excited-state transition dipole vectors are parallel. The anisotropy decay of a few hundred ps is due to rotational diffusion of the entire molecule, and is solvent viscosity dependent.

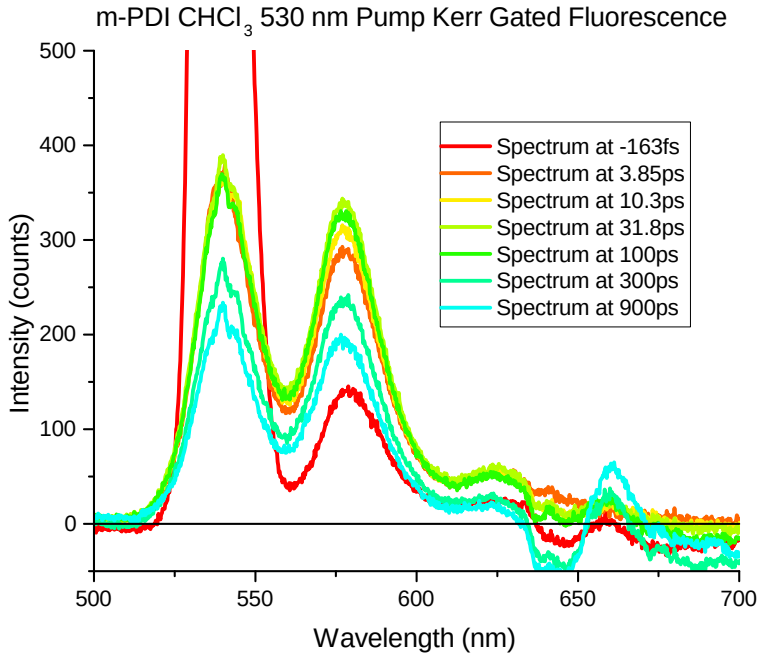

Figure B.18: Time-resolved fluorescence measured with a transient Kerr gate of m-PDI in chloroform excited at 540 nm. The earliest time spectrum in red shows scatter of the pump pulse. The subsequent fluorescence dynamics are in agreement with the fsTA data.

We note one subtle feature in the Kerr-gated fluorescence of the monomer: the 0-0 peak remains relatively constant in intensity while that 0-1 peak grows in over the first 10–30 ps. This indicates a relaxation of the excited-state geometry, most likely along the ϕ coordinate.

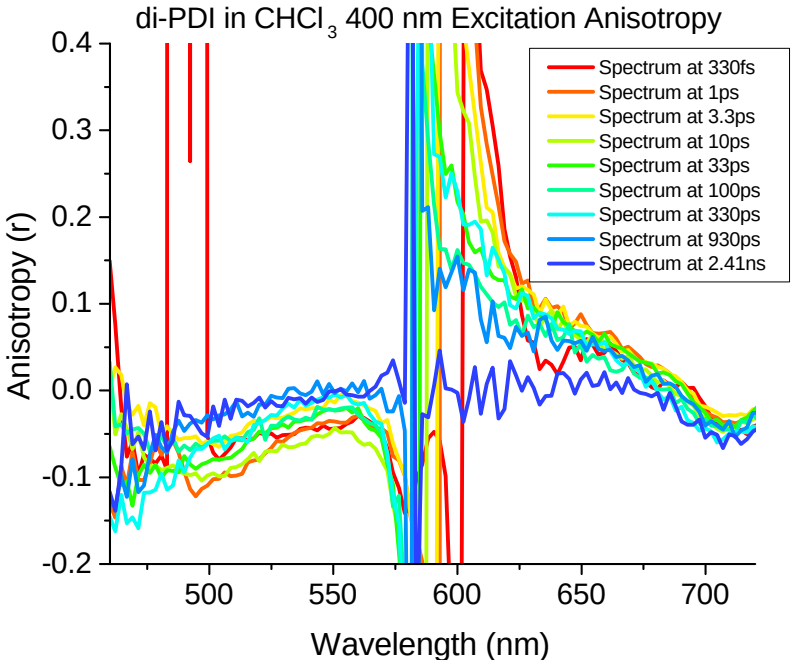

Figure B.19: Experimental fsTA anisotropy for di-PDI in chloroform following excited at 400 nm.

Figure B.19 shows the transient anisotropy of di-PDI excited at 400 nm. At this excitation wavelength, the ground-state bleach anisotropy is negative while the early-time anisotropy for the ESA is positive, and there is very little anisotropic spectral dynamics. The most logical explanation for this observation, consistent with the TD-DFT calculations described above, is that 400-nm excitation involves so many states from both conformations of di-PDI that the anisotropy is averaged out to be relatively featureless.

B.7.5.2 Bromoform

To decouple features in the fsTA due to the electronic structure of di-PDI and those from dynamic solvent relaxation and rotational diffusion, repeated the transient absorption experiments in multiple solvent environments. We begin with bromoform, which has a similar dielectric constant ($\varepsilon_{bromoform}$ = 4.3 compared to $\varepsilon_{chloroform}$ = 4.8) but a higher viscosity by a factor of $\sim$4. The fsTA dynamics of di-PDI in bromoform are shown in Figures B.20 to B.23. We see that the spectral shift in the 550-600 nm region in bromoform indeed tracks roughly with the expected factor of 3-4 due to increased viscosity. This adds credence to the idea of this feature resulting from inhomogeneous broadening or a Stokes shift along the ϕ coordinate, requiring large-amplitude motion. The third spectral minimum at early times near 575 nm is also far more pronounced in bromoform and its decay also follows the trend in viscosity. The narrower vibronic features and previously mentioned solvatochromism in bromoform may be due to interactions that change the relative energetics of the open and closed di-PDI conformers and thus the degree of inhomogeneous broadening.

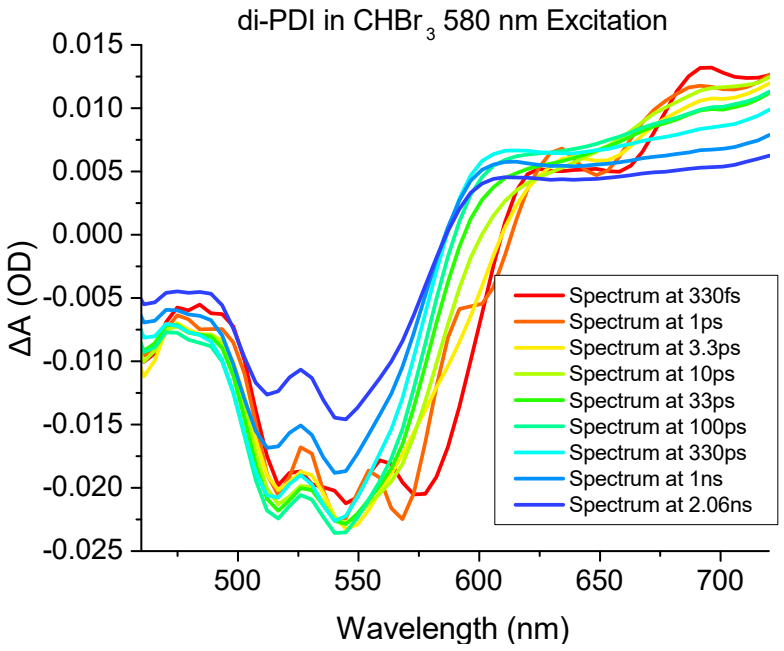

Figure B.20: fsTA with pump-probe polarizations at the magic angle transient for di-PDI in bromoform following 580-nm excitation.

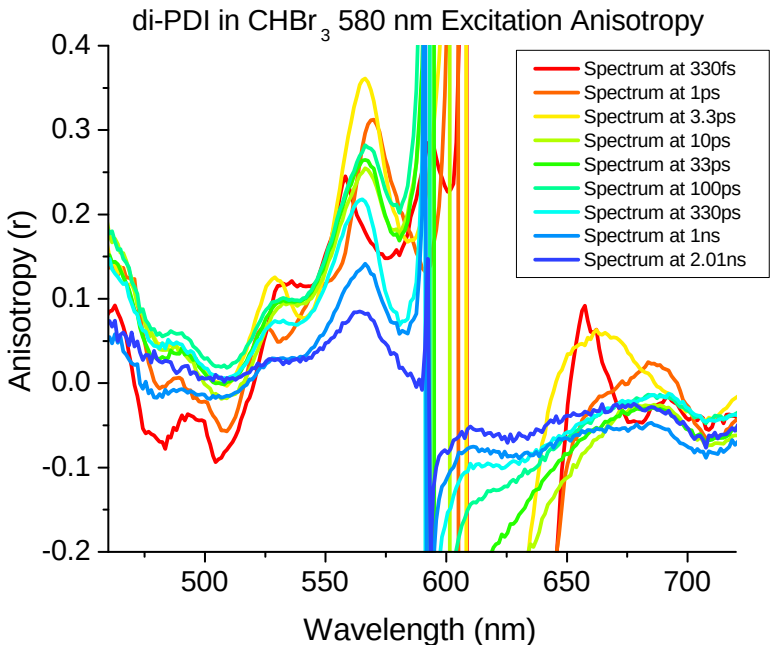

Figure B.21: Pump-probe anisotropy of di-PDI in bromoform after 580-nm excitation.

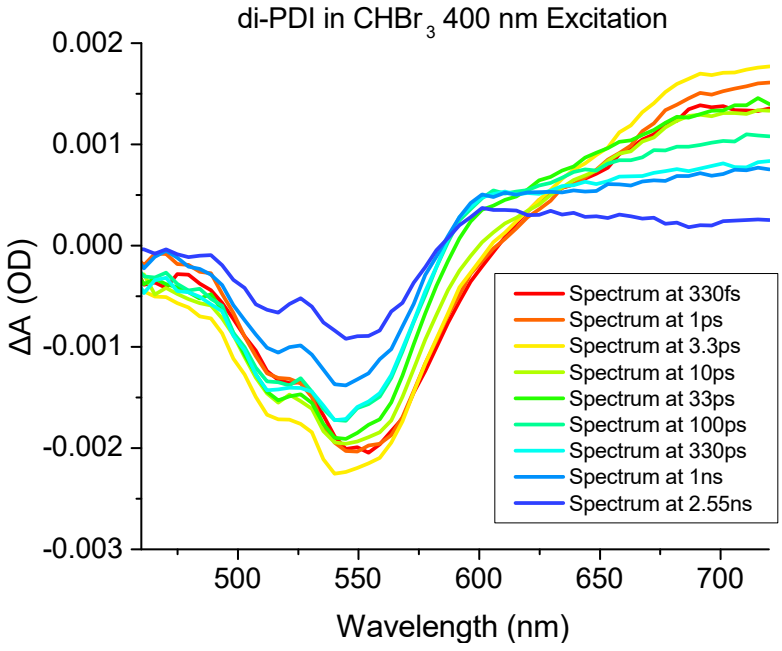

Figure B.22: fsTA of di-PDI in bromoform after excitation at 400 nm.

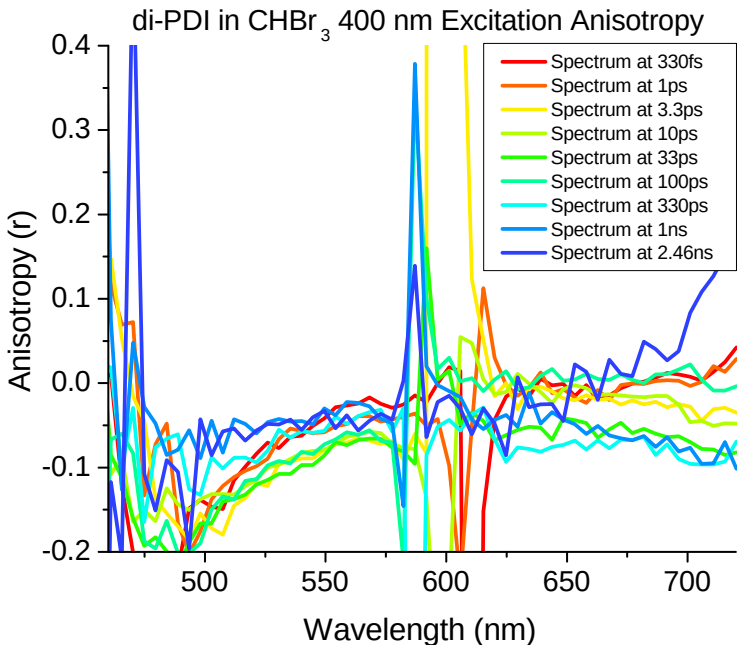

Figure B.23: Pump-probe anisotropy of di-PDI in bromoform following 400-nm excitation. This dynamics follow a similar trend as in chloroform, where the 400-nm excitation showed negative anisotropy for the bleach and slightly higher values for the excited-state absorption (although the absorption here shows a negative anisotropy).

B.7.5.3 1-Butanol

Our choice of 1-butanol as another solvent environment in which to explore the dynamics of di-PDI was to explore the limit of a high-dielectric environment. 1-butanol has a static dielectric constant that is ∼3.5 times larger than chloroform and bromoform. We see that in 1-butanol, the overall lifetime of di-PDI is shorter by about a factor of 2. The spectral shifting dynamics are similar to bromoform, even though the bulk viscosity of 1-butanol is larger than that of bromoform. 1-butanol does have the possibility for fast -OH motions, which could be responsible for increased inhomogeneous broadening at the earliest times, explaining the narrower features in the transient bleach. The excited-state absorption of di-PDI in 1-butanol clearly shows more than one contributing spectral feature, although we find no conclusive evidence for a long-lived CT state even in this higher-dielectric environment. Instead, we believe that the shorter lifetime is likely due to faster sampling of the barrier between conformers or more efficient nonadiabatic relaxation. The fsTA dynamics of di-PDI in 1-butanol are shown in Figures B.24 to B.27.

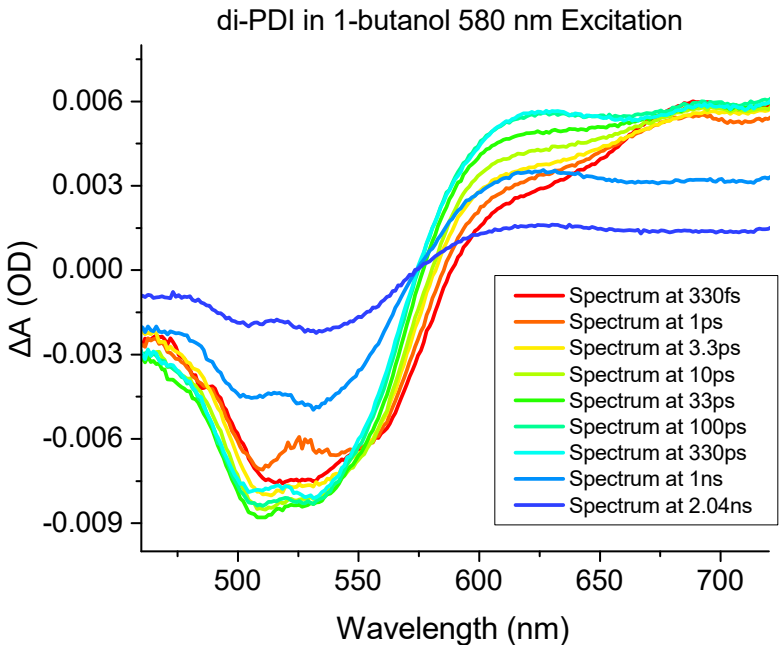

Figure B.24: Selected spectra from fsTA of di-PDI in 1-butanol with pump-probe polarizations at the magic angle.

The transient anisotropy of di-PDI in 1-butanol is qualitatively similar to those found in other solvents. The excited transition shows a small positive anisotropy where it is cleanly resolved around

580 nm, but a multitude of additional transitions with orthogonal transition dipole vectors produce an anisotropy of near 0 elsewhere. The lack of vibronic structure in the bleach is unsurprising considering the increased spectral broadening seen in 1-butanol: the lack of vibronic structure at even the earliest times (<300 fs) suggests that either the broadening happens on a timescale faster than this, likely due to solvation by -OH groups.

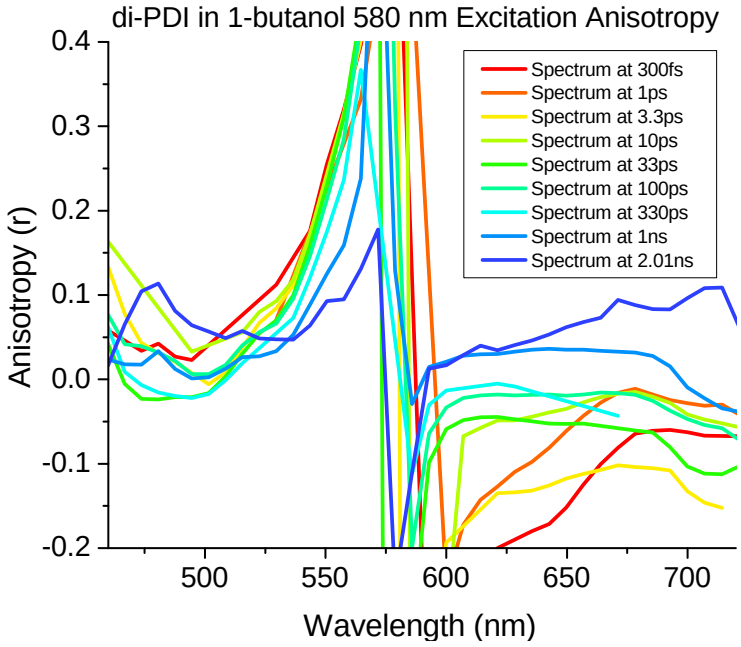

Figure B.25: Pump-probe transient anisotropy of di-PDI in 1-butanol after 580-nm excitation.

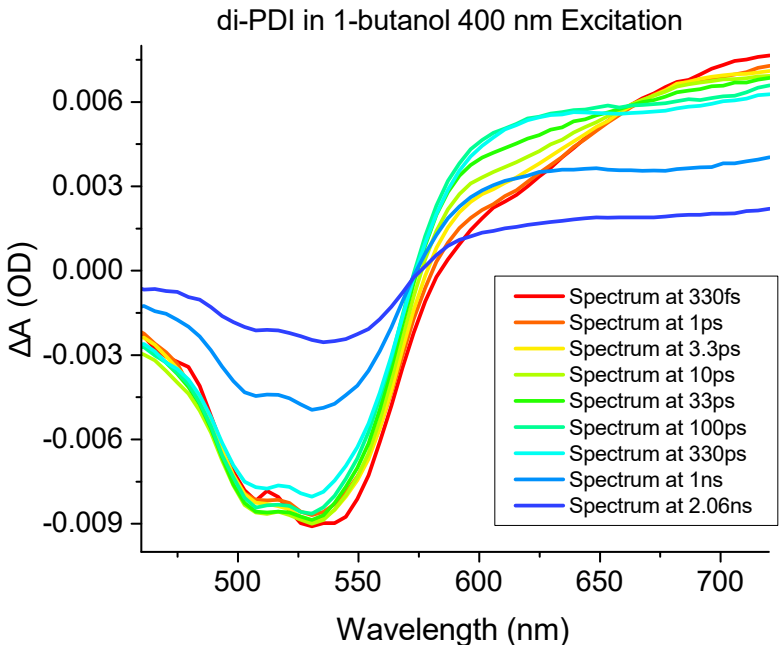

Figure B.26: Selected spectra from the fsTA of di-PDI in 1-butanol excited at 400 nm.

Finally, we also measured the transient anisotropy of di-PDI in 1-butanol, although this data was more difficult to interpret than that in the other solvents. The sign of the anisotropy switches systematically after 1 ns, but with no other comparable timescale in the fsTA the origin of this switch remains elusive.

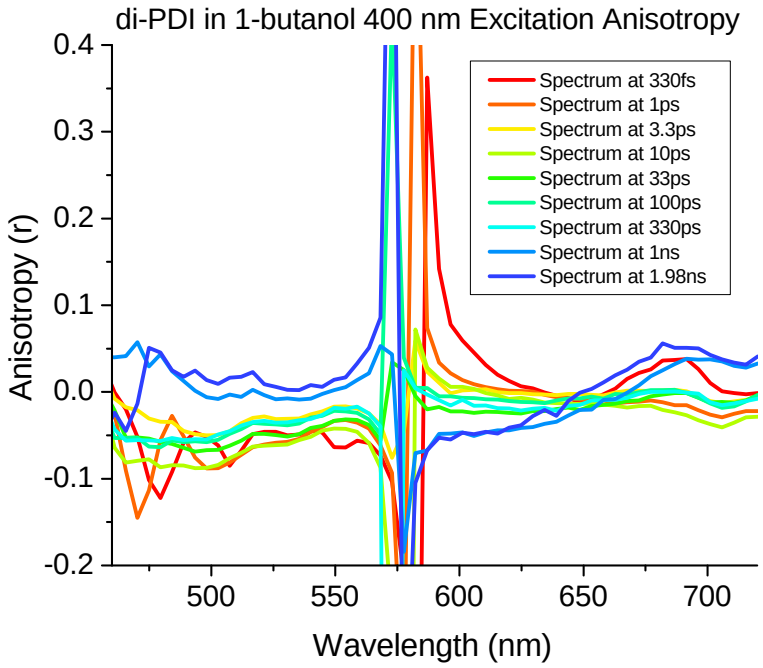

Figure B.27: Anisotropy dynamics of di-PDI in 1-butanol upon 400-nm excitation.

B.7.5.4 Films

As mentioned in Chapter 4, we also performed fsTA experiments on both di-PDI and its corresponding monomer (m-PDI) when spin-cast into thin films, as shown in Figures B.28 to B.32.

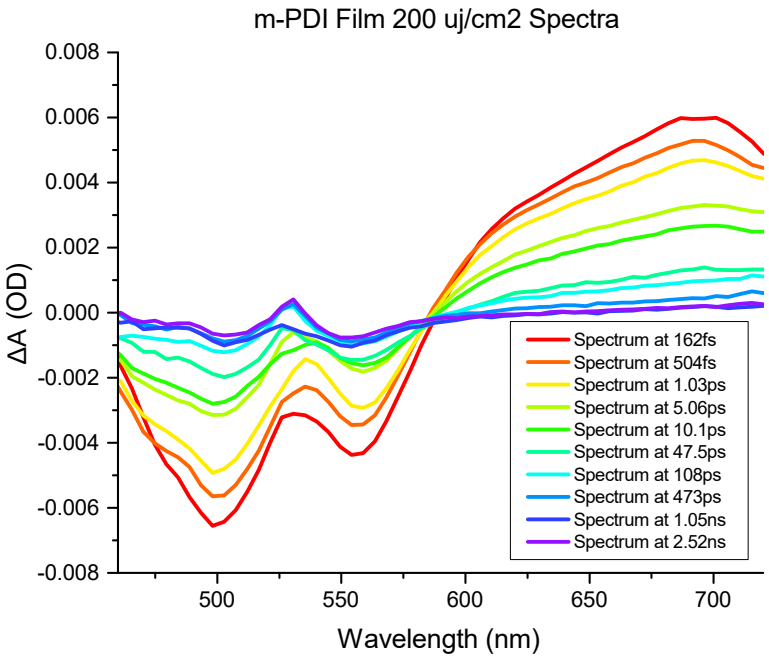

Figure B.28: fsTA of m-PDI in a spin-cast film excited at 530 nm. Because the films scatter the excitation wavelength strongly, the data between 500 and 560 nm is artificially skewed at late times. Unlike the long lifetime in solution, In the film m-PDI shows a significantly shorter lifetime of only ∼50 ps. Very little excited-state relaxation is observed, leading to a discernible isosbestic point at 580 nm, clearly indicating simple two-state kinetic relaxation.

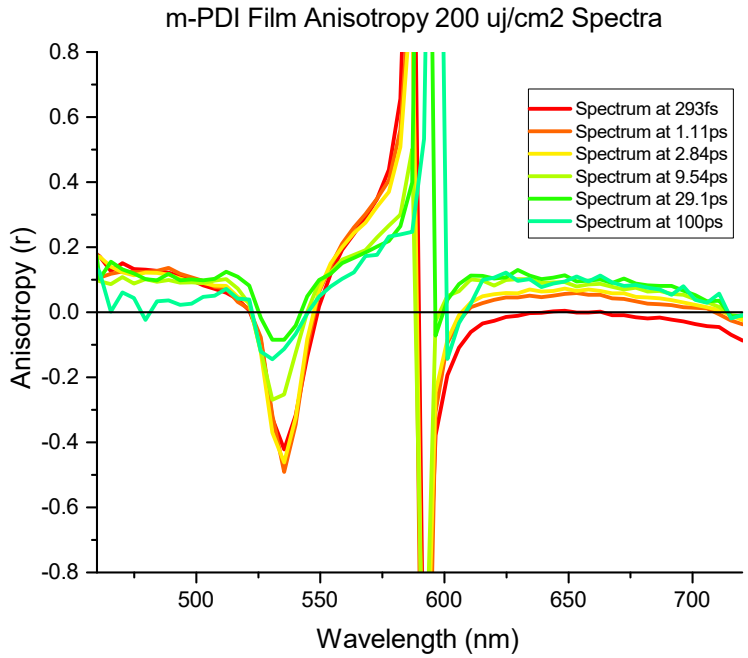

Figure B.29: Pump-probe transient anisotropy for m-PDI films excited at 530 nm. The divergence near 530 nm is due to pump scatter, and that in the region between 580–610 nm results from the fact that the net transient absorption signal is zero.

Figure B.29 shows that in the region of the ground-state bleach, m-PDI films have an anisotropy value of only 0.15, even at the earliest times. This suggests that excitation in films is to a delocalized state with a transition dipole direction that depends on the local environment, consistent with varying degrees of aggregation in the film. The excited-state absorption, however, exhibits the opposite trend: the anisotropy starts near 0 and then grows to roughly 0.1 where it remains for the duration of the (short) excited-state lifetime. This suggests the aggregated excited state has a preferred transition dipole vector oriented at nearly the magic angle relative to that of the isolated monomer.

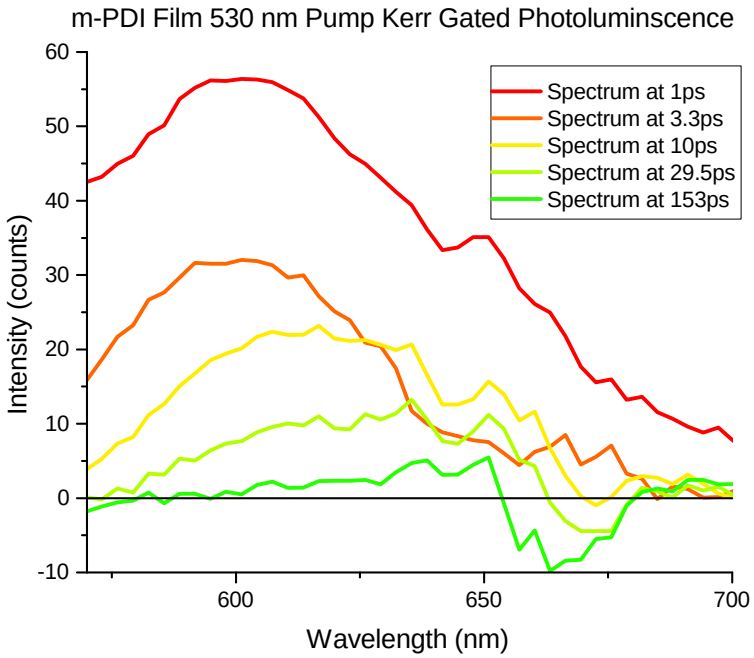

Figure B.30: Time-resolved fluorescence for m-PDI in a spin-cast film excited at 530 nm. The small negative signal between 650 and 680 is noise from the Kerr gate process and can be ignored. In the film, m-PDI emission shows similar relaxation time scales as seen in the fsTA.

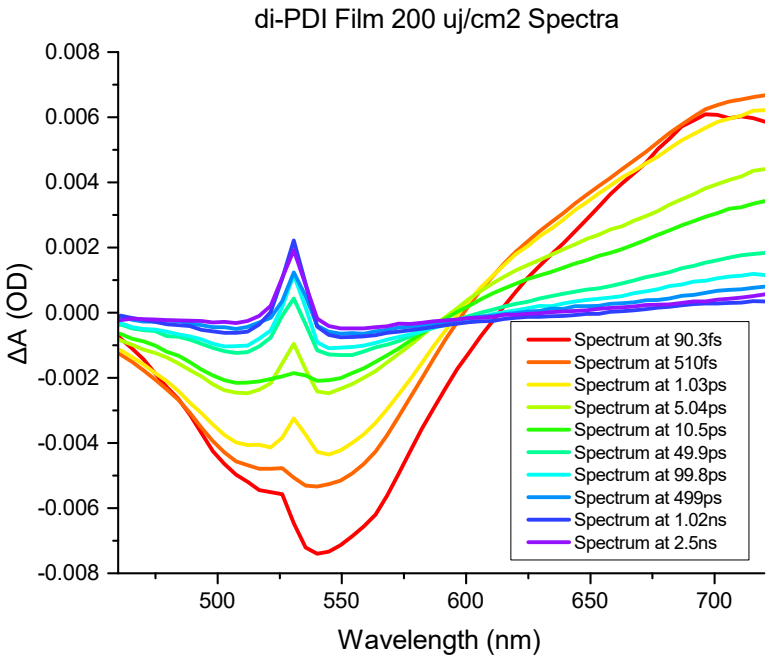

Figure B.31: fsTA dynamics of di-PDI in a spin-cast film excited at 530 nm. The sharp feature at 530 nm is scatter of the excitation light by the film. The transient features are broadened so that there are no spectrally-resolved vibronic features as with the steady-state spectra. Most of the signal decays within roughly 20 ps, suggestive of aggregation interactions between di-PDI molecules, but there is a small component that remains to the ns time scale, likely due to di-PDI molecules in uncoupled environments. Compared to the di-PDI transient absorption in solution, the excited-state absorption is far more pronounced, also indicative of enhanced coupling and delocalization in the film.

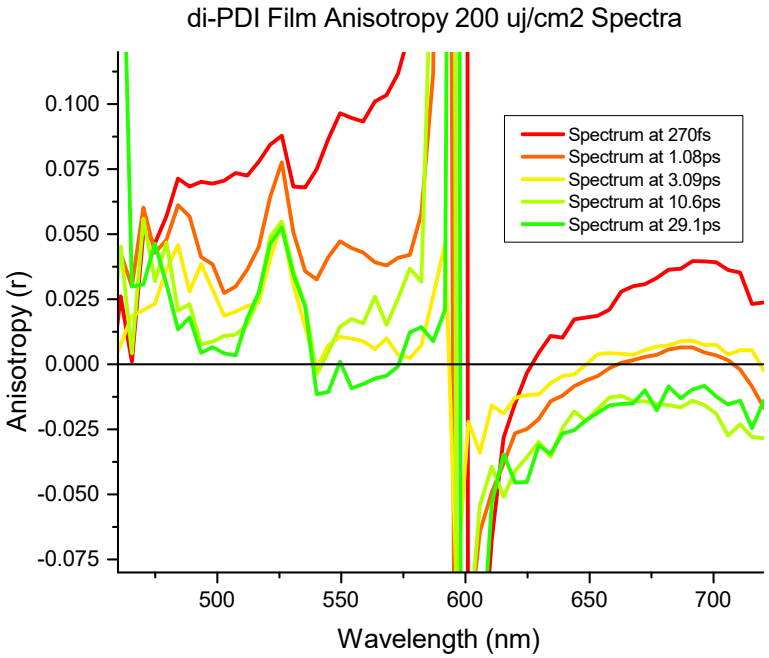

Figure B.32: Anisotropy dynamics of di-PDI in a spin-cast film excited at 530 nm. The data at 530 nm are affected by pump scattering, and the divergence in the region between 580–610 results from the fact that the net transient absorption in this region is zero. At the earliest times there is a small and uniform positive anisotropy for the bleach, while the excited-state absorption shows a negative anisotropy. Given the significant spectral broadening in the film, this is consistent with the small, generally negative, values found for di-PDI in solution. Although the anisotropy decay timescales are roughly similar for solution and film (a few tens of picoseconds), the mechanisms must differ. Without the ability to rotationally diffuse, the main mechanism for anisotropy loss in the film must be energy transfer between neighboring di-PDI molecules with different transition dipole orientations.

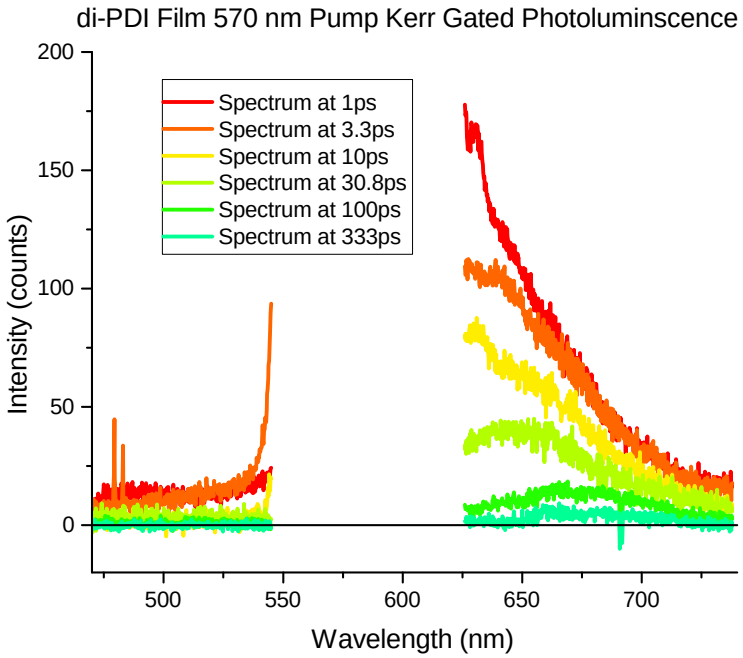

Figure B.33: Kerr-gated fluorescence from di-PDI in a spin-cast film excited at 580 nm. The short emission lifetime of roughly 20 ps agrees with the fsTA data. The emission data, however, show a clean time-dependent Stokes shift that is undiscernable in the congested fsTA spectra. The rate of this shift likely corresponds to the time scale for excitations to transfer between neighboring di-PDI molecules.

B.8 Final Remarks

This bay-linked di-PDI molecule clearly populates two minima along its dihedral coordinate, each having unique spectral signatures. We were able to deconvolve their absorption and emission spectra with a global fitting procedure, isolating the general envelopes for each geometry and the underlying vibronic progressions of the major transitions. These spectral components and assignments are consistent with previous data, but differ in interpretation.[263] No evidence was found for interconversion between the open and closed di-PDI geometries, as implied by the cleanly separable steady-state emission components.

The spectral assignments of the two geometries are reasonably consistent with our dispersion-corrected TD-DFT calculations. The broad absorption/emission feature corresponds to the closed di-PDI geometry, which has a low emission yield but high population fraction. The narrow absorption/emission feature is consistent with the open di-PDI geometry, which is more monomer-like with a higher emission quantum yield but lower overall population. We note that the underlying transitions we extracted from the available spectral data do not agree perfectly with the TD-DFT calculations, even through the overall conclusions are clear: a simple picture of two-level interacting monomers cannot adequately explain any of the observations.

With a spectroscopic understanding of this di-PDI in hand, we now have additional insight to why this molecule and related derivatives are successful acceptor materials in organic solar cells. First, both the open and closed stable di-PDI geometries have a non-planar arrangement of the monomer subunits: this prevents the overaggregation associated with monomeric PDIs. Furthermore, each geometry has an intense and relatively broad absorption, especially compared to fullerene derivatives, allowing for better solar harvesting. This presence of multiple geometries—each with unique photophysics—offers some novel avenues for further improvement. One possibility is that trap states based on distortions of the dihedral are likely to be present; these could be remedied with additional steric hindrance. Moreover, the presence of spectrally distinct geometries of the same molecule offers a tempting alternative for 'ternary blends' having unique regions of the solar spectrum absorbed by the same molecule, but in different conformations.

APPENDIX C

Supporting Information for Chapter 5

C.1 Experimental Details

C.1.1 Organic Materials

All materials were purchased commercially and used as received. P3HT was purchased from Rieke Metals, Inc. (4002-EE; RR ∼94%, M_w = 50-70 kDa) and F_4TCNQ was purchased from TCI America.

C.1.2 Doping Fabrication Procedures

The first step in the fabrication process was cleaning glass substrates. First, the glass substrates were sonicated for approximately ten minutes in each cleaning solution (detergent, deionized water, acetone, and isopropanol). The substrates were dried with nitrogen gas before being put under vacuum for approximately 10 minutes.

P3HT solutions at concentrations of 0.5%, 2%, and 5% were prepared by respectively dissolving 5 mg, 20 mg, and 50 mg P3HT in 1 mL *ortho*-dichlorobenzene. Films were prepared in a nitrogen atmosphere by spin-casting the P3HT solution on glass substrates at 1000 rpm for 60 s, followed by 3000 rpm for 5 s. The 0.5%, 2%, and 5% solutions respectively gave 25 nm, 110 nm, and 400 nm thick films. The 2 μm thick films were prepared by slow-drying: 30 μL of a 2% P3HT solution was drop-cast onto the glass substrate and placed into a covered Petri dish for two days for complete drying. Annealed films were heated at 240 °C for 5 minutes in an argon environment. After the annealing procedure finished, the hot plate was set to 25 °C and the films cooled on the hot plate for three hours.

Evaporation sequential doping proceeded via thermal evaporation. F_4TCNQ was thermally evaporated onto P3HT films using an Angstrom Engineering Nexdep thermal evaporator: the F_4TCNQ powder was placed in an alumina crucible resistively heated at pressures <1 x 10^{-6} Torr to induce sublimation towards exposed P3HT samples fixed to an actively-cooled rotating sample stage; due to the low vapor pressure of F_4TCNQ, only low powers were needed to sublime the material, further ensuring the films were constantly cooled. The evaporation rate was 0.5 Å/s for the entire evaporation and the thickness of evaporated dopant was monitored using a quartz crystal microbalance located next to the sample stage. Solution sequential doping proceeded via spin coating a solution of F_4TCNQ dissolved in dichloromethane (DCM) onto the P3HT film. The F_4TCNQ solution was cast directly on the P3HT film and spun at 4000 rpm for 10 s.

C.2 Optical Characterization

C.2.1 UV-Visible Spectroscopy

UV-Visible absorption experiments were carried out using a Lambda 25 UV-Vis spectrometer.

As shown in Figure C.3, there is close agreement in the spectral profiles for the solution- and evaporation-doped 110-nm- and 400-nm-thick pre-cast P3HT films that yield the highest electrical conductivities. We note that the 25-nm pre-cast P3HT film doped with the 1 mg/mL solution has the optimal conductivity, yet by UV-vis has a large F_4TCNQ neutral peak. This observation agrees with the report by Hamidi-Sakr et al. and our "overhead" analysis where some extra dopant is required for optimal doping.[276] Since this additional dopant is required to reorient and does not contribute to the doping, for thin films we expect to see a larger intensity for the F_4TCNQ neutral peak. We also note that the 25 nm evaporation-doped P3HT film does not have a large F_4TCNQ neutral peak, but instead has a high dopant:polymer thickness ratio. Thus, both evaporation and solution-sequential doping require extra F_4TCNQ, but the identification is different for each doping method. This highlights that despite the similarities in doping the film, some differences do exist and they are more apparent in the thinner films.

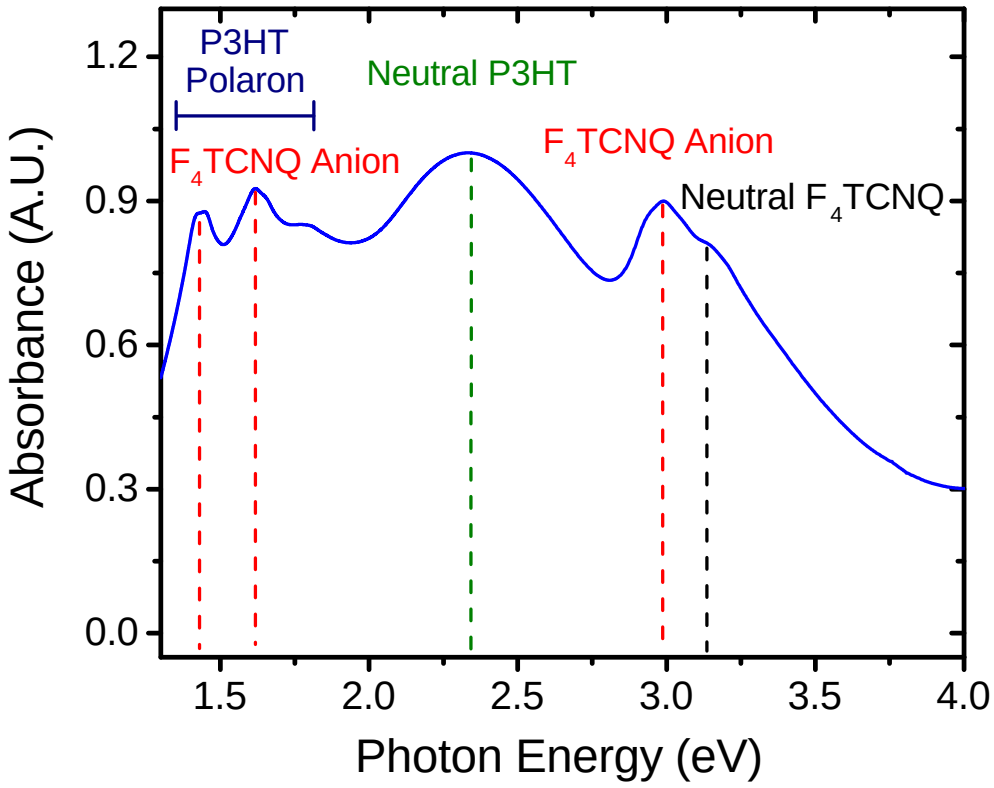

Figure C.1: Normalized UV-Visible spectra for a P3HT film doped with F_4TCNQ. Chemical doping results in the following peaks: P3HT polaron (navy), F_4TCNQ anion (red), neutral P3HT (green), and neutral F_4TCNQ, (black).

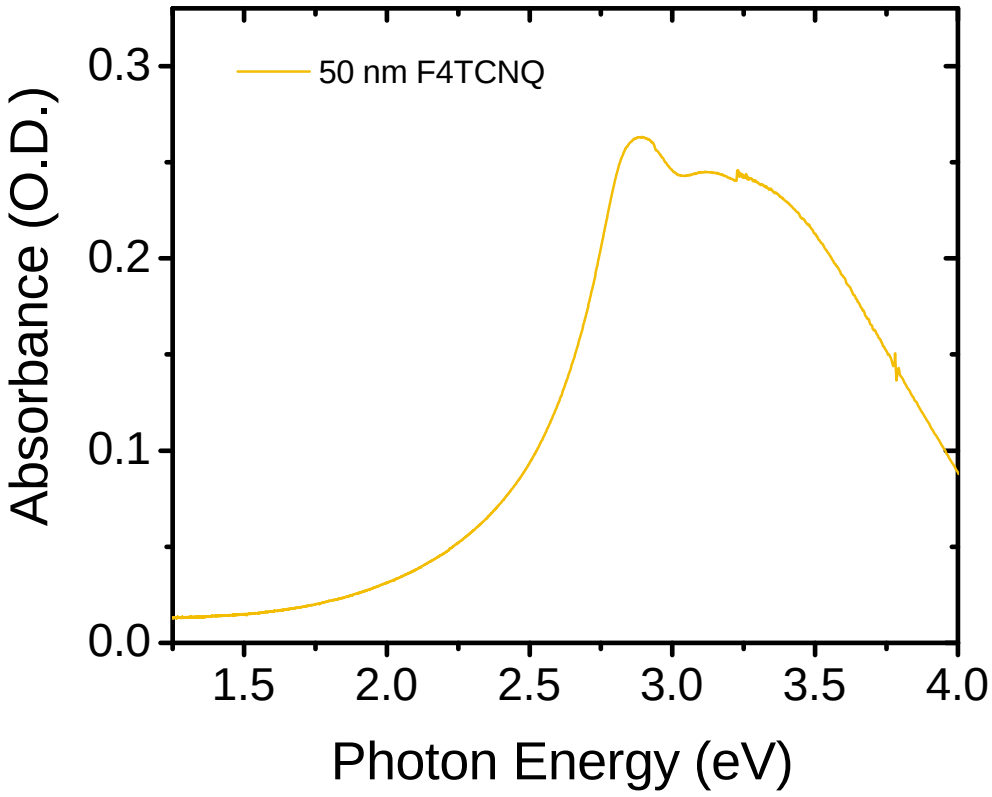

Figure C.2: UV-Visible spectrum of 50 nm evaporated F_4TCNQ on glass.

C.3 Calculating the F_4TCNQ Overhead Thickness

Since the 25 nm, 110 nm, and 400 nm pre-cast P3HT films require, respectively, 15 nm, 40 nm, and 150 nm of evaporated F_4TCNQ in order to achieve optimal conductivity values, we can calculate the F_4TCNQ:P3HT thickness ratios: respectively, these values are 0.60, 0.36, and 0.38. The thickness required to orient the polymer, or "overhead" thickness can be calculated assuming that it does not contribute significantly to the conductivity. It is important to note that the dopant-to-polymer thickness ratios to maximize the electrical conductivity calculated above all assume each nm of dopant contributes to the conductivity. Once subtracting the "overhead" thickness, t, the optimal doping thicknesses for the 25 nm, 110 nm, and 400 nm films are, respectively, 15 - t, 40 - t, and 150 - t. We find that when t = 7 nm, the dopant-to-polymer thickness ratios are, respectively, 0.32, 0.30, and 0.36. Due to the increased resolution of the conductivity measurements for the 25 nm and 110 nm pre-cast P3HT films, we calculated this value to favor matching the ratios of these two films since we know with greater confidence the F_4TCNQ thickness required for optimal doping.

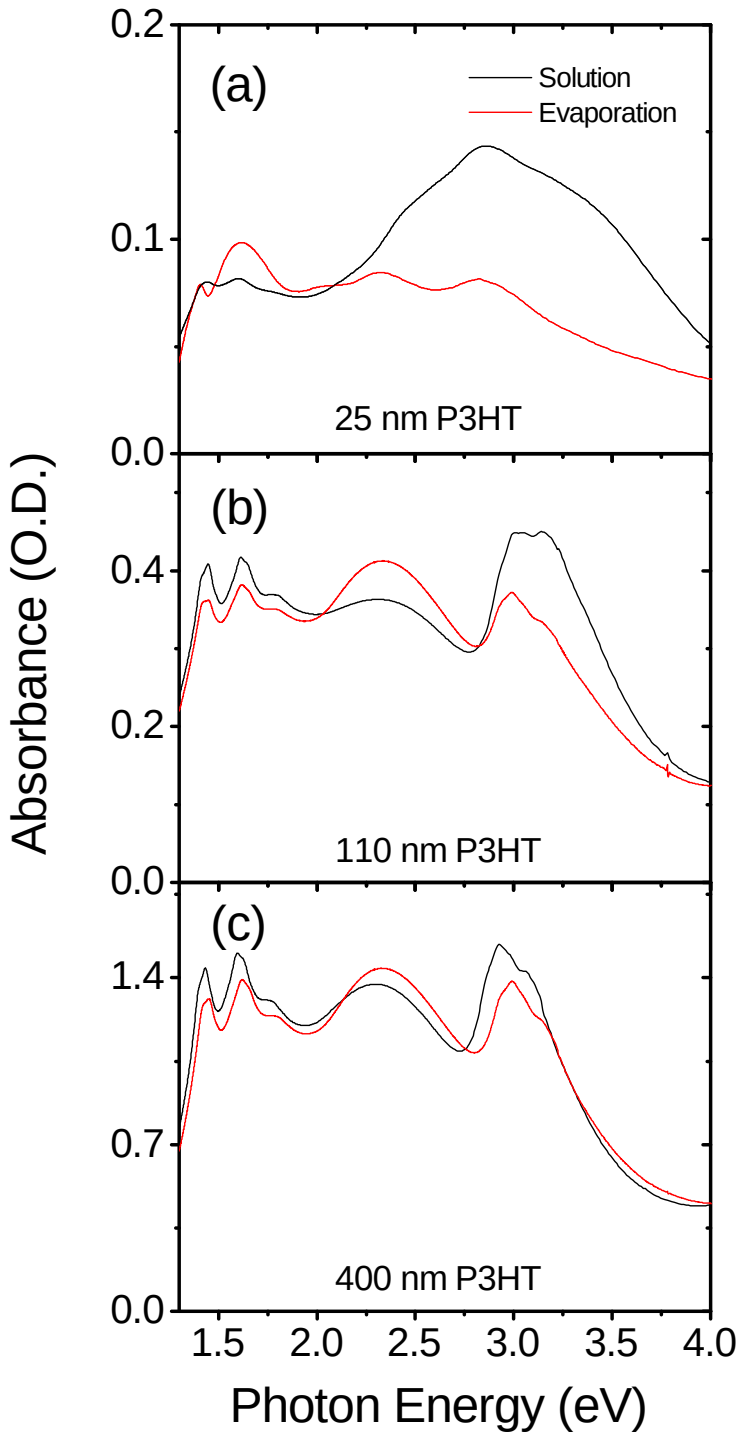

Figure C.3: UV-visible spectra for solution- and evaporation-doped P3HT films with the highest electrical conductivity. The films compared are (a) 25 nm pre-cast P3HT films, (b) 110 nm pre-cast P3HT films, and (c) 400 nm pre-cast P3HT films. Varying thicknesses of F_4TCNQ were evaporated on the P3HT films. As the thickness of P3HT increases, an increasing thickness of F_4TCNQ is required to effectively dope the film, as indicated by a decrease the in P3HT neutral peak and the increase of the F_4TCNQ anion peaks. For all films, as the film is saturated with F_4TCNQ, the neutral F_4TCNQ peak grows in as the primary feature.

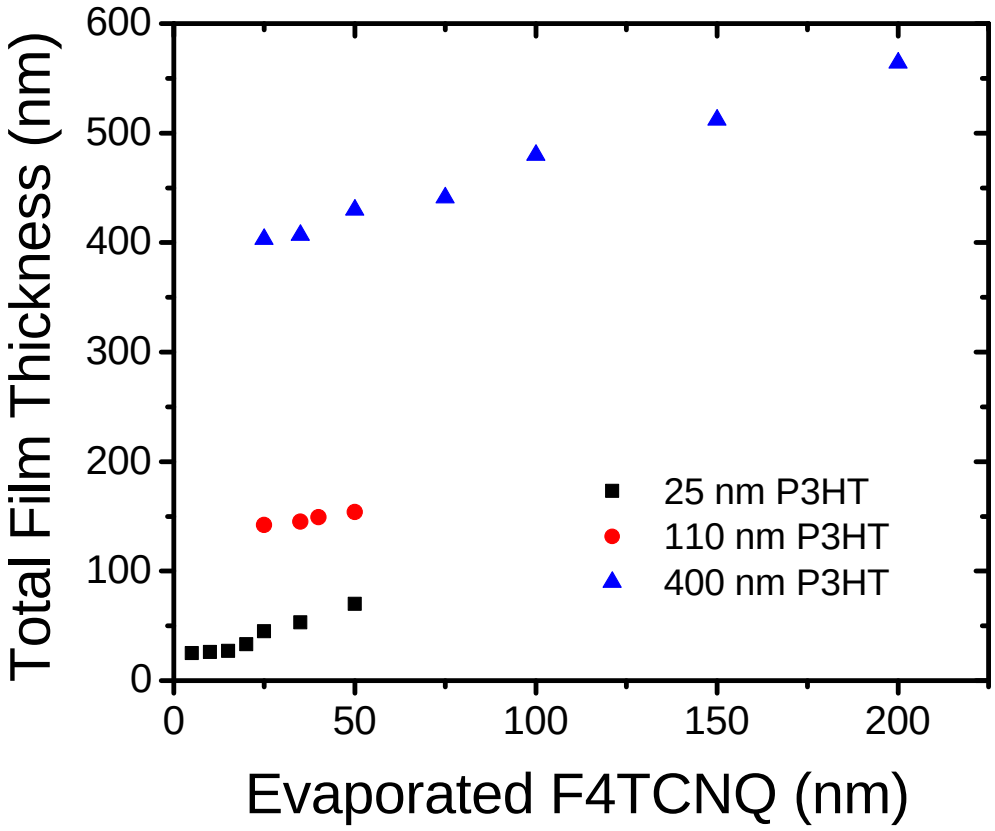

Figure C.4: Total film thickness for 25 nm (black squares), 110 nm (red circles), and 400 nm (blue triangles) pre-cast P3HT films after F_4TCNQ evaporation. For the initial evaporation of F_4TCNQ, the thickness change is very small.

Therefore, this suggests that doping the polymer film requires 7 nm of "overhead" F_4TCNQ.

C.4 Electrical Measurements

C.4.1 Conductivity Measurements

Conductivity measurements were collected in the Van der Pauw geometry using a custom-made apparatus. The measurements were collected in ambient atmosphere using a Keithley 2400 sourcemeter where the max current ranged from 10 μA to 100 μA. The current was swept from negative to positive, rotated 90°, and repeated. The slope of the IâĂŞV curves were subsequently fit to the Van der Pauw equation. Samples in the Van der Pauw geometry were prepared as described in Chapter 5, with silver paste applied at the corners of the film to act as contacts.

C.4.2 Thermoelectric Measurements

Samples for the Seebeck measurement were prepared as earlier described in the text, but to reduce contact resistance required the evaporation of 15 nm molybdenum oxide (MoO_3) followed by 60 nm silver. To ensure reproducibility of the Seebeck measurement, the electrodes were evaporated through a shadow-mask ensuring the electrodes were separated by 7 mm. The measurements were collected in an argon atmosphere.

Measurement of the Seebeck measurement requires the use of a HP 6632A DC power supply to power both thermoelectrics (the hot and cold sinks), a Keithley 2400 source meter to run the RTDs that measure the temperature of each thermoelectric, and a Keithley 2000 digital multimeter to measure the thermoelectric voltage.

A home-built computer interface controls the measurement and operates as follows. A thermoelectric voltage is first defined, which is established by the hot thermoelectric heating up and the cold thermoelectric cooling down. Once the temperature difference stabilized, the voltage drop across the two electrodes was measured. Following this, a new thermovoltage was defined and the process was repeated a few times to construct a line (thermovoltage vs. temperature difference). The thermovoltages sampled ranged from 2 °C to 9°C. The data was fit to a line and the Seebeck

coefficient was determined from the corresponding slope. All R^2 values were 0.999.

C.4.3 Seebeck Empirical Power Law Fitting

It has been empirically observed that the Seebeck coefficient follows the proportionality $S \propto \sigma^{-1/4}$.[68,78] More, precisely the corresponding power law is defined as:

$$S = \frac{k_B}{e}\left(\frac{\sigma}{\sigma_\alpha}\right)^{-1/4}$$

where S is the Seebeck coefficient, k_B is the Boltzmann constant, e is the fundamental unit charge, σ is the electrical conductivity, and σ_α is an empirical constant fitted to 1 S/cm.[78] For convenience, the term $\frac{e}{k_B}$ is represented in the unit of thermopower as 86.17 μV K^{-1}. We plotted the Seebeck coefficient for both evaporation and solution sequential-doped as a function of the electrical conductivity. The data points used are from the samples that produced the highest electrical conductivities for each doping method, as shown in Chapter 5. As shown in Figure C.7 the evaporation and solution sequential-doped films match the empirical power law well.

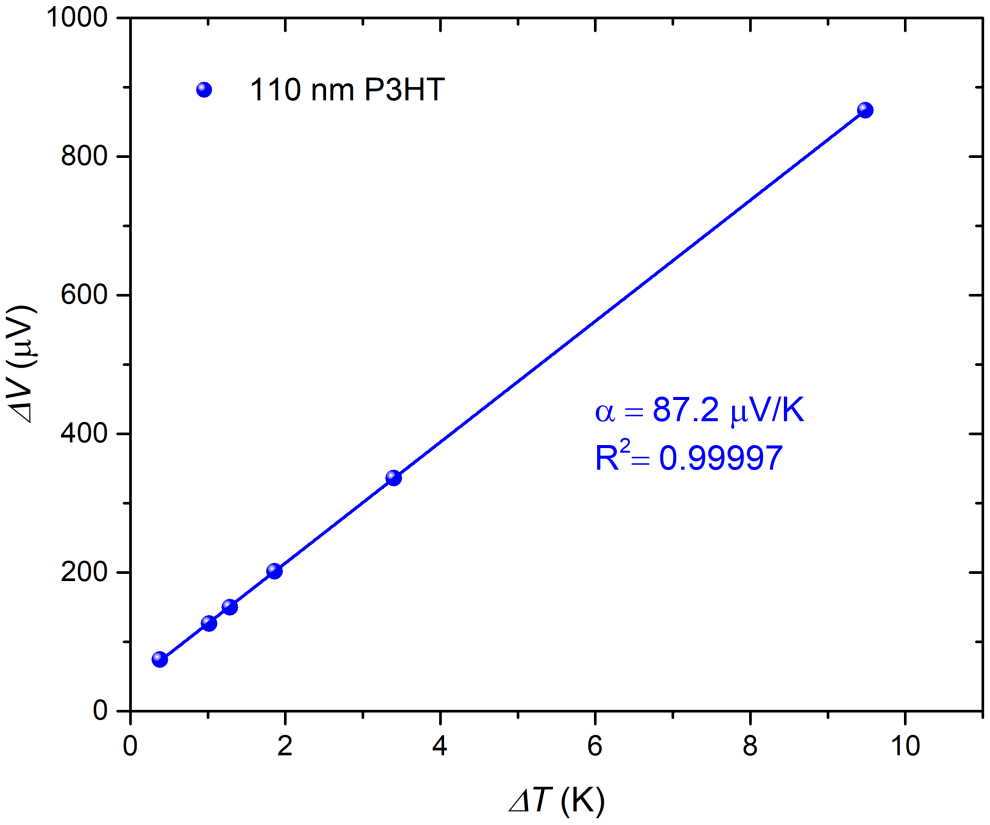

Figure C.5: Graphical determination of the Seebeck coefficient for a pre-cast 110 nm P3HT film doped with a 1 mg/mL F_4TCNQ solution. Two thermoelectrics (the hot and cold sinks) are powered to established a temperature difference (ΔT). For each temperature difference, the thermovoltage (ΔV) was measured, allowing a line to be constructed. Using the slope of the line, the Seebeck coefficient was determined.

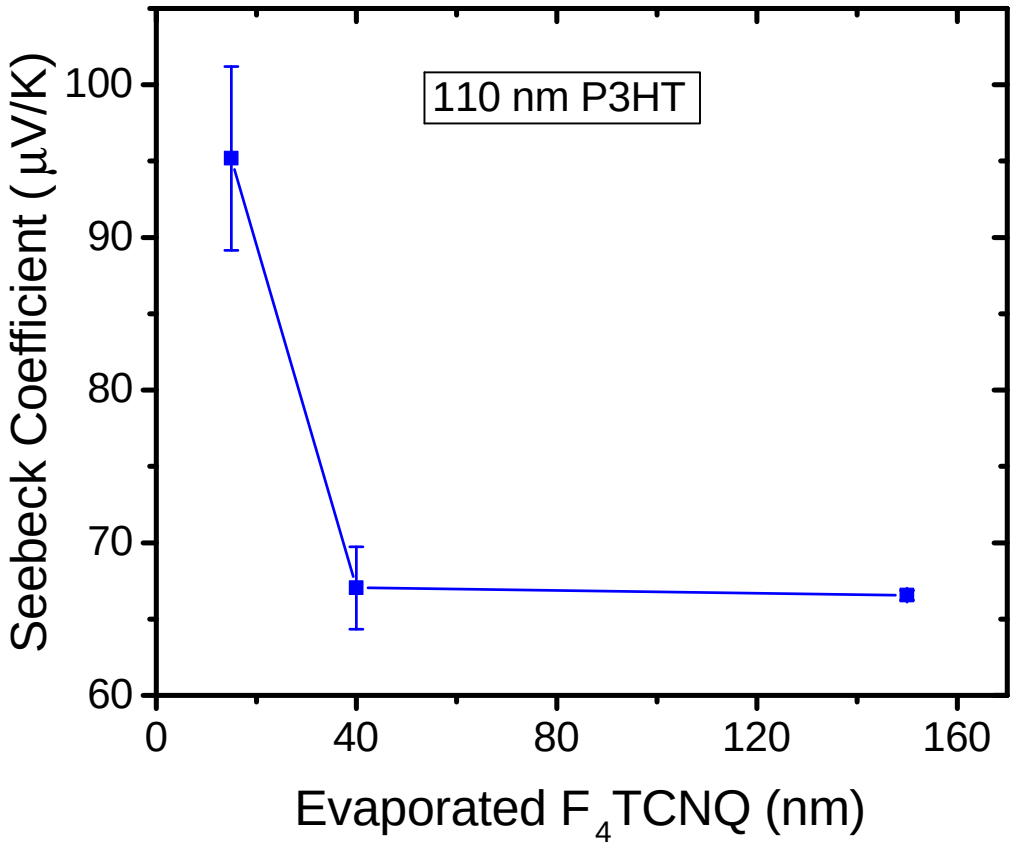

Figure C.6: Seebeck coefficients for pre-cast 110 nm P3HT films doped with 15 nm, 40 nm, and 150 nm of F_4TCNQ. The three thicknesses were selected to under-dope, optimally-dope, and over-dope with respect to the electrical conductivity. Once optimally doing the film with 40 nm of dopant, the Seebeck coefficient remains constant to higher doping levels.

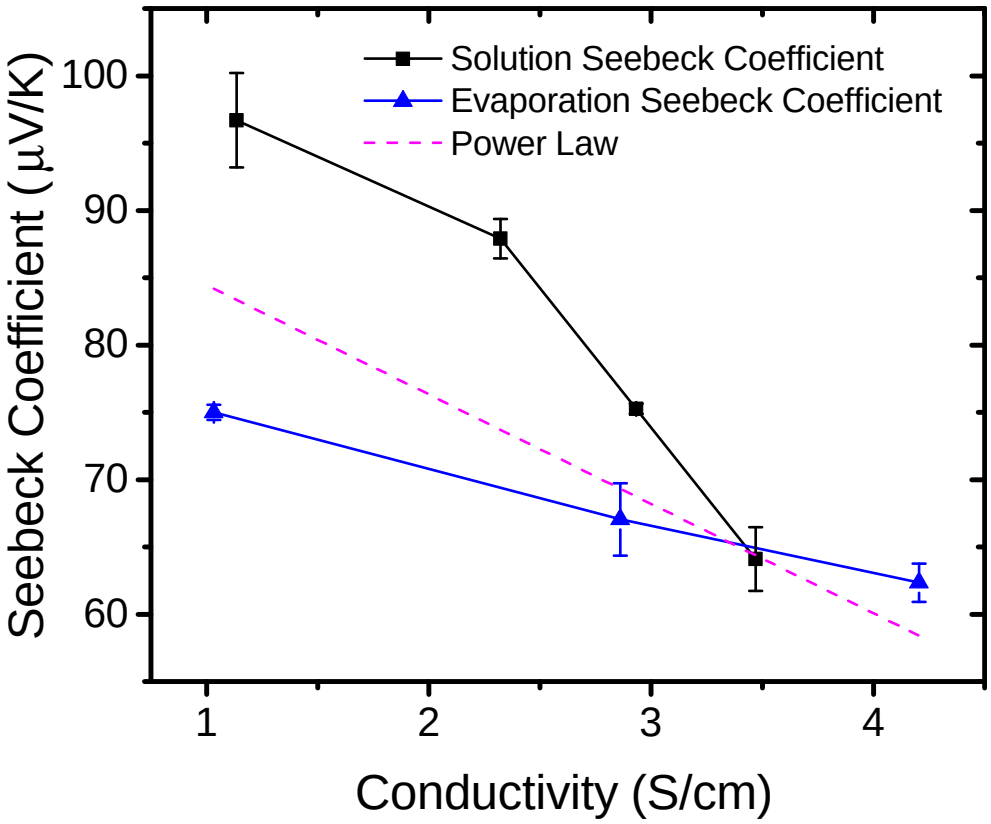

Figure C.7: Solution (black squares) and evaporation (blue triangles) Seebeck coefficient (*S*) plotted as a function of the electrical conductivity (σ). The purple line is a plot of the empirical power law. Good agreement is found between the solution and evaporation sequential-doped samples and the empirical power law.

REFERENCES

[1] S. Subramaniyan, H. Xin, F. S. Kim, and S. A. Jenekhe, "New Thiazolothiazole Copolymer Semiconductors for Highly Efficient Solar Cells," *Macromolecules*, vol. 44, pp. 6245–6248, 2011.

[2] J. C. Aguirre, S. A. Hawks, A. S. Ferreira, P. Yee, S. Subramaniyan, S. A. Jenekhe, S. H. Tolbert, and B. J. Schwartz, "Sequential Processing for Organic Photovoltaics: Design Rules for Morphology Control by Tailored Semi-Orthogonal Solvent Blends," *Advanced Energy Materials*, vol. 5, no. 11, p. 1402020, 2015.

[3] Y. Liang, Z. Xu, J. Xia, S.-T. Tsai, Y. Wu, G. Li, C. Ray, and L. Yu, "For the Bright Future - Bulk Heterojunction Polymer Solar Cells with Power Conversion Efficiency of 7.4%," *Advanced Materials*, vol. 22, pp. E135–E138, 2010.

[4] H.-J. Jhuo, S.-H. Liao, Y.-L. Li, P.-N. Yeh, S.-A. Chen, W.-R. Wu, C.-J. Su, J.-J. Lee, N. L. Yamada, and U.-S. Jeng, "The Novel Additive 1-Naphthalenethiol Opens a New Processing Route to Efficiency-Enhanced Polymer Solar Cells," *Advanced Functional Materials*, vol. 26, pp. 3094–3104, 2016.

[5] D. T. Duong, C. Wang, E. Antono, M. F. Toney, and A. Salleo, "The Chemical and Structural Origin of Efficient p-Type Doping in P3HT," *Org. Electron.*, vol. 14, no. 5, pp. 1330–1336, 2013.

[6] Y. Zang, C. Z. Li, C.-C. Chueh, S. T. Williams, W. Jiang, Z.-H. Wang, J.-S. Yu, and A. K.-Y. Jen, "Integrated Molecular, Interfacial, and Device Engineering Towards High-Performance Non-Fullerene Based Organic Solar Cells," *Advanced Materials*, vol. 26, no. 32, pp. 5708–5714, 2014.

[7] S. Schott, A. Steinbacher, J. Buback, P. Nuernberger, and T. Brixner, "Generalized Magic Angle for Time-Resolved Spectroscopy with Laser Pulses of Arbitrary Ellipticity," *Journal of Physics B: Atomic, Molecular and Optical Physics*, vol. 47, no. 12, p. 124014, 2014.

[8] M. T. Fontana, T. J. Aubry, D. T. Scholes, S. A. Hawks, and B. J. Schwartz, "Sequential Processing: A Rational Route for Bulk Heterojunction Formation via Polymer Swelling," in *Handbook of Organic Optoelectronic Devices*, vol. 2, ch. 8, World Scientific, 2018.

[9] J. Tsao, N. Lewis, and G. Crabtree, "Solar FAQs," tech. rep., 2006.

[10] British Petroleum, "BP Statistical Review of World Energy 2017," tech. rep., 2017.

[11] A. Blakers, N. Zin, K. R. McIntosh, and K. Fong, "High Efficiency Silicon Solar Cells," *Energy Procedia*, vol. 33, pp. 1–10, 2013.

[12] M. A. Green, Y. Hishikawa, E. D. Dunlop, D. H. Levi, J. Hohl-Ebinger, and A. W. Ho-Baillie, "Solar Cell Efficiency Tables (Version 51)," *Progress in Photovoltaics: Research and Applications*, vol. 26, no. 1, pp. 3–12, 2018.

[13] W. Shockley and H. J. Queisser, "Detailed Balance Limit of Efficiency of p-n Junction Solar Cells," *Journal of Applied Physics*, vol. 32, no. 3, pp. 510–519, 1961.

[14] A. De Vos, "Detailed Balance Limit of the Efficiency of p-n Junction Solar Cells," *Journal of Physics D: Applied Physics*, vol. 13, no. 83946, pp. 839–846, 1980.

[15] P. Dai, L. Ji, M. Tan, S. Uchida, Y. Wu, A. Abuduwayiti, M. Heini, Q. Guo, L. Bian, S. Lu, and H. Yang, "Electron Irradiation Study of Room-Temperature Wafer-Bonded Four-Junction Solar Cell Grown by MBE," *Solar Energy Materials and Solar Cells*, vol. 171, no. 6, pp. 118–122, 2017.

[16] C. Deibel and V. Dyakonov, "Polymer-Fullerene Bulk Heterojunction Solar Cells," *Reports Prog. Phys.*, no. 73, p. 96401, 2010.

[17] A. J. Heeger, "25th Anniversary Article: Bulk Heterojunction Solar Cells: Understanding the Mechanism of Operation," *Advanced Materials*, vol. 26, pp. 10–28, 2014.

[18] R. Gaudiana and C. Brabec, "Organic Materials: Fantastic Plastic," *Nature Photonics*, vol. 2, no. 5, pp. 287–289, 2008.

[19] N. Espinosa, M. Hösel, D. Angmo, and F. C. Krebs, "Solar Cells with One-Day Energy Payback for the Factories of the Future," *Energy Environ. Sci.*, vol. 5, no. 1, pp. 5117–5132, 2012.

[20] S. Li, L. Ye, W. Zhao, H. Yan, B. Yang, D. Liu, W. Li, H. Ade, and J. Hou, "A Wide Band-Gap Polymer with a Deep HOMO Level Enables 14.2% Efficiency in Polymer Solar Cells," *Journal of the American Chemical Society*, p. jacs.8b02695, 2018.

[21] J.-H. Chang, H.-F. Wang, W.-C. Lin, K.-M. Chiang, K.-C. Chen, W.-C. Huang, Z.-Y. Huang, H.-F. Meng, R.-M. Ho, and H.-W. Lin, "Efficient Inverted Quasi-Bilayer Organic Solar Cells Fabricated by using Non-Halogenated Solvent Processes," *Journal of Materials Chemistry A*, vol. 2, pp. 13398–13406, 2014.

[22] H. W. Ro, J. M. Downing, S. Engmann, A. A. Herzing, D. M. Delongchamp, L. J. Richter, S. Mukherjee, H. Ade, M. Abdelsamie, L. K. Jagadamma, A. Amassian, Y. Liu, and H. Yan, "Morphology Changes Upon Scaling a High-Efficiency, Solution-Processed Solar Cell," *Energy & Environmental Science*, vol. 9, pp. 2835–2846, 2016.

[23] J. C. Aguirre, A. Ferreira, H. Ding, S. A. Jenekhe, N. Kopidakis, M. Asta, L. Pilon, Y. Rubin, S. H. Tolbert, B. J. Schwartz, B. Dunn, and V. Ozolins, "Panoramic View of Electrochemical Pseudocapacitor and Organic Solar Cell Research in Molecularly Engineered Energy Materials," *Journal of Physical Chemistry C*, vol. 118, pp. 19505–19523, 2014.

[24] Y. Tamai, H. Ohkita, H. Benten, and S. Ito, "Exciton Diffusion in Conjugated Polymers: From Fundamental Understanding to Improvement in Photovoltaic Conversion Efficiency," *Journal of Physical Chemistry Letters*, vol. 6, no. 17, pp. 3417–3428, 2015.

[25] B. Y. Finck and B. J. Schwartz, "Drift-Diffusion Studies of Compositional Morphology in Bulk Heterojunctions: The Role of the Mixed Phase in Photovoltaic Performance," *Physical Review Applied*, vol. 6, no. 5, p. 054008, 2016.

[26] J. Zhao, Y. Li, G. Yang, K. Jiang, H. Lin, H. Ade, M. Wei, and H. Yan, "Efficient Organic Solar Cells Processed from Hydrocarbon Solvents," *Nature Energy*, vol. 1, p. 15027, 2016.

[27] J. C. Bijleveld, V. S. Gevaerts, D. D. Nuzzo, M. Turbiez, S. G. J. Mathijssen, D. M. de Leeuw, M. M. Wienk, R. A. J. Janssen, D. M. de Leeuw, M. M. Wienk, and R. A. J. Janssen, "Efficient Solar Cells Based on an Easily Accessible Diketopyrrolopyrrole Polymer," *Adv. Mater.*, vol. 2, pp. E242—-E246, 2010.

[28] C. M. Amb, S. Chen, K. R. Graham, J. Subbiah, C. E. Small, F. So, and J. R. Reynolds, "Dithienogermole As a Fused Electron Donor in Bulk Heterojunction," *Journal of the American Chemical Society*, vol. 133, pp. 10062–10065, 2011.

[29] X. Guo, C. Cui, M. Zhang, L. Huo, Y. Huang, and Y. Li, "High Efficiency Polymer Solar Cells Based on Poly(3-hexylthiophene)/Indene-C70 Bisadduct with Solvent Additive," *Energy and Environmental Science*, vol. 5, pp. 7943–7949, 2012.

[30] J. S. Moon, C. J. Takacs, S. Cho, R. C. Coffin, H. Kim, G. C. Bazan, and A. J. Heeger, "Effect of Processing Additive on the Nanomorphology of a Bulk Heterojunction Material," *Nano Letters*, vol. 10, pp. 4005–4008, 2010.

[31] A. Zusan, M. Zerson, V. Dyakonov, and R. Magerle, "The Effect of Diiodooctane on the Charge Carrier Generation in Organic Solar Cells Based on the Copolymer PBDTTT-C," *Scientific Reports*, vol. 5, p. 8286, 2015.

[32] S. Kwon, J. K. Park, G. Kim, J. Kong, G. C. Bazan, and K. Lee, "Synergistic Effect of Processing Additives and Optical Spacers in Bulk-Heterojunction Solar Cells," *Adv. Energy Mater.*, vol. 2, pp. 1420–1424, 2012.

[33] B. A. Collins, Z. Li, J. R. Tumbleston, E. Gann, C. R. Mcneill, and H. Ade, "Absolute Measurement of Domain Composition and Nanoscale Size Distribution Explains Performance in PTB7:PC71BM Solar Cells," *Advanced Energy Materials*, vol. 3, pp. 65–74, 2013.

[34] C. V. Hoven, X.-D. Dang, R. C. Coffin, J. Peet, T.-Q. Nguyen, and G. C. Bazan, "Improved Performance of Polymer Bulk Heterojunction Solar Cells Through the Reduction of Phase Separation via Solvent Additives," *Advanced Energy Materials*, vol. 22, pp. 63–66, 2010.

[35] M.-S. Su, C.-Y. Kuo, M.-C. Yuan, U.-S. Jeng, C.-J. Su, and K.-H. Wei, "Improving Device Efficiency of Polymer/Fullerene Bulk Heterojunction Solar Cells Through Enhanced Crystallinity and Reduced Grain Boundaries Induced by Solvent Additives," *Advanced Materials*, vol. 23, pp. 3315–3319, 2011.

[36] Y. Zhang, Z. Li, S. Wakim, S. Alem, S.-W. Tsang, J. Lu, J. Ding, and Y. Tao, "Bulk Heterojunction Solar Cells Based on a New Low-Band-Gap Polymer: Morphology and Performance," *Organic Electronics*, vol. 12, no. 7, pp. 1211–1215, 2011.

[37] A. L. Ayzner, C. J. Tassone, S. H. Tolbert, and B. J. Schwartz, "Reappraising the Need for Bulk Heterojunctions in Polymer-Fullerene Photovoltaics: The Role of Carrier Transport in All-Solution-Processed P3HT/PCBM Bilayer Solar Cells," *J. Phys. Chem. C*, vol. 113, pp. 20050–20060, 2009.

[38] J. C. Aguirre, C. Arntsen, S. Hernandez, R. Huber, A. M. Nardes, M. Halim, D. Kilbride, Y. Rubin, S. H. Tolbert, N. Kopidakis, B. J. Schwartz, and D. Neuhauser, "Understanding Local and Macroscopic Electron Mobilities in the Fullerene Network of Conjugated Polymer-Based Solar Cells: Time-Resolved Microwave Conductivity and Theory," *Advanced Functional Materials*, vol. 24, pp. 784–792, feb 2014.

[39] S. van Franeker, Jacobus J Kouijzer, X. Lou, M. Turbiez, M. M. Wienk, and R. A. J. Janssen, "Depositing Fullerenes in Swollen Polymer Layers via Sequential Processing of Organic Solar Cells," *Advanced Energy Materials*, vol. 5, p. 1500464, 2015.

[40] B. K. Vandewal, A. Gadisa, W. D. Oosterbaan, S. Bertho, F. Banishoeib, I. V. Severen, L. Lutsen, T. J. Cleij, D. Vanderzande, and J. V. Manca, "The Relation Between Open-Circuit Voltage and the Onset of Photocurrent Generation by Charge-Transfer Absorption in Polymer: Fullerene Bulk Heterojunction Solar Cells," *Advanced Functional Materials*, vol. 18, pp. 2064–2070, 2008.

[41] T. Kirchartz, B. E. Pieters, J. Kirkpatrick, U. Rau, and J. Nelson, "Recombination via Tail States in Polythiophene:Fullerene Solar Cells," *Physical Review B - Condensed Matter and Materials Physics*, vol. 83, no. 11, p. 115209, 2011.

[42] S. A. Hawks, F. Deledalle, J. Yao, D. G. Rebois, G. Li, J. Nelson, Y. Yang, T. Kirchartz, and J. R. Durrant, "Relating Recombination , Density of States , and Device Performance in an Efficient Polymer: Fullerene Organic Solar Cell Blend," *Advanced Energy Materials*, vol. 3, pp. 1201–1209, 2013.

[43] S. Venkatesan, N. Adhikari, J. Chen, E. C. Ngo, A. Dubey, D. W. Galipeau, and Q. Qiao, "Interplay of Nanoscale Domain Purity on Charge Transport and Recombination Dynamics in Polymer Solar Cells," *Nanoscale*, vol. 6, pp. 1011–1019, 2014.

[44] Y. Lin, L. Ma, Y. Li, Y. Liu, D. Zhu, and X. Zhan, "Small-Molecule Solar Cells with Fill Factors up to 0.75 via a Layer-by-Layer Solution Process," *Advanced Energy Materials*, vol. 4, p. 1300626, 2014.

[45] M. C. Scharber, D. Mühlbacher, M. Koppe, P. Denk, C. Waldauf, A. J. Heeger, and C. J. Brabec, "Design Rules for Donors in Bulk-Heterojunction Solar Cells - Towards 10 % Energy-Conversion Efficiency," *Advanced Materials*, vol. 18, no. 6, pp. 789–794, 2006.

[46] A. C. Morteani, P. Sreearunothai, L. M. Herz, R. H. Friend, and C. Silva, "Exciton Regeneration at Polymeric Semiconductor Heterojunctions," *Physical Review Letters*, vol. 92, no. 24, p. 247402, 2004.

[47] Y. He, H.-Y. Chen, J. Hou, and Y. Li, "Indene-C60 Bisadduct: A New Acceptor for High-Performance Polymer Solar Cells," *Journal of the American Chemical Society*, vol. 132, no. 4, pp. 1377–1382, 2010.

[48] B. Kim, J. Lee, J. H. Seo, F. Wudl, S. H. Park, and C. Yang, "Regioselective 1,2,3-bisazfulleroid: Doubly N-Bridged bisimino-PCBMs for Polymer Solar Cells," *Journal of Materials Chemistry*, vol. 22, no. 43, pp. 22958–22963, 2012.

[49] S. Huang, G. Zhang, N. S. Knutson, M. T. Fontana, R. C. Huber, A. S. Ferreira, S. H. Tolbert, J. Schwartz, and Y. Rubin, "Beyond PCBM: Methoxylated 1,4-Bisbenzyl[60]fullerene Adducts for Efficient Organic Solar Cells," *Journal of Materials Chemistry A: Materials for energy and sustainability*, vol. 4, no. 2, pp. 416–424, 2015.

[50] C. Huang, S. Barlow, and S. R. Marder, "Perylene-3,4,9,10-Tetracarboxylic Acid Diimides: Synthesis, Physical Properties, and Use in Organic Electronics," *Journal of Organic Chemistry*, vol. 76, no. 8, pp. 2386–2407, 2011.

[51] G. Zhang, J. Zhao, P. C. Y. Chow, K. Jiang, J. Zhang, Z. Zhu, J. Zhang, F. Huang, and H. Yan, "Nonfullerene Acceptor Molecules for Bulk Heterojunction Organic Solar Cells," *Chemical Reviews*, vol. 118, pp. 3447–3507, 2018.

[52] H. Langhals, O. Krotz, K. Polborn, and P. Mayer, "A Novel Fluorescent Dye with Strong, Anisotropic Solid-State Fluorescence, Small Stokes Shift, and High Photostability," *Angewandte Chemie - International Edition*, vol. 44, no. 16, pp. 2427–2428, 2005.

[53] X. Zhan, A. Facchetti, S. Barlow, T. J. Marks, M. A. Ratner, M. R. Wasielewski, and S. R. Marder, "Rylene and related diimides for organic electronics," *Advanced Materials*, vol. 23, no. 2, pp. 268–284, 2011.

[54] F. J. Céspedes-Guirao, S. García-Santamaría, F. Fernández-Lázaro, A. Sastre-Santos, and H. J. Bolink, "Efficient Electroluminescence from a Perylenediimide Fluorophore Obtained from a Simple Solution Processed OLED," *Journal of Physics D: Applied Physics*, vol. 42, no. 10, p. 105106, 2009.

[55] E. Kozma, W. Mróz, F. Villafiorita-Monteleone, F. Galeotti, A. Andicsová-Eckstein, M. Catellani, and C. Botta, "Perylene Diimide Derivatives as Red and Deep Red-Emitters for Fully Solution Processable OLEDs," *RSC Advances*, vol. 6, no. 66, pp. 61175–61179, 2016.

[56] S. Rajaram, R. Shivanna, S. K. Kandappa, and K. S. Narayan, "Nonplanar Perylene Diimides as Potential Alternatives to Fullerenes in Organic Solar Cells," *Journal of Physical Chemistry Letters*, vol. 3, no. 17, pp. 2405–2408, 2012.

[57] W. Jiang, L. Ye, X. Li, C. Xiao, F. Tan, W. Zhao, J. Hou, and Z. Wang, "Bay-Linked Perylene Bisimides as Promising Non-Fullerene Acceptors for Organic Solar Cells," *Chem. Commun.*, vol. 50, no. 8, pp. 1024–1026, 2014.

[58] C.-H. Wu, C.-C. Chueh, Y.-Y. Xi, H.-L. Zhong, G.-P. Gao, Z.-H. Wang, L. D. Pozzo, T.-C. Wen, and A. K.-Y. Jen, "Influence of Molecular Geometry of Perylene Diimide Dimers and Polymers on Bulk Heterojunction Morphology Toward High-Performance Nonfullerene Polymer Solar Cells," *Advanced Functional Materials*, vol. 25, no. 33, pp. 5326–5332, 2015.

[59] J. Zhao, Y. Li, H. Lin, Y. Liu, K. Jiang, C. Mu, T. Ma, J. Y. Lin Lai, H. Hu, D. Yu, and H. Yan, "High-Efficiency Non-Fullerene Organic Solar Cells Enabled by a Difluorobenzothiadiazole-Based Donor Polymer Combined with a Properly Matched Small Molecule Acceptor," *Energy Environ. Sci.*, vol. 8, no. 2, pp. 520–525, 2015.

[60] D. Sun, D. Meng, Y. Cai, B. Fan, Y. Li, W. Jiang, L. Huo, Y. Sun, and Z. Wang, "Non-Fullerene-Acceptor-Based Bulk-Heterojunction Organic Solar Cells with Efficiency Over 7%," *J. Am. Chem. Soc.*, vol. 137, no. 34, pp. 11156–11162, 2015.

[61] D. Meng, D. Sun, C. Zhong, T. Liu, B. Fan, L. Huo, Y. Li, W. Jiang, H. Choi, T. Kim, J. Y. Kim, Y. Sun, Z. Wang, and A. J. Heeger, "High-Performance Solution-Processed Non-Fullerene Organic Solar Cells Based on Selenophene-Containing Perylene Bisimide Acceptor," *Journal of the American Chemical Society*, vol. 138, no. 1, pp. 375–380, 2016.

[62] J. Zhang, Y. Li, J. Huang, H. Hu, G. Zhang, T. Ma, P. C. Chow, H. Ade, D. Pan, and H. Yan, "Ring-Fusion of Perylene Diimide Acceptor Enabling Efficient Nonfullerene Organic Solar Cells with a Small Voltage Loss," *Journal of the American Chemical Society*, vol. 139, no. 45, pp. 16092–16095, 2017.

[63] Q. Yan, Y. Zhou, Y.-Q. Zheng, J. Pei, and D. Zhao, "Towards Rational Design of Organic Electron Acceptors for Photovoltaics: A Study Based on Perylenediimide Derivatives," *Chemical Science*, vol. 4, no. 12, pp. 4389–4394, 2013.

[64] F. C. Spano, "The Spectral Signatures of Frenkel Polarons in H- and J-Aggregates," *Accounts of Chemical Research*, vol. 43, no. 3, pp. 429–439, 2010.

[65] N. J. Hestand and F. C. Spano, "Molecular Aggregate Photophysics beyond the Kasha Model: Novel Design Principles for Organic Materials," *Accounts of Chemical Research*, vol. 50, pp. 341–350, 2017.

[66] J. P. Heremans, "Thermoelectricity: The Ugly Duckling," *Nature*, vol. 508, no. 1, pp. 327–328, 2008.

[67] G. J. Snyder and E. S. Toberer, "Complex Thermoelectric Materials," *Nature Materials*, vol. 7, no. 2, pp. 105–114, 2008.

[68] B. Russ, A. Glaudell, J. J. Urban, M. L. Chabinyc, and R. A. Segalman, "Organic Thermoelectric Materials for Energy Harvesting and Temperature Control," *Nature Reviews Materials*, vol. 1, no. 10, pp. 1–14, 2016.

[69] K.-H. Yim, G. L. Whiting, C. E. Murphy, J. J. M. Halls, J. H. Burroughes, R. H. Friend, and J.-S. Kim, "Controlling Electrical Properties of Conjugated Polymers via a Solution-Based p-Type Doping," *Advanced Materials*, vol. 20, no. 17, pp. 3319–3324, 2008.

[70] Y. Zhang, B. de Boer, and P. W. M. Blom, "Controllable Molecular Doping and Charge Transport in Solution-Processed Polymer Semiconducting Layers," *Advanced Functional Materials*, vol. 19, no. 12, pp. 1901–1905, 2009.

[71] P. Pingel and D. Neher, "Comprehensive picture of p-type doping of P3HT with the molecular acceptor F4TCNQ," *Physical Review B*, vol. 87, no. 11, p. 115209, 2013.

[72] J. Gao, J. D. Roegling, Y. Li, H. Guo, A. J. Moulé, and J. K. Grey, "The Effect of 2,3,5,6-Tetrafluoro-7,7,8,8-tetracyanoquinodimethane Charge Transfer Dopants on the Conformation and Aggregation of Poly(3-hexylthiophene)," *Journal of Materials Chemistry C*, vol. 1, no. 36, pp. 5638–5646, 2013.

[73] J. Gao, E. T. Niles, and J. K. Grey, "Aggregates Promote Efficient Charge Transfer Doping of Poly(3-hexylthiophene)," *Journal of Physical Chemistry Letters*, vol. 4, no. 17, pp. 2953–2957, 2013.

[74] D. T. Scholes, S. A. Hawks, P. Y. Yee, H. Wu, J. R. Lindemuth, S. H. Tolbert, and B. J. Schwartz, "Overcoming Film Quality Issues for Conjugated Polymers Doped with F4TCNQ by Solution Sequential Processing: Hall Effect, Structural, and Optical Measurements," *The Journal of Physical Chemistry Letters*, vol. 6, pp. 4786–4793, 2015.

[75] D. T. Scholes, P. Y. Yee, J. R. Lindemuth, H. Kang, J. Onorato, R. Ghosh, C. K. Luscombe, F. C. Spano, S. H. Tolbert, and B. J. Schwartz, "The Effects of Crystallinity on Charge Transport and the Structure of Sequentially Processed F4TCNQ-Doped Conjugated Polymer Films," *Advanced Functional Materials*, vol. 1702654, pp. 1–13, 2017.

[76] F. Deschler, D. Riedel, A. Deák, B. Ecker, E. von Hauff, and E. Da Como, "Imaging of Morphological Changes and Phase Segregation in Doped Polymeric Semiconductors," *Synthetic Metals*, vol. 199, pp. 381–387, 2015.

[77] L. Müller, D. Nanova, T. Glaser, S. Beck, A. Pucci, A. K. Kast, R. R. Schröder, E. Mankel, P. Pingel, D. Neher, W. Kowalsky, and R. Lovrincic, "Charge-Transfer-Solvent Interaction Predefines Doping Efficiency in p-Doped P3HT Films," *Chem. Mater.*, vol. 28, no. 12, pp. 4432–4439, 2016.

[78] A. M. Glaudell, J. E. Cochran, S. N. Patel, and M. L. Chabinyc, "Impact of the Doping Method on Conductivity and Thermopower in Semiconducting Polythiophenes," *Advanced Energy Materials*, vol. 5, no. 4, p. 1401072, 2015.

[79] K. Kang, S. Watanabe, K. Broch, A. Sepe, A. Brown, I. Nasrallah, M. Nikolka, Z. Fei, M. Heeney, D. Matsumoto, K. Marumoto, H. Tanaka, S.-i. Kuroda, and H. Sirringhaus, "2D Coherent Charge Transport in Highly Ordered Conducting Polymers Doped by Solid State Diffusion," *Nature Materials*, vol. 15, no. 5, pp. 896–903, 2016.

[80] S. N. Patel, A. M. Glaudell, D. Kiefer, and M. L. Chabinyc, "Increasing the Thermoelectric Power Factor of a Semiconducting Polymer by Doping from the Vapor Phase," *ACS Macro Letters*, vol. 5, no. 3, pp. 268–272, 2016.

[81] S. N. Patel, A. M. Glaudell, K. A. Peterson, E. M. Thomas, K. A. O'Hara, E. Lim, and M. L. Chabinyc, "Morphology Controls the Thermoelectric Power Factor of a Doped Semiconducting Polymer," *Science Advances*, vol. 3, no. 6, pp. 24–26, 2017.

[82] J. Hynynen, D. Kiefer, L. Yu, R. Kroon, R. Munir, A. Amassian, M. Kemerink, and C. Müller, "Enhanced Electrical Conductivity of Molecularly p-Doped Poly(3-hexylthiophene) Through Understanding the Correlation with Solid-State Order," *Macromolecules*, vol. 50, no. 20, pp. 8140–8148, 2017.

[83] E. Lim, K. A. Peterson, G. M. Su, and M. L. Chabinyc, "Thermoelectric Properties of Poly(3-hexylthiophene) (P3HT) Doped with 2,3,5,6-Tetrafluoro-7,7,8,8-tetracyanoquinodimethane (F4TCNQ) by Vapor-Phase Infiltration," *Chemistry of Materials*, vol. 30, no. 3, pp. 998–1010, 2018.

[84] G. Yu, J. Gao, J. C. Hummelen, W. F, and A. J. Heeger, "Polymer Photovoltaic Cells: Enhanced Efficiencies via a Network of Internal Donor- Acceptor Heterojunctions," *Science*, vol. 270, no. 5243, pp. 1789–1791, 1995.

[85] B. C. Thompson and J. M. J. Fréchet, "Polymer - Fullerene Composite Solar Cells," *Angew. Chemie*, vol. 47, pp. 58–77, 2008.

[86] Y. Liang and L. Yu, "A New Class of Semiconducting Polymers for Bulk Heterojunction Solar Cells with Exceptionally High Performance," *Accounts of Chemical Research*, vol. 43, no. 9, pp. 1227–1236, 2010.

[87] P. W. M. Blom, V. D. Mihailetchi, L. J. A. Koster, and D. E. Markov, "Device Physics of Polymer:Fullerene Bulk Heterojunction Solar Cells," *Adv. Mater.*, vol. 19, pp. 1551–1566, 2007.

[88] I. A. Howard, J. M. Hodgkiss, X. Zhang, K. R. Kirov, H. A. Bronstein, C. K. Williams, R. H. Friend, S. Westenhoff, and N. C. Greenham, "Charge Recombination and Exciton Annihilation Reactions in Conjugated Polymer Blends," *Journal of the American Chemical Society*, vol. 132, no. 16, pp. 328–335, 2010.

[89] G. Li, R. Zhu, and Y. Yang, "Polymer Solar Cells," *Nature Photonics*, vol. 6, no. February, pp. 153–161, 2012.

[90] A. A. Bakulin, A. Rao, V. G. Pavelyev, P. H. M. van Loosdrecht, M. S. Pshenichnikov, D. Niedzialek, J. Cornil, D. Beljonne, and R. H. Friend, "The Role of Driving Energy and Delocalized States for Charge Separation in Organic Semiconductors," *Science*, vol. 335, no. March, pp. 1340–1344, 2012.

[91] K. Vandewal, S. Albrecht, E. T. Hoke, K. R. Graham, J. Widmer, J. D. Douglas, M. Schubert, W. R. Mateker, J. T. Bloking, G. F. Burkhard, A. Sellinger, J. M. J. Fréchet, A. Amassian, M. K. Riede, M. D. Mcgehee, D. Neher, and A. Salleo, "Efficient Charge Generation by Relaxed Charge-Transfer States at Organic Interfaces," *Nat. Mater.*, vol. 13, no. 1, pp. 63–68, 2014.

[92] T. M. Clarke and J. R. Durrant, "Charge Photogeneration in Organic Solar Cells," *Chemical Reviews*, vol. 110, pp. 6736–6767, 2010.

[93] F. Gao, W. Tress, J. Wang, and O. Inganäs, "Temperature Dependence of Charge Carrier Generation in Organic Photovoltaics," *Phys. Rev. Lett.*, vol. 114, no. 3, p. 128701, 2015.

[94] S. S. van Bavel, E. Sourty, G. D. With, and J. Loos, "Three-Dimensional Nanoscale Organization of Bulk Heterojunction Polymer Solar Cells," *Nano Letters*, vol. 9, no. 2, pp. 507–513, 2009.

[95] J. J. M. Halls, C. A. Walsh, N. C. Greenham, E. A. Marseglia, R. H. Friend, S. C. Moratti, and A. B. Holmes, "Efficient Photodiodes from Interpenetrating Polymer Networks," *Nature*, vol. 376, pp. 498–500, 1995.

[96] S. E. Shaheen, C. J. Brabec, N. S. Sariciftci, F. Padinger, T. Fromherz, and J. C. Hummelen, "2.5% Efficient Organic Plastic Solar Cells," *Applied Physics Letters*, vol. 78, pp. 841–843, 2001.

[97] B. A. Collins, J. R. Tumbleston, and H. Ade, "Miscibility, Crystallinity, and Phase Development in P3HT/PCBM Solar Cells: Toward an Enlightened Understanding of Device Morphology and Stability," *Journal of Physical Chemistry Letters*, vol. 2, pp. 3135–3145, 2011.

[98] B. W. Ma, C. Yang, X. Gong, K. Lee, and A. J. Heeger, "Thermally Stable, Efficient Polymer Solar Cells with Nanoscale Control of the Interpenetrating Network Morphology," *Advanced Functional Materials*, vol. 15, pp. 1617–1622, 2005.

[99] A. L. Ayzner, D. D. Wanger, C. J. Tassone, S. H. Tolbert, and B. J. Schwartz, "Room to Improve Conjugated Polymer-Based Solar Cells: Understanding How Thermal Annealing Affects the Fullerene Component of a Bulk Heterojunction Photovoltaic Device," *J. Phys. Chem. C Lett.*, vol. 112, pp. 18711–18716, 2008.

[100] K. H. Lee, Y. Zhang, P. L. Burn, I. R. Gentle, M. James, A. Nelson, and P. Meredith, "Correlation of Diffusion and Performance in Sequentially Processed P3HT/PCBM Heterojunction Films by Time-Resolved Neutron Reflectometry," *Journal of Materials Chemistry C*, vol. 1, pp. 2593–2598, 2013.

[101] K. H. Lee, P. E. Schwenn, A. R. G. Smith, H. Cavaye, P. E. Shaw, M. James, K. B. Krueger, I. R. Gentle, P. Meredith, and P. L. Burn, "Morphology of All-Solution-Processed "Bilayer" Organic Solar Cells," *Advanced Materials*, vol. 23, no. 2011, pp. 766–770, 2011.

[102] G. Zhang, R. C. Huber, A. S. Ferreira, S. D. Boyd, C. K. Luscombe, S. H. Tolbert, and B. J. Schwartz, "Crystallinity Effects in Sequentially Processed and Blend-Cast Bulk-Heterojunction Polymer/Fullerene Photovoltaics," *The Journal of Physical Chemistry C*, vol. 118, pp. 18424–18435, 2014.

[103] B. G. Li, Y. Yao, H. Yang, V. Shrotriya, G. Yang, and Y. Yang, ""Solvent Annealing" Effect in Polymer Solar Cells Based on Poly(3-hexylthiophene) and Methanofullerenes," *Advanced Functional Materials*, vol. 17, pp. 1636–1644, 2007.

[104] Y. Zhao, Z. Xie, Y. Qu, Y. Geng, L. Wang, Y. Zhao, Z. Xie, Y. Qu, Y. Geng, and L. Wang, "Solvent-Vapor Treatment Induced Performance Enhancement of Poly(3-hexylthiophene):Methanofullerene Bulk-Heterojunction Photovoltaic Cells," *Applied Physics Letters*, vol. 90, no. 2007, p. 043504, 2007.

[105] B. Walker, A. Tamayo, D. T. Duong, X.-D. Dang, C. Kim, J. Granstrom, and T.-Q. Nguyen, "A Systematic Approach to Solvent Selection Based on Cohesive Energy Densities in a Molecular Bulk Heterojunction System," *Advanced Energy Materials*, vol. 1, pp. 221–229, 2011.

[106] J. Peet, C. Soci, R. C. Coffin, T. Q. Nguyen, A. Mikhailovsky, D. Moses, and G. C. Bazan, "Method for Increasing the Photoconductive Response in Conjugated Polymer/Fullerene Composites," *Applied Physics Letters*, vol. 89, p. 252105, 2006.

[107] J. Peet, J. Y. Kim, N. E. Coates, W. L. Ma, D. Moses, A. J. Heeger, and G. C. Bazan, "Efficiency Enhancement in Low-Bandgap Polymer Solar Cells by Processing with Alkane Dithiols," *Nat. Mater.*, vol. 6, pp. 497–500, 2007.

[108] X. Guo, M. Zhang, W. Ma, L. Ye, S. Zhang, S. Liu, H. Ade, F. Huang, and J. Hou, "Enhanced Photovoltaic Performance by Modulating Surface Composition in Bulk Heterojunction Polymer Solar Cells Based on PBDTTT-C-T/PC 71BM," *Advanced Materials*, vol. 26, pp. 4043–4049, 2014.

[109] Y. Liu, J. Zhao, Z. Li, C. Mu, W. Ma, H. Hu, K. Jiang, H. Lin, H. Ade, and H. Yan, "Aggregation and Morphology Control Enables Multiple Cases of High-Efficiency Polymer Solar Cells," *Nature Communications*, vol. 5, no. 9, p. 5293, 2014.

[110] S. Kwon, H. Kang, J.-H. Lee, J. Lee, S. Hong, H. Kim, and K. Lee, "Effect of Processing Additives on Organic Photovoltaics: Recent Progress and Future Prospects," *Advanced Energy Materials*, vol. 7, no. 10, p. 1601496, 2016.

[111] L. Lu, T. Zheng, Q. Wu, A. M. Schneider, D. Zhao, and L. Yu, "Recent Advances in Bulk Heterojunction Polymer Solar Cells," *Chemical Reviews*, vol. 115, pp. 12666–12731, 2015.

[112] F. C. Krebs, "Fabrication and Processing of Polymer Solar Cells : A Review of Printing and Coating Techniques," *Solar Energy Materials and Solar Cells*, vol. 93, pp. 394–412, 2009.

[113] M. Jørgensen, J. E. Carlé, R. R. Søndergaard, M. Lauritzen, N. A. Dagnæs-Hansen, S. L. Byskov, T. R. Andersen, T. T. Larsen-Olsen, A. P. L. Böttiger, B. Andreasen, L. Fu, L. Zuo, Y. Liu, E. Bundgaard, X. Zhan, H. Chen, and F. C. Krebs, "The State of Organic Solar Cells-A Meta Analysis," *Sol. Energy Mater. Sol. Cells*, vol. 119, pp. 84–93, 2013.

[114] P. Cheng, Y. Lin, N. K. Zawacka, T. R. Andersen, W. Liu, E. Bundgaard, M. Jorgensen, H. Chen, F. C. Krebs, X. Zhan, M. Jørgensen, H. Chen, F. C. Krebs, and X. Zhan, "Comparison of additive amount used in spin-coated and roll-coated organic solar cells," *Journal of Materials Chemistry A*, vol. 2, no. 45, pp. 19542–19549, 2014.

[115] D. H. Wang, H. K. Lee, D.-G. Choi, J. H. Park, and O. O. Park, "Solution-Processable Polymer Solar Cells from a poly(3-hexylthiophene/[6,6]-phenyl C 61 -Butyric Acidmethyl Ester Concentration Graded Bilayers," *Applied Physics Letters*, vol. 95, no. 2009, p. 043505, 2009.

[116] A. Loiudice, A. Rizzo, G. Latini, C. Nobile, M. D. Giorgi, and G. Gigli, "Graded Vertical Phase Separation of Donor/Acceptor Species for Polymer Solar Cells," *Solar Energy Materials and Solar Cells*, vol. 100, pp. 147–152, 2012.

[117] Z. Xu, L.-M. Chen, G. Yang, C.-H. Huang, J. Hou, Y. Wu, G. Li, C.-S. Hsu, and Y. Yang, "Vertical Phase Separation in Poly(3-hexylthiophene): Fullerene Derivative Blends and its Advantage for Inverted Structure Solar Cells," *Advanced Functional Materials*, vol. 19, pp. 1227–1234, 2009.

[118] S. A. Mauger, L. Chang, S. Friedrich, C. W. Rochester, D. M. Huang, P. Wang, and A. J. Moulé, "Self-Assembly of Selective Interfaces in Organic Photovoltaics," *Advanced Functional Materials*, vol. 23, pp. 1935–1946, 2013.

[119] N. D. Treat, M. A. Brady, G. Smith, M. F. Toney, E. J. Kramer, C. J. Hawker, and M. L. Chabinyc, "Interdiffusion of PCBM and P3HT Reveals Miscibility in a Photovoltaically Active Blend," *Advanced Energy Materials*, vol. 1, pp. 82–89, 2011.

[120] A. Gadisa, J. R. Tumbleston, D.-H. Ko, M. Aryal, R. Lopez, and E. T. Samulski, "The Role of Solvent and Morphology on Miscibility of Methanofullerene and Poly(3-hexylthiophene)," *Thin Solid Films*, vol. 520, no. 16, pp. 5466–5471, 2012.

[121] Z. M. Beiley, E. T. Hoke, R. Noriega, J. Dacuña, G. F. Burkhard, J. A. Bartelt, A. Salleo, M. F. Toney, and M. D. McGehee, "Morphology-Dependent Trap Formation in High Performance Polymer Bulk Heterojunction Solar Cells," *Advanced Energy Materials*, vol. 1, no. 5, pp. 954–962, 2011.

[122] Y. Gu, C. Wang, and T. P. Russell, "Multi-Length-Scale Morphologies in PCPDTBT/PCBM Bulk-Heterojunction Solar Cells," *Advanced Energy Materials*, vol. 2, pp. 683–690, 2012.

[123] T. Wang, A. J. Pearson, A. D. F. Dunbar, P. A. Staniec, D. C. Watters, H. Yi, A. J. Ryan, R. A. L. Jones, A. Iraqi, and D. G. Lidzey, "Correlating Structure with Function in Thermally Annealed PCDTBT:PC70BM Photovoltaic Blends," *Adv. Funct. Mater.*, vol. 22, no. 7, pp. 1399–1408, 2012.

[124] J. A. Bartelt, Z. M. Beiley, E. T. Hoke, W. R. Mateker, J. D. Douglas, B. A. Collins, J. R. Tumbleston, K. R. Graham, A. Amassian, H. Ade, J. M. J. Fréchet, M. F. Toney, and M. D. McGehee, "The Importance of Fullerene Percolation in the Mixed Regions of Polymer-Fullerene Bulk Heterojunction Solar Cells," *Advanced Energy Materials*, vol. 3, pp. 364–374, mar 2013.

[125] S. H. Park, A. Roy, S. Beaupré, S. Cho, N. Coates, J. S. Moon, D. Moses, M. Leclerec, K. Lee, and A. J. Heeger, "Bulk Heterojunction Solar Cells with Internal Quantum Efficiency Approaching 100%," *Nat. Photonics*, vol. 3, no. 4, pp. 297–303, 2009.

[126] T.-Y. Chu, S. Alem, S.-W. Tsang, S.-C. Tse, S. Wakim, J. Lu, G. Dennler, R. Gaudiana, and Y. Tao, "Morphology Control in Polycarbazole Based Bulk Heterojunction Solar Cells and its Impact on Device Performance," *Appl. Phys. Lett.*, vol. 98, p. 253301, 2011.

[127] S. A. Hawks, J. C. Aguirre, L. T. Schelhas, R. J. Thompson, R. C. Huber, A. S. Ferreira, G. Zhang, A. A. Herzing, S. H. Tolbert, and B. J. Schwartz, "Comparing Matched Polymer:Fullerene Solar Cells Made by Solution-Sequential Processing and Traditional Blend Casting: Nanoscale Structure and Device Performance," *J. Phys. Chem. C*, vol. 118, pp. 17413–17425, 2014.

[128] A. L. Ayzner, S. C. Doan, B. Tremolet de Villers, and B. J. Schwartz, "Ultrafast Studies of Exciton Migration and Polaron Formation in Sequentially Solution-Processed Conjugated Polymer/Fullerene Quasi-Bilayer Photovoltaics," *Journal of Physical Chemistry Letters*, vol. 3, pp. 2281–2287, 2012.

[129] A. M. Nardes, A. L. Ayzner, S. R. Hammond, A. J. Ferguson, B. J. Schwartz, and N. Kopidakis, "Photoinduced Charge Carrier Generation and Decay in Sequentially Deposited Polymer / Fullerene Layers : Bulk Heterojunction vs Planar Interface," *Journal of Physical Chemistry C*, vol. 116, pp. 7293–7305, 2012.

[130] C. Tao, M. Aljada, P. E. Shaw, K. H. Lee, H. Cavaye, M. N. Balfour, R. J. Borthwick, M. James, P. L. Burn, I. R. Gentle, and P. Meredith, "Controlling Hierarchy in Solution-Processed Polymer Solar Cells Based on Crosslinked P3HT," *Adv. Energy Mater.*, vol. 3, pp. 105–112, 2013.

[131] V. S. Gevaerts, L. J. A. Koster, M. M. Wienk, and R. A. J. Janssen, "Discriminating Between Bilayer and Bulk Heterojunction Polymer: Fullerene Solar Cells Using the External Quantum Efficiency," *ACS Applied Materials & Interfaces*, vol. 3, pp. 3252–3255, 2011.

[132] B. Yang, Y. Yuan, and J. Huang, "Reduced Bimolecular Charge Recombination Loss in Thermally Annealed Bilayer Heterojunction Photovoltaic Devices with Large External Quantum Efficiency and Fill Factor," *The Journal of Physical Chemistry C*, vol. 118, pp. 5196–5202, 2014.

[133] D. Chen, F. Liu, C. Wang, A. Nakahara, and T. P. Russell, "Bulk Heterojunction Photovoltaic Active Layers via Bilayer Interdiffusion," *Nano Letters*, vol. 11, pp. 2071–2078, 2011.

[134] D. H. Wang, J. K. Kim, O. O. Park, and J. H. Park, "Analysis of Surface Morphological Changes in Organic Photovoltaic Devices: Bilayer versus Bulk-Heterojunction," *Energy and Environmental Science*, vol. 4, pp. 1434–1439, 2011.

[135] D. H. Wang, J. S. Moon, J. Seifter, J. Jo, J. H. Park, O. O. Park, and A. J. Heeger, "Sequential Processing: Control of Nanomorphology in Bulk Heterojunction Solar Cells," *Nano Letters*, vol. 11, pp. 3163–3168, 2011.

[136] R. Zhu, A. Kumar, and Y. Yang, "Polarizing Organic Photovoltaics," *Advanced Materials*, vol. 23, pp. 4193–4198, 2011.

[137] S.-M. Cho, J.-H. Bae, E. Jang, M.-H. Kim, C. Lee, and S.-D. Lee, "Solvent Effect of the Fibrillar Morphology on the Power Conversion Efficiency of a Polymer Photovoltaic Cell in a Diffusive Heterojunction," *Semiconductor Science and Technology*, vol. 27, p. 125018, 2012.

[138] H. Li, Y.-F. Li, and J. Wang, "Optimizing Performance of Layer-by-Layer Processed Polymer Solar Cells," *Applied Physics Letters*, vol. 101, p. 033907, 2012.

[139] A. Loiudice, A. Rizzo, M. Biasiucci, and G. Gigli, "Bulk Heterojunction versus Diffused Bilayer: The Role of Device Geometry in Solution p-Doped Polymer-Based Solar Cells," *The Journal of Physical Chemistry Letters*, vol. 3, pp. 1908–1915, 2012.

[140] V. Vohra, K. Higashimine, T. Murakami, and H. Murata, "Addition of Regiorandom Poly(3-hexylthiophene) to Solution Processed Graded Bilayers to Tune the Vertical Concentration Gradient," *Applied Physics Letters*, vol. 101, p. 173301, 2012.

[141] V. Vohra, G. Arrighetti, L. Barba, K. Higashimine, W. Porzio, and H. Murata, "Enhanced Vertical Concentration Gradient in Rubbed P3HT:PCBM Graded Bilayer Solar Cells," *The Journal of Physical Chemistry Letters*, vol. 3, pp. 1820–1823, 2012.

[142] V. Vohra, K. Higashimine, S. Tsuzaki, K. Ohdaira, and H. Murata, "Formation of Vertical Concentration Gradients in Poly(3-hexylthiophene-2,5,-diyl): Phenyl-C61-butyric Acid Methyl Ester-Graded Bilayer Solar Cells," *Thin Solid Films*, vol. 1500, pp. 1–5, 2013.

[143] V. Vohra, B. Dorling, K. Higashimine, and H. Murata, "Investigating the Effect of Solvent Boiling Temperature on the Morphology of P3HT:PCBM Diffusive Bilayer Solar Cells," *Appl. Phys. Express*, vol. 9, p. 112301, 2016.

[144] H. Y. Yang, N. S. Kang, J.-M. Hong, Y.-W. Song, T. W. Kim, and J. A. Lim, "Efficient Bilayer Heterojunction Polymer Solar Cells with Bumpy Donor - Acceptor Interface Formed by Facile Polymer Blend," *Organic Electronics*, vol. 13, no. 11, pp. 2688–2695, 2012.

[145] J. Y. Oh, T. I. Lee, W. S. Jang, S. S. Chae, J. H. Park, J.-M. Myoung, and H. K. Baik, "Mass Production of a 3D Non-Woven Nanofabric with Crystalline P3HT Nanofibrils for Organic Solar Cells," *Energy and Environmental Science*, vol. 6, pp. 910–917, 2013.

[146] C. W. Rochester, S. A. Mauger, and A. J. Moulé, "Investigating the Morphology of Polymer/Fullerene Layers Coated Using Orthogonal Solvents," *Journal of Physical Chemistry C*, vol. 116, pp. 7287–7292, 2012.

[147] P. Cheng, Y. Li, and X. Zhan, "A DMF-Assisted Solution Process Boosts the Efficiency in P3HT: PCBM Solar Cells," *Nanotechnology*, vol. 24, p. 484008, 2013.

[148] H. Li, Z. Qi, and J. Wang, "Layer-by-Layer Processed Polymer Solar Cells with Self-Assembled Electron Buffer Layer," *Applied Physics Letters*, vol. 102, p. 213901, 2013.

[149] B. Liu, R.-Q. Png, L.-H. Zhao, L.-L. Chua, R. H. Friend, and P. K. H. Ho, "High Internal Quantum Efficiency in Fullerene Solar Cells Based on Crosslinked Polymer Donor Networks," *Nat. Commun.*, vol. 3, pp. 1321–1328, 2012.

[150] H. J. Park, J. Y. Lee, T. Lee, and L. J. Guo, "Advanced Heterojunction Structure of Polymer Photovoltaic Cell Generating High Photocurrent with Internal Quantum Efficiency Approaching 100 %," *Advanced Energy Materials*, vol. 3, pp. 1135–1142, 2013.

[151] P. Cheng, C. Yan, Y. Wu, S. Dai, W. Ma, and X. Zhan, "Efficient and Stable Organic Solar Cells via a Sequential Process," *Journal of Materials Chemistry C*, vol. 4, pp. 8086–8093, 2016.

[152] Y. Liu, F. Liu, H.-W. Wang, D. Nordlund, Z. Sun, S. Ferdous, and T. P. Russell, "Sequential Deposition: Optimization of Solvent Swelling for High-Performance Polymer Solar Cells," *ACS Appl. Mater. Interfaces*, vol. 7, pp. 653–661, 2015.

[153] J. Seok, T. J. Shin, S. Park, C. Cho, J.-Y. Lee, D. Y. Ryu, M. H. Kim, and K. Kim, "Efficient Organic Photovoltaics Utilizing Nanoscale Heterojunctions in Sequentially Deposited Polymer/Fullerene Bilayer," *Scientific Reports*, vol. 5, p. 8373, 2015.

[154] W. Chen, Z. Du, M. Xiao, J. Zhang, C. Yang, L. Han, X. Bao, and R. Yang, "High-Performance Small Molecule/Polymer Ternary Organic Solar Cells Based on a Layer-By-Layer Process," *ACS Appl. Mater. Interfaces*, vol. 7, pp. 23190–23196, 2015.

[155] H. Li and J. Wang, "Layer-by-Layer Processed High-Performance Polymer Solar Cells," *Applied Physics Letters*, vol. 101, p. 263901, 2012.

[156] H. Li, Z.-G. Zhang, Y. Li, and J. Wang, "Tunable Open-Circuit Voltage in Ternary Organic Solar Cells," *Applied Physics Letters*, vol. 101, p. 163302, 2012.

[157] L. N. S. A. Thummalakunta, C. H. Yong, K. Ananthanarayanan, and J. Luther, "P3HT Based Solution-Processed Pseudo Bi-layer Organic Solar Cell with Enhanced Performance," *Organic Electronics*, vol. 13, no. 10, pp. 2008–2016, 2012.

[158] A. J. Clulow, C. Tao, K. H. Lee, M. Velusamy, J. A. Mcewan, P. E. Shaw, N. L. Yamada, M. James, P. L. Burn, I. R. Gentle, and P. Meredith, "Time-Resolved Neutron Reflectometry and Photovoltaic Device Studies on Sequentially Deposited PCDTBT-Fullerene Layers," *Langmuir*, vol. 30, pp. 11474–11484, 2014.

[159] D. Bartesaghi, G. Ye, R. C. Chiechi, and L. J. A. Koster, "Compatibility of PTB7 and [70]PCBM as a Key Factor for the Stability of PTB7:[70] PCBM Solar Cells," *Adv. Energy Mater.*, vol. 201502338, p. 1502338, 2016.

[160] D. H. Kim, J. Mei, A. L. Ayzner, K. Schmidt, G. Giri, A. L. Appleton, F. Toney, Z. Bao, M. F. Toney, Z. Bao, F. Toney, and Z. Bao, "Sequentially Solution-Processed, Nanostructured Polymer Photovoltaics Using Selective Solvents," *Energy Environ. Sci.*, vol. 7, pp. 1103–1109, 2014.

[161] L. Xie, J. S. Lee, Y. Jang, H. Ahn, Y.-H. Kim, and K. Kim, "Organic Photovoltaics Utilizing a Polymer Nanofiber/Fullerene Interdigitated Bilayer Prepared by Sequential Solution Deposition," *The Journal of Physical Chemistry C*, vol. 120, pp. 12933–12940, 2016.

[162] C. Lang, J. Fan, Y. Zhang, F. Guo, and L. Zhao, "Utilizing Intermixing of Conjugated Polymer and Fullerene from Sequential Solution Processing for Efficient Polymer Solar Cells," *Organic Electronics*, vol. 36, pp. 82–88, 2016.

[163] K. Yao, J. J. Intemann, H.-L. Yip, P.-W. Liang, and C.-Y. Chang, "Efficient All Polymer Solar Cells from Layer-Evolved Processing of a Bilayer Inverted Structure," *Journal of Materials Chemistry C*, vol. 2, pp. 416–420, 2014.

[164] T. Ghoos, O. Malinkiewicz, B. Conings, L. Lutsen, D. J. Vanderzande, J. Bolink, and W. Maes, "Solution-Processed Bi-Layer Polythiophene-Fullerene Organic Solar Cells," *RSC Advances*, vol. 3, pp. 25197–25203, 2013.

[165] C. E. Rogers, V. Stannett, and M. Szwarc, "The Sorption of Organic Vapors by Polyethylene," *Journal of Physical Chemistry*, vol. 63, no. 6, pp. 1406–1413, 1959.

[166] H. R. Brown, "Flory-Huggins-Rehner Theory and the Swelling of Semicrystalline Polymers by Organic Fluids," *Journal of Polymer Science: Polymer Physics Edition*, vol. 16, pp. 1887–1889, 1978.

[167] H.-C. Liao, C.-C. Ho, C.-Y. Chang, M.-H. Jao, S. B. Darling, and W.-F. Su, "Additives for Morphology Control in High-Efficiency Organic Solar Cells," *Mater. Today*, vol. 16, no. 9, pp. 326–336, 2013.

[168] J. K. Lee, W. L. Ma, C. J. Brabec, J. Yuen, J. S. Moon, J. Y. Kim, K. Lee, G. C. Bazan, and A. J. Heeger, "Processing Additives for Improved Efficiency from Bulk Heterojunction Solar Cells," *Journal of the American Chemical Society*, vol. 130, no. 17, pp. 3619–3623, 2008.

[169] J. S. Papanu, D. W. Hess, A. T. Bell, and S. D. S, "In Situ Ellipsometry to Monitor Swelling and Dissolution of Thin Polymer Films," *J. Electrochem. Soc.*, vol. 136, no. 4, pp. 1195–1200, 1989.

[170] A. Ng, C. H. Li, M. K. Fung, A. B. Djurišić, J. A. Zapien, W. K. Chan, K. Y. Cheung, and W.-Y. Wong, "Accurate Determination of the Index of Refraction of Polymer Blend Films by Spectroscopic Ellipsometry," *Journal of Physical Chemistry C*, vol. 114, no. 35, pp. 15094–15101, 2010.

[171] M. Campoy-Quiles, M. I. Alonso, D. D. C. Bradley, and L. J. Richter, "Advanced Ellipsometric Characterization of Conjugated Polymer Films," *Advanced Functional Materials*, vol. 24, pp. 2116–2134, 2014.

[172] H. Elbs and G. Krausch, "Ellipsometric Determination of Flory-Huggins Interaction Parameters in Solution," *Polymer*, vol. 45, pp. 7935–7942, 2004.

[173] H. Sven, M. Sommer, A. Chiche, G. Krausch, U. Steiner, and M. Thelakkat, "Controlled Solvent Vapour Annealing for Polymer Electronics," *Soft Matter*, vol. 5, pp. 4206–4211, 2009.

[174] W. Ogieglo, H. van der Werf, K. Tempelman, H. Wormeester, M. Wessling, A. Nijmeijer, and N. E. Benes, "n-Hexane Induced Swelling of Thin PDMS Films Under Non-Equilibrium Nanofiltration Permeation Conditions , Resolved by Spectroscopic Ellipsometry," *Journal of Membrane Science*, vol. 431, pp. 233–243, 2013.

[175] V. D. A. G. Bruggeman, "Berechnung Verschiedener Physikalischer Konstanten von Heterogenen Substanzen. I. Dielektrizitätskonstanten und Leitfähigkeiten der Mischkörper aus Isotropen Substanzen," *Ann. Phys.*, vol. 416, pp. 665–679, 1935.

[176] K. Spaeth, G. Kraus, and G. Gauglitz, "In-Situ Characterization of Thin Polymer Films for Applications in Chemical Sensing of Volatile Organic Compounds by Spectroscopic Ellipsometry," *Fresenius' Journal of Analytical Chemistry*, vol. 357, no. 3, pp. 292–296, 1997.

[177] K. Chan and K. K. Gleason, "Initiated Chemical Vapor Deposition of Linear and Cross-linked Poly (2-hydroxyethyl methacrylate) for Use as Thin-Film Hydrogels," *Langmuir*, vol. 21, no. 25, pp. 8930–8939, 2005.

[178] P. J. Flory, "Thermodynamics of High Polymer Solutions," *Journal of Chemical Physics*, vol. 10, pp. 51–61, 1942.

[179] P. J. Flory, "Statistical Thermodynamics of Liquid Mixtures," *Journal of the American Chemical Society*, vol. 87, no. 9, pp. 1833–1838, 1964.

[180] F. Machui, S. Langner, X. Zhu, S. Abbott, and C. J. Brabec, "Determination of the P3HT: PCBM Solubility Parameters via a Binary Solvent Gradient Method: Impact of Solubility on the Photovoltaic Performance," *Sol. Energy Mater. Sol. Cells*, vol. 100, pp. 138–146, 2012.

[181] M. R. Hammond, R. J. Kline, A. A. Herzing, L. J. Richter, D. S. Germack, H.-W. Ro, C. L. Soles, D. A. Fischer, T. Xu, L. Yu, M. F. Toney, and D. M. DeLongchamp, "Molecular Order in High-Efficiency Polyme/Fullerene Bulk Heterojunction Solar Cells," *ACS Nano*, vol. 5, no. 10, pp. 8248–8257, 2011.

[182] F. Liu, W. Zhao, J. R. Tumbleston, C. Wang, Y. Gu, D. Wang, A. L. Briseno, H. Ade, and T. P. Russell, "Understanding the Morphology of PTB7:PCBM Blends in Organic Photovoltaics," *Advanced Energy Materials*, vol. 4, no. 5, p. 1301377, 2014.

[183] A. C. Mayer, M. F. Toney, S. R. Scully, J. Rivnay, C. J. Brabec, M. Scharber, M. Koppe, M. Heeney, I. McCulloch, and M. D. McGehee, "Bimolecular Crystals of Fullerenes in Conjugated Polymers and the Implications of Molecular Mixing for Solar Cells," *Advanced Functional Materials*, vol. 19, no. 8, pp. 1173–1179, 2009.

[184] N. C. Cates, R. Gysel, Z. Beiley, C. E. Miller, M. F. Toney, M. Heeney, I. McCulloch, and M. D. McGehee, "Tuning the Properties of Polymer Bulk Heterojunction Solar Cells by Adjusting Fullerene Size to Control Intercalation," *Nano Letters*, vol. 9, no. 12, pp. 4153–4157, 2009.

[185] G. Li, V. Shrotriya, J. Huang, Y. Yao, T. Moriarty, K. Emery, and Y. Yang, "High-Efficiency Solution Processable Polymer Photovoltaic Cells by Self-Organization of Polymer Blends," *Nat. Mater.*, vol. 4, no. 11, pp. 864–868, 2005.

[186] U. Zhokhavets, T. Erb, H. Hoppe, G. Gobsch, and N. S. Sariciftci, "Effect of Annealing of Poly(3-hexylthiophene)/Fullerene Bulk Heterojunction Composites on Structural and Optical Properties," *Thin Solid Films*, vol. 496, no. 2, pp. 679–682, 2006.

[187] H. Yang, T. J. Shin, L. Yang, K. Cho, C. Y. Ryu, and Z. Bao, "Effect of Mesoscale Crystalline Structure on the Field-Effect Mobility of Regioregular Poly(3-hexyl thiophene) in Thin-Film Transistors," *Advanced Functional Materials*, vol. 15, no. 4, pp. 671–676, 2005.

[188] M. T. Dang, G. Wantz, H. Bejbouji, M. Urien, O. J. Dautel, L. Vignau, and L. Hirsch, "Polymeric Solar Cells Based on P3HT:PCBM: Role of the Casting Solvent," *Solar Energy Materials and Solar Cells*, vol. 95, no. 12, pp. 3408–3418, 2011.

[189] C. J. Tassone, A. L. Ayzner, R. D. Kennedy, M. Halim, M. So, Y. Rubin, S. H. Tolbert, and B. J. Schwartz, "Using Pentaarylfullerenes to Understand Network Formation in Conjugated Polymer-Based Bulk-Heterojunction Solar Cells," *The Journal of Physical Chemistry C*, vol. 115, pp. 22563–22571, 2011.

[190] L. J. Richter, D. M. Delongchamp, F. A. Bokel, S. Engmann, K. W. Chou, A. Amassian, E. Schaible, and A. Hexemer, "In Situ Morphology Studies of the Mechanism for Solution Additive Effects on the Formation of Bulk Heterojunction Films," *Advanced Energy Materials*, vol. 5, p. 1400975, 2015.

[191] B. Kan, Q. Zhang, M. Li, X. Wan, W. Ni, G. Long, Y. Wang, X. Yang, H. Feng, and Y. Chen, "Solution-Processed Organic Solar Cells Based on Dialkylthiol- Substituted Benzodithiophene Unit with Efficiency Near 10%," *Journal of the American Chemical Society*, vol. 136, pp. 15529–15532, 2014.

[192] S. Zhang, L. Ye, W. Zhao, B. Yang, Q. Wang, and J. Hou, "Realizing Over 10% Efficiency in Polymer Solar Cell by Device Optimization," *Science China Chemistry*, vol. 58, no. 2, pp. 248–256, 2015.

[193] Z. He, B. Xiao, F. Liu, H. Wu, Y. Yang, S. Xiao, C. Wang, T. P. Russell, and Y. Cao, "Single-Junction Polymer Solar Cells with High Efficiency and Photovoltage," *Nature Photonics*, vol. 9, no. 3, pp. 174–179, 2015.

[194] A. Pivrikas, P. Stadler, H. Neugebauer, and N. S. Sariciftci, "Substituting the Postproduction Treatment for Bulk-Heterojunction Solar Cells Using Chemical Additives," *Org. Electron.*, vol. 9, pp. 775–782, 2008.

[195] H.-Y. Chen, H. Yang, G. Yang, S. Sista, R. Zadoyan, G. Li, and Y. Yang, "Fast-Grown Interpenetrating Network in Poly(3-hexylthiophene):Methanofulleres Solar Cells Processed with Additive," *Journal of Physical Chemistry C*, vol. 113, pp. 7946–7953, 2009.

[196] K. R. Graham, P. M. Wieruszewski, R. Stalder, M. J. Hartel, J. Mei, F. So, and J. R. Reynolds, "Improved Performance of Molecular Bulk-Heterojunction Photovoltaic Cells through Predictable Selection of Solvent Additives," *Advanced Functional Materials*, vol. 22, pp. 4801–4813, 2012.

[197] S. J. Lou, J. M. Szarko, T. Xu, L. Yu, T. J. Marks, and L. X. Chen, "Effects of Additives on the Morphology of Solution Phase Aggregates Formed by Active Layer Components of High-Efficiency Organic Solar Cells," *Journal of the American Chemical Society*, vol. 133, pp. 20661–20663, 2011.

[198] Z. Xiao, Y. Yuan, B. Yang, J. Vanderslice, J. Chen, and O. Dyck, "Universal Formation of Compositionally Graded Bulk Heterojunction for Efficiency Enhancement in Organic Photovoltaics," *Advanced Materials*, vol. 26, pp. 3068–3075, 2014.

[199] C. Liu, X. Hu, C. Zhong, M. Huang, K. Wang, Z. Zhang, X. Gong, Y. Cao, and A. J. Heeger, "The Influence of Binary Processing Additives on the Performance of Polymer Solar Cells," *Nanoscale*, vol. 6, pp. 14297–14304, 2014.

[200] Y. Yao, J. Hou, Z. Xu, G. Li, and Y. Yang, "Effects of Solvent Mixtures on the Nanoscale Phase Separation in Polymer Solar Cells," *Advanced Functional Materials*, vol. 18, pp. 1783–1789, 2008.

[201] Y. Sun, G. C. Welch, W. L. Leong, C. J. Takacs, G. C. Bazan, and A. J. Heeger, "Solution-Processed Small-Molecule Solar Cells with 6.7% Efficiency," *Nature Materials*, vol. 11, no. 1, pp. 44–48, 2011.

[202] B. J. Tremolet de Villers, K. A. O. Hara, D. P. Ostrowski, P. H. Biddle, S. E. Shaheen, M. L. Chabinyc, D. C. Olson, and N. Kopidakis, "Removal of Residual Diiodooctane Improves Photostability of High-Performance Organic Solar Cell Polymers," *Chemistry of Materials*, vol. 28, pp. 876–884, 2016.

[203] L. Ye, Y. Jing, X. Guo, H. Sun, S. Zhang, M. Zhang, L. Huo, and J. Hou, "Remove the Residual Additives toward Enhanced Efficiency with Higher Reproducibility in Polymer Solar Cells," *Journal of Physical Chemistry C*, vol. 117, no. October 2015, pp. 14920–14928, 2013.

[204] A. Tournebize, A. Rivaton, H. Peisert, and T. Chassé, "The Crucial Role of Confined Residual Additives on the Photostability of P3HT:PCBM Active Layers," *The Journal of Physical Chemistry C*, vol. 119, no. 17, pp. 9142–9148, 2015.

[205] N. Shin, L. J. Richter, A. A. Herzing, R. J. Kline, and D. M. Delongchamp, "Effect of Processing Additives on the Solidification of Blade-Coated Polymer/Fullerene Blend Films via In-Situ Structure Measurements," *Advanced Energy Materials*, vol. 3, pp. 938–948, 2013.

[206] M. T. Fontana, H. Kang, P. Y. Yee, Z. Fan, S. A. Hawks, L. T. Schelhas, S. Subtamaniyan, Y.-J. Hwang, S. A. Jenekhe, S. H. Tolbert, and B. J. Schwartz, "Low-Vapor-Pressure Solvent Additives Function as Polymer Swelling Agents in Bulk Heterojunction Organic Photovoltaics," *Journal of Physical Chemistry C*, 2018.

[207] J. Kong, I.-W. Hwang, and K. Lee, "Top-Down Approach for Nanophase Reconstruction in Bulk Heterojunction Solar Cells," *Advanced Materials*, vol. 26, no. 36, pp. 6275–6283, 2014.

[208] C. K. Chiang, C. R. Fincher, Y. W. Park, A. J. Heeger, H. Shirakawa, E. J. Louis, S. C. Gau, and A. G. MacDiarmid, "Electrical Conductivity in Doped Polyacetylene," *Physical Review Letters*, vol. 39, no. 17, pp. 1098–1101, 1977.

[209] I. Salzmann and G. Heimel, "Toward a Comprehensive Understanding of Molecular Doping Organic Semiconductors (Review)," *Journal of Electron Spectroscopy and Related Phenomena*, vol. 204, pp. 208–222, 2015.

[210] J. E. Cochran, M. J. N. Junk, A. M. Glaudell, P. L. Miller, J. S. Cowart, M. F. Toney, C. J. Hawker, B. F. Chmelka, and M. L. Chabinyc, "Molecular Interactions and Ordering in Electrically Doped Polymers: Blends of PBTTT and F4TCNQ," *Macromolecules*, vol. 47, pp. 6836–6846, 2014.

[211] I. E. Jacobs, E. W. Aasen, J. L. Oliveira, T. N. Fonseca, J. D. Roehling, J. Li, G. Zhang, M. P. Augustine, M. Mascal, and A. J. Moulé, "Comparison of Solution-Mixed and Sequentially Processed P3HT:F4TCNQ Films: Effect of Doping-Induced Aggregation on Film Morphology," *Journal of Materials Chemistry C*, vol. 4, no. 16, pp. 3454–3466, 2016.

[212] V. A. Kolesov, C. Fuentes-Hernandez, W.-F. Chou, N. Aizawa, F. A. Larrain, M. Wang, A. Perrotta, S. Choi, S. Graham, G. C. Bazan, T.-Q. Nguyen, S. R. Marder, and B. Kippelen, "Solution-Based Electrical Doping of Semiconducting Polymer Films Over a Limited Depth," *Nature Materials*, vol. 1, no. December, pp. 1–8, 2016.

[213] C. Wang, D. T. Duong, K. Vandewal, J. Rivnay, and A. Salleo, "Optical Measurement of Doping Efficiency in Poly(3-hexylthiophene) Solutions and Thin Films," *Physical Review B - Condensed Matter and Materials Physics*, vol. 91, no. 8, p. 085205, 2015.

[214] W. Zhao, S. Li, H. Yao, S. Zhang, Y. Zhang, B. Yang, and J. Hou, "Molecular Optimization Enables Over 13% Efficiency in Organic Solar Cells," *Journal of the American Chemical Society*, vol. 139, pp. 7148–7151, 2017.

[215] R. C. Coffin, J. Peet, J. Rogers, and G. C. Bazan, "Streamlined Microwave-Assisted Preparation of Narrow-Bandgap Conjugated Polymers for High-Performance Bulk Heterojunction Solar Cells," *Nature Chemistry*, vol. 1, no. 11, pp. 657–661, 2009.

[216] H.-Y. Chen, J. Hou, S. Zhang, Y. Liang, G. Yang, and Y. Yang, "Polymer Solar Cells with Enhanced Open-Circuit Voltage and Efficiency," *Nature Photonics*, vol. 3, no. November, pp. 649–653, 2009.

[217] Y. Xie, X. Hu, J. Yin, L. Zhang, X. Meng, G. Xu, Q. Ai, W. Zhou, and Y. Chen, "Butanedithiol Solvent Additive Extracting Fullerenes from Donor Phase To Improve Performance and Photostability in Polymer Solar Cells," *ACS Applied Materials and Interfaces*, vol. 9, no. 11, pp. 9918–9925, 2017.

[218] I. E. Jacobs, F. Wang, Z. I. Bedolla Valdez, A. N. Ayala Oviedo, D. J. Bilsky, and A. J. Moulé, "Photoinduced Degradation from Trace 1,8-diiodooctane in Organic Photovoltaics," *Journal of Materials Chemistry C*, vol. 6, no. 2, pp. 219–225, 2018.

[219] L. Li, L. Xiao, H. Qin, K. Gao, J. Peng, Y. Cao, F. Liu, T. P. Russell, and X. Peng, "High-Efficiency Small Molecule-Based Bulk-Heterojunction Solar Cells Enhanced by Additive Annealing," *ACS Applied Materials and Interfaces*, vol. 7, pp. 21495–21502, 2015.

[220] E. F. Manley, J. Strzalka, T. J. Fauvell, N. E. Jackson, M. J. Leonardi, N. D. Eastham, T. J. Marks, and L. X. Chen, "In Situ GIWAXS Analysis of Solvent and Additive Effects on PTB7 Thin Film Microstructure Evolution During Spin Coating," *Advanced Materials*, vol. 29, no. 43, p. 1703933, 2017.

[221] E. H. Immergut and H. F. Mark, "Principles of Plasticization," *Advances in Chemistry*, vol. 48, pp. 1–26, 1965.

[222] S. Subramaniyan, H. Xin, F. S. Kim, S. Shoaee, J. R. Durrant, and S. A. Jenekhe, "Effects of Side Chains on Thiazolothiazole-Based Copolymer Semiconductors for High Performance Solar Cells," *Advanced Energy Materials*, vol. 1, no. 5, pp. 854–860, 2011.

[223] Y. M. Yang, W. Chen, L. Dou, W.-H. Chang, H.-S. Duan, B. Bob, G. Li, and Y. Yang, "High-Performance Multiple-Donor Bulk Heterojunction Solar Cells," *Nature Photonics*, vol. 9, no. 3, pp. 190–198, 2015.

[224] G. Zhang, S. A. Hawks, C. Ngo, L. T. Schelhas, D. T. Scholes, H. Kang, J. C. Aguirre, S. H. Tolbert, and B. J. Schwartz, "Extensive Penetration of Evaporated Electrode Metals into Fullerene Films: Intercalated Metal Nanostructures and Influence on Device Architecture," *ACS Applied Materials and Interfaces*, vol. 7, pp. 25247–25258, 2015.

[225] Molebase, "1,8-Diiodooctane," 2017.

[226] Molebase, "1,8-Octanedithiol," 2017.

[227] PubChem, "1,2-Dichlorobenzene," 2017.

[228] E. L. Ratcliff, J. L. Jenkins, K. Nebesny, and N. R. Armstrong, "Films for Photovoltaic Applications," *Chemistry of Materials*, vol. 20, no. 8, pp. 5796–5806, 2008.

[229] A. Orimo, K. Masuda, S. Honda, H. Benten, S. Ito, H. Ohkita, and H. Tsuji, "Surface Segregation at the Aluminum Interface of Poly(3-hexylthiophene)/Fullerene Solar Cells," *Applied Physics Letters*, vol. 96, p. 043305, 2010.

[230] S. Das, J. K. Keum, J. F. Browning, G. Gu, B. Yang, O. Dyck, C. Do, W. Chen, J. Chen, I. N. Ivanov, K. Hong, A. J. Rondinone, P. C. Joshi, D. B. Geohegan, G. Duscher, and K. Xiao, "Correlating High Power Conversion Efficiency of PTB7:PC71BM Inverted Organic Solar Cells with Nanoscale Structures," *Nanoscale*, vol. 7, no. 38, pp. 15576–15583, 2015.

[231] PubChem, "Dichloromethane," 2017.

[232] J. S. Moon, C. J. Takacs, Y. Sun, and A. J. Heeger, "Spontaneous Formation of Bulk Heterojunction Nanostructures: Multiple Routes to Equivalent Morphologies," *Nano Letters*, vol. 11, pp. 1036–1039, 2011.

[233] W. Kim, J. K. Kim, E. Kim, T. K. Ahn, D. H. Wang, and J. H. Park, "Conflicted Effects of a Solvent Additive on PTB7:PC71BM Bulk Heterojunction Solar Cells," *Journal of Physical Chemistry C*, vol. 119, pp. 5954–5961, 2015.

[234] W. Wang, L. Song, D. Magerl, D. Moseguí González, V. Körstgens, M. Philipp, J. F. Moulin, and P. Müller-Buschbaum, "Influence of Solvent Additive 1,8-Octanedithiol on P3HT:PCBM Solar Cells," *Advanced Functional Materials*, p. 1800209, 2018.

[235] L. G. Krauskopf and A. Godwin, "Plasticizers," in *PVC Handbook*, pp. 173–193, 2005.

[236] A. D. Godwin and L. G. Krauskopf, "Monomeric Plasticizers," in *Handbook of Vinyl Formulating* (R. F. Grossman, ed.), ch. Seven, pp. 173–238, John Wiley & Sons, Inc., second ed., 2008.

[237] S. Cehreli, B. Tatli, and P. Bagman, "(Liquid + Liquid) Equilibria of (Water + Propionic Acid + Cyclohexanone) at Several Temperatures," *Journal of Chemical Thermodynamics*, vol. 37, no. 12, pp. 1288–1293, 2005.

[238] C. Yan, S. Barlow, Z. Wang, H. Yan, A. K. Jen, S. R. Marder, and X. Zhan, "Non-Fullerene Acceptors for Organic Solar Cells," *Nature Reviews Materials*, vol. 3, pp. 1–19, 2018.

[239] A. Austin, N. J. Hestand, I. G. McKendry, C. Zhong, X. Zhu, M. J. Zdilla, F. C. Spano, and J. M. Szarko, "Enhanced Davydov Splitting in Crystals of a Perylene Diimide Derivative," *The Journal of Physical Chemistry Letters*, vol. 8, pp. 1118–1123, 2017.

[240] Y. Fan, K. Ziabrev, S. Zhang, B. Lin, S. Barlow, and S. R. Marder, "Comparison of the Optical and Electrochemical Properties of Bi(perylene diimide)s Linked through Ortho and Bay Positions," *ACS Omega*, vol. 2, no. 2, pp. 377–385, 2017.

[241] B. A. Gregg, J. Sprague, and M. W. Peterson, "Long-Range Singlet Energy Transfer in Perylene Bis(phenethylimide) Films," *The Journal of Physical Chemistry B*, vol. 101, no. 27, pp. 5362–5369, 1997.

[242] J. Qu, J. Zhang, A. C. Grimsdale, K. Mullen, F. Jaiser, X. Yang, and D. Neher, "Dendronized Perylene Diimide Emitters: Synthesis, Luminescence, and Electron and Energy Transfer Studies," *Macromolecules*, vol. 37, no. 22, pp. 8297–8306, 2004.

[243] W. Jiang, C. Xiao, L. Hao, Z. Wang, H. Ceymann, C. Lambert, S. Di Motta, and F. Negri, "Localization/Delocalization of Charges in Bay-Linked Perylene Bisimides," *Chem. - A Eur. J.*, vol. 18, no. 22, pp. 6764–6775, 2012.

[244] A. Herrmann, T. Weil, V. Sinigersky, U. M. Wiesler, T. Vosch, J. Hofkens, F. C. De Schryver, and K. Müllen, "Polyphenylene Dendrimers with Perylene Diimide as a Luminescent Core," *Chemistry - A European Journal*, vol. 7, no. 22, pp. 4844–4853, 2001.

[245] R. M. Hochstrasser and M. Kasha, "Application of the Exciton Model To Mono-Molecular Lamellar Systems," *Photochemistry and Photobiology*, vol. 3, no. 4, pp. 317–331, 1964.

[246] M. Kasha, H. R. Rawls, and M. Ashraf El-Bayoumi, "The Exciton Model in Molecular Spectroscopy," *Pure Appl. Chem.*, vol. 11, no. 3-4, pp. 371–392, 1965.

[247] F. Gao, Y. Zhao, and W. Liang, "Vibronic Spectra of Perylene Bisimide Oligomers: Effects of Intermolecular Charge-Transfer Excitation and Conformational Flexibility," *Journal of Physical Chemistry B*, vol. 115, no. 12, pp. 2699–2708, 2011.

[248] F. Spreitler, M. Sommer, M. Hollfelder, M. Thelakkat, S. Gekle, and J. Köhler, "Unravelling the Conformations of Di-(Perylene Bisimide Acrylate) by Combining Time-Resolved Fluorescence-Anisotropy Experiments and Molecular Modelling," *Physical Chemistry Chemical Physics*, vol. 16, no. 47, pp. 25959–25968, 2014.

[249] F. Würthner, C. R. Saha-Möller, B. Fimmel, S. Ogi, P. Leowanawat, and D. Schmidt, "Perylene Bisimide Dye Assemblies as Archetype Functional Supramolecular Materials," *Chemical Reviews*, vol. 116, no. 3, pp. 962–1052, 2016.

[250] H. and others Frisch, MJ and Trucks, GW and Schlegel, HB and Scuseria, GE and Robb, MA and Cheeseman, JR and Scalmani, G and Barone, V and Petersson, GA and Nakatsuji, "Gaussian 16 Revision A. 03. 2016; Gaussian Inc.," *Wallingford CT*, 2016.

[251] P. M. Krylov, Anna I and Gill, "Q-Chem: An Engine for Innovation," *Wiley Interdisciplinary Reviews: Computational Molecular Science*, vol. 3, no. 317–326, pp. 317—-326, 2013.

[252] C. Adamo and V. Barone, "Toward Reliable Density Functional Methods Without Adjustable Parameters: The PBE0 Model," *Journal of Chemical Physics*, vol. 110, no. 13, pp. 6158–6170, 1999.

[253] S. Grimme, J. Antony, S. Ehrlich, and H. Krieg, "A Consistent and Accurate ab initio Parametrization of Density Functional Dispersion Correction (DFT-D) for the 94 elements H-Pu," *Journal of Chemical Physics*, vol. 132, no. 15, 2010.

[254] C. Zhan and J. Yao, "More than Conformational "Twisting" or "Coplanarity": Molecular Strategies for Designing High-Efficiency Nonfullerene Organic Solar Cells," *Chemistry of Materials*, vol. 28, no. 7, pp. 1948–1964, 2016.

[255] S. Hwang, W. J. Potscavage, R. Nakamichi, and C. Adachi, "Processing and Doping of Thick Polymer Active Layers for Flexible Organic Thermoelectric Modules," *Organic Electronics*, vol. 31, pp. 31–40, 2016.

[256] P. E. Hartnett, H. S. Ramakrishna Matte, N. D. Eastham, N. E. Jackson, Y. Wu, L. X. Chen, M. A. Ratner, R. P. Chang, M. C. Hersam, M. R. Wasielewski, and T. J. Marks, "Ring-Fusion as a Perylenediimide Dimer Design Concept for High-Performance Non-Fullerene Organic Photovoltaic Acceptors," *Chemical Science*, vol. 7, no. 6, pp. 3543–3555, 2016.

[257] B. Wang, W. Liu, H. Li, J. Mai, S. Liu, X. Lu, H. Li, M. Shi, C. Z. Li, and H. Chen, "Electron Acceptors with Varied Linkages Between Perylene Diimide and Benzotrithiophene for Efficient Fullerene-Free Solar Cells," *Journal of Materials Chemistry A*, vol. 5, no. 19, pp. 9396–9401, 2017.

[258] J. Cann, S. Dayneko, J. P. Sun, A. D. Hendsbee, I. G. Hill, and G. C. Welch, "N-Annulated Perylene Diimide Dimers: Acetylene Linkers as a Strategy for Controlling Structural Conformation and the Impact on Physical, Electronic, Optical and Photovoltaic Properties," *Journal of Materials Chemistry C*, vol. 5, no. 8, pp. 2074–2083, 2017.

[259] V. Barone and M. Cossi, "Quantum Calculation of Molecular Energies and Energy Gradients in Solution by a Conductor Solvent Model," *Journal of Physical Chemistry A*, vol. 102, no. 11, pp. 1995–2001, 1998.

[260] R. S. Mulliken, "Electronic Population Analysis on LCAO-MO Molecular Aave Functions. I," *The Journal of Chemical Physics*, vol. 23, no. 10, pp. 1833–1840, 1955.

[261] E. P. Farr, C. C. Zho, J. R. Challa, and B. J. Schwartz, "Temperature Dependence of the Hydrated Electron's Excited-State Relaxation. II. Elucidating the Relaxation Mechanism Through Ultrafast Transient Absorption and Stimulated Emission spectroscopy," *Journal of Chemical Physics*, vol. 147, no. 7, p. 074504, 2017.

[262] T. A. A. Oliver, Y. Zhang, A. Roy, M. N. R. Ashfold, and S. E. Bradforth, "Exploring Autoionization and Photoinduced Proton-Coupled Electron Transfer Pathways of Phenol in Aqueous Solution," *The Journal of Physical Chemistry Letters*, vol. 6, no. 20, pp. 4159–4164, 2015.

[263] H. Horinouchi, H. Sakai, Y. Araki, T. Sakanoue, T. Takenobu, T. Wada, N. V. Tkachenko, and T. Hasobe, "Controllable Electronic Structures and Photoinduced Processes of Bay-Linked Perylenediimide Dimers and a Ferrocene-Linked Triad," *Chemistry - A European Journal*, vol. 22, no. 28, pp. 9631–9641, 2016.

[264] W. E. Ford and P. V. Kamat, "Photochemistry of 3,4,9,10-Perylenetetracarboxylic Dianhydride Dyes. 3. Singlet and Triplet Excited-State Properties of the bis(2,5-di-tert-butylphenyl)imide Derivative," *Journal of Physical Chemistry*, vol. 91, no. 25, pp. 6373–6380, 1987.

[265] R. Gvishi, R. Reisfeld, and Z. Burshtein, "Spectroscopy and Laser Action of the "Red Perylimide Dye" in Various Solvents," *Chemical Physics Letters*, vol. 213, no. 3-4, pp. 338–344, 1993.

[266] M. Supur, M. E. El-Khouly, J. H. Seok, J. H. Kim, K.-Y. Kay, and S. Fukuzumi, "Efficient Electron Transfer Processes of the Covalently Linked Perylenediimide- Ferrocene Systems: Femtosecond and Nanosecond Transient Absorption Studies," *The Journal of Physical Chemistry C*, vol. 114, no. 24, pp. 10969–10977, 2010.

[267] T. P. Kaloni, P. K. Giesbrecht, G. Schreckenbach, and M. S. Freund, "Polythiophene: From Fundamental Perspectives to Applications," *Chemistry of Materials*, vol. 29, no. 24, pp. 10248–10283, 2017.

[268] Y. Li, "Molecular Design of Photovoltaic Materials for Polymer Solar Cells: Toward Suitable Electronic Energy Levels and Broad Absorption," *Accounts of Chemical Research*, vol. 45, no. 5, pp. 723–733, 2012.

[269] R. Søndergaard, M. Hösel, D. Angmo, T. T. Larsen-Olsen, and F. C. Krebs, "Roll-to-Roll Fabrication of Polymer Solar Cells," *Materials Today*, vol. 15, no. 1-2, pp. 36–49, 2012.

[270] B. McCulloch, V. Ho, M. Hoarfrost, C. Stanley, C. Do, W. T. Heller, and R. A. Segalman, "Polymer Chain Shape of poly(3-alkylthiophenes) in Solution Ssing Small-Angle Neutron Scattering," *Macromolecules*, vol. 46, no. 5, pp. 1899–1907, 2013.

[271] A. J. Spakowitz and Z. G. Wang, "Exact Results for a Semiflexible Polymer Chain in an Aligning Field," *Macromolecules*, vol. 37, no. 15, pp. 5814–5823, 2004.

[272] C. Duan, F. Huang, and Y. Cao, "Recent Development of Push-Pull Conjugated Polymers for Bulk-Heterojunction Photovoltaics: Rational Design and Fine Tailoring of Molecular Structures," *Journal of Materials Chemistry*, vol. 22, no. 21, p. 10416, 2012.

[273] U. Giovanella, C. Botta, F. Galeotti, B. Vercelli, S. Battiato, and M. Pasini, "Perfluorinated Polymer with Unexpectedly Efficient Deep Blue Electroluminescence for Full-Colour OLED Displays and Light Therapy Applications," *Journal of Materials Chemistry C*, vol. 1, pp. 5322–5329, 2013.

[274] J. Sun, M. L. Yeh, B. J. Jung, B. Zhang, J. Feser, A. Majumdar, and H. E. Katz, "Simultaneous Increase in Seebeck Coefficient and Conductivity in a Doped Poly(alkylthiophene) Blend with Defined Density of States," *Macromolecules*, vol. 43, no. 6, pp. 2897–2903, 2010.

[275] B. T. McGrail, A. Sehirlioglu, and E. Pentzer, "Polymer Composites for Thermoelectric Applications," *Angewandte Chemie - International Edition*, vol. 54, no. 6, pp. 1710–1723, 2015.

[276] A. Hamidi-Sakr, L. Biniek, J. L. Bantignies, D. Maurin, L. Herrmann, N. Leclerc, P. Lévêque, V. Vijayakumar, N. Zimmermann, and M. Brinkmann, "A Versatile Method to Fabricate Highly In-Plane Aligned Conducting Polymer Films with Anisotropic Charge Transport and Thermoelectric Properties: The Key Role of Alkyl Side Chain Layers on the Doping Mechanism," *Advanced Functional Materials*, vol. 27, no. 25, pp. 1–13, 2017.

[277] D. Kiefer, L. Yu, E. Fransson, A. Gómez, D. Primetzhofer, A. Amassian, M. Campoy-Quiles, and C. Müller, "A Solution-Doped Polymer Semiconductor:Insulator Blend for Thermoelectrics," *Advanced Science*, vol. 4, no. 1, p. 1600203, 2017.

[278] H. Yao, Z. Fan, H. Cheng, X. Guan, C. Wang, K. Sun, and J. Ouyang, "Recent Development of Thermoelectric Polymers and Composites," *Macromolecular Rapid Communications*, vol. 39, no. 6, p. 1700727, 2018.

[279] A. Jha, H.-G. Duan, V. Tiwari, M. Thorwart, and R. J. D. Miller, "Origin of Poor Doping Efficiency in Solution Processed Organic Semiconductors," *Chemical Science*, vol. 9, p. 4468, 2018.

[280] J. Hynynen, D. Kiefer, and C. Müller, "Influence of Crystallinity on the Thermoelectric Power Factor of P3HT Vapour-Doped with F4TCNQ," *RSC Advances*, vol. 8, no. 3, pp. 1593–1599, 2018.

[281] G. Zuo, O. Andersson, H. Abdalla, and M. Kemerink, "High Thermoelectric Power Factor from Multilayer Solution-Processed Organic Films," *Applied Physics Letters*, vol. 112, no. 8, pp. 2–6, 2018.

[282] P. Reiser, L. Mu, V. Sivanesan, R. Lovrincic, S. Barlow, S. R. Marder, A. Pucci, W. Jaegermann, E. Mankel, S. Beck, and U. States, "Dopant Diffusion in Sequentially Doped Poly(3-hexylthiophene) Studied by Infrared and Photoelectron Spectroscopy," *Journal of Physical Chemistry C*, 2018.

[283] J. Li, G. Zhang, D. M. Holm, I. E. Jacobs, B. Yin, P. Stroeve, M. Mascal, and A. J. Moulé, "Introducing Solubility Control for Improved Organic P-Type Dopants," *Chemistry of Materials*, vol. 27, no. 16, pp. 5765–5774, 2015.

[284] NIST, "Resistivity and Hall Reasurements," 2018.

[285] F. C. Spano, "Modeling Disorder in Polymer Aggregates: The Optical Spectroscopy of Regioregular poly(3-hexylthiophene) Thin Films," *Journal of Chemical Physics*, vol. 122, no. 23, p. 234701, 2005.

[286] J. Clark, J. F. Chang, F. C. Spano, R. H. Friend, and C. Silva, "Determining Exciton Bandwidth and Film Microstructure in Polythiophene Films Using Linear Absorption Spectroscopy," *Applied Physics Letters*, vol. 94, no. 16, p. 163306, 2009.

[287] F. C. Spano, J. Clark, C. Silva, and R. H. Friend, "Determining Exciton Coherence from the Photoluminescence Spectral Line Shape in poly(3-hexylthiophene) Thin Films," *Journal of Chemical Physics*, vol. 130, no. 7, p. 074904, 2009.

[288] M. Wohlgenannt, X. M. Jiang, and Z. V. Vardeny, "Confined and Delocalized Polarons in π-conjugated Oligomers and Polymers: A Study of the Effective Conjugation Length," *Physical Review B - Condensed Matter and Materials Physics*, vol. 69, no. 24, p. 241204, 2004.

[289] C. M. Pochas and F. C. Spano, "New Insights on the Nature of Two-Dimensional Polarons in Semiconducting Polymers: Infrared Absorption in Poly(3-hexylthiophene)," *Journal of Chemical Physics*, vol. 140, no. 24, p. 244902, 2014.

[290] R. Ghosh, C. M. Pochas, and F. C. Spano, "Polaron Delocalization in Conjugated Polymer Films," *Journal of Physical Chemistry C*, vol. 120, no. 21, pp. 11394–11406, 2016.

[291] R. Ghosh, A. R. Chew, J. Onorato, V. Pakhnyuk, C. K. Luscombe, A. Salleo, and F. C. Spano, "Spectral Signatures and Spatial Coherence of Bound and Unbound Polarons in P3HT Films: Theory Versus Experiment," *Journal of Physical Chemistry C*, 2018.

[292] R. A. Street, A. Krakaris, and S. R. Cowan, "Recombination Through Different Types of Localized States in Organic Solar Cells," *Advanced Functional Materials*, vol. 22, no. 21, pp. 4608–4619, 2012.

[293] T. Kirchartz, F. Deledalle, P. S. Tuladhar, J. R. Durrant, and J. Nelson, "On the Differences Between Dark and Light Ideality Factor in Polymer:Fullerene Solar Cells," *The Journal of Physical Chemistry Letters*, vol. 4, no. 14, pp. 2371–2376, 2013.

[294] J. M. Shah, Y. L. Li, T. Gessmann, and E. F. Schubert, "Experimental Analysis and Theoretical Model for Anomalously High Ideality Factors (n>2.0) in AlGaN/GaN p-n Junction Diodes," *Journal of Applied Physics*, vol. 94, no. 4, pp. 2627–2630, 2003.

[295] A. Cuevas, "The Recombination Parameter J0," *Energy Procedia*, vol. 55, pp. 53–62, 2014.

[296] C. G. Shuttle, A. Maurano, R. Hamilton, B. O'Regan, J. C. De Mello, and J. R. Durrant, "Charge Extraction Analysis of Charge Carrier Densities in a Polythiophene/Fullerene Solar Cell: Analysis of the Origin of the Device Dark Current," *Applied Physics Letters*, vol. 93, no. 18, p. 183501, 2008.

[297] G. Juska, K. Arlauskas, and M. Viliunas, "Extraction Current Transients: New method of Study of Charge Transport in Microcrystalline Silicon," *Physical Review Letters*, vol. 84, no. 21, pp. 4946–4949, 2000.

[298] J. W. Kiel, B. J. Kirby, C. F. Majkrzak, B. Maranville, and M. E. Mackay, "Nanoparticle Concentration Profile in Polymer-Based Solar Cells," *Soft Matter*, vol. 6, pp. 641–646, 2010.

[299] H. Chen, R. Hegde, J. Browning, and M. D. Dadmun, "The Miscibility and Depth Profile of PCBM in P3HT: Thermodynamic Information to Improve Organic Photovoltaics," *Physical Chemistry Chemical Physics*, vol. 14, pp. 5635–5641, 2012.

[300] S. Engmann, F. A. Bokel, A. A. Herzing, W. Ro, C. Girotto, B. Caputo, C. V. Hoven, E. Schaible, A. Hexemer, M. Delongchamp, and L. J. Richter, "Real-Time X-Ray Scattering Studies of Film Evolution in High Performing Small-Molecule-Fullerene Organic Solar Cells," *Journal of Materials Chemistry A*, vol. 3, no. 1, pp. 8764–8771, 2015.

[301] S. Engmann, F. A. Bokel, H. W. Ro, D. M. Delongchamp, and L. J. Richter, "Real-Time Photoluminescence Studies of Structure Evolution in Organic Solar Cells," *Advanced Energy Materials*, vol. 6, p. 1502011, 2016.

[302] P. H. Daniels, "A Brief Overview of Theories of PVC Plasticization and Methods Used to Evaluate PVC-Plasticizer Interaction," *Journal of Vinyl and Additive Technology*, vol. 15, no. 4, pp. 219–223, 2009.

[303] M. Rahman and C. S. Brazel, "The Plasticizer Market: An Assessment of Traditional Plasticizers and Research Trends to Meet New Challenges," *Progress in Polymer Science*, vol. 29, pp. 1223–1248, 2004.

[304] J. Seibt, P. Marquetand, V. Engel, Z. Chen, V. Dehm, and F. Würthner, "On the Geometry Dependence of Molecular Dimer Spectra with an Application to Aggregates of Perylene Bisimide," *Chemical Physics*, vol. 328, no. 1-3, pp. 354–362, 2006.

[305] K. A. Kistler, C. M. Pochas, H. Yamagata, S. Matsika, and F. C. Spano, "Absorption, Circular Dichroism, and Photoluminescence in Perylene Diimide Bichromophores: Polarization-Dependent H- and J-Aggregate Behavior," *Journal of Physical Chemistry B*, vol. 116, no. 1, pp. 77–86, 2012.

[306] J. Huang, Y. Wu, H. Fu, X. Zhan, J. Yao, S. Barlow, and S. R. Marder, "Photoinduced Intramolecular Electron Transfer in Conjugated Perylene Bisimide-Dithienothiophene Systems: A Comparative Study of a Small Molecule and a Polymer.," *The journal of physical chemistry. A*, vol. 113, no. 17, pp. 5039–5046, 2009.

[307] H. Yin, Y. Geng, G. Y. Sun, and Z. M. Su, "Theoretical Design of Perylene Diimide Dimers with Different Linkers and Bridged Positions as Promising Non-Fullerene Acceptors for Organic Photovoltaic Cells," *Journal of Physical Chemistry C*, vol. 121, no. 4, pp. 2125–2134, 2017.

[308] W. Jiang, Y. Li, and Z. Wang, "Tailor-Made Rylene Arrays for High Performance n-Channel Semiconductors," *Accounts of Chemical Research*, vol. 47, no. 10, pp. 3135–3147, 2014.

[309] K. A. Kistler, F. C. Spano, and S. Matsika, "A Benchmark of Excitonic Couplings Derived from Atomic Transition Charges," *Journal of Physical Chemistry B*, vol. 117, no. 7, pp. 2032–2044, 2013.

[310] K. E. Brown, W. A. Salamant, L. E. Shoer, R. M. Young, and M. R. Wasielewski, "Direct observation of ultrafast excimer formation in covalent perylenediimide dimers using near-infrared transient absorption spectroscopy," *Journal of Physical Chemistry Letters*, vol. 5, no. 15, pp. 2588–2593, 2014.

[311] M. Son, K. H. Park, C. Shao, F. Würthner, and D. Kim, "Spectroscopic Demonstration of Exciton Dynamics and Excimer Formation in a Sterically Controlled Perylene Bisimide Dimer Aggregate," *Journal of Physical Chemistry Letters*, vol. 5, no. 20, pp. 3601–3607, 2014.

[312] N. J. Hestand and F. C. Spano, "Interference Between Coulombic and CT-Mediated Couplings in Molecular Aggregates: H- to J-Aggregate Transformation in Perylene-Based π-Stacks," *Journal of Chemical Physics*, vol. 143, no. 24, p. 244707, 2015.

[313] N. J. Hestand, R. V. Kazantsev, A. S. Weingarten, L. C. Palmer, S. I. Stupp, and F. C. Spano, "Extended-Charge-Transfer Excitons in Crystalline Supramolecular Photocatalytic Scaffolds," *Journal of the American Chemical Society*, vol. 138, no. 36, pp. 11762–11774, 2016.

[314] J. Sung, A. Nowak-Król, F. Schlosser, B. Fimmel, W. Kim, D. Kim, and F. Würthner, "Direct Observation of Excimer-Mediated Intramolecular Electron Transfer in a Cofacially-Stacked Perylene Bisimide Pair," *Journal of the American Chemical Society*, vol. 138, no. 29, pp. 9029–9032, 2016.

[315] A. Kubas, F. Gajdos, A. Heck, H. Oberhofer, M. Elstner, and J. Blumberger, "Electronic Couplings for Molecular Charge Transfer: Benchmarking CDFT, FODFT and FODFTB Against High-Level ab Initio Calculations. II," *Physical Chemistry Chemical Physics*, vol. 17, no. 22, pp. 14342–14354, 2015.

[316] R. Singh, J. Lee, M. Kim, P. E. Keivanidis, and K. Cho, "Control of the Molecular Geometry and Nanoscale Morphology in Perylene Diimide Based Bulk Heterojunctions Enables an Efficient Non-Fullerene Organic Solar Cell," *Journal of Materials Chemistry A*, vol. 5, no. 1, pp. 210–220, 2017.

[317] R. Shivanna, S. Shoaee, S. Dimitrov, S. K. Kandappa, S. Rajaram, J. R. Durrant, and K. S. Narayan, "Charge Generation and Transport in Efficient Organic Bulk Heterojunction Solar Sells with a Perylene Acceptor," *Energy Environ. Sci.*, vol. 7, no. 1, pp. 435–441, 2014.

[318] J. Hofkens, L. Latterini, G. De Belder, T. Gensch, M. Maus, T. Vosch, Y. Karni, G. Schweitzer, F. C. De Schryver, A. Hermann, and K. Müllen, "Photophysical Study of a Multi-Chromophoric Dendrimer by Time-Resolved Fluorescence and Femtosecond Transient Absorption Spectroscopy," *Chemical Physics Letters*, vol. 304, no. 1-2, pp. 1–9, 1999.

[319] G. S. Jas, E. J. Larson, C. K. Johnson, and K. Kuczera, "Microscopic Details of Rotational Diffusion of Perylene in Organic Solvents: Molecular Dynamics Simulation and Experiment vs Debye-Stokes-Einstein Theory," *Journal of Physical Chemistry A*, vol. 104, no. 44, pp. 9841–9852, 2000.

[320] M. W. Holman, R. Liu, L. Zang, P. Yan, S. A. DiBenedetto, R. D. Bowers, and D. M. Adams, "Studying and Switching Electron Transfer: From the Ensemble to the Single Molecule," *Journal of the American Chemical Society*, vol. 126, no. 49, pp. 16126–16133, 2004.

[321] M. W. Holman, P. Yan, D. M. Adams, S. Westenhoff, and C. Silva, "Ultrafast Spectroscopy of the Solvent Dependence of Electron Transfer in a Perylenebisimide Dimer," *The Journal of Physical Chemistry A*, vol. 109, no. 38, pp. 8548–8552, 2005.

[322] K. D. Belfield, M. V. Bondar, F. E. Hernandez, and O. V. Przhonska, "Photophysical Characterization, Two-Photon Absorption and Optical Power Limiting of Two Fluorenylperylene Diimides," *Journal of Physical Chemistry C*, vol. 112, no. 14, pp. 5618–5622, 2008.

[323] E. Fron, R. Pilot, G. Schweitzer, J. Qu, A. Herrmann, K. Müllen, J. Hofkens, M. Van Der Auweraer, and F. C. De Schryver, "Photoinduced Electron-Transfer in Perylenediimide Triphenylamine-Based Dendrimers: Single Photon Timing and Femtosecond Transient Absorption Spectroscopy," *Photochemical and Photobiological Sciences*, vol. 7, no. 5, pp. 597–604, 2008.

[324] J. M. Giaimo, J. V. Lockard, L. E. Sinks, A. M. Scott, T. M. Wilson, and M. R. Wasielewski, "Excited Singlet States of Covalently Bound, Cofacial Dimers and Trimers of Perylene-3,4:9,10-bis(dicarboximide)s," *Journal of Physical Chemistry A*, vol. 112, no. 11, pp. 2322–2330, 2008.

[325] H. Marciniak, X. Q. Li, F. Würthner, and S. Lochbrunner, "One-Dimensional Exciton Diffusion in Perylene Bisimide Aggregates," *Journal of Physical Chemistry A*, vol. 115, no. 5, pp. 648–654, 2011.

[326] K. E. Brown, B. S. Veldkamp, D. T. Co, and M. R. Wasielewski, "Vibrational Dynamics of a Perylene-Perylenediimide Donor-Acceptor Dyad Probed with Femtosecond Stimulated Raman Spectroscopy," *Journal of Physical Chemistry Letters*, vol. 3, no. 17, pp. 2362–2366, 2012.

[327] E. Vauthey, "Photoinduced Symmetry-Breaking Charge Separation," *ChemPhysChem*, vol. 13, no. 8, pp. 2001–2011, 2012.

[328] L. G. Kaake, D. Moses, and A. J. Heeger, "Coherence and Uncertainty in Nanostructured Organic Photovoltaics," *Journal of Physical Chemistry Letters*, vol. 4, no. 14, pp. 2264–2268, 2013.

[329] J. M. Lim, P. Kim, M. C. Yoon, J. Sung, V. Dehm, Z. Chen, F. Würthner, and D. Kim, "Exciton Delocalization and Dynamics in Helical π-stacks of Self-Assembled Perylene Bisimides," *Chemical Science*, vol. 4, no. 1, pp. 388–397, 2013.

[330] A. Schubert, V. Settels, W. Liu, F. Würthner, C. Meier, R. F. Fink, S. Schindlbeck, S. Lochbrunner, B. Engels, and V. Engel, "Ultrafast Exciton Self-Trapping Upon Geometry Deformation in Perylene-Based Molecular Aggregates," *Journal of Physical Chemistry Letters*, vol. 4, no. 5, pp. 792–796, 2013.

[331] L. G. Kaake, C. Zhong, J. A. Love, I. Nagao, G. C. Bazan, T. Q. Nguyen, F. Huang, Y. Cao, D. Moses, and A. J. Heeger, "Ultrafast Charge Generation in an Organic Bilayer Film," *Journal of Physical Chemistry Letters*, vol. 5, no. 11, pp. 2000–2006, 2014.

[332] P. E. Hartnett, A. Timalsina, H. S. Matte, N. Zhou, X. Guo, W. Zhao, A. Facchetti, R. P. Chang, M. C. Hersam, M. R. Wasielewski, and T. J. Marks, "Slip-Stacked Perylenediimides as an Alternative Strategy for High Efficiency Nonfullerene Acceptors in Organic Photovoltaics," *Journal of the American Chemical Society*, vol. 136, no. 46, pp. 16345–16356, 2014.

[333] C. Ramanan, C. H. Kim, T. J. Marks, and M. R. Wasielewski, "Excitation Energy Transfer Within Covalent Tetrahedral Perylenediimide Tetramers and Their Intermolecular Aggregates," *Journal of Physical Chemistry C*, vol. 118, no. 30, pp. 16941–16950, 2014.

[334] A. Schubert, M. Falge, M. Kess, V. Settels, S. Lochbrunner, W. T. Strunz, F. Würthner, B. Engels, and V. Engel, "Theoretical Analysis of the Relaxation Dynamics in Perylene Bisimide Dimers Excited by Femtosecond Laser Pulses," *Journal of Physical Chemistry A*, vol. 118, no. 8, pp. 1403–1412, 2014.

[335] Y. Zhong, M. T. Trinh, R. Chen, W. Wang, P. P. Khlyabich, B. Kumar, Q. Xu, C. Y. Nam, M. Y. Sfeir, C. Black, M. L. Steigerwald, Y. L. Loo, S. Xiao, F. Ng, X. Y. Zhu, and C. Nuckolls, "Efficient Organic Solar Cells with Helical Perylene Diimide Electron Acceptors," *Journal of the American Chemical Society*, vol. 136, no. 43, pp. 15215–15221, 2014.

[336] M. Son, K. H. Park, M. C. Yoon, P. Kim, and D. Kim, "Excited-State Vibrational Coherence in Perylene Bisimide Probed by Femtosecond Broadband Pump-Probe Spectroscopy," *Journal of Physical Chemistry A*, vol. 119, no. 24, pp. 6275–6282, 2015.

[337] C. Zhong, H. Choi, J. Y. Kim, H. Y. Woo, T. L. Nguyen, F. Huang, Y. Cao, and A. J. Heeger, "Ultrafast Charge Transfer in Operating Bulk Heterojunction Solar Cells," *Advanced Materials*, vol. 27, no. 12, pp. 2036–2041, 2015.

[338] Y. Zhong, M. T. Trinh, R. Chen, G. E. Purdum, P. P. Khlyabich, M. Sezen, S. Oh, H. Zhu, B. Fowler, B. Zhang, W. Wang, C. Y. Nam, M. Y. Sfeir, C. T. Black, M. L. Steigerwald, Y. L. Loo, F. Ng, X. Y. Zhu, and C. Nuckolls, "Molecular Helices as Electron Acceptors in High-Performance Bulk Heterojunction Solar Cells," *Nature Communications*, vol. 6, pp. 1–8, 2015.

[339] Y. Wu, R. M. Young, M. Frasconi, S. T. Schneebeli, P. Spenst, D. M. Gardner, K. E. Brown, F. Würthner, J. F. Stoddart, and M. R. Wasielewski, "Ultrafast Photoinduced Symmetry-Breaking Charge Separation and Electron Sharing in Perylenediimide Molecular Triangles," *Journal of the American Chemical Society*, vol. 137, no. 41, pp. 13236–13239, 2015.

[340] Z. Yu, Y. Wu, Q. Peng, C. Sun, J. Chen, J. Yao, and H. Fu, "Accessing the Triplet State in Heavy-Atom-Free Perylene Diimides," *Chemistry - A European Journal*, vol. 22, no. 14, pp. 4717–4722, 2016.

[341] T. Eder, T. Stangl, M. Gmelch, K. Remmerssen, D. Laux, S. Höger, J. M. Lupton, and J. Vogelsang, "Switching Between H- and J-Type Electronic Coupling in Single Conjugated Polymer Aggregates," *Nature Communications*, vol. 8, no. 1, p. 1641, 2017.

[342] N. Engel, S. I. Bokarev, A. Moguilevski, A. A. Raheem, R. Al-Obaidi, T. Möhle, G. Grell, K. R. Siefermann, B. Abel, S. G. Aziz, O. Kühn, M. Borgwardt, I. Y. Kiyan, and E. F. Aziz, "Light-Induced Relaxation Dynamics of the Ferricyanide Ion Revisited by Ultrafast XUV Photoelectron Spectroscopy," *Physical Chemistry Chemical Physics*, vol. 19, no. 22, pp. 14248–14255, 2017.

[343] D. H. Waldeck, "Photoisomerization Dynamics of Stilbenes in Polar Solvents," *Journal of Molecular Liquids*, vol. 57, no. C, pp. 127–148, 1990.